CRANFIELD UNIVERSITY

S TAKEUCHI

Computational Analysis of the Flow Around an Exposed Wheel

SCHOOL OF ENGINEERING

MSc by Research in the School of Engineering

MSc THESIS
Academic year: 2010

Supervisor: Dr. E. Shapiro
November 2010

CRANFIELD UNIVERSITY

SCHOOL OF ENGINEERING
MSc by Research in the School of Engineering
MSc THESIS

Academic Year 2010

S TAKEUCHI

Computational Analysis of the Flow Around an Exposed Wheel

Supervisor: Dr. E. Shapiro

November 2010

This thesis is submitted in partial fulfilment of the requirements
for the degree of Master of Science

Abstract

This thesis presents an investigation of RANS and LES models for the isolated rotating exposed wheel with moving ground with the aim of analyzing the flow behavior and comparing the results in cost/quality context. This is motivated by general demand for the drag reduction in automobile industry. In addition the demand is even stronger from high-performance car competition where the tyre wake has a great impact on total performance such as lift force or aerodynamic stability aspect.

Firstly, going through intensive grid optimization work, we successfully established a computational domain with 6.8 million cells with boundary layer mesh which have enough resolution for LES with given a Re number, $2x10^5$, allowing us to do a validation work with published past experimental data.

Overall the results indicate that adequate prediction of drag characteristics can be obtained with the reference experimental data providing a drag coefficient in the range of 0.56-0.63 and the overall computational envelope of RANS and LES models being 0.5-0.65 and 0.7-0.72 respectively.

Further investigation revealed that the drag results observed correlate quite well with the separation properties and the wake structure with LES simulation predicting, on average, earlier separation both over the top and the sides of the wheel and a more disturbed wake with a distinctive vortex shedding pattern and realisable k-e predicts overall a smaller separation, particularly over the sides of the wheel leading to a smaller drag coefficient.

We also evaluated computational efficiency for all turbulent models and found it is reasonably proportional to the complexity of the turbulent mode in the case of RANS. However, LES simulations with relatively coarse time-step are much faster than expected, approaching feasible level in the comparison with conventional RANS model.

Acknowledgement

Firstly I sincerely would like to thank Dr. Evgeniy Shapiro for his help throughout this project. I wouldn’t have achieved any progression without his advice and kind support. Furthermore, I also thank him for offering the place to go for off-site MSc project, which was precious opportunity for me to extend my boundary without compromising anything else.

I also take this opportunity to thank all people in Cranfield University offering many help to me. Especially, I express my honest appreciation to the member in the library including S.O.S. team who helped me in many aspects throughout this project.

Last but not least, I thank my partner and children for great help throughout this my academic project. Their warm hearts always support me to find the way forward.

Table of Contents

Table of Figures

Table of Tables

Nomenclature

C_d	drag coefficient
A	frontal area
C_p	pressure coefficient
Y^+	Non-dimensional wall distance
Re	Reynolds number
E	total energy
C_{Lw}	lift coefficient of the wheel
C_{dw}	drag coefficient of the wheel
D	diameter
C_S	Smagorinsky Constant

Greek Symbols

ρ	density
κ	kinetic energy
ε	dispassion rate
ν_T	turbulent viscosity
η	Kolmogorov length scale

Abbreviations

PIV	Particle Image Velocimetry
CFD	Computational Fluid Dynamics
LES	Large Eddy Simulation
RANS	Reynolds-Averaged Navier Stokes
MGP	Moving Ground Plane
DNS	Direct numerical Simulation
RSM	Reynolds Stress Model
ASM	Algebraic Reynolds stress Model
DES	Detached Eddy Simulation
URANS	Unsteady RANS
VLES	Very Large Eddy Simulation
RNG	Re-Normalization Group method
VMS-LES	Variational Multi-Scale closure LES
S-A model	Spalart-Allmaras model
RKE	Realizable κ-ε
SIMPLE	Semi-Implicit Method for Pressure-Linked Equations
SST	Shear-Stress Transport
S-L model	Smagorinsky-Lilly model
WALE model	Wall-adapting Local Eddy-Viscosity model

SF	Size Function
B-L	Boundary Layer
SGS	Subgrid Scale
HPC	High Performance Computing
CPU	Central Processing Unit
TKE	Turbulent Kinetic Energy
FFT	Fast Fourier Transform

1.0 Motivation & Objectives

The methodology allowing accurate simulation of the flow structure around a car is a subject of great importance in the automotive industry.

One of the design objectives is to achieve the reduction of the aerodynamic drag where we expect a contribution to the reduction of fuel consumption. Because of recent emphasis on energy efficiency, this problem is getting extremely important not just for commercial success but also for meeting environmental regulations such as carbon neutral policy in some countries.

Aerodynamic drag is a defining factor of fuel consumption at a given speed [2]. In motorsport, some racing governing bodies require that the wheels must be exposed to the airflow in various formula-type competitions, such as Formula One World Championship [3]. For this type of vehicle, aerodynamic wheel drag can account for 40 percent of the overall total drag [4]. Therefore, the drag induced by wheels is a major factor determining the overall racing car performance.

Exposed wheels not only contribute to the overall drag force but have a strong effect on the other forces which are important for high performance car control, such as the vertical aerodynamic force applied to body and wheels which is often referred to as the ‘down force’. High vertical force on exposed tyres results in larger steering and braking forces at a given friction coefficient of tyre. The remaining forces and moments acting on the car, such as side force increase its influence on controllability as the speed increases [2] [5].

Furthermore, Tsubokura et al [6] suggested that wheel wake structure could be the factor contributing to the control of the under flow, leading to the negative lift force which enhances the grip of tyres. This study also indicated that the drag on the wheels can amount to 50% of total drag by computational approach.

In motor sport, most representative performance index is lap-time, time to complete one circle in given circuit course. Figure 1 shows an example of the circuit designed for motor sport competitions such as Formula One Championship.

Figure 1 An example of motorsport circuit [7]

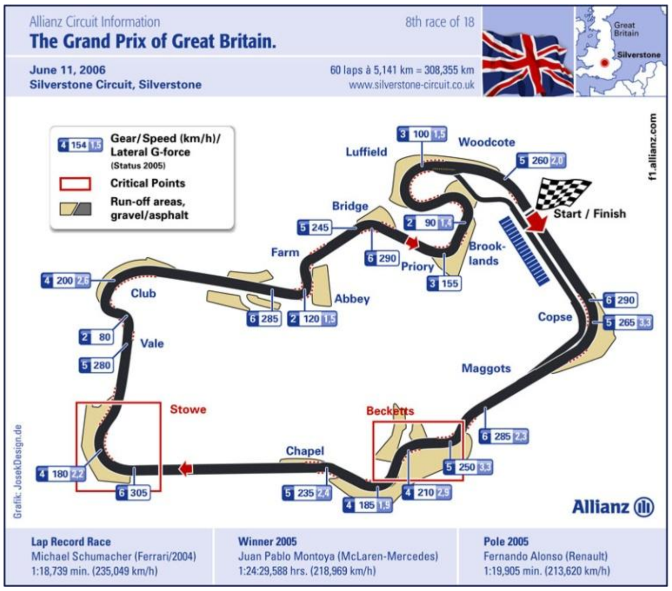

The figure also shows typical speed a Formula 1 car can achieve at specific points. It suggests 300km/h is achievable in this specific course. This information can be used to define typical Reynolds numbers for flows around exposed wheels.

Figure 2 also shows typical lap-time sensitivity to aerodynamic drag and down force. It suggests a 25% increase of Cd•A, drag normalized by speed, can increase the lap-time by one second. Given that the difference between lap-times of all competitors in Formula 1 is of the order of a couple of seconds in a typical competition, the improvement of aerodynamic drag can have a significant effect on the competition results. Therefore aerodynamics is a major issue for the motorsport-car development.

Figure 2 Downforce and drag versus lap time in a performance simulation [8]

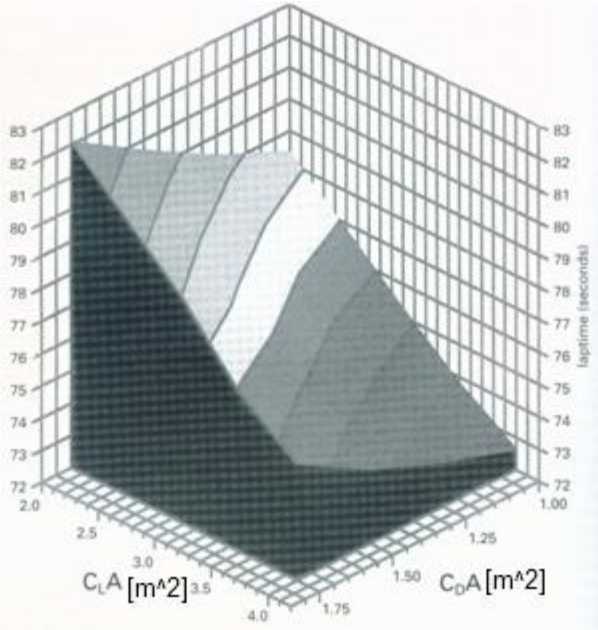

Exposed wheels have a significant effect on the aerodynamic drag and, therefore, significant impact on the performance in a motorsport competition.

However, the organizations governing this type of competitions control geometries of the wheel and the bodywork around it to give even condition for all competitors. As a particular example, FIA (Federation internationale de l’automobile) regulates the wheel geometry [3], which results in restriction of the wheel's width and diameter. In addition, the position of the tyre relative to the car main body is also restricted. Namely we cannot cover the wheel by any bodywork, which is called as ‘open-wheel’ condition in motor sport.

Figure 3 shows the current wheel dimensions defined in Formula 1 technical regulation.

.

Figure 3 Formula one technical regulation on wheel dimensions [3]

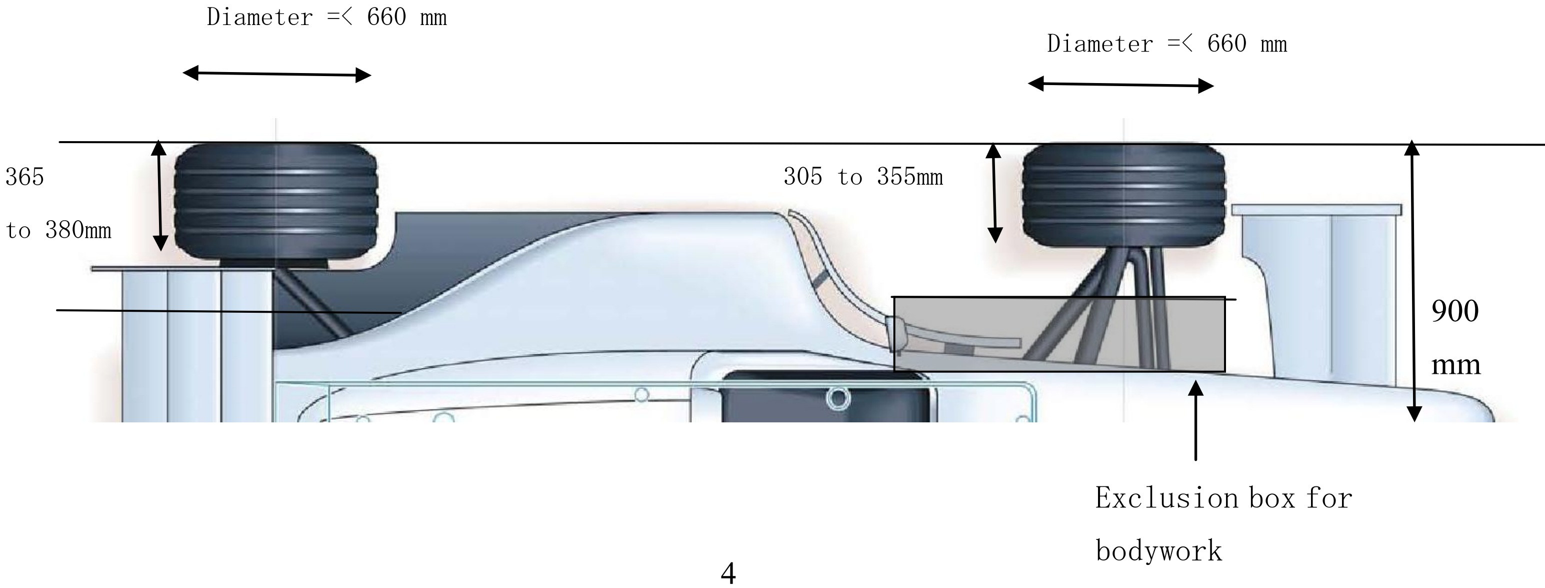

As seen in the figure, the regulations define the wheel dimensions and the exclusion box for the bodywork around front wheels. The former one naturally restricts frontal area of the wheel and the whole car because of the specification of the maximum width, 900mm from car centre line in this particular case. Wheel dimensions also restrict the area of contact patch between the tyre and the ground, which limits lateral and longitudinal forces generated by the tyre friction, so-called ‘tyre grip’. The contact patch also affects the flow features around the wheel [9] as we will show later.

The importance of aerodynamic drag for high performance car competitions and particular regulations enforcing the “open wheel” configuration provide the motivation for the academic research of the flow around an open wheel. The flow around the complete car body is very complicated and due to the complexity of the geometry is currently significantly time-consuming process once the time-accurate turbulence modeling approaches are employed although there are many state-of-the-art computational investigation in transient state in recent years (For example, see [42]). The exposed wheel condition provides an opportunity to consider an isolated wheel case which greatly reduces the geometrical complexity and makes it possible to consider a time-accurate simulation with iterative turnarounds. Even with the interaction with the car body neglected, such study should provide valuable insight into the flow features and help understand the flow-field around for the whole car case in such a way that the design process can achieve more efficient aerodynamics not only for high performance car but also passenger car, which results in CO2 mitigation for the automotive industry in the long run.

Experimental approach such as surface-pressure measurement, multi-hole pitot tube and Particle Image Velocimetry (PIV) have been and expected to be promising candidate to resolve the flow-field around wheel. However, the nature of isolated wheels, featured by rotating geometry with contact on the ground, gives complications to install measurement equipment such as telemetry system[1], which could prevent us from intensive geometrical study of the wheel itself and limits scalability to full-car representation in wind tunnel.

Accordingly, a possible future scenario is that computational simulation will be kept correlated with a representative result obtained experimentally with advanced methodology such as 3-dimentional PIV with higher temporal resolution and actual design process in automobile industry will take numerical simulation more to adapt to quick turnaround time for design modification.

In this case, the application of the most advanced CFD simulation available at the present is a significant step not only to enhance the methodology to understand the flow structure around a wheel but also to set strategies to develop geometries around wheels with effective manner in time and cost, therefore, improve industrial applicability.

The thesis concentrates on numerical approach to simulate an isolated wheel and refer to published experimental results from relevant literatures.

Although many CFD solvers in commercial sector as well as public domain solvers provide LES capability nowadays, ANSYS FLUENT is used in this project for its superiorities; 1) Numerous RANS options to compare with ;2) The scalability in parallel computation to expect large models, millions of grids for LES. It was worth mentioning that Star-CD (CD adapco) could be another candidate to give an equivalent capabilities and it is as popular as ANSYS FLUENT in automobile industry.

Based on the discussions in this chapter, the objectives of this project are:

- To model the flow around an exposed wheel using RANS and LES turbulence models available in the commercial CFD solvers (ANSYS FLUENT).
- To evaluate the accuracy of the LES and RANS simulation and the effect of the model parameters on the comparisons with available experimental data.
- To analyze the cost-efficiency parallel LES simulations in the context of open wheel modeling.

2.0 Literature Review

In this chapter, the publications are reviewed to understand past and on-going experimental and computational effort addressing the flow around an isolated tyre. Primary purpose of the review is to investigate the advantages which can be offered by the unsteady flow simulation, in particular, Large Eddy Simulation (LES) approach, in the context of Formula 1 external wheels modeling.

2.1 Overview of flow physics for a flow around an exposed wheel

The wheel geometry features a cylindrical shape with the contact area on the ground, ‘contact patch’. The rotational movement of the wheel complicates the experimental wind tunnel tests, which require moving ground plane (MGP) and a mechanical arrangement to spin wheel [1].

The flow structure around the rotating wheel is similar to that of a low aspect-ratio bluff body forming large wake structure, which also sheds four vortices from the corner in front view.

An early but comprehensive study has been carried out in 1970s by Fackrell et al [9], which concentrated on the investigation of the separation point on the tyre surface under rotating condition and 'jetting' phenomena from its contact patch by experimental and computational means. However the jet from the contact patch predicted by CFD was not observed by in the experiments at that point. Figure 4 shows a schematic of flow features around an isolated wheel with contact with ground suggested by Fackrell et al.

Figure 4 Flow features around a rotating wheel [9]

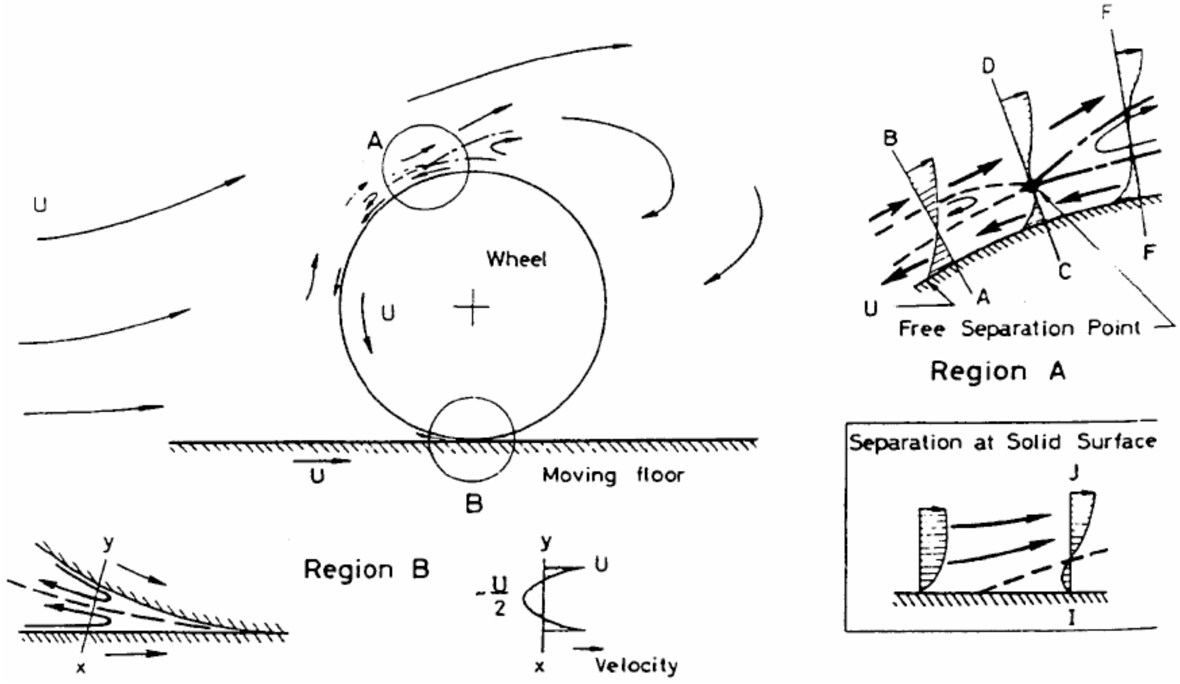

It has been also suggested by Fackrell et al [9], that the rotation added extra features to the flow structure. The rotation involves the movement of the separation points forward at the top of the wheel. The other notable change appeared in the scale of the wake structure. In the section parallel to the main flow, the wake is distorted in height resulting in much taller shape.

Cogotti [10] investigated an isolated wheel with and without the ground plane. It was found that the no-ground case gives the minimum of the static pressure around θ=100 deg., while the existence of the ground plane gives the minimum static pressure at θ=300deg, where θ=0 corresponds to foremost point in side view and the angle is measured clockwise. This upper suction peak is supposed to be induced by the flow bent up due to the large stagnation area of the front of wheel. Rotating tread also contributes to forward-shift of this suction peak.

Figure 5 shows an example of the measured wheel surface pressure distributions presented by Axon [11]. In the rotating case, Cp reached more than 1.0 in front of the contact to the ground, which is supposed to be caused by the rotating wheel and moving ground with viscosity effects.

Because of the high-pressure gradient around the peak area, special care should be paid to resolve the phenomena in case of a computational simulation as will be discussed later.

Figure 5 Experimental Cp results on rotating wheels on ground

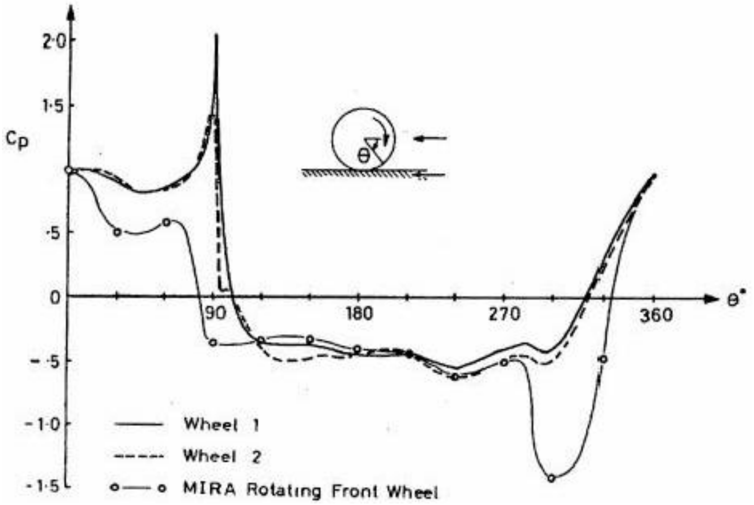

All flow features described above contribute to the pressure distribution around the wheel resulting in the change of lift and drag. For example, the separation point on the top of the wheel moves forward when the wheel is rotating and that reduces the lift of the wheel because of the earlier pressure recovery on the top surface.

Up to recent days, most notable effort was put on this problem by Mears, A.P. [1][12][13], who focused on the drag prediction based on the wake total pressure, followed by highly resolved PIV investigation. This work also includes 3D steady state CFD calculation which succeeded in predicting the rear jet phenomena from the contact patch with the optimization of y+ and wall condition settings. However, the numerical prediction of the separation point on the wheel is not in agreement with the PIV measurements, which results in delayed prediction of the point in CFD case. The author mentioned that advanced modeling strategy could improve the accuracy of the prediction. This underlines the necessity of advanced turbulence models.

In regard with the aerodynamic performance of the wheel in Formula 1 car, W.P. Keller investigated front wheel experimentally ($Re=0.65x10^6$) [24] (Figure6). This suggested that the flow structure consists of a significant region of separated flow, which formed by flow separating at the top and sidewalls of the wheel. Then, this separated region is found to join to the lower part of the wake form the contact patch

Figure 6 Smoke flow test results; representative plan view of wheel flowfield [24]

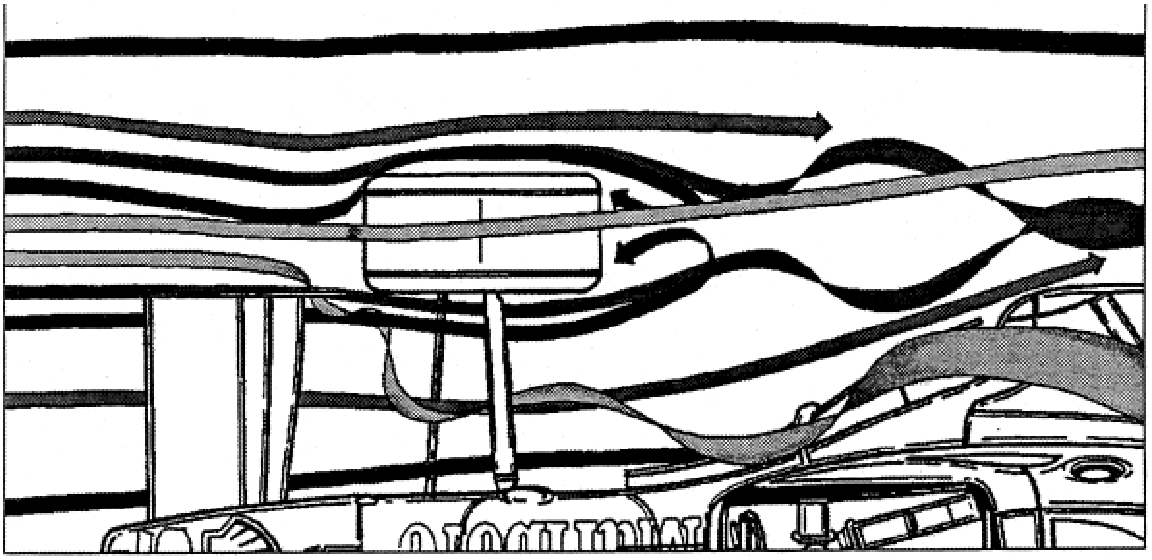

As a recent experimental achievement for isolated wheel case, Laser Doppler Anemometry (LDA) measurement was applied by Saddington et al [28].

It presented a trailing vortex system consisting of two contra-rotating vortex pairs, one and the upper vortex pair merged with the ground vortex pair within one diameter downstream of the wheel's axis as shown in Figure 7 (Re=6.8×10^5).

Figure 7 Proposed model of the trailing vortex system of an isolated wheel rotating in ground contact [26]

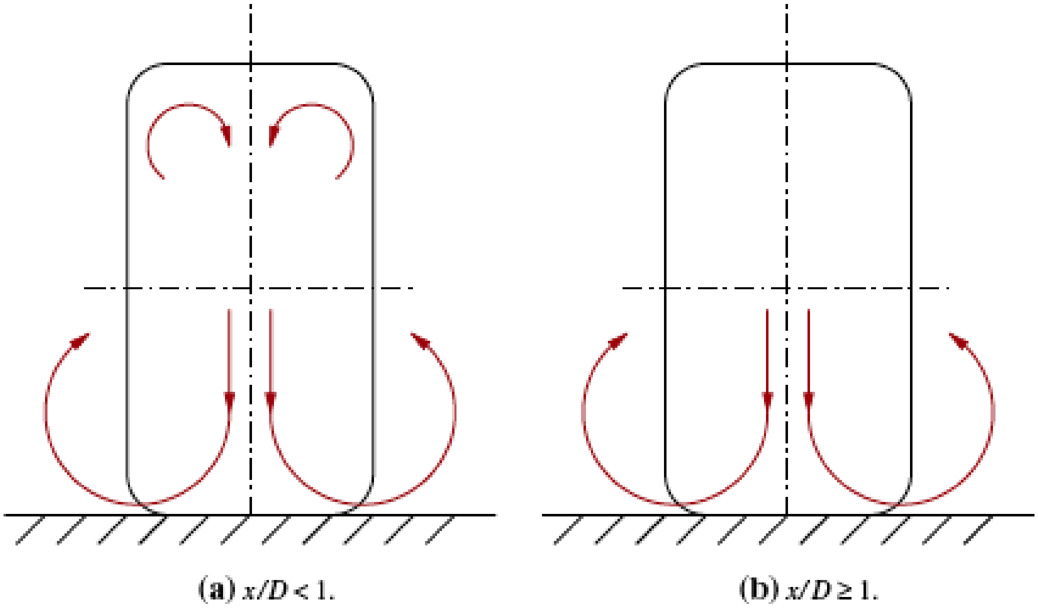
(a) $x/D < 1$.
(b) $x/D \geq 1$.

There are other vortices which are generated by the hub rotation along the wheel axis and then turned into longitudinal vortices by freestream. It is informative to note that those hub vortices were not observed by LDA measurement by Saddington et al [26]. This implies those vortices are relatively weak or significantly affected by the detail shape around the hub.

Although this thesis will focus on isolated tyre case as discussed in previous chapter, it is worth mentioning that there are many literatures investigating the aerodynamics of a wheel in situ on vehicles experimentally and computationally.

Axon et al [36] carried out a CFD investigation a wheel located within a wheelhouse cavity as a simplified representation of the wheel in situ on the car as well as a wind tunnel investigation based on same geometry. This study suggested that the rotating wheel within a wheelhouse cavity produced more drag than the stationary wheel. Other wheel arch model was investigated by Skea et al [37] and the case with wheel arch demonstrated significantly less disturbance to the free stream by CFD and experimental results. The experimental result also highlighted the implication of a transient flow nature under the wheel arch by static pressure distribution at the centre plane, which encourages time-accurate simulation on isolated wheel case to give an insight for the cause of this phenomenon.

Regarding a wheel in situ on complete whole car, Morelli [39] presented aerodynamics of the wheel and wheel-arch in the context which enables the design of passenger car to reduce aerodynamics interference of the wheels. This literature explained that the three pairs of counter rotating longitudinal vortices in the wake, which was discussed earlier in presented thesis earlier in isolated wheel case, are reduced to one pair on the ground and a single vortex from outer hub centre when the wheel is partially closed as seen on the common design of passenger car. This experimental research work suggested that the jetting vortices at the bottom could be reduced by the presence of a centrifugal fan arranged such a way induced circulation by the flow from the rim canceled that of the bottom jetting partially. Landström et al[40] carried out a detailed flow field investigation around the wheels in close proximity to the vehicle by omnidirectional 12-hole pressure probes. For front wheel, this experimental investigation identified two significant wake structures, a ground wake, which is supposed to originate from the jetting phenomena occurring at tyre contact patch, and one upper vortex structure as seen in what has been published to date. Results for rear wheel showed a reduction in total pressure concentrated towards the ground with an evidence of a jetting effect at the contact patch although the decrease in total pressure was not as significant as at the front .It also exhibited a noticeable increase in in-wash toward the ground once moving ground is activated, which gives an insight into the lower wake structure with moving ground.

Duncan et al [41] carried out a correlation work between on-road coast-down test and computational result regarding the aerodynamic drag design of the wheels in the situ of the whole car, which demonstrated a successful simulation as a reliable way correlated to experimental approach. This study suggested that an angular velocity boundary, which is a common representation of wheel rotation, gave sufficient for capturing the relevant phenomena compared to the true rotating approach.

Whilst those all publications about wheel-in-situ condition implies the importance to consider full-vehicle representation for industrial applicability, they also motivates isolated wheel case to understand how a wheel shape and its rotation induce the flow field because some major features such as jetting phenomena from the contact patch are still observed.

In the recent publications regarding the isolated tyre, Mears’ study in 2004[1] was found to give comprehensive experimental data including surface pressure, drag force and lift force along with the wake investigation by PIV and pressure measurement, successfully capturing phenomena specific for isolated wheel case such as rear jet phenomenon. Therefore we selected it for validation work in this thesis.

2.2 Numerical Modelling of exposed wheels

2.2.1 Motivation for computational study on flow-field around an isolated tyre

As discussed in the previous chapters, the flow-field of an exposed wheel with rotation is characterized by the separated turbulence flow. Although remarkable effort has been put into this problem in a series of experimental studies including surface pressure measurements with a telemetry system, five-hole pitot measurements and PIV by Mears, computational studies have so far been limited to time-averaged RANS turbulence models [13] in spite of availability of other advanced models we discuss below, presumably, due to the limitation of computational resource. In this chapter, based on the latest computational environment available, turbulence models are reviewed in the context of applicability for an isolated wheel flow-field.

In general, the following turbulence modeling approaches are published and most of them are available in commercial solvers.

- Direct numerical Simulation (DNS) [29]
- Reynolds-averaged Navier-Stokes models

  - Zero-equation Reynolds-averaged Navier-Stokes model (Prandtls Mixing Length Model[31])
  - One-equation Reynolds-averaged Navier-Stokes model (Modeling only for turbulent kinematic energy)
  - Two-equation Reynolds-averaged Navier-Stokes model (K-ε model and k-ω model)
  - Reynolds stress model (RSM)[30]
  - Algebraic Reynolds stress model (ASM)[31]
- Large Eddy Simulation (LES)
- Detached Eddy Simulations (DES)

2.2.2 General discussion of RANS turbulence model

The flow of constant-property Newtonian fluid is governed by the Navier-Stokes equations, which is derived from the momentum equation based on Newton's second law, together with the equations of continuity which corresponds to mass conservation law.

The equation of continuity is described as follows:

$$\frac{\partial u_i}{\partial x_i} = 0 \tag{2.1}$$

Where u_i and x_i denotes the velocity in i th direction and the suffix implies summation.

And Navier-Stokes equation in in compressible flow is described as follows:

$$\frac{\partial u_i}{\partial t} + u_j \frac{\partial u_i}{\partial x_j} = -\frac{1}{\rho}\frac{\partial p}{\partial x_i} + \nu \frac{\partial^2 u_i}{\partial x_j \partial x_j} + F_i \tag{2.2}$$

where u_i , p, ν and F_i denote the velocity in the i th direction, pressure, kinematic viscosity and body force in i th direction , respectively. The left-hand side represents

Since turbulence flows are characterized by random fluctuations, statistical approach has been studied extensively in the past. The basis of this approach is formed by ensemble averages in order to separate the mean quantities from fluctuations. This process leads to a well-known Reynolds-averaged Navier-Stokes (RANS) family of turbulence models. After the averaging, the momentum equation (2.2) becomes [14]:

$$\frac{\partial \overline{u}_i}{\partial t} + \overline{u}_j \frac{\partial \overline{u}_i}{\partial x_j} = -\frac{1}{\rho}\frac{\partial \overline{p}}{\partial x_i} + \nu \frac{\partial^2 \overline{u}_i}{\partial x_j^2} - \frac{\partial}{\partial x_j}(\overline{u_i' u_j'}) \qquad (2.3)$$

where u_i is the velocity in the ith direction and the directional tensors, x_i is defined for ith directions. Mean and fluctuating quantities are indicated by the overbar and the prime, respectively.

The third term of the right hand of the equation $\overline{u_i' u_j'}$ represents Reynolds stress tensor. It adds 6 unknown variables to be determined by additional equations forming the turbulence closure.

In the first of RANS approaches, the Reynolds stresses are obtained from a turbulent-viscosity model, which is based on the turbulent –viscosity hypothesis. According to this hypothesis, the Reynolds stress is given by

$$\overline{u_i u_j} = \frac{2}{3}k\delta_{ij} - \nu_T\left(\frac{\partial \overline{u}_i}{\partial x_j} + \frac{\partial \overline{u}_j}{\partial x_i}\right) \qquad (2.4)$$

where k is turbulent kinetic energy and ν_T is the turbulent viscosity, or eddy, viscosity, respectively.

RANS modeling requires additional assumptions in order to determine ν_T. and many models have been suggested.

the *k*- ε model is arguably the simplest complete turbulence model. Although one-equation models such as the mixing-length model [15] are less computationally expensive due to the smaller number of the equations required to close the system, the applicability of these models is typically limited.

In the standard *k*- ε model, υ_T is given by

$$\nu_T = C_\mu \frac{k^2}{\varepsilon} \tag{2.5}$$

where C_μ is a model constant and ε is the dispassion rate. k and ε are determined by their own transport equation as follows:

$$\frac{\partial k}{\partial t} + \frac{\partial(\overline{u}_i k)}{\partial x_i} = \frac{\partial}{\partial x_i}\left\{\left(\nu + \frac{\nu_T}{\sigma_k}\right)\frac{\partial k}{\partial x_i}\right\} + P_k - \varepsilon \tag{2.6}$$

$$\frac{\partial \varepsilon}{\partial t} + \frac{\partial(\overline{u}_i \varepsilon)}{\partial x_i} = \frac{\partial}{\partial x_i}\left\{\left(\nu + \frac{\nu_T}{\sigma_\varepsilon}\right)\frac{\partial \varepsilon}{\partial x_i}\right\} + C_{\varepsilon 1}\frac{P_k \varepsilon}{k} - C_{\varepsilon 2}\frac{\varepsilon^2}{k} \tag{2.7}$$

where P_k represents the generation of kinetic turbulence energy due to mean flow gradient. σ_k , σ_ε , $C_{\varepsilon 1}$ and $C_{\varepsilon 2}$ are model constants. Launder and Sharma(1974)[16] suggested the standard value for these constants derived empirically.

Notice that the first, second and third terms on the right-hand side of (2.6) and (2.7) correspond to the transport, production and dissipation terms, respectively.

Although the k-ε model is usually acceptably accurate for simple flows, it can be quite inaccurate for complex flow due to turbulence-viscosity hypothesis itself and the ε equation. Over the years, many modifications have been suggested for the standard k-ε model but most of them contribute to modeling of a particular class of flows, and not necessary lead to superior overall performance.

In ANSYS FLUENT, various two-equation RANS models are available and some of them are to be evaluated with isolated wheel case in this thesis. Their features will be discussed in next chapter.

Reynolds-stress models (RSM) solve model transport equation for the individual components of the Reynolds stresses and the dissipation ε. Therefore, they don’t include the turbulent-viscosity hypothesis, which is a weak point of two equation models discussed above. For curved flows, sudden changes in strain rate and rotation, RSM is expected to give more accurate results than one or two equation models. It could be applicable to a complex flow-field such as an isolated rotating wheel case

However, the fidelity of RSM predictions is still limited by the closure assumptions employed to model various terms such as modeling of pressure-strain and dissipation-rate term, which can compromise accuracy of RSM predictions [14].

RANS modeling approach can be used for unsteady flow (Unsteady RANS, or URANS). However, it is usually limited to capture large-scale unsteadiness only as it filters the solution in time over a certain time window resulting in partially resolved unsteadiness.

2.2.3 Direct numerical simulation

Direct numerical simulation (DNS) implies numerical solution of the Navier-Stokes equations which resolves all scales of motion. DNS provides the deterministic method that cannot be equaled by other approaches. However, the drawback is the high computational cost. In DNS, the N-S equations are solved directly with refined meshes capable of representing all turbulence length scales up to the Kolmogorov microscale [17], which defines the smallest lengthscale of eddies at which the dispassion occurs. This requirement leads to the number of grid points in 3-D proportional to

$$N = \mathrm{Re}^{9/4} \tag{2.8}$$

where Re is the Reynolds number based on the large scale of the flow. In an isolated tyre case, The Reynolds number can reach 10^6, hence, the required number of grid points is expected to be in the order of 10^{13}. The computational demands of DNS are far above the capabilities of modern supercomputers.

2.2.4 Large eddy simulation

In large-eddy simulation (LES), the larger three-dimensional unsteady turbulent motions are directly represented, while the effects of the smaller motions are modeled [18]. Therefore LES can be expected to be more accurate and reliable than RANS models for flow in which large-scale unsteadiness is dominant such as the flow over bluff bodies with unsteady separation and vortex shedding, which are observed in an isolated wheel case as discussed in previous chapter.

LES employs the following assumption to model the smaller motions.

Figure8 is a schematic energy spectrum on wave number space, which can be divided into three regions: the region of energy containing large eddies, followed by the inertial subrange and energy dispassion range [17].

The inertial subrange is characterized by a straight line, known as the Kolmogorov's -5/3 law,

$$E(\kappa) = \alpha \varepsilon^{2/3} \kappa^{-5/3} \tag{2.9}$$

where α is constant. In LES, filtering methods are deployed such the way the subgrid stress corresponding to sub-filter components of the flow represents the wavelengths in the solution which are in in the dissipation range or at least fa down the inertial range.

Figure 8 Energy spectrum vs wave number space (log-log scales)[17]

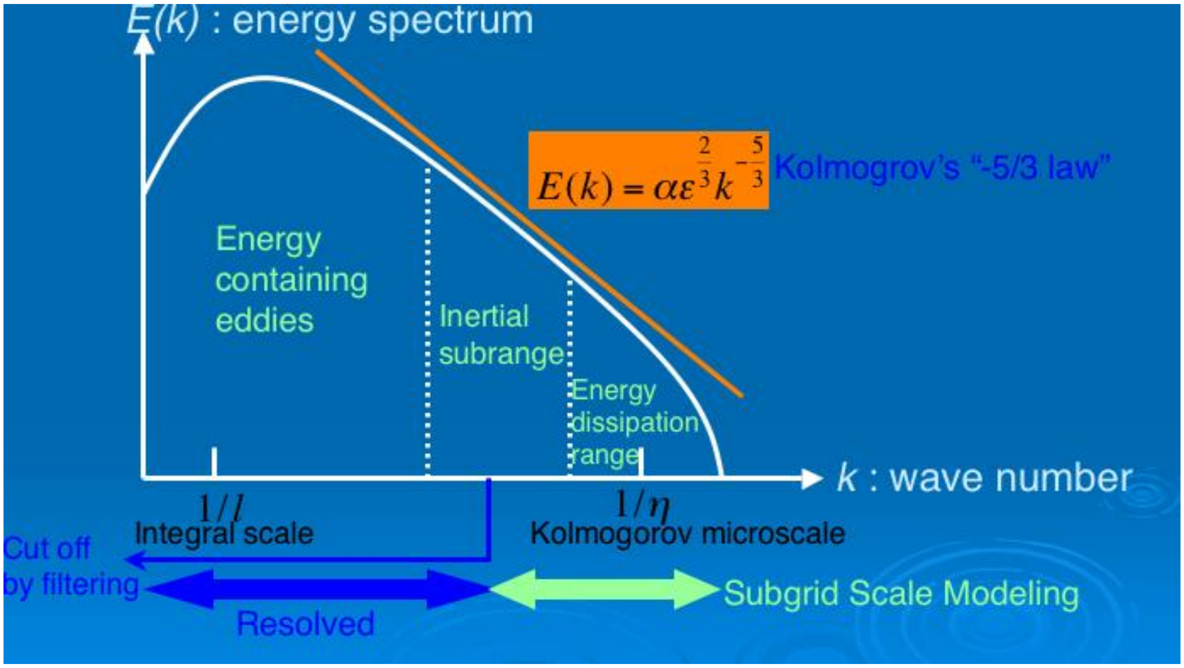

Thus, there are two major steps involved in the LES analysis: filtering and subgrid scale modeling. Using one-dimensional notation for simplicity, the filtered variable f may be written as:

$$\bar{f} = \int G(x,\xi) f(\xi) d\xi \qquad (2.10)$$

with filter function G satisfying

$$\int G(x,\xi)d\xi = 1 \tag{2.11}$$

Traditionally, filtering is carried out using the box function, Gaussian function or Fourier cutoff function (See, for example, [15])

Filtering operation yields the momentum equation as follows:

$$\frac{\partial \bar{u}_i}{\partial t} + \frac{\partial}{\partial x_i}(\bar{u}_i \bar{u}_j) = -\frac{1}{\rho}\frac{\partial P}{\partial x_i} + \frac{\partial}{\partial x_j}\left(\nu \frac{\partial \sigma_{ij}}{\partial x_j}\right) - \frac{1}{\rho}\frac{\partial \tau_{ij}}{\partial x_j} \tag{2.12}$$

where σ_{ij} is the stress tensor due to molecular viscosity and τ_{ij} is the subgrid-scale stress, which introduces 6 additional unknowns as a result of filtering operation and requires modeling.

The simplest modeling method is called the Smagorinsky model (1963). This method relies on the linear eddy-viscosity model and analogy to the mixing-length hypothesis to represent the subgrid-scale stress. This Smagorinsky model also forms the basis of following more advanced models. The details of subgrid-scale stress modeling in this thesis will be discussed in the following chapter.

As LES requires resolving inertial range, the grid resolution should be fine enough to cover this range. Regarding wall-bounded flow, this requirement is intensive because the scale of the important near-wall motion decreases as Re number increases. The required resolution can be difficult to predict a-priori however we will evaluate the spectral properties of the solution a-posteriori in order to demonstrate that the inertial range with the corresponding -5/3 exponent is observed in computations.

For the general 3-D flows in engineering application, the computational resource required to solve the LES equations is much greater than that required for RANS. With the growth of the computational power available many commercial CFD solvers started to deploy ‘LES option’. However, for the complicated geometries and large Reynolds number the limitations of the computational resource usually lead to maximum grid sizes corresponding to Very Large Eddy Simulation (VLES) level.

2.2.5 The applicability of the modeling approaches

As RANS describe flows in a statistical sense leading to ensemble-averaged pressure and velocity field hence RANS cannot distinguish quasi-periodic large scale and turbulent chaotic small-scale features. This makes a significant disadvantage for the flow field is governed by both scales such as a bluff body flow.

Steady RANS as it says cannot describe the unsteady characteristics of the flow hence unsteady phenomena are not reproduced [25]. In isolated wheel case, unsteady phenomena such as vortex shedding are expected to be a dominant feature to look into. Therefore the expected accuracy is significantly limited by nature.

On the other hand, LES operates with unsteady flow fields for the higher computational cost. Despite of the advantage of the expected accuracy, computational cost should be evaluated to leave scalability to industrial applications.

2.2.6 Overview of the existing state-of-art studies of an isolated wheel & LES in the automotive flows context

The k-e RNG turbulence model on this problem and extensive comparison with many available turbulence models is carried out by Skea et al [38]. He suggested k-ω model as best case at that point, which showed reasonably good agreement in pressure profile at centre section as shown figure 8 below.

Figure 9 Centre Surface Static Pressure Distribution Obtained Through Experiment and CFD [15]

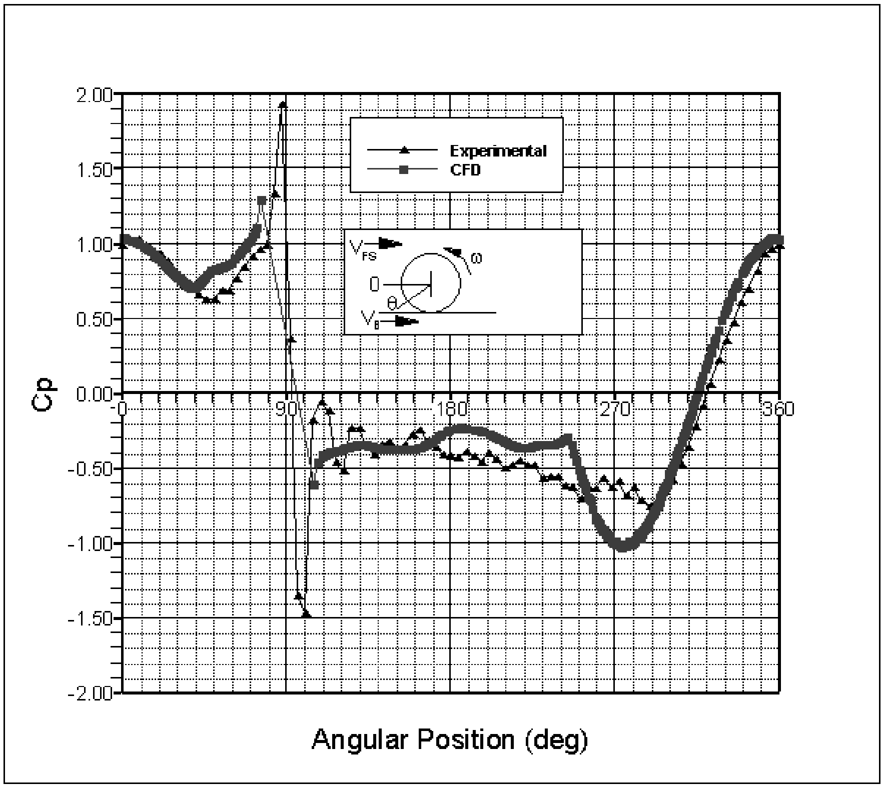

A new hybrid RANS/LES approach, blending between k-e RANS and the Smagorinsky VMS-LES (LES with variational multi-scale closure) is presented by Marcello Meldi in 2007[32]. In this study, using a circular cylinder at Re=140000 as a benchmark model, the sensitivity of the model to blending parameter variations, grid refinements and preconditioning changes were investigated. The results were compared with those obtained using the detached eddy simulation (DES) approach and with experimental data available in the literature. This approach showed closer results to experimental data than DES even coarser grid resolution in terms of the accuracy of the boundary-layer’s angle of separation prediction.

One of latest accomplishments on LES application to automobile flows is the LES study of unsteady flow around a Formula 1 car carried out by Tsubokura et al., which involved around 120 million cells to fill computational domain. The computation is carried out on the Earth Simulator in Japan, which has 40Tflops as total peak performance. The result shows excellent agreement with experimental result in lift prediction, estimating only about 1% larger number. However, the drag has been over-predicted by 10% approximately.

.

In 1998, Axon et al [26] carried out an extensive comparisons between CFD and experimental results (Fackrell's results [9]) in surface static pressure and wake total pressure for rotational and static wheel case, which suggested RNG k-ε turbulent model (Re=5.3x10^5 with 538350 structural meshes) could give us a good qualitative results to experimental results as shown in Table 1 as well as an evidence to support flow details found experimentally at the front contact point of the wheel-ground interface, being called 'jetting' phenomena as in Fackrell's experimental results [9].

Table 1: Computational Force Coefficients and Comparison with Experimental Data [26]

	$C_{L\omega}$	% Error in $C_{L\omega}$	$C_{D\omega}$	% Error in $C_{D\omega}$
Rotating	0.476	8.2	0.602	3.8
Stationary	0.630	-17.1	0.707	-8.2

As another recent achievement, McManus et al [27] computed an isolated wheel in contact with the ground as the experiments of Fackrell and Harvey by Unsteady Reynolds-Averaged Navier-Stokes (URANS) and presented a detailed picture of the flow structures shown in Figure10. The comparison with the experimental result suggested the agreement on surface pressure near to the line of contact was poor hence the lift coefficient showed greater error than drag coefficient (Table 2).

Table2 also suggested the drag coefficient computed is different from the experimental result by 8% and 17% approximately in Spalart-Allmaras and Realizable k-ε respectively. So, in this URANS study, Spalart-Allmaras showed an advantage in accuracy over realizable k-ε model although the mesh-resolution dependency was also greater with Spalart-Allmaras. Interestingly, refinement of the mesh didn’t lead to improvement for the accuracy with realizable k-ε model.

This could suggest the applicability of URANS on isolated wheel case is questionable to improve accuracy irrelevant to the mesh resolution. One possible explanation is RANS approach (ensemble-averaged turbulence flow field) cut off smaller scale of the turbulent flow which still impacts on dominant features such as the flow separation. The adaptation of LES, one of the objectives in this thesis, is expected to give more accuracy because by definition it could resolve all scales in inertial range by finer mesh resolution.

Figure 10 Schematic diagrams of the general isolated wheel flow with rotation [27]

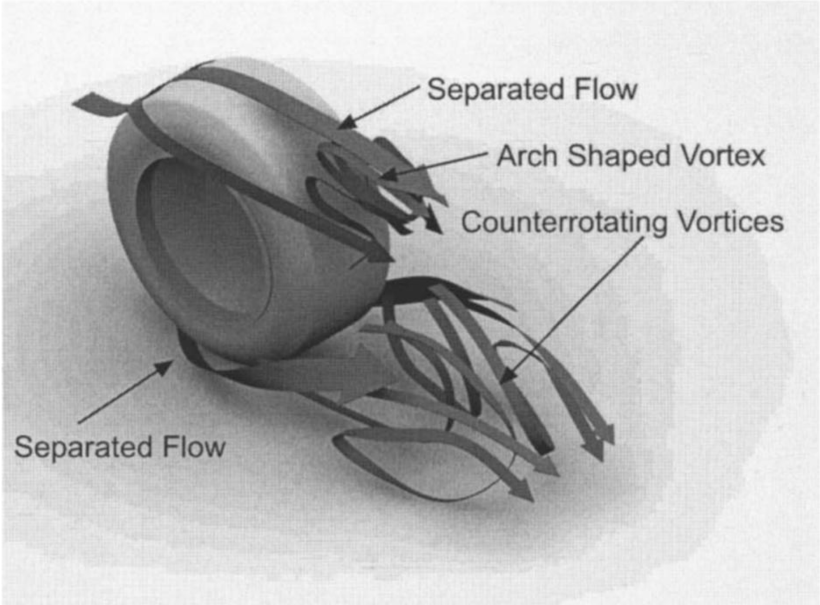

Table 2 Time averaged pressure lift and drag force coefficients computed by Spalart-Allmaras (S-A) model and Realizable k-ε (RKE) model

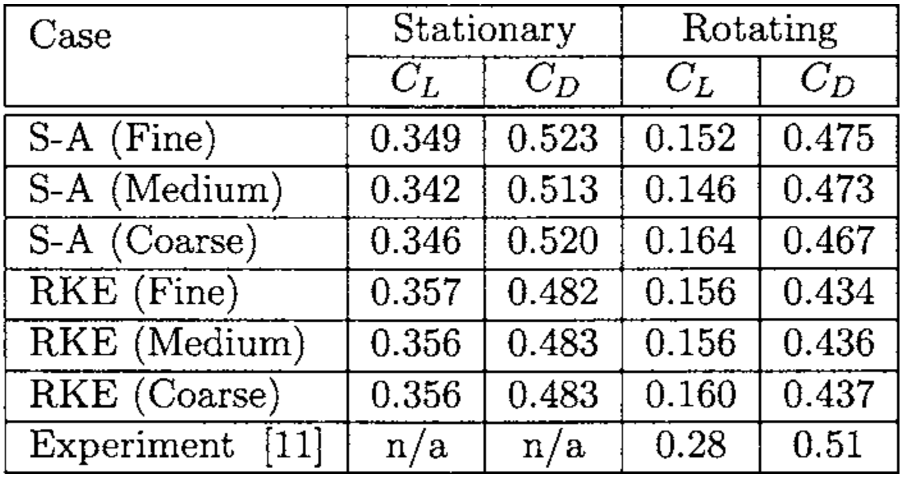

Case	Stationary		Rotating	
	C_L	C_D	C_L	C_D
S-A (Fine)	0.349	0.523	0.152	0.475
S-A (Medium)	0.342	0.513	0.146	0.473
S-A (Coarse)	0.346	0.520	0.164	0.467
RKE (Fine)	0.357	0.482	0.156	0.434
RKE (Medium)	0.356	0.483	0.156	0.436
RKE (Coarse)	0.356	0.483	0.160	0.437
Experiment [11]	n/a	n/a	0.28	0.51

3.0 Methodology

3.1 Introduction

As discussed in previous chapter, incompressive fluid flow can be described by continuity and Navier-Stokes equations (equations 2.1 and 2.2) but capturing all scales of motions requires excessive computational demand which is far beyond our reach at present time. On the other hand, all past literature suggested separated flow with strong unsteadiness around isolated tyre case hence numerical approach should be arranged to resolve this flow field in space and time. Hereafter computational methodology will be discussed to meet the condition specific for isolated tyre case as par defined in objectives in earlier chapter.

3.2 Overview of numerical approach in ANSYS FLUENT

As our primary target solver is ANSYS FLUENT (version 12.1.4) as discussed in chapter one, it is informative to give an overview of its numerical method. ANSYS FLUENT uses a control-volume-based technique. For example, the unsteady conservation equation for transport of a scalar quantity ϕ for an arbitrary control volume can be written as follows[33]:

$$\int_V \frac{\partial \rho\phi}{\partial t} dV + \oint \rho\phi\vec{v}\cdot d\vec{A} = \oint \Gamma_\phi \nabla\phi \cdot d\vec{A} + \int_V S_\varphi dV \qquad (3.1)$$

where

ρ = density

$\vec{v}$ = velocity vector

$\vec{A}$ = surface area vector

Γ_ϕ= diffusion coefficient for ϕ

$\nabla\phi$=gradient of ϕ

S_ϕ = source of ϕ per unit volume

For spatial discretization, ANSYS FLUENT uses upwind scheme to interpolate the value on cell face from stored cell centre value. As a default, ANSYS FLUENT takes first order upwind scheme, which set the face quantities equal to the upwind cell-center value. ANSYS FLUENT also has second-order upstream scheme where the face value is computed using the gradient of cell-centered value to offer higher-order accuracy. Due to high demand for accuracy, second order scheme will be used throughout in this project where available.

On the other hand, in the case of LES, central-differencing scheme is ideal for improved accuracy. In central differencing scheme, face value is computed by two adjacent cell value and their gradients hence low numerical diffusion is expected at the cost of computational instability which could lead to unphysical oscillations. ANSYS FLUENT uses Bounded central differencing scheme to overcome this possible numerical instability [33].

In transient simulations, temporal discretization is considered while the spatial discretization for the time-dependent equation is identical to the steady-state case. In LES simulation in this thesis, a second order implicit method is used, which can be written as follows.

$$\frac{3\phi^{n+1} - 4\phi^{n} + \phi^{n-1}}{\Delta t} = F(\phi) \tag{3.2}$$

where

ϕ = a scalar quantity

n+1 = value at the next time level, $t + \Delta t$

n = value at the current time level, t

n-1 = value at the previous time level, $t - \Delta t$

The resulting scheme is second order accurate in space and time. This might prove to be a disadvantage of the CFD solver used as in general higher order schemes are required for LES computations [34].

3.3 Computational schemes for incompressible viscous flow

In the computation for incompressible flow, one of widely used algorism is SEMI-IMPLICIT METHOD FOR PRESSURE-LINKED EQUATIONS (SIMPLE). This algorism obtains a solution as follows.

(a) Guess the pressure at each grid point

(b) Solve the momentum equation to obtain velocity

(c) Compute pressure correction until it satisfy the equation of continuity under computed velocity and guessed pressure

(d) Correct pressure and velocity components by obtained pressure correction

Steps (b) to (d) are iterative processes where the speed of convergence could be unsatisfactory therefore improved approximations have been suggested such as SIMPLE-Consistent (SIMPLEC).

3.4 RANS models

As discussed earlier, the applicability of standard κ-ε model for complex flow is limited due to lack of the consideration for anisotropic effect of near-wall region, for example. Therefore many derivatives of standard κ-ε model have been developed to overcome those weaknesses.

In ANSYS FLUENT, various RANS models are available. The following RANS models have been selected for evaluation in order to provide a representative broad description of the capacity:

One-equation models:

*Spalart-Allmaras model

Two-equation models

*Realizable k-ε model

*k-ω model

*Shear-Stress Transport (SST) k-ω model

Transitional models:

*k-kl-ω Transition model

*Transition SST model

Table3 gives an overview for the models used for the computation ion this thesis.

Table 3 the turbulence models used for the computations [33]

models	**Features and advantages**
Spalart-Allmaras model	One-equation turbulence model solving the kinematic eddy viscosity. The near –wall gradients of the transported variable are much smaller than those in k-ε and k-ω model, which makes the model less sensitive to numerical errors when no-layered mesh is used near wall.
Realizable k-ε model	This adapted certain mathematical constrains on the Reynolds stresses to ensure the realizability, not to violate the physics of turbulent flows, alongside new transport equation for the dissipation rate, which has been derived from an exact equation for the transport of the mean-square vorticity fluctuations. This model would provide superior performance for flows involving rotation, boundary layers under strong adverse pressure gradient, separation and recirculation.
k-ω model	This is an empirical model base on model transport equation for the turbulence kinetic energy and the specific dissipation rate, which can also be thought of as the ratio of ε to k. In ANSYS FLUENT, the k-ω model is based on Wilcox k-ω model which

	incorporates modifications for low-Reynolds-number effects, compressibility and shear flow spreading.
SST k-ω	This uses the k-ω model in the near-wall region and the k-ε model in the far field. The SST k-ω model is more accurate and reliable for a wider class of flows, such as adverse pressure gradient flow, than the standard k-ω model.
k-kl-ω Transition model	This solves transport equations for turbulent kinetic energy, laminar kinetic energy and the inverse turbulent time scale. This model is used to predict boundary layer development and calculate transition onset hence the transition of the boundary layer from a laminar to a turbulent regime.
Transition SST model	This is based on the coupling of the SST k-ω transport equations with the transport equations for the intermittency and the transition onset criteria in terms of momentum-thickness Reynolds number.

The application of the transition models above is of interest for the isolated wheel case in this thesis as it will be computed with relatively low Reynolds number, $2x10^5$, to incorporate experimental data for the validation.

3.5 Near-Wall Treatment

Generally no-slip condition on solid wall affects mean flow in significant manner. On the other hand, the presence of walls also play great part role in turbulent flow. Basically, viscous damping reduces the fluctuation of the velocity while the larger gradient near walls produces turbulent kinetic energy. In ANSYS FLUENT, there are two approaches for modeling near walls, wall functions and near-wall model. Wall functions method uses semi-empirical formula to bridge the viscosity-affected region between solid wall and the fully-turbulent region. In high Reynolds number flow, this approach saves significant computational cost as near-wall region is most demanding area to resolve due to rapid change of variables. This also improves applicability of the turbulence models without near-wall treatment.

In spite of the practicality as seen in industrial application at the present day, wall functions have significant disadvantage on applicability when the flow cannot retain ideal conditions such as severe adverse pressure gradient leading separation. This is the case for isolated tyre flow.

Therefore this thesis adapts the latter method, near-wall model for all following turbulent model evaluation, which resolve all way through the boundary layer to the wall with the meshes fine enough to resolve viscous sub-layer. So the target mesh resolution is then based on Y^+ of order 1.

3.6 LES

As discussed in chapter 2.2.4, in LES subgrid-scale stress is modeled while it resolves large eddies. In this thesis, Smagorinsky-Lilly model and Wall-adapting Local Eddy-Viscosity (WALE) model are evaluated for isolated wheel case. In Smagorinsky-Lilly model, the eddy-viscosity is calculated by resolved the rate-of-strain tensor and the mixing length which includes a constant called Smagorinsky constant, C_s. Although C_s=0.17 is suggested for homogeneous isotropic turbulent flow, this constant value is not a universal constant value. Therefore an advanced model called Dynamic Smagorinsky-Lilly model is developed to compute Cs based on the information provided by the resolved scales of motion. This model is available in ANSYS FLUENT as dynamic stress option in which user doesn’t need to set Cs value.

The WALE model is other eddy-viscosity-type subgrid modeling which is designed to return the correct wall asymptotic behavior for wall bounded flows.

It should be noted that LES in this thesis use no perturbations option for the inlet boundary condition as the turbulence is mainly generated by the body boundary and shear layers although the turbulence intensity at the inlet could play a role on turbulent flow field in general.

For the sake of completeness, the full configuration of the solver is presented in Appendix A.

4.0 Description of Computations

4.1 Problem formulation

All investigation in this thesis refers to a specific geometry and measurement condition from Mears' Thesis [1] representing advanced and comprehensive study for an isolated wheel flow-field in computational and experimental aspects to present time.

- Moving ground, freestream and circumferential velocities are set to $14.7ms^{-1}$.
- The wheel has a diameter of 0.246m giving a test Reynolds number of $2x10^{5}$.
- The aspect ratio of the wheel is 0.53, which is typical of a Formula One front wheel.
- Rotational moving wall condition applied on the wheel surface corresponding to the grand speed (119.5 rad/s).

Note that 14.7m/s (52.9 km/h) is a very relatively low speed for a typical F1 race. However there are limitations associated with the experimental setup.

The following measurements are adapted to evaluate the correlation between experimental and computational results.

- The lift and drag coefficient of the wheel
- The surface pressure distribution on the center section of the wheel

4.2 Grid Generation

4.2.1 Initial grid generation for familiarization

An initial attempt has been conducted with parameters as reported by Mears' case[18] as follows:

- Calculation domain is defined as shown in Figure 11, which forms a box shape with 10D x 10D inlet and 30D longitudinal length where D is the diameter of the wheel. The wheel spanwise position corresponds to the center of the domain and streamwise position is at 10D from the inlet.
- The wheel is raised from the ground by 1.5mm and a plinth is added to fill the gap to the ground to ease the mesh generation along the boundary of contact patch (see Figure 13 and 14 for details of the mesh around contact patch).
- Tetrahedral cells were chosen. The mesh size of the wheel surface is set as 1mm and it grows up to 200mm toward the domain boundaries with the growth ratio set to 1.1.

Figure 11 Calculation domain

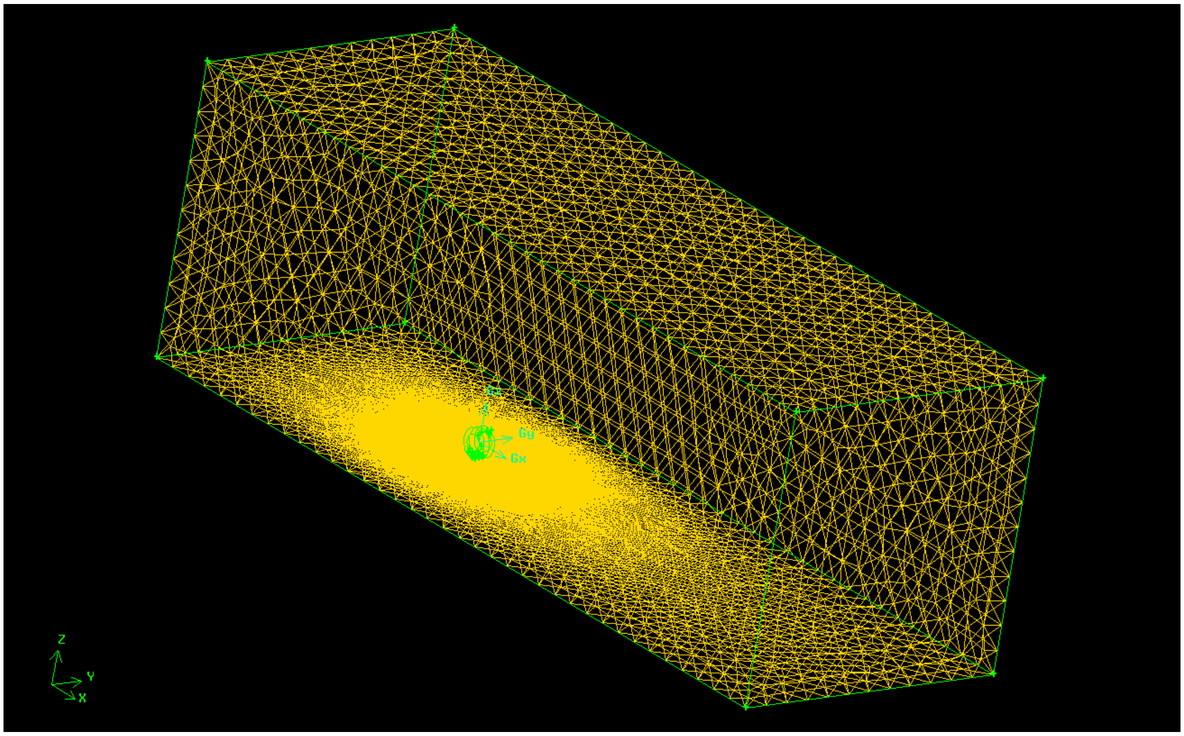

Figure 12 Cut-section at the center line

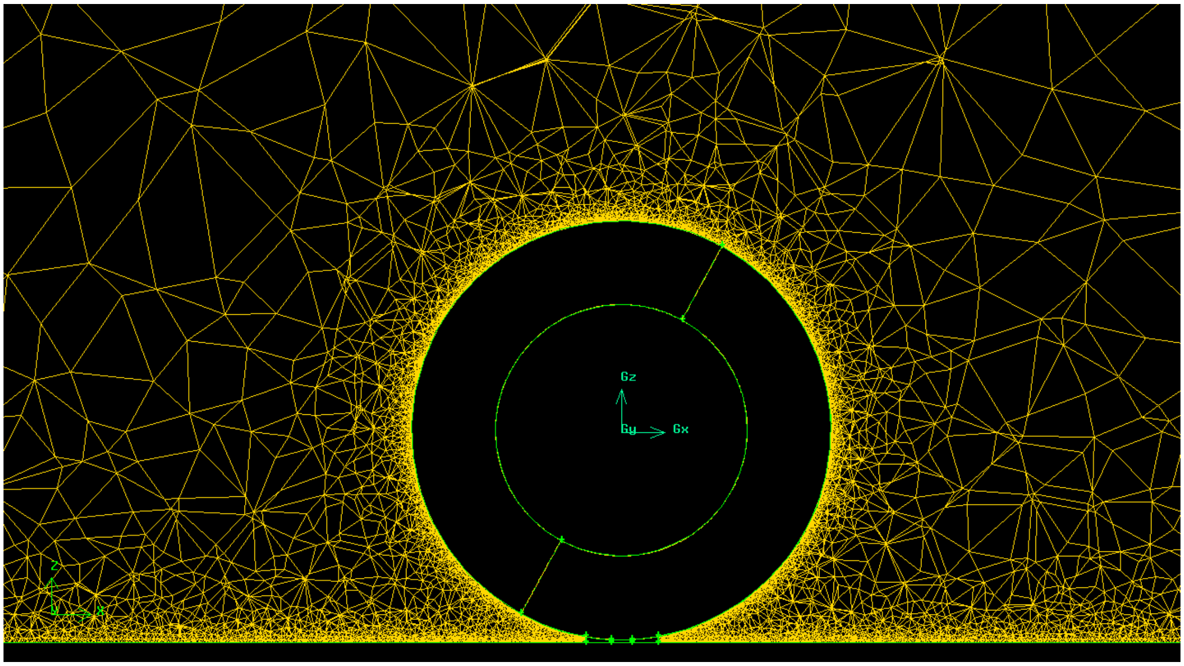

Figure 13 The detail of cut section at the center line around contact patch

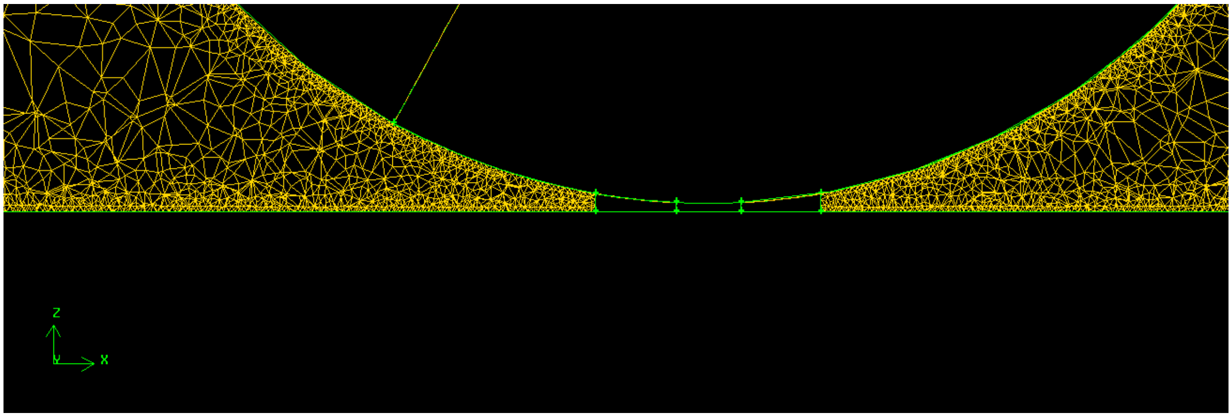

The initial mesh generated 4.4 million tetrahedral cells, which is almost same as Mears' case, 4.3 million cells.

As Mears' case doesn't describe the detail of contact patch, artificial adjustment has been applied the corner radius of the contact patch in plan view.

Figure 14 lateral vertical section around wheel bottom corner

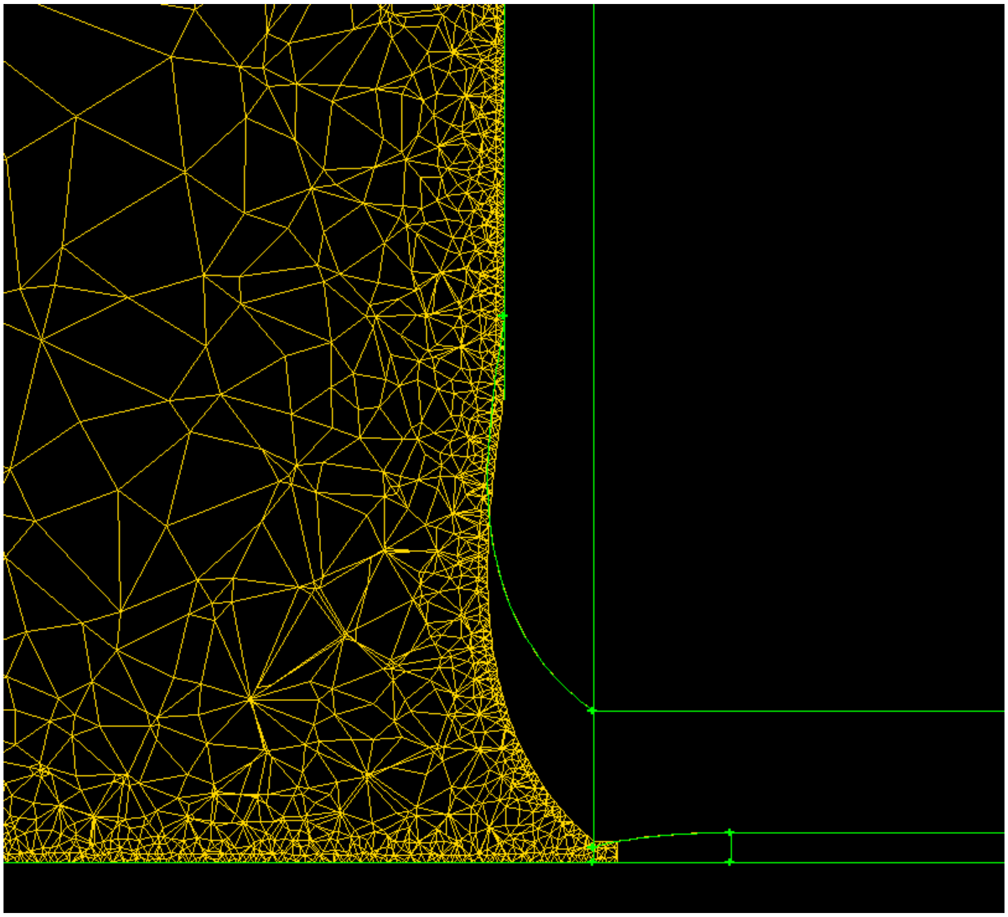

4.2.2 Mesh generation for isolated wheel analysis

After familiarization process on initial mesh, a standard mesh has been established for all following computational methods. Basic strategy for the mesh generation is to deploy tetrahedral mesh all over the domain and resolve around solid wall with boundary layer mesh hence prism mesh to enhance the resolution without exploding the number of mesh as a whole. This approach turned out beneficial to minimize manual adjustment to complete mesh generation because of adaptability for complicate local shape around contact patch and rim area although fully controlled structured mesh could have been an alternative to control the mesh density under limited number of meshes.

As LES is our primary target, the surface mesh on wheel was arranged to meet relevant the Y+ requirement. In this case, the value of the Y+ is supposed to be around unity to resolve the velocity gradient in the boundary layer without any modeled wall treatment. Having run test cases with RANS calculation, the first layer of the boundary mesh was adjusted to 0.03 mm to reach this resolution. The wake area has been adjusted by Size Function (SF), which controls mesh size by a source geometry in GAMBIT, to have minimum size, 1.5mm as a start point. Note that the shape of calculation domain, wheel shape and its location to the domain stay same as for the familiarization stage in previous chapter.

After final adjustment, the mesh contained 6.8 x 10^6 cells. Figure15 shows this finalized mesh as a whole.

Figure 16 highlighted how mesh density distributed in side view. It concentrated to lower part of the wake where the initial study spotted primary wake structure was. This high resolution area ranged up to two times of wheel diameter in X and smoothly blended into the rest of the domain with the progressive factor, 1.2.

Figure 17 shows mesh arrangement on the side of the contact patch. Compared with the initial mesh shown in figure15, this final mesh improved not only mesh resolution but also transition to coarser part of the domain.

Note that the origin of the coordinate is set to the wheel centre on the symmetrical plane.

Figure 15 the over view of computational domain

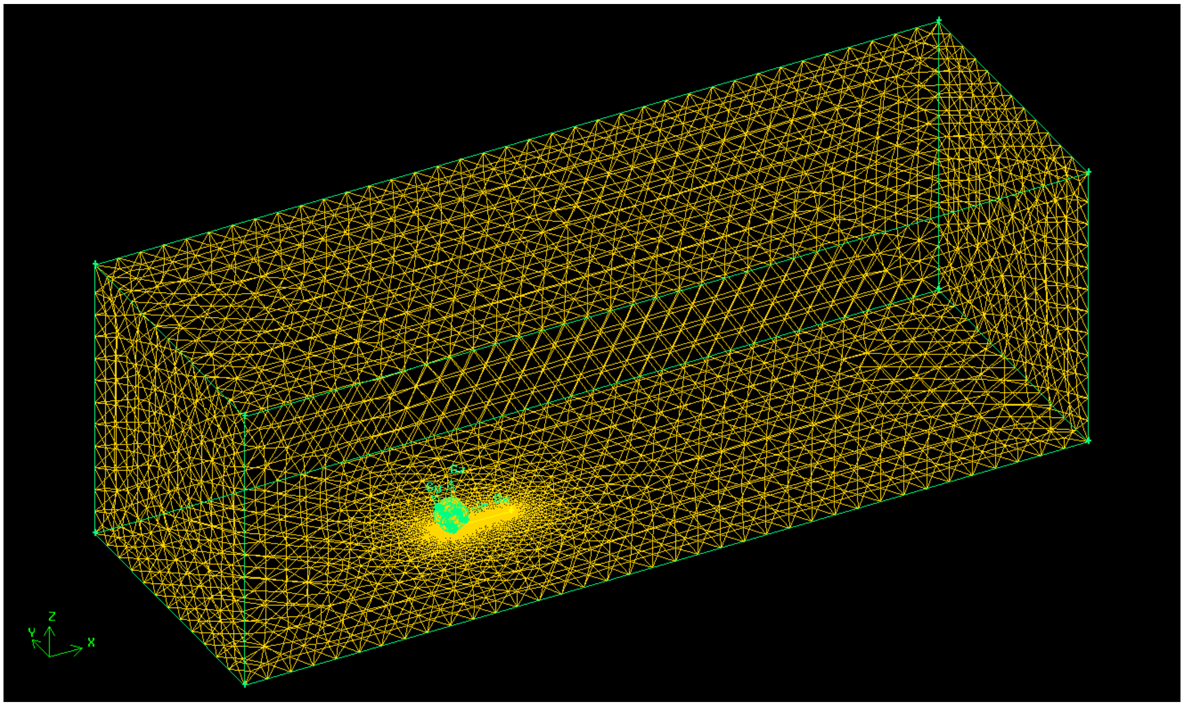

Figure 16 computational volume mesh on XZ plane

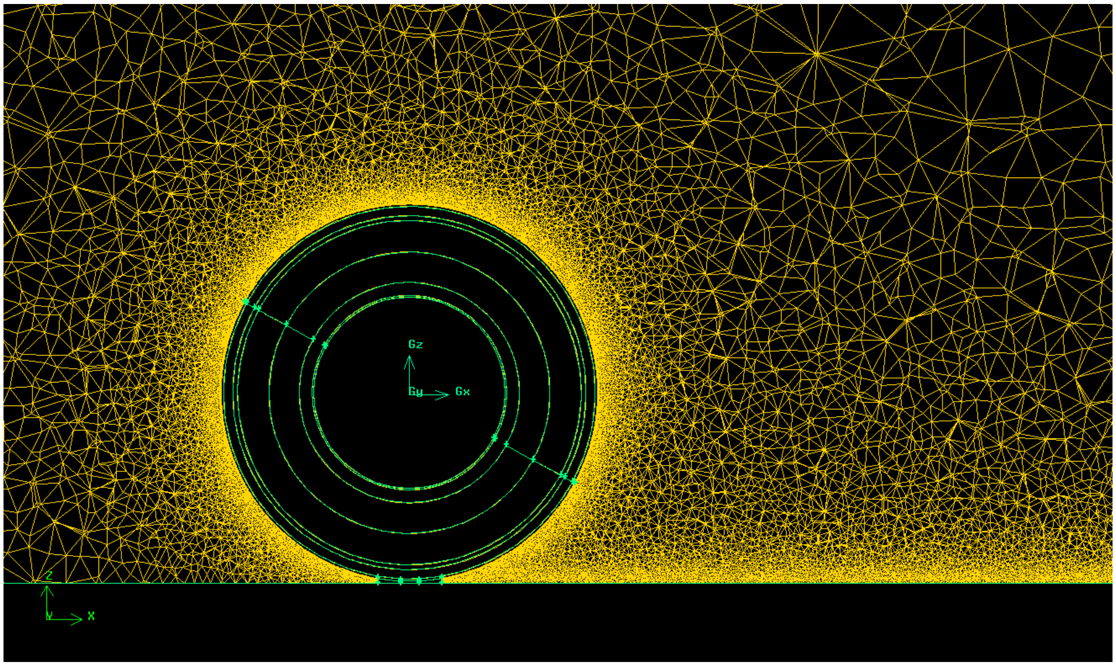

Figure 17 computational volume mesh on YZ plane

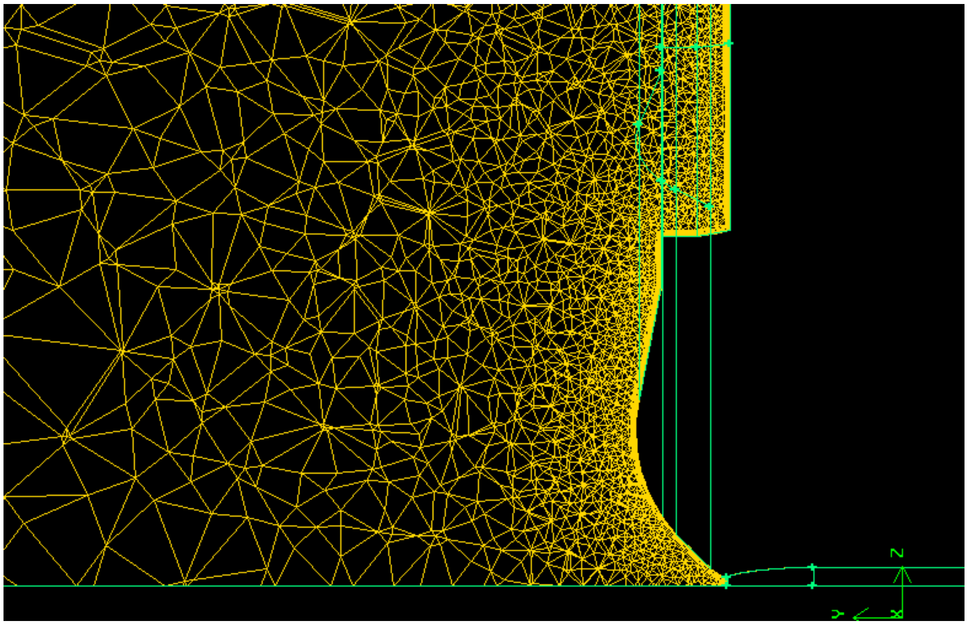

4.2.3 Mesh refinement process

Although previous chapter has introduced the final mesh in this thesis, it would be informative to show some representative stages in the evolution of mesh generation because the relevance of this process would impact on total efficiency of all following computations in terms of calculation resource and time. Generally, despite reasonably finer mesh density to minimum shape feature and less aggressive progression factor in basic strategy discussed earlier, the mesh generation was often stopped due to problematic meshes made around the contact patch and the ground in early attempts. Boundary layer mesh is also responsible as an acutely folded boundary around this area can leave distorted prism meshes if the total thickness of the boundary layer meshes grew taller excessively. As a summary for this whole iterative and time-consuming process, three cases including the final mesh are shown with mesh quality information in figure 18, figure 19 and table 4.

As seen familiarization process, in 2.5-million case, 1mm surface mesh could produce reasonably finer mesh around the tyre and its wake region, however, the lack of the boundary layer results in Y+ = 30, which is determined by the resolution of the surface mesh. This is far from the target for LES application context. The introduction of Y+=1 equivalent boundary layer mesh led to significant increase of the number of the mesh to 3.8 million despite no significant improvement on the resolution in the wake region. 6.8 million case, which is used for all following computations, gives notable improvement on the resolution in the wake with the boundary layer mesh equivalent to Y+=1.

Table 4 suggests the maximum aspect ratio is more than 30 even for 6.8million case despite it have been improved as finer mesh introduced. As seen in figure 20 and figure 21, there were the problematic meshes on the boundary of the contact patch between the ground and the tyre. As this problem is limited to very local region and further improvement could increase the number of the meshed beyond feasible level, this 6.8million mesh was accepted for further computation.

Figure 18 volume mesh cut by centre plane

[2.5million mesh / no BL mesh]

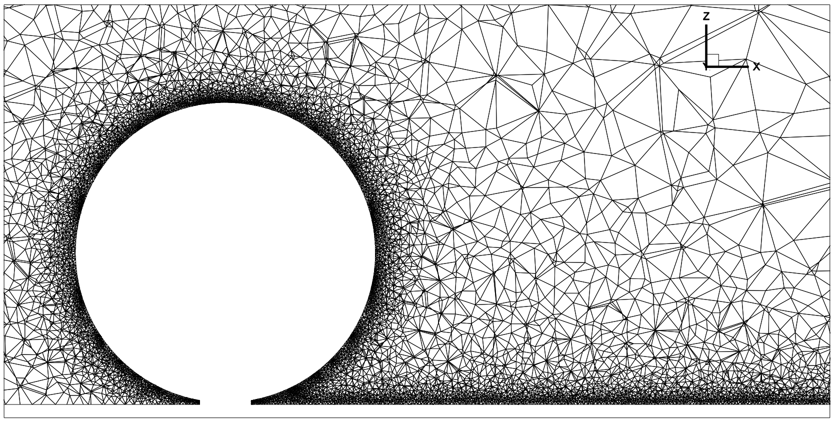

[3.8million mesh]

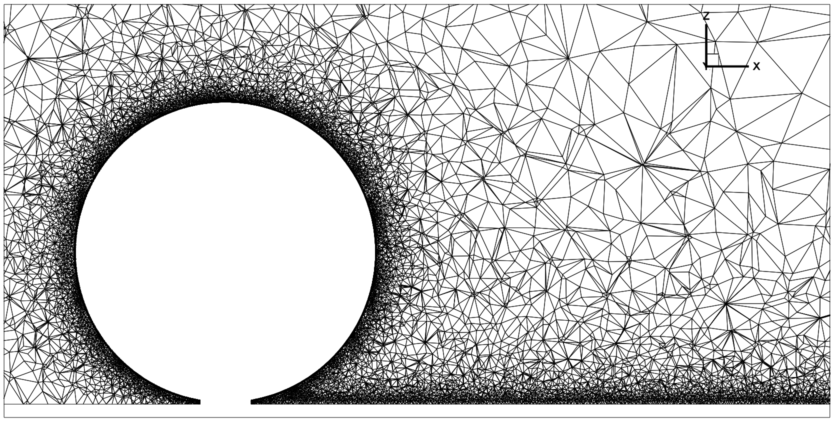

[6.8million mesh]

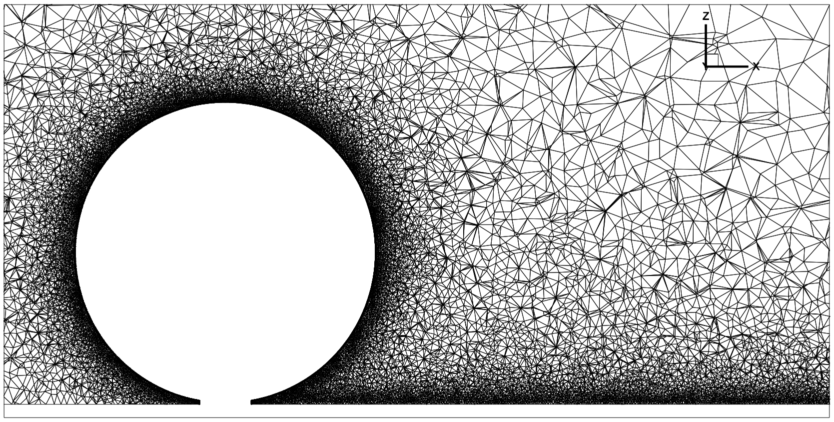

Figure 19 volume mesh cut by YZ plane

[2.5million mesh / no BL mesh]

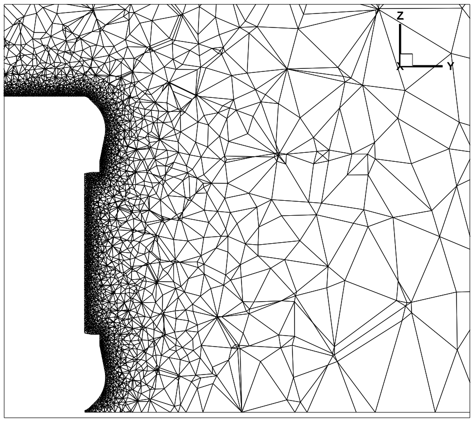

[3.8million mesh]

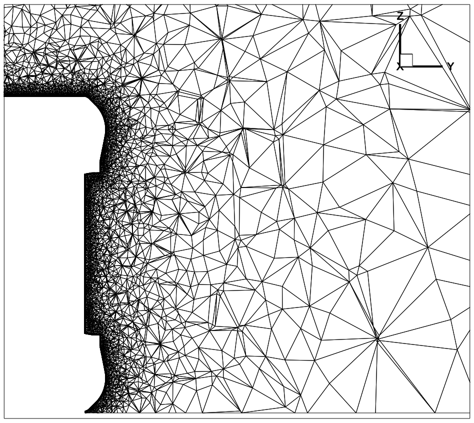

[6.8million mesh]

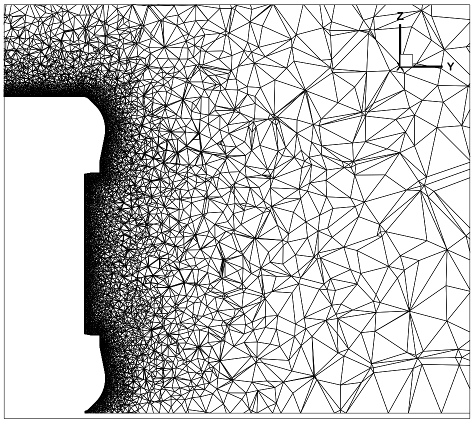

Table 4 Mesh quality information

	2.5 million	3.8 million	6.8million
B.L. mesh	N/A	1st layer 0.03mm	1st layer 0.03mm
Maximum cell squish	8.55107e-01	9.13013e-01	8.92413e-01
Maximum cell skewness	9.68257e-01	9.71141e-01	9.63307e-01
Maximum aspect ratio	3.31673e+01	1.59873e+02	1.18219e+02

Figure 20 the location of the high aspect-ratio meshes in 6.8million case

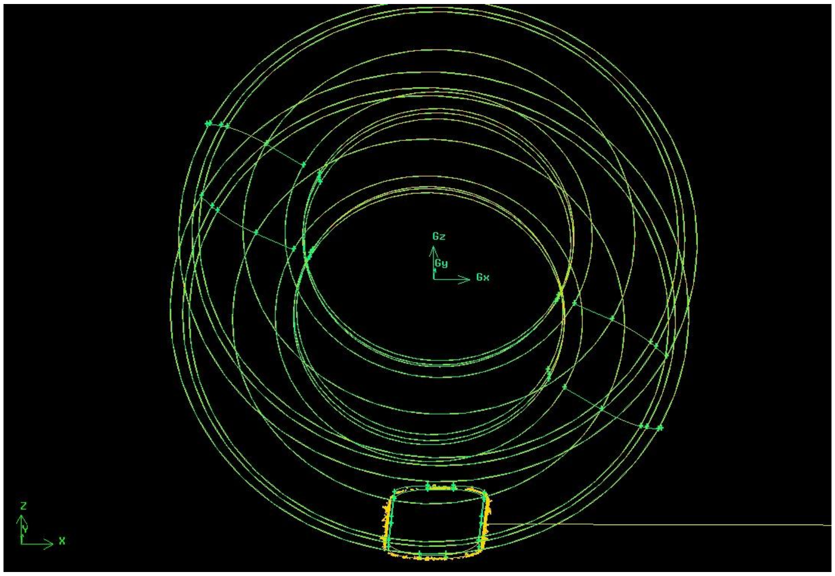

Figure 21 the location of the high aspect-ratio meshes in 6.8milloon case (magnified image around the contact patch)

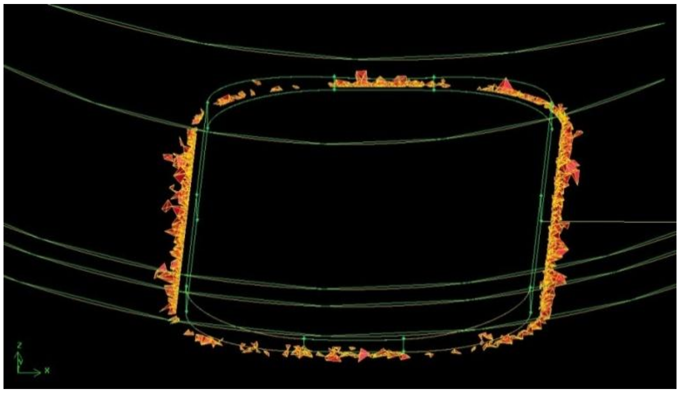

4.2.4 Boundary conditions

Hereafter the same boundary conditions in the domain are applied for all following calculations, which are relevant to Mears' case [1] to have comparable data for the validation. Table5 shows the boundary conditions applied.

Table5 the boundary conditions

Boundary	**Applied BL condition**
inlet	**velocity inlet with 14.7m/s in x direction**
outlet	**outflow**
Wheel surface	**rotational moving wall with 119.5rad/s around wheel center axis**
the ground plane	**moving wall with 14.7m/s in x direction**
side and top walls	**Slipping wall (shear stress set to zero)**

4.2.5 Preliminary calculations with mesh-resolution variations

Some preliminary computations were carried out to evaluate the conversion of the solution with the mesh resolutions discussed above. Note that Realizable k-ε model was used for those computations. Figure22 suggests that all cases can reach to 10E-4 without any notable signs of the divergence. It is noted that 6.8 million case showed an oscillation after global convergence as well as relatively slower convergence initially.

Figure 22 the residual of the continuity term for mesh variations

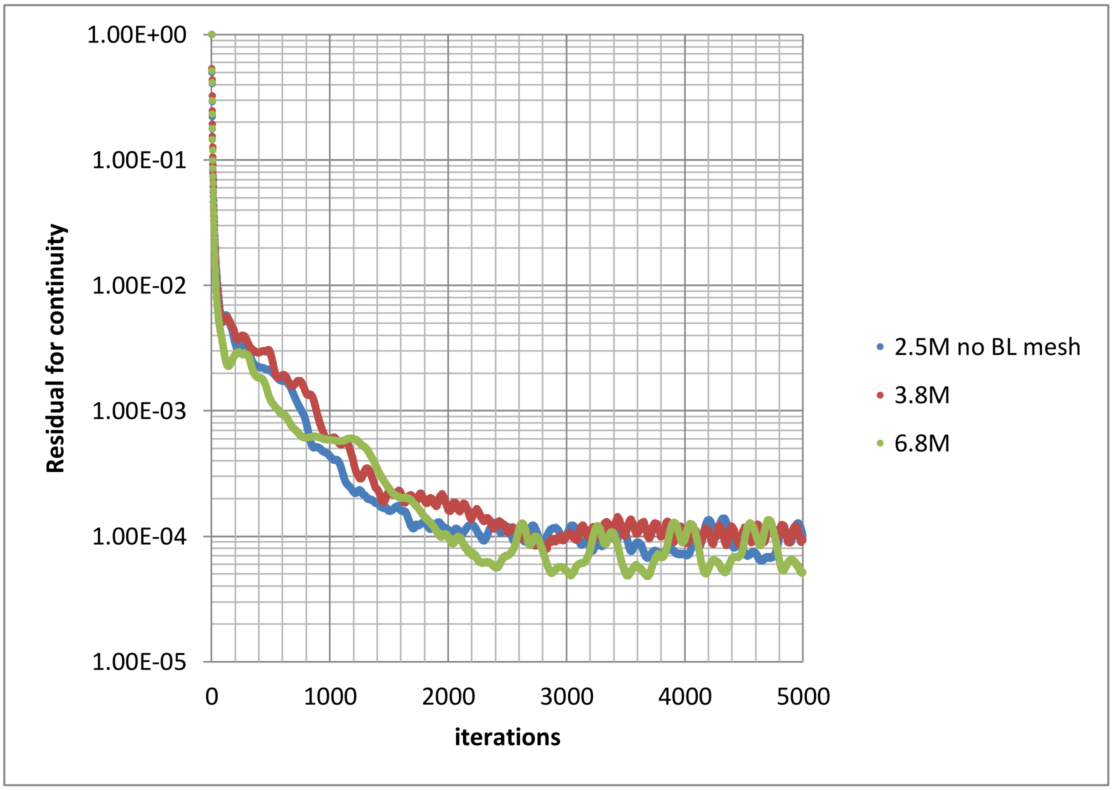

Figure 23 shows the convergence profile in Cd for same mesh variations. As expected from the residual conversion, all cases settled down within +/-2% of absolute Cd value as a sign of the conversion. This, however, is overshadowed by the fact that each mesh resolution converged to the different Cd value with the 10% error at worst case (Table 6). Although we could get 2.5M case out of the scope because of the lack of the boundary layer mesh, it still suggests mesh dependency could remain for the following computations.

Figure 23 the convergence of Cd for mesh variations

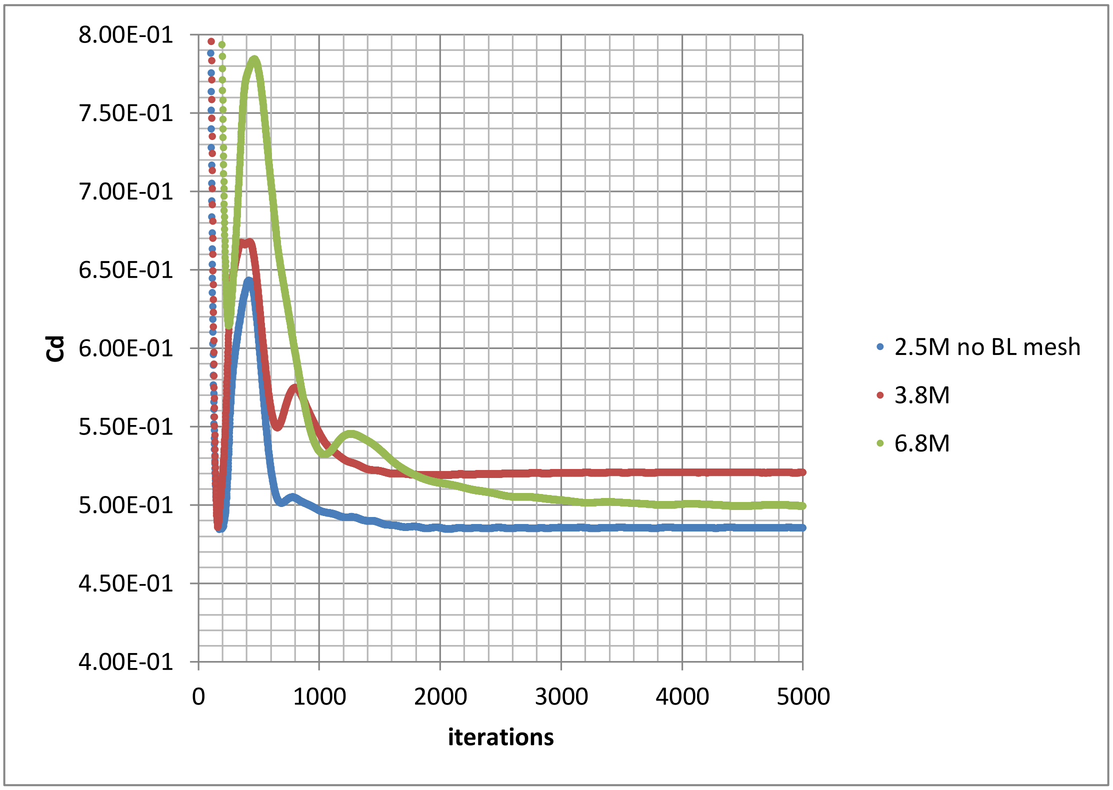

Table 6 Cd value for each mesh resolution after 5000 steps

The number of the mesh	Cd
2.5 million (no BL mesh)	0.485
3.8 million	0.521
6.8 million	0.499

The achieved Y^+ value with finalized mesh, 6.8 million, will be shown in the next chapter.

5.0 Results and Discussion

5.1 Introduction

In this chapter, all computational results for the isolated wheel case with RANS models and LES are presented by 3D and 2D flow description leading integrated aerodynamics property such as drag coefficient to evaluate each turbulence models along this context of this thesis.

5.2 Grid convergence

5.2.1 RANS models

Figure 24 and Figure 25 show the convergence profile for all RANS models used in the residual of the continuity and the drag coefficient respectively. Most notable problem is S-A model and two transition models could not reach the 10E-04 criteria as opposed to the preliminary computations in previous chapter suggested with k-e realizable model. S-A model also showed an oscillations after initial convergence. k-ε realizable, k- ω and k-ω SST suggested reasonably converged condition to 10E-4, although k-ω model showed a few sign of violent divergence suggesting numerical instabilities in comparison to other all RANS models. In this regards, k-realizable and k-ω SST could give most reliable results from numerical point of view whilst the adaptability of RANS model is questionable for the unsteady nature of the flow around rotational wheel case as discussed earlier.

Figure 24 the residual convergence for RANS models

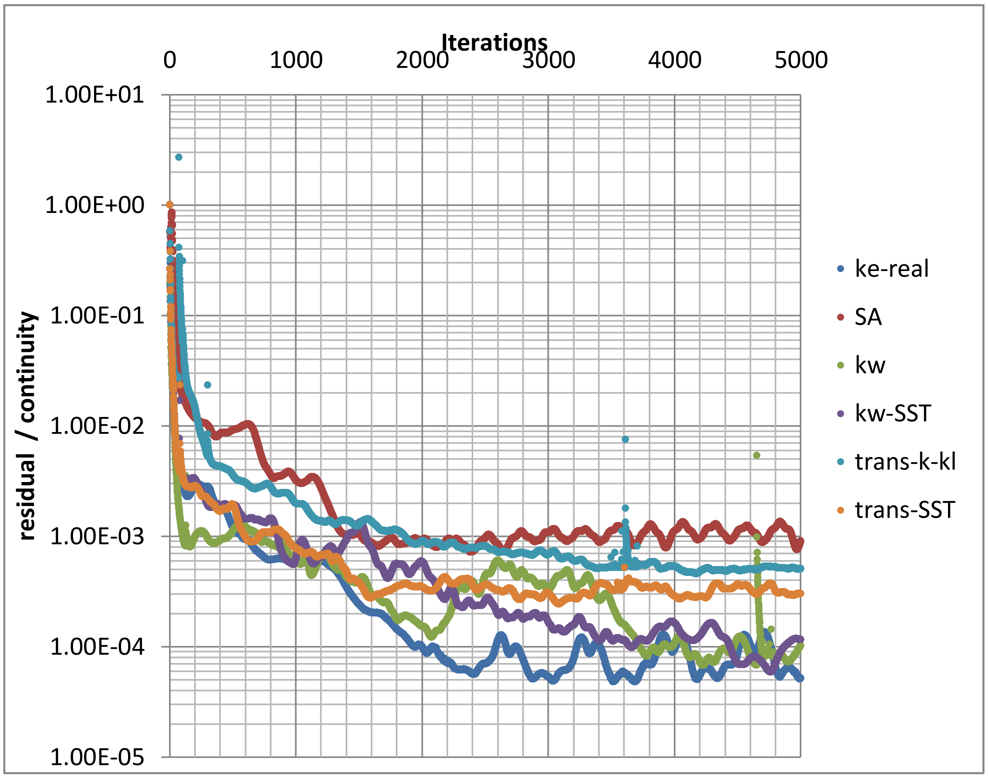

Figure 25 the convergence of Cd for RANS models

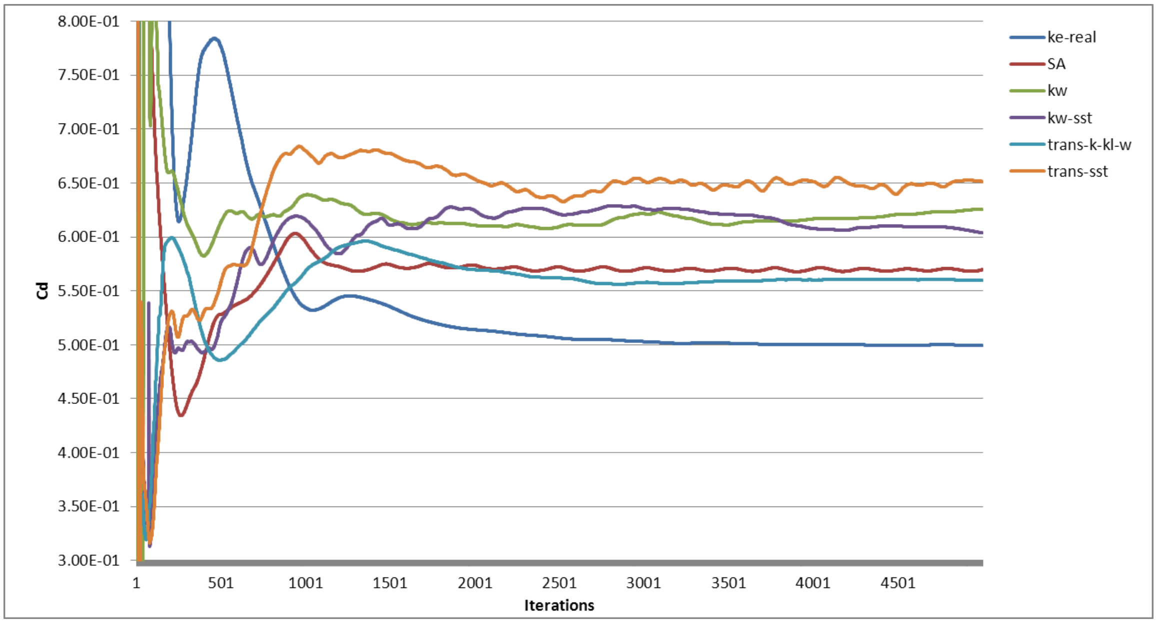

5.2.2 LES

In this thesis, LES computations are started from the converged solution of the RANS case with k-ε realizable model. Figure 26 shows the initial conversion by Cd-time profile with LES S-L model, which suggests that the Cd value increased to 0.76 approximately and then a periodic feature appeared although still random fluctuation remains. Note that we set the time-step to 0.001 second for this LES S-L computation.

The latter part of the profile suggests the averaged value is decreasing as time step goes but the averaged value is far from the experimental result, 0.63 suggested by Mears [1].

Other notable feature is that the periodic pattern with the frequency, 0.05 approximately, is not far from the time of a rotation of the tyre, 0.0525 rotations per second. The spike with higher frequency seems to be correlated to the time period the freestream passes through the tyre length in X direction, 0.167 approximately.

Figure 26 the initial convergence of the LES S-L case

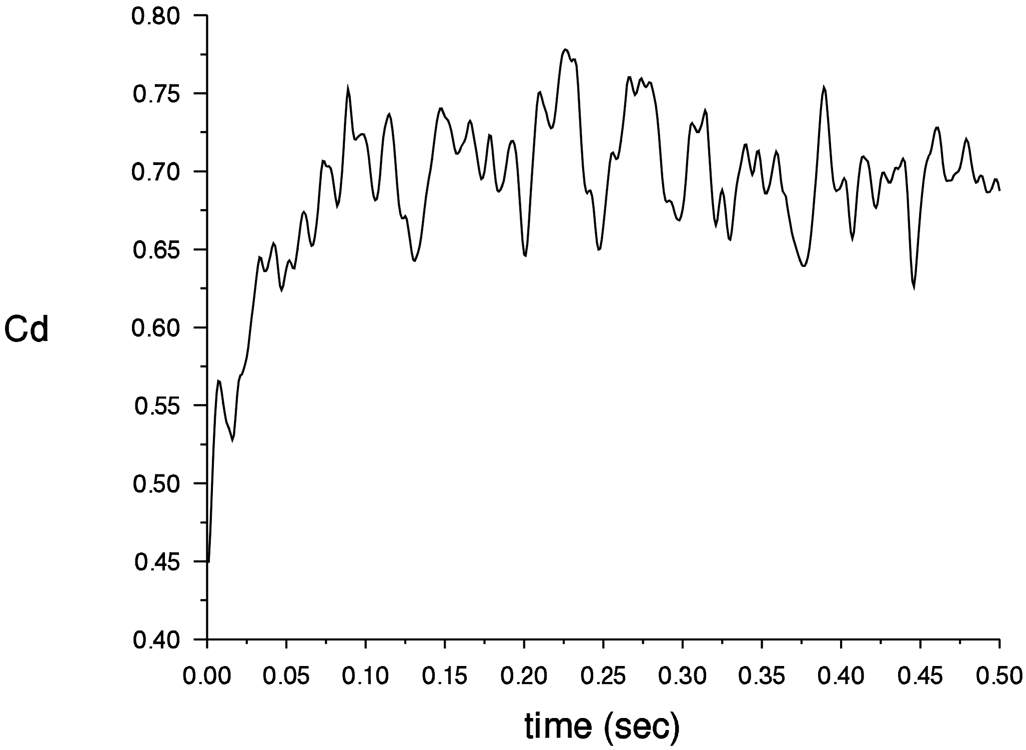

5.3 Unsteadiness in LES

This chapter gives an indication for the level of unsteadiness. Firstly it should be noted that we ran S-L model first with 0.001-second time-step and then WALE with finer time-step, 0.0001 second as it was prone to divergence. Those time-steps correspond to 26.7 and 2.7 of Kolomogorov time-scale respectively, which is feasible to LES.

Figure 27 shows Cd-time profile for S-L and WALE model, which suggests randomly scattered profile ranged from 0.6 to 0.8 in Cd approximately

Figure 27 the Cd-time profile in LES

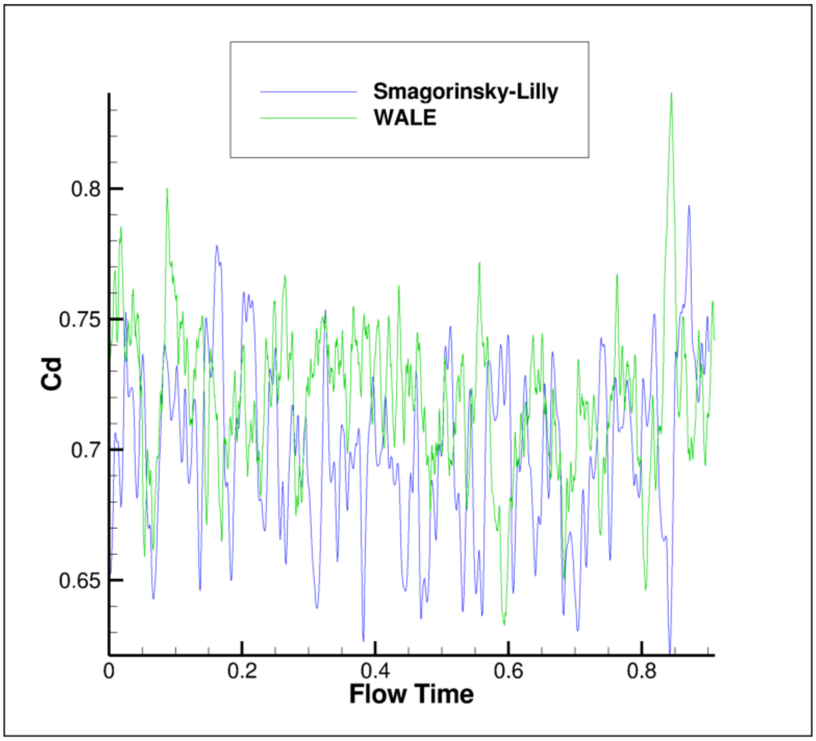

Figure28 shows the time trend of the velocity magnitude in the points distributed just behind the tyre with LES WALE . The locations of the markers have selected to capture unsteady phenomena in the circulation zone behind the separation at the top of the wheel and the wake from the contact patch referring proceeding RANS calculations (figure29).

As an example around the separation point, the point around the top separation labeled as wk_top_lh arguably indicated the periodic feature with 25Hz approximately. The general amplitude including random spikes seemed to +/-4.5 m/s approximately showed a similarity to the value of the square of the maximum turbulent kinetic energy observed in k-ε realizable model.

Notably the point, wk_side_btm, shows very violent unsteadiness. This could be explainable because this location is supposed be right in the middle of the jetting phenomena from the contact patch. So this would be the area LES can capture the flow structure which all RANS models miss out due to ensemble-averaged modeling approach.

Based on this analysis of the unsteadiness, we set the sampling interval to 0.91s based on the lowest denominator seen in LES WALE calculation.

The investigation with FFT spectrum along the energy cascade context will be discussed later.

Figure 28 the time-trend profile of the velocity magnitude at the makers in the wake (WALE SGS model)

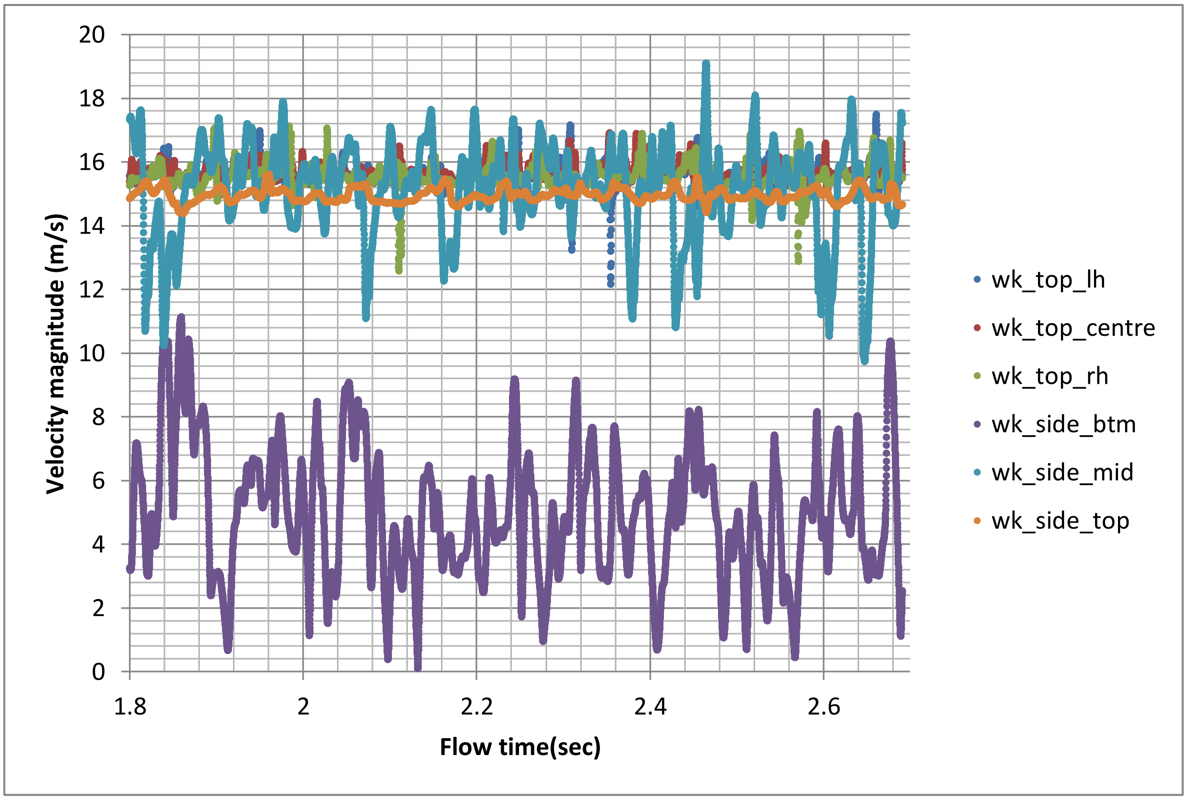

Figure 29 the locations of the markers

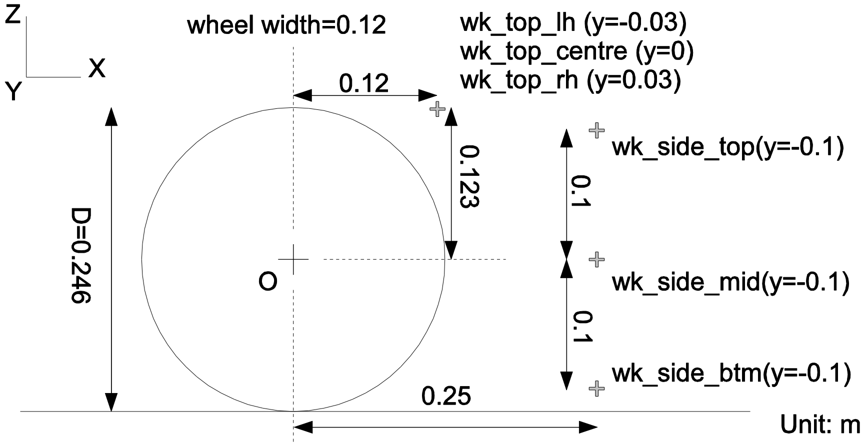

5.4 Run times of computations

We used Cranfield University's Astral HPC facility for all computations in this thesis. Table7 shows its specifications.

Table8 shows runtime comparison among the turbulent models to give idea for the efficiency of the computations. The result suggested that run-times for RANS correlate quite well with the complexity of the model, or the number of the equations. Interestingly, LES S-L with 0.001 timestep showed less run-time than expected form its complexity. However finer timestep, 0.0001sec, applied LES WALE model scaled up the run-time consistently to expected level.

Table 7 HPC hardware specification

HPC name	**Cranfield University HPC ASTRAL**
The number of cores	**856**
CPU	**EM64T Xeon 51xx(Woodcrest)**
CPU clock	**3.0 GHz**

Table 8 Run times with 16 CPU parallel computation

turbulent models	Full computation time (hrs.)
Realizable k-ε	26
k-ω	25
k-ω SST	28
SA	22
trans k-kl-ω	37
trans SST	37
LES S-L (time step =0.001sec)	75*[1]
LES WALE (time step=0.0001sec)	365*[2]

*[1] including initial calculation with RKE model

*[2] excluding initial calculation with RKE and LES S-L model

5.5 Comparable 3-Dimentional description

Figures 31 shows streamlines involved in lower contra-rotational vortex leading main wake structure with different turbulence models. Seeding locations to generate the streamlines are shown in Figure 30 with schematic image, which are adjusted to capture the vortex structure behind the contact patch such that the difference of the flow structure in the wake among the turbulent models is identified. Note that the seeding locations are same for all cases.

Figure 30 seeding positions

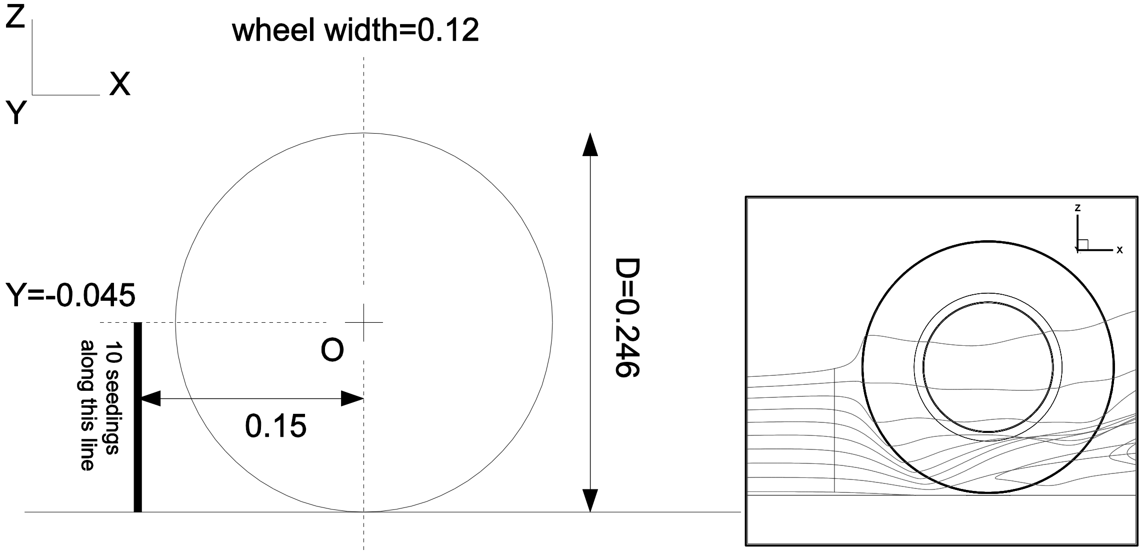

Unit: m

Figure 31 stream lines behind contact patch and surface contour by static pressure (Pa)

Figure31 (a) Realizable κ-ε model

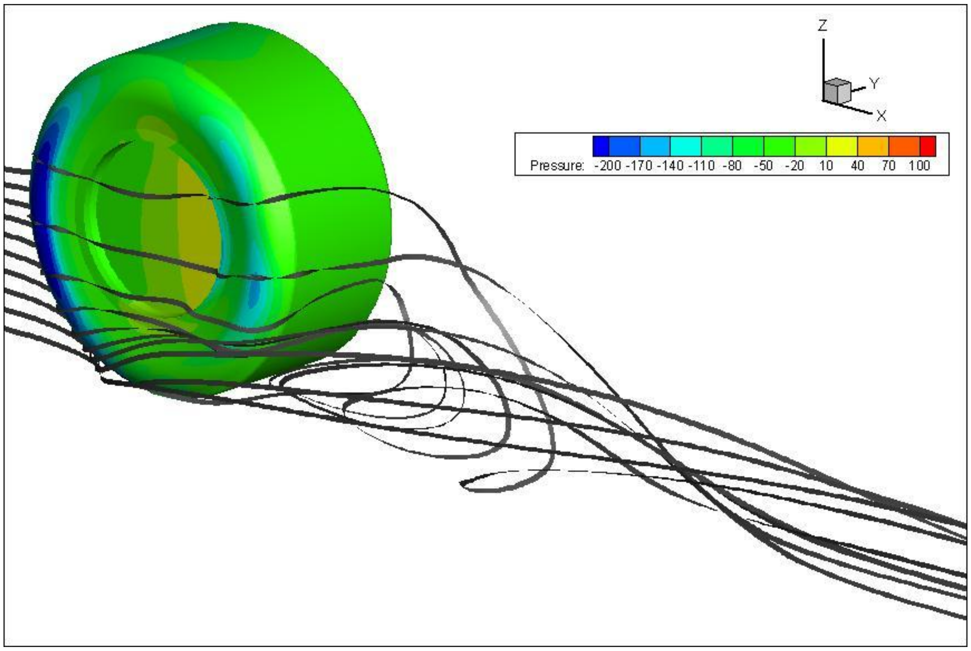

Figure31 (b) Spalart-Allmaras model

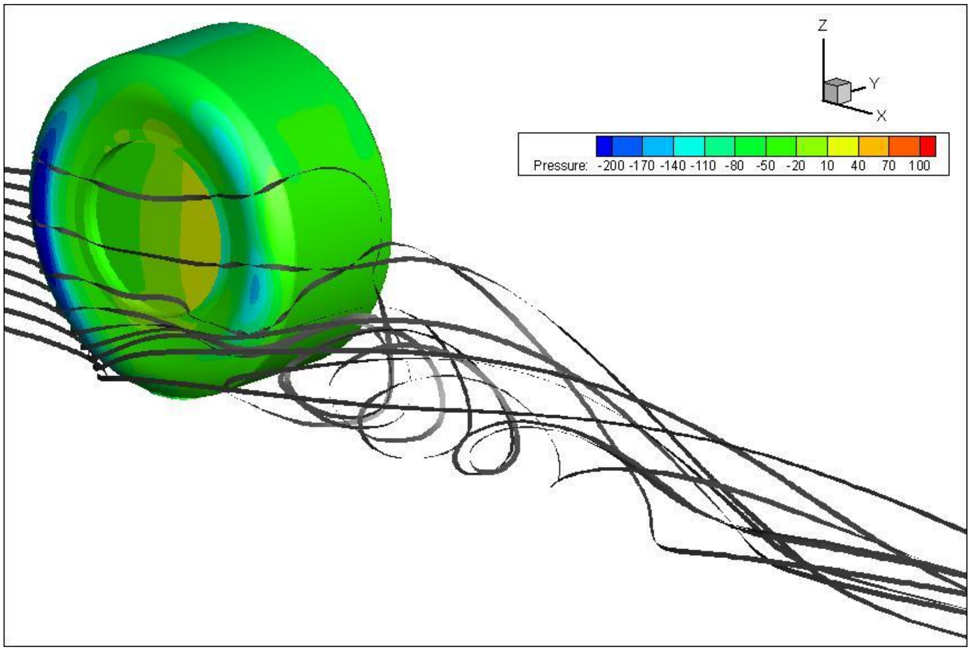

Figure31 (c) k-ω model

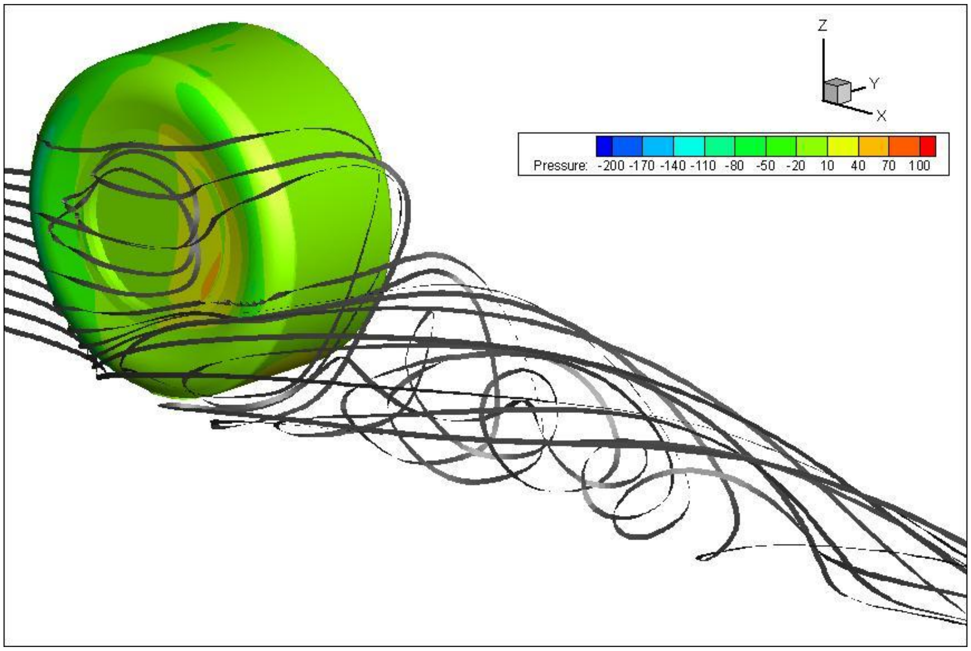

Figure31 (d) SST k-ω

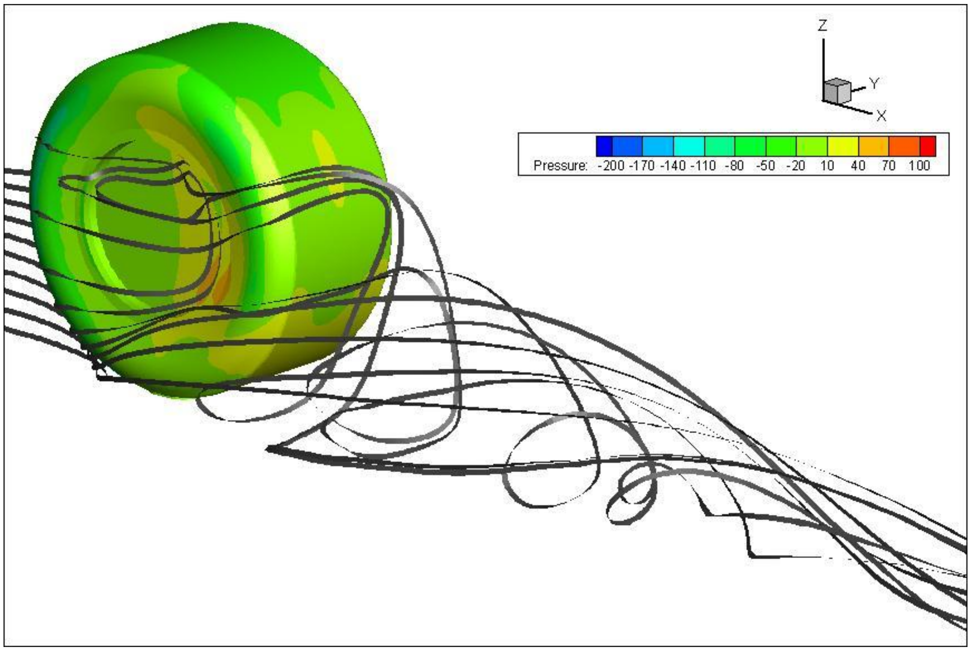

Figure31 (e) trans-k-kl-w model

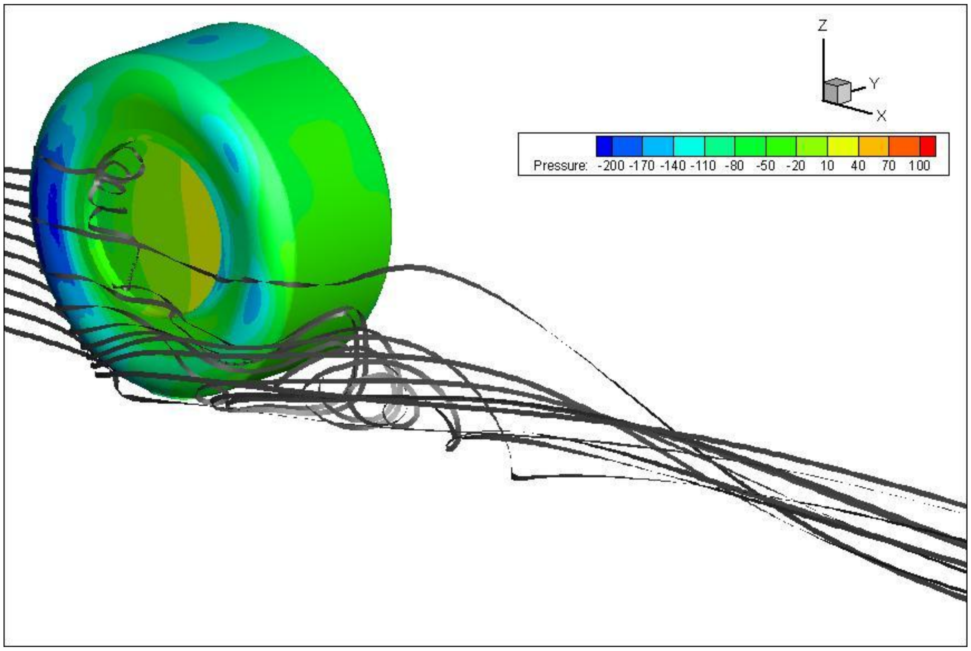

Figure31 (f) trans-SST model

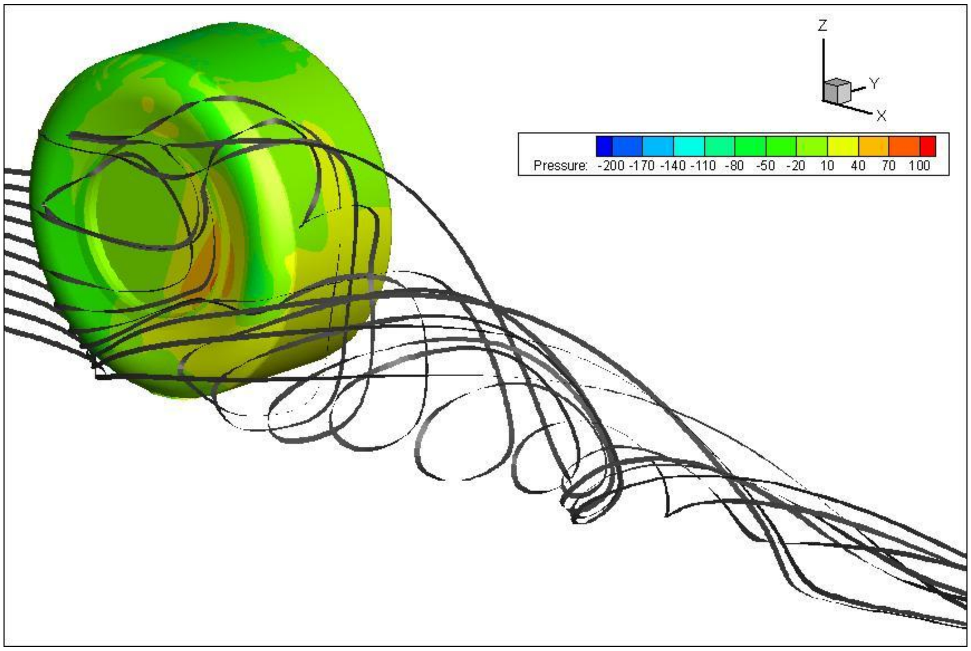

Figure31 (g) LES t=T_1

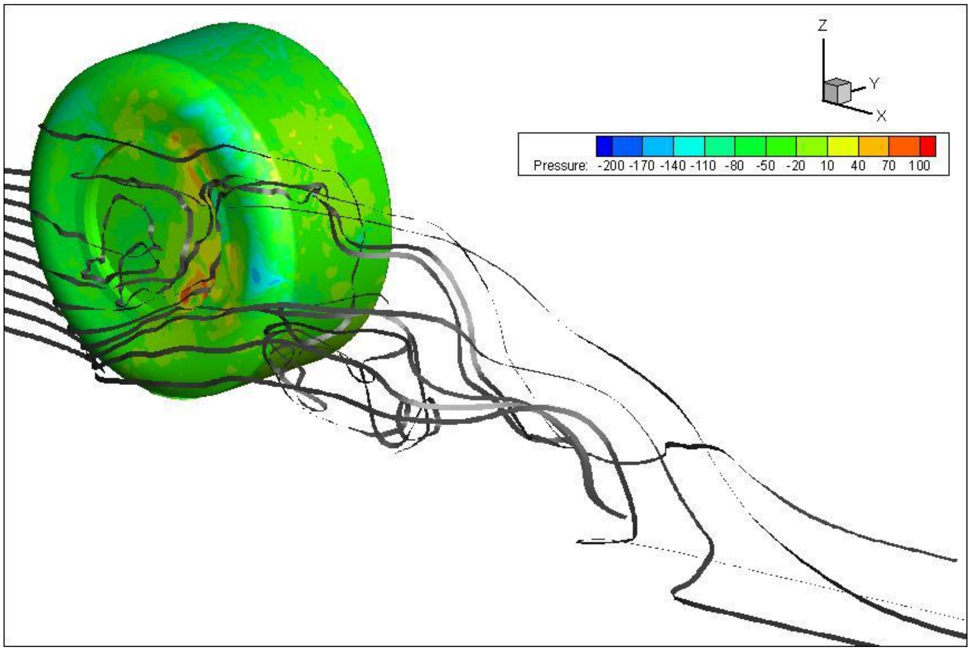

Figure31 (h) LES t=T_1-0.01sec

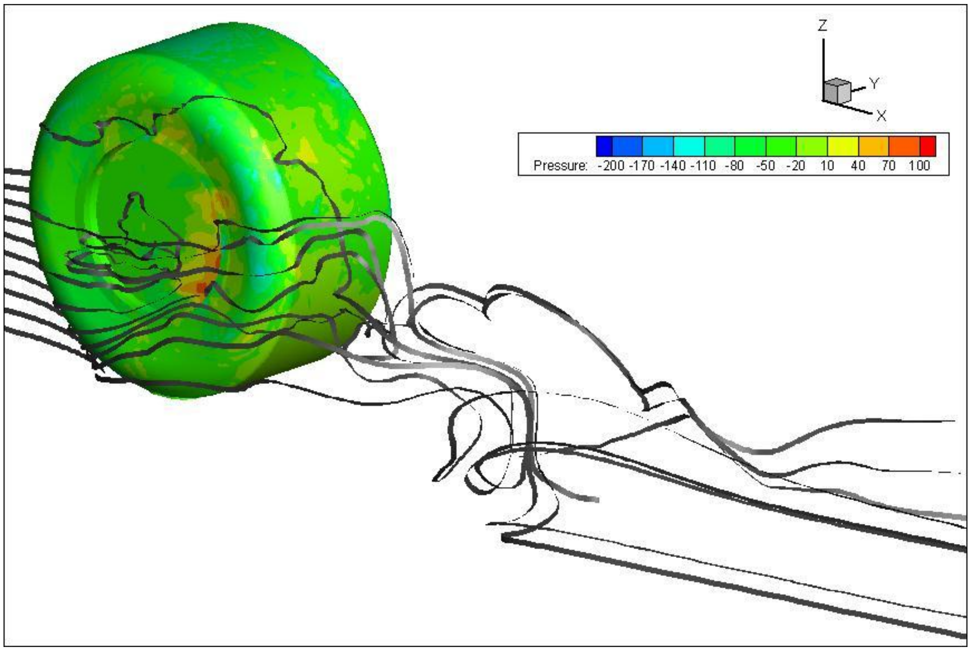

Figure31 (i) LES WALE t=T_1

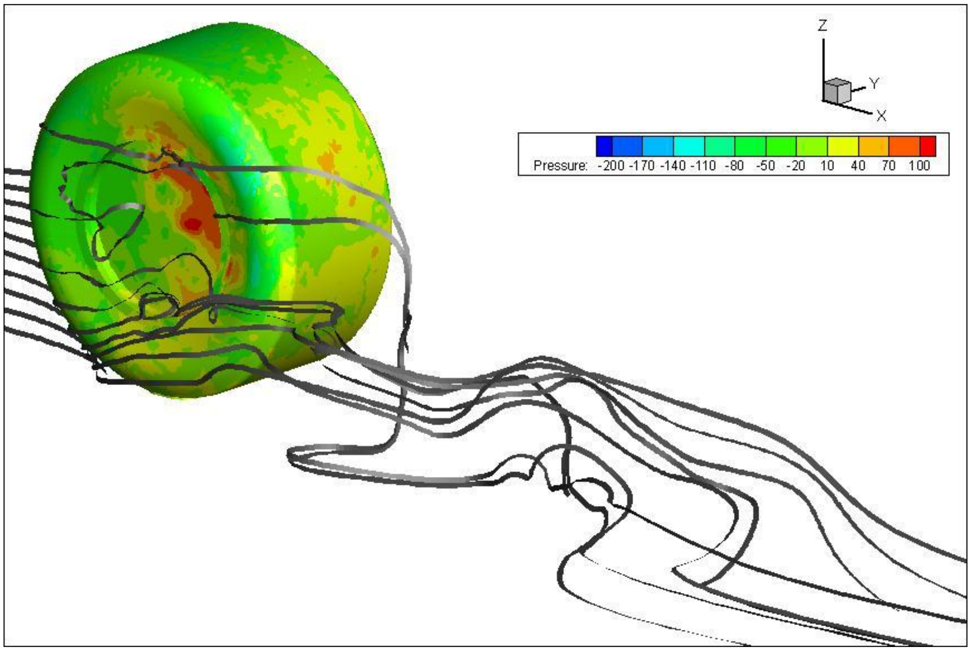

Figure31 (j) LES WALE t=T_1-0.01sec

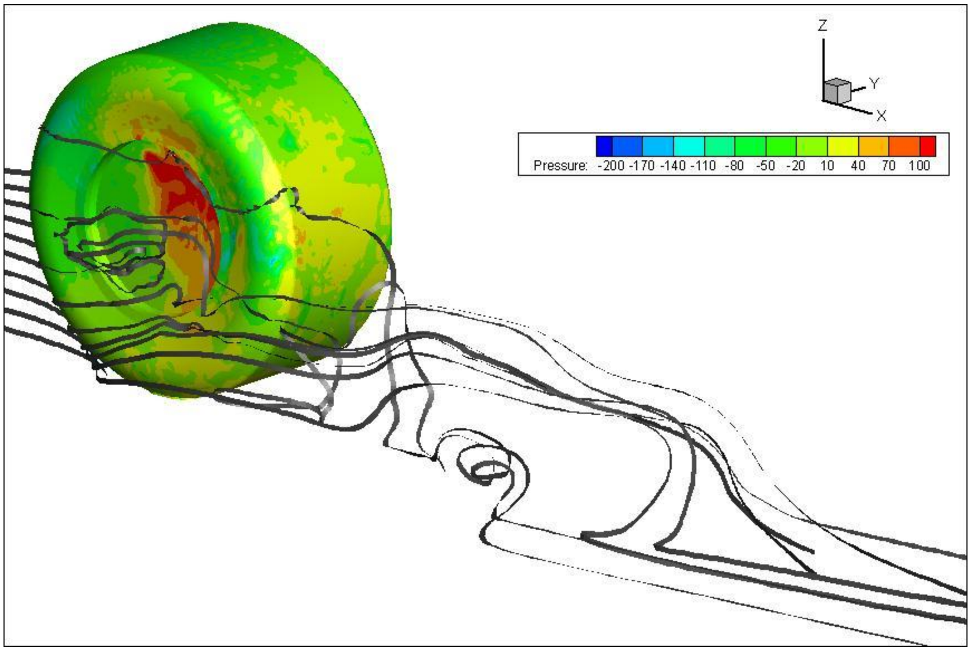

Firstly, Realizabke k-ε model and S-A model exhibited relatively less disturbed condition on the side of the wheel where the flow goes over the recess formed by the centre hub of the wheel. In the wake, S-A model showed high intensity in rotational component, which results in the less tidy flow at the back of the wake in this view than k-e realizable suggested. Those two model suggested strong suction peak at the leading edge of the wheel so it probably contributed to smaller drag as appeared in Cd value in Figure24(b). Furthermore, notable less drag with k-e realizable model could be explained by arguably smallest wake structure compared to other all cases.

Following two cases, k-w and k-ω SST, showed more disturbed flow in the center hub like the cavity flow while the suction peak was reduced at the leading edge compared to former two cases. So it would explain relatively higher Cd value in Figure25. The rotational component is clearer in the wake with those two cases and upper streams lines are involved into this rotation and form a single vortex structure. K-ω model showed more high intensity of the vortex structure in the wake compared to SST k-ω.

One notable feature with k-ω SST model is positive pressure appeared behind the contact patch. This implies fully separated flow but it's not very clear with this 3d description.

Trans-k-kl-w model gained notable suction peak at the leading edge as seen in k-e realizable model and S-A model. The wake structure was reduced in its size. Surface pressure suggested less separated flow at the back. This evidence suggests later separation and more dispassion in whole domain.

Regarding LES, two snapshots are picked up for each SGS model. The constant T1 is the most advanced point in time line where we observed statistical conversion as discussed earlier. Other point is 0.01sec minus from T2, which is arbitrary period to show other phase in transient flow. This manner applies for all following LES results unless otherwise stated.

As a nature of the transient flow, the streamline at a particular time step didn’t give a clear picture so we rather identify the location where the unsteadiness appeared most from those two snapshots. In LES, which deploys Smagorinsky-Lilly SGS model as default, the length of the wake varied significantly while the flow around the bottom of the wheel kept a certain steadiness we can see the similar structure to all RANS case suggested. On the other hand, WALE SGS model showed similarity between two snapshots to some extent. However, we have to be cautious to draw any conclusion by randomly picked-up two snapshots. Both LES cases didn’t show strong suction peak as seen in some RANS cases.

5.6 Comparative analysis in 2D

Figure 32 shows the velocity components on the centre plane with coloured by x-velocity magnitude for all turbulence models computed in this thesis.

As expected from 3d streamlines in previous chapter, S-A model showed lower profile of the wake than realizable k-ε model. This seems to be caused by delayed separation at the top of the wheel.

The kω and kω-SST model are featured by larger reverse-flow region behind the contact patch as X-velocity contour suggested. Interestingly, kω-SST showed lower profile of the wake, which was not apparent in 3d stream lines in previous chapter.

Trans-k-kl-ω model moved the top separation point back hence it reduced the height of the wake significantly as appeared in 3d streamlines while trans-SSTarguably followed this trend in the comparison of all no-transient RANS models. Trans-SST also exhibited larger reverse flow region suggesting the turbulence generation exaggerated by the shear layer after the boundary layer separation.

In contrast to unclear picture in 3d streams lines, this description sheds light on the wake structure for LES cases. The top separation point moved rearward more than any RANS models used. Although the shear layer on the upper boundary of the wake didn’t break up clearly, the lower region of the wake suggests very violent turbulent feature and non-uniform dispassion process toward the tail of the wake. This trend stays when we switched SGS model into WALE model. However, the larger reversed flow was observed behind the contact patch and developed the break-up of the shear layer at the top resulting in lower profile of the wake.

Other notable aspect in those figures is the thickness of the mixing layer between the free-stream and the recirculation zone appeared behind the top separation point. S-A model suggests thinner layer than k-e realizable whilst kw model follows the trend realizable k-ε model showed in this regard. Kω-SST model has arguably thinner layer in the comparison with kω model. In two transitional models, trans-k-kl-w has thinner layer than trans-SST although this could be affected significantly by the separation point itself and the size of the recirculation zone.

Regarding LES cases, despite of the difficulty to identify the thickness, the break-up of the shear layer between the recirculation zone and the outer flow at the top of the wheel is observed clearly hence x-velocity recovered quickly relative to RANS calculations contributing to make the wake low. Note that this shear layer. Note that this shear layer shows clearly the Kelvin-Helmholts instability which leads to shedding of vortices [35].

Figure 32 velocity components on y=0 plain (contoured by x velocity in m/s)

Figure32 (a) Realizable k-ε model

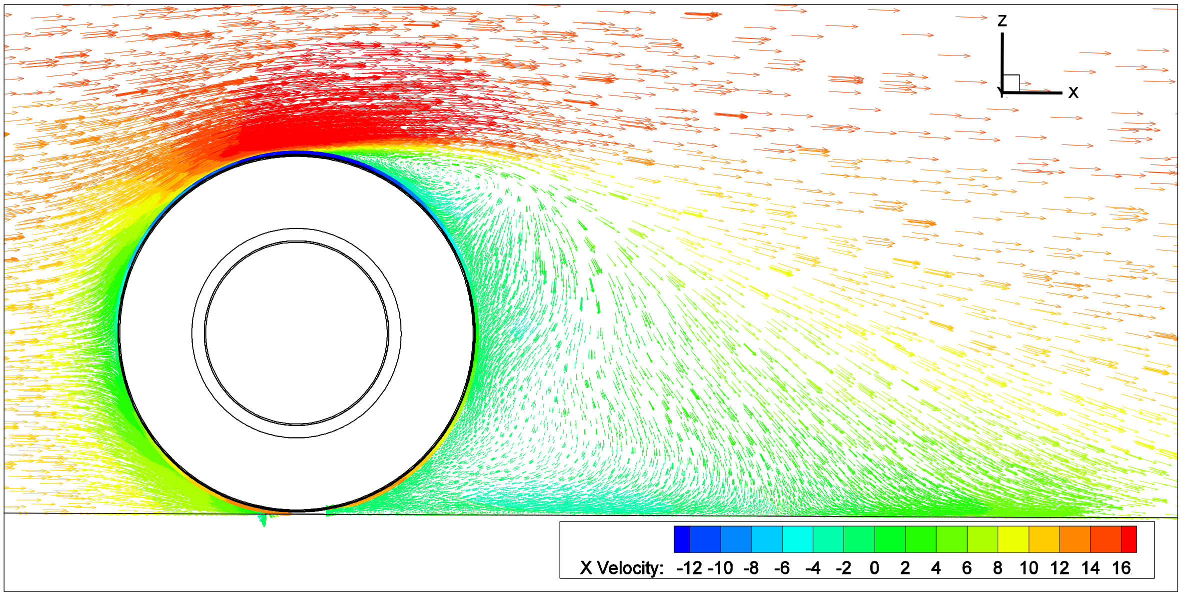

Figure32 (b) Spalart-Allmaras model

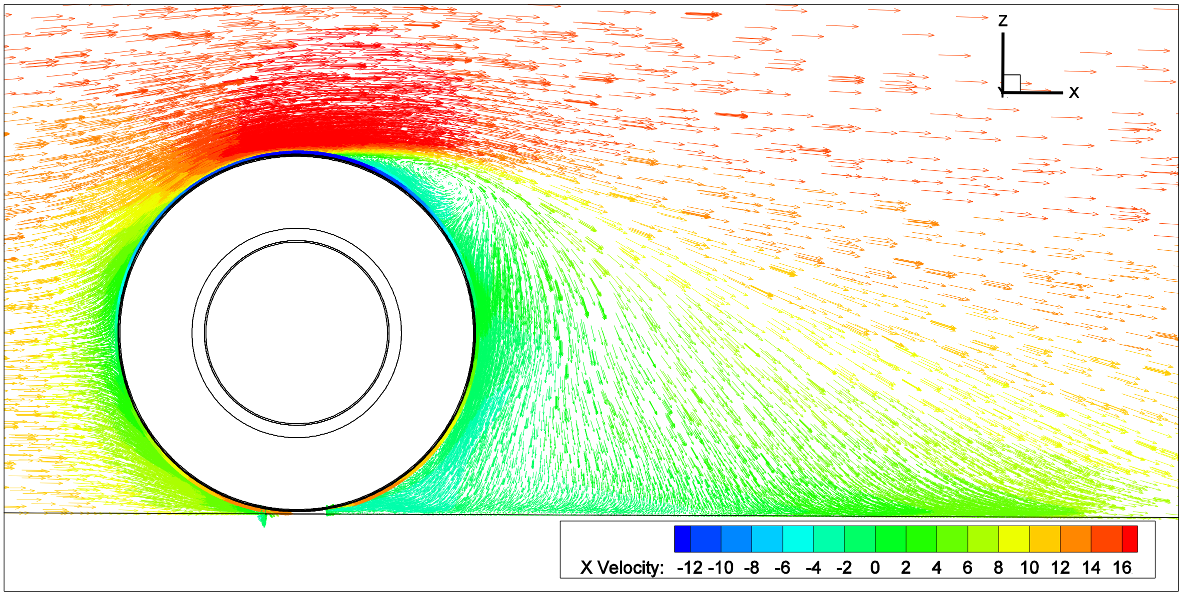

Figure32 (c) k-ω model

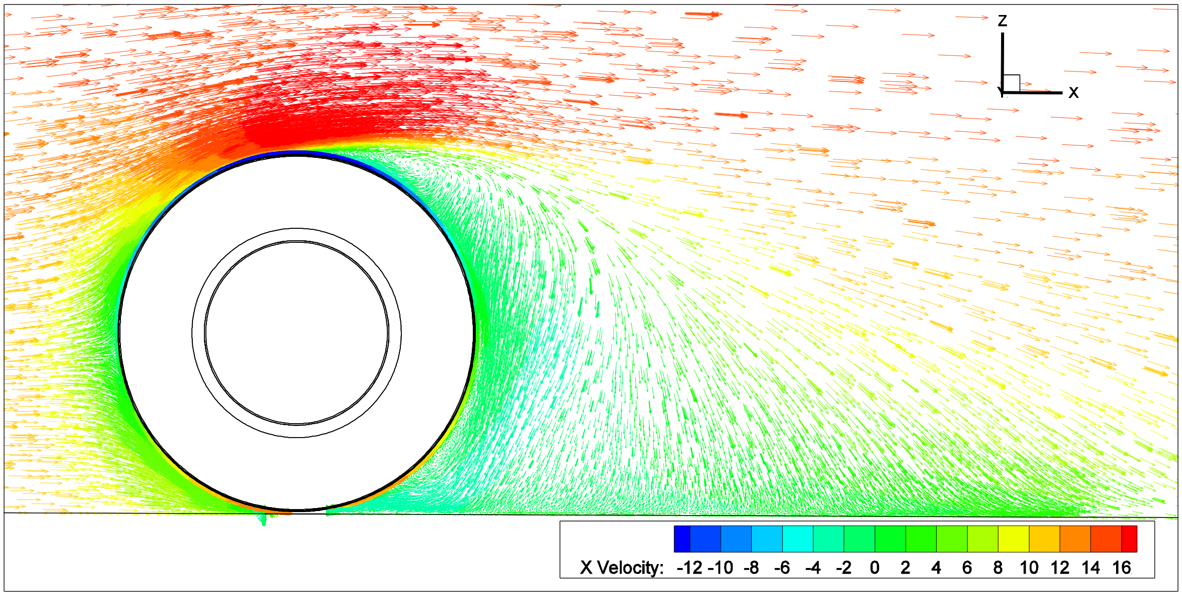

Figure32 (d) k-ω SST model

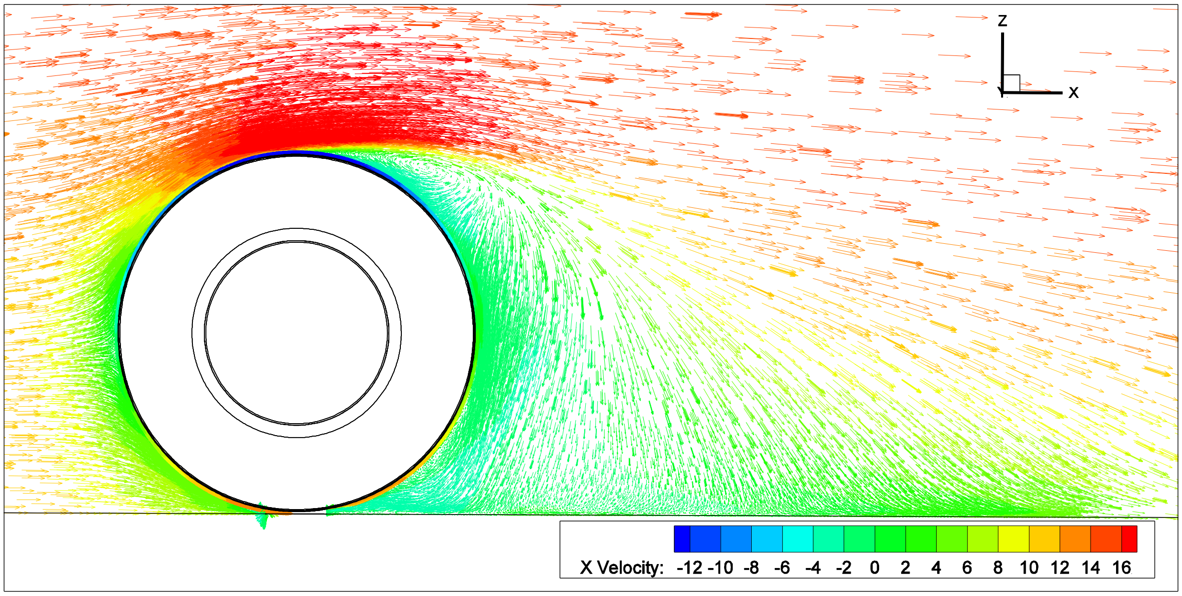

Figure32 (e) trans-k-kl-w model

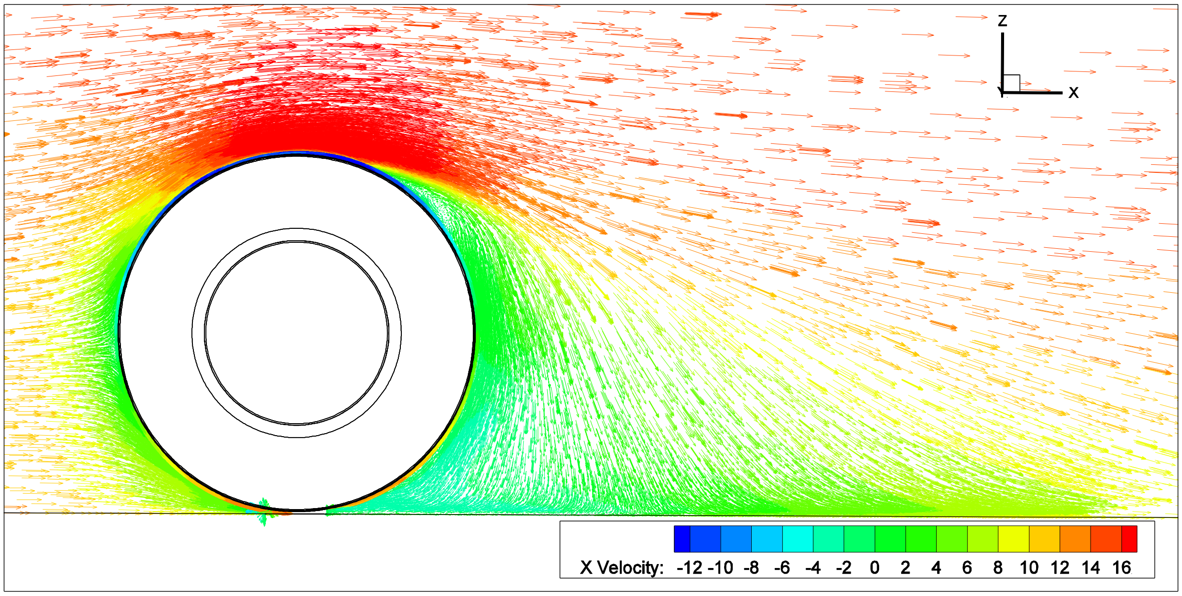

Figure32 (f) trans-SST model

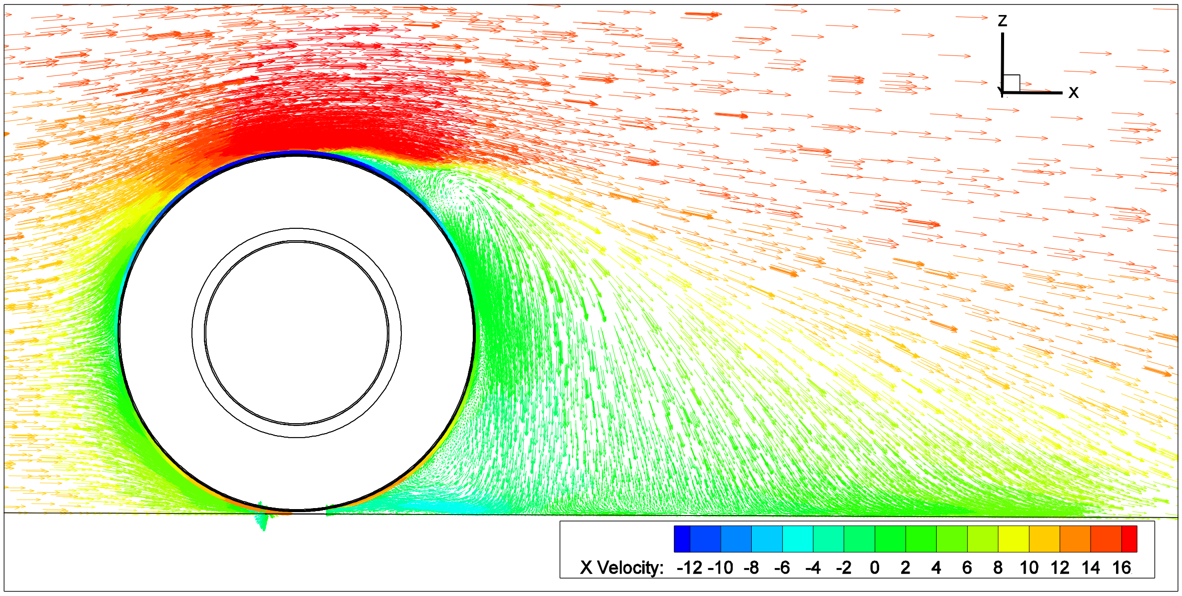

Figure32 (g) LES t=T_1

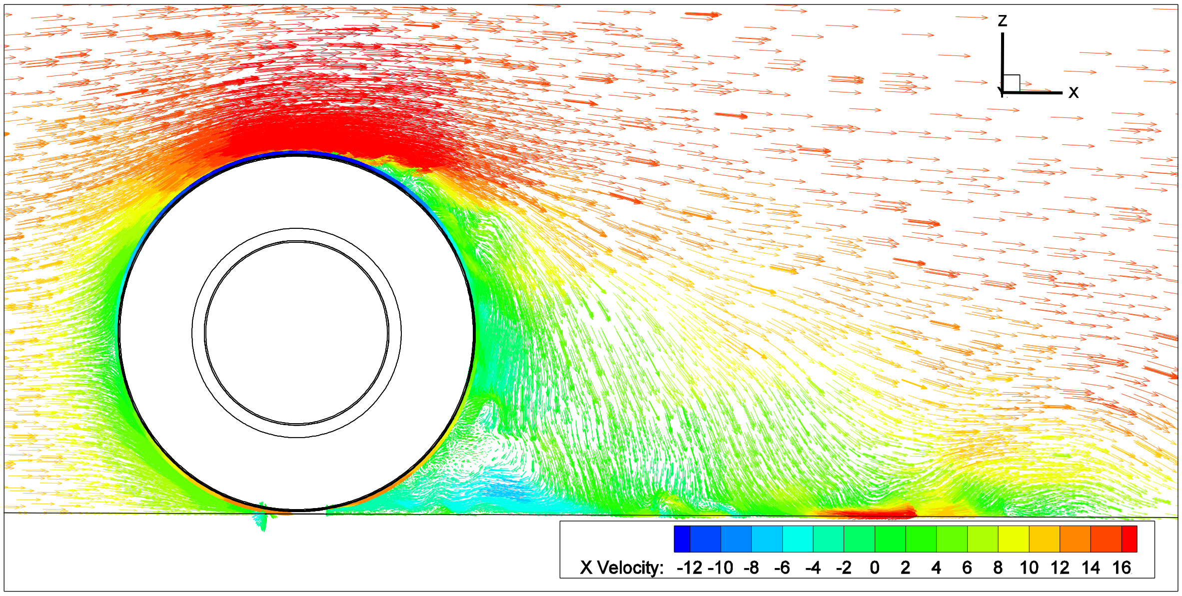

Figure32 (h) LES t=T_1-0.01sec

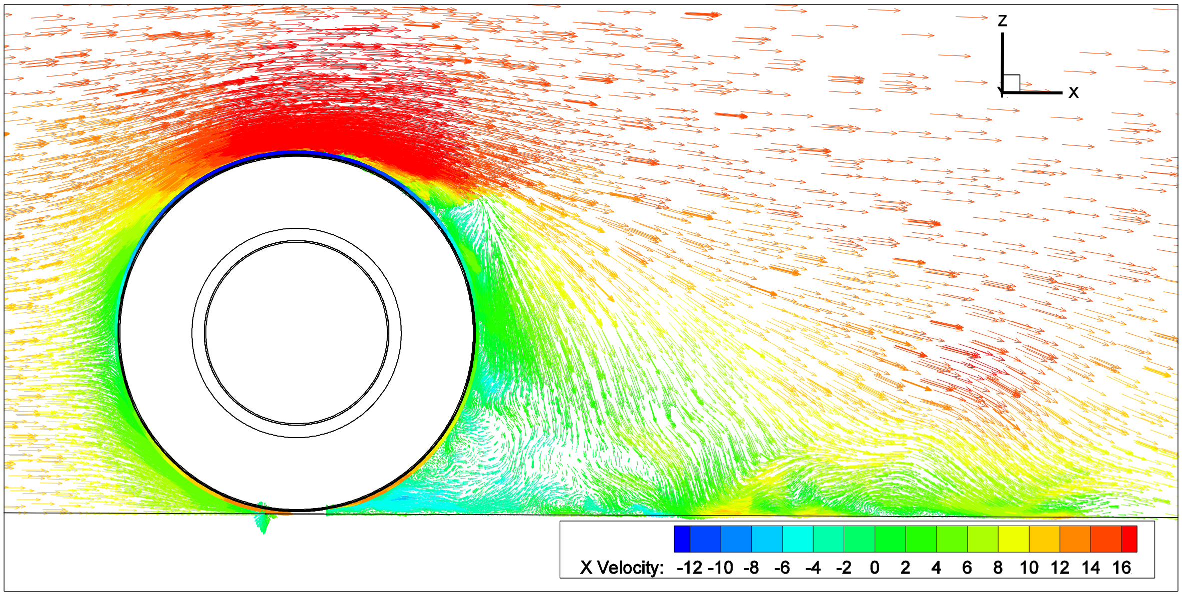

Figure32 (i) LES WALE t=T_1

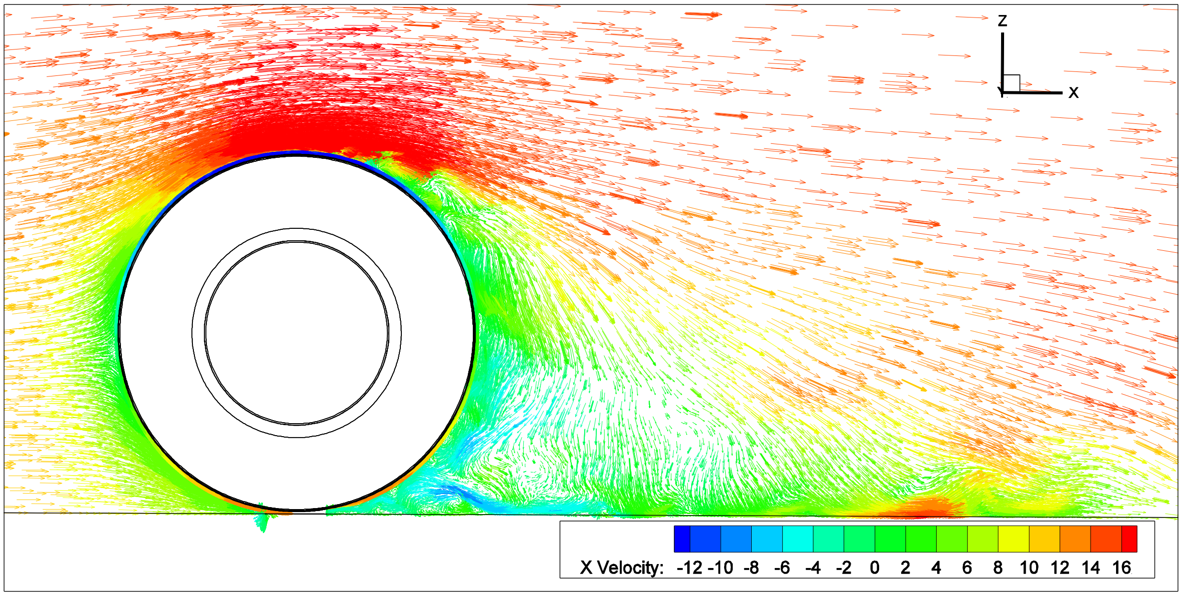

Figure32 (j) LES WALE t=T_1-0.01sec

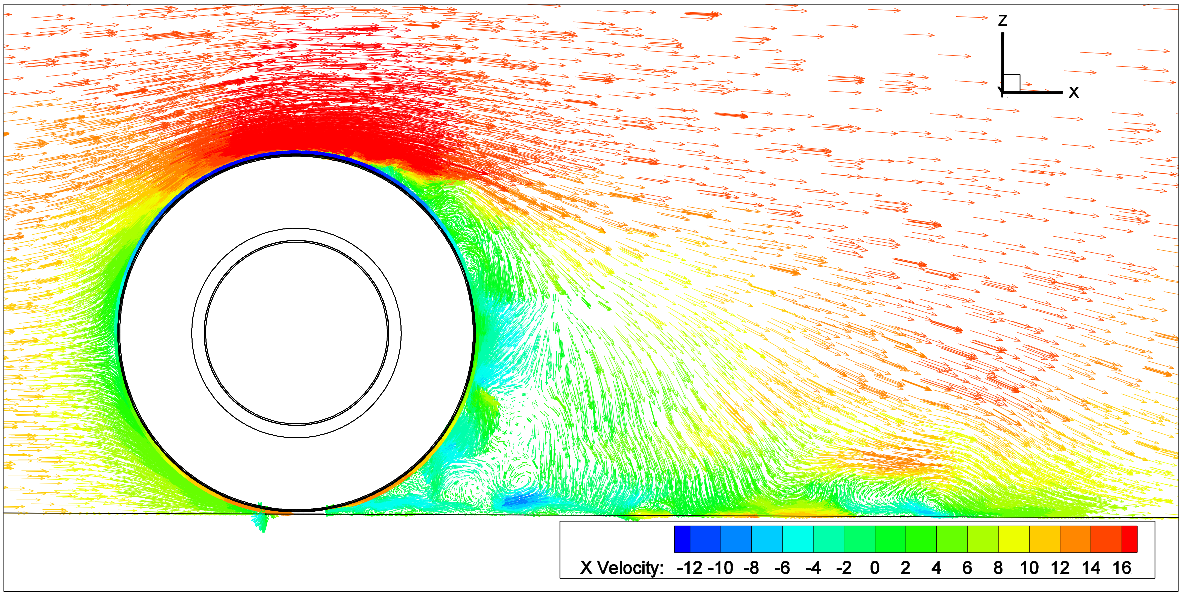

Figure 33 shows velocity components on the z plane cutting across the contact patch. K-e realizable model and S-A model shows no significant difference globally. However, S-A model results in more attached flow at the front corner of the contact patch as suggested by x-velocity magnitude while the separated area appeared clearly with k-e realizable model. It, however, didn't result in any significant change in term of the width of the wake.

Kω and kω-SST model showed the trend how the flow turned along the front corner of the contact patch although the width of the wake is arguably larger than k-e realizable and S-A models.

As seen so far, trans-k-kl-w model showed more attached feature even this aspect resulting in notably narrower wake. On the other hand, trans-SST shows very similar flow pattern to S-A model and other no-transient kw models.

The flow around the contact patch has not been changed much with LES models, which showed similarity to k-ω model and its derivatives, although it contained many vortices and had the evidence of the vortex-shedding phenomena inside the wake. However, the shear layer on the outer boundary of the wake broke up more hence wider wake compared to all RANS model computed, which indicates higher energy loss in the flow due to the presence of the wheel so higher drag number is expected. On the WALE SGS model didn’t add any notable difference from Smagorinsky-Lilly SGS model.

The size of the wake and separation over the side of the wheel is likely to correlate with the drag coefficient. Therefore smaller separation appeared with RKE and Trans-k-kl-ω is expected to lead to lower drag.

For the sake of completeness, an extended set of 2D slices is presented in Appendix B in order to illustrate the velocity distribution in the wake.

Figure 33 velocity components on z=-0.123 plane

Figure33 (a) Realizable k-ε model

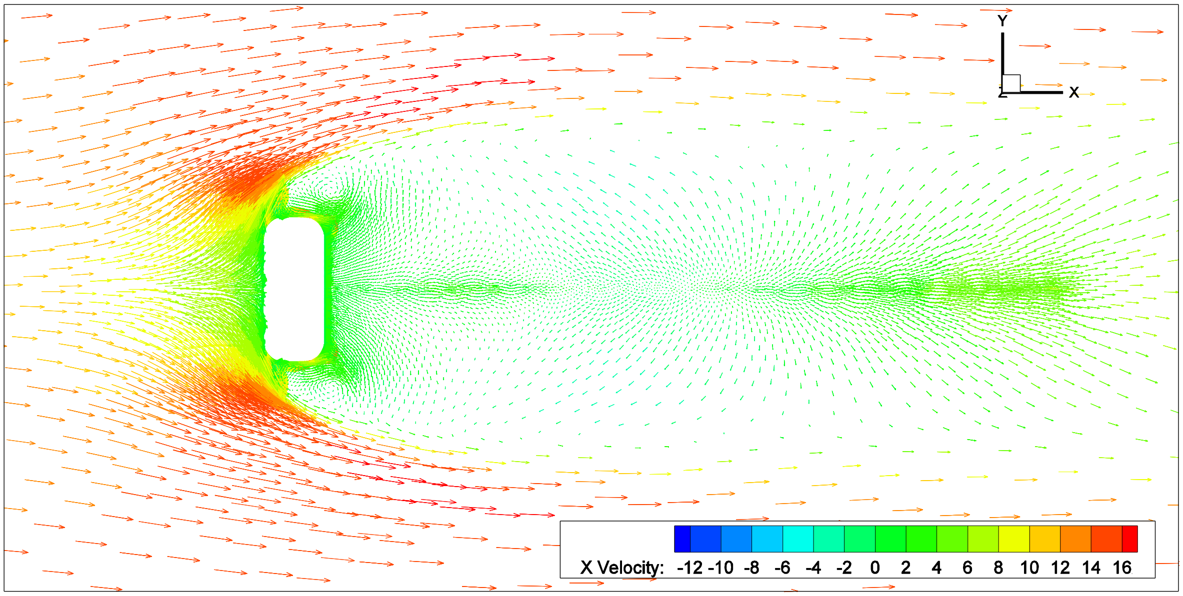

Figure33 (b) Spalart-Allmaras model

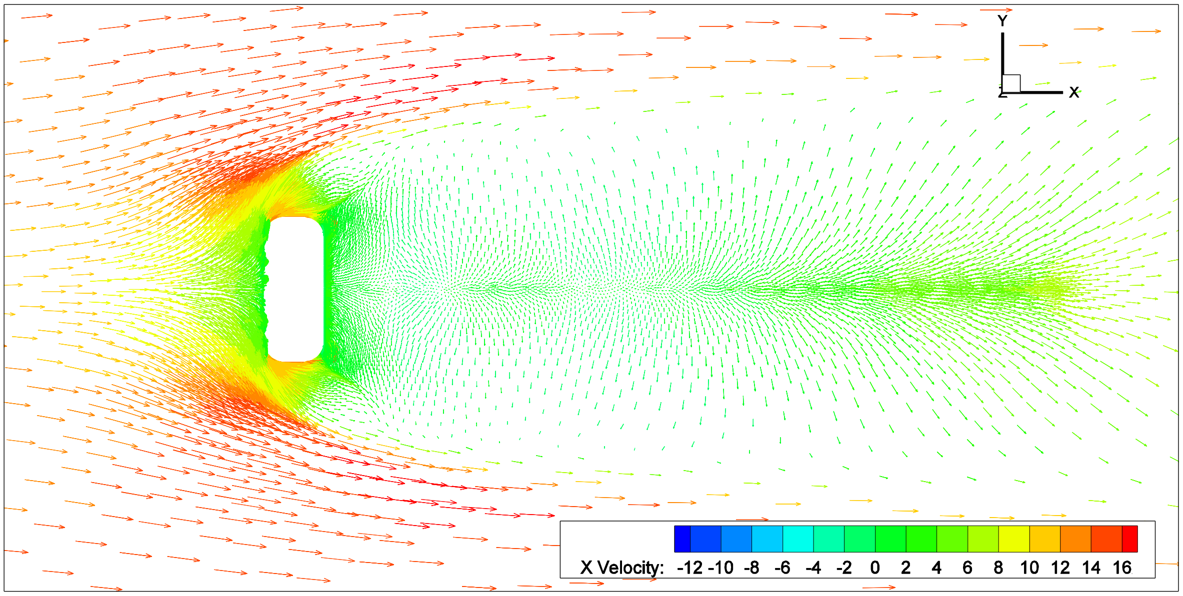

Figure33 (c) k-ω model

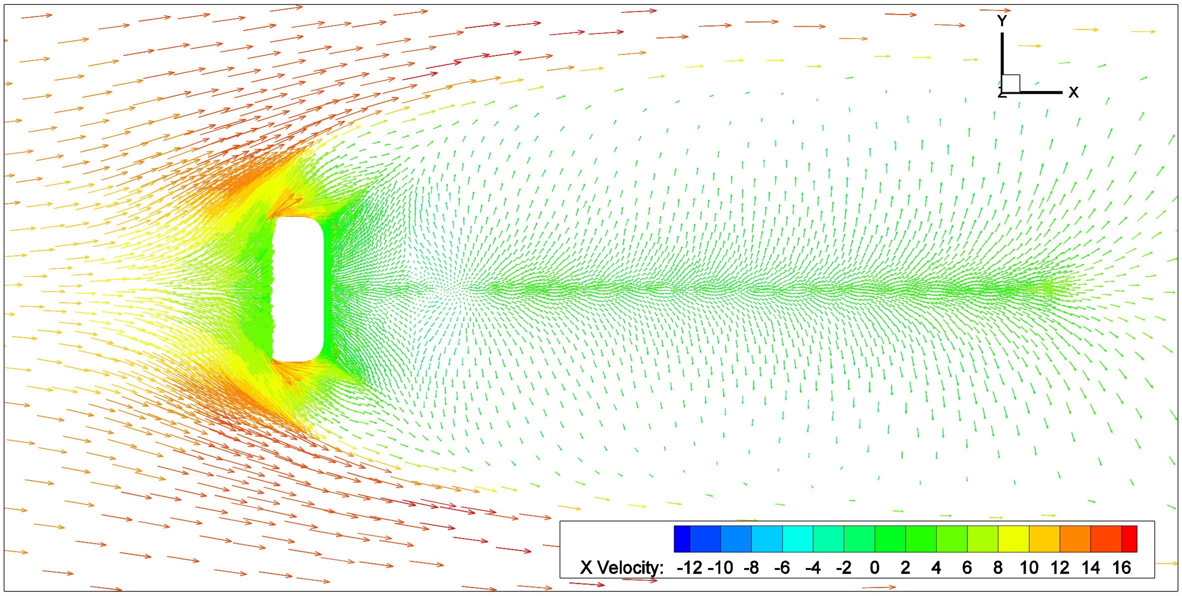

Figure33 (d) k-ω SST model

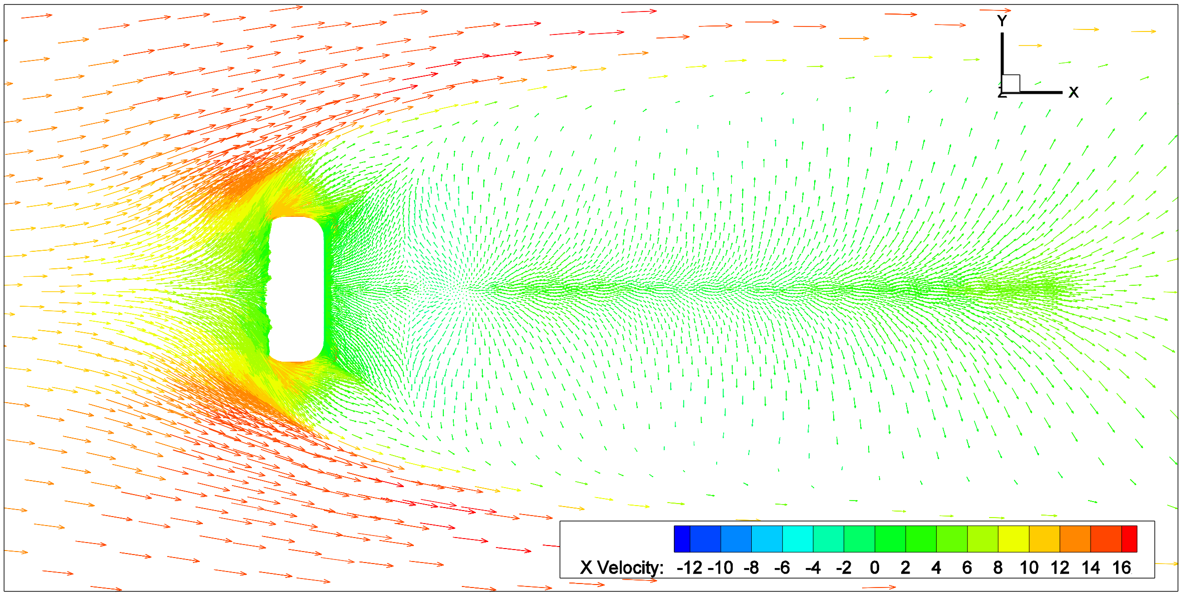

Figure33 (e) trans-k-kl-w model

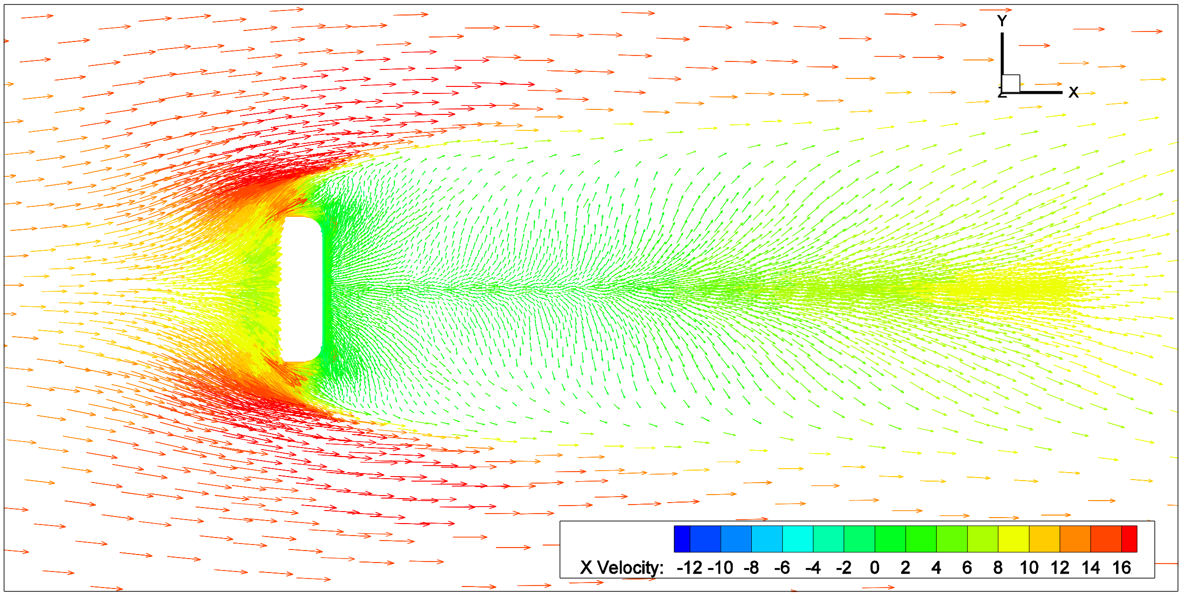

Figure33 (f) trans-SST model

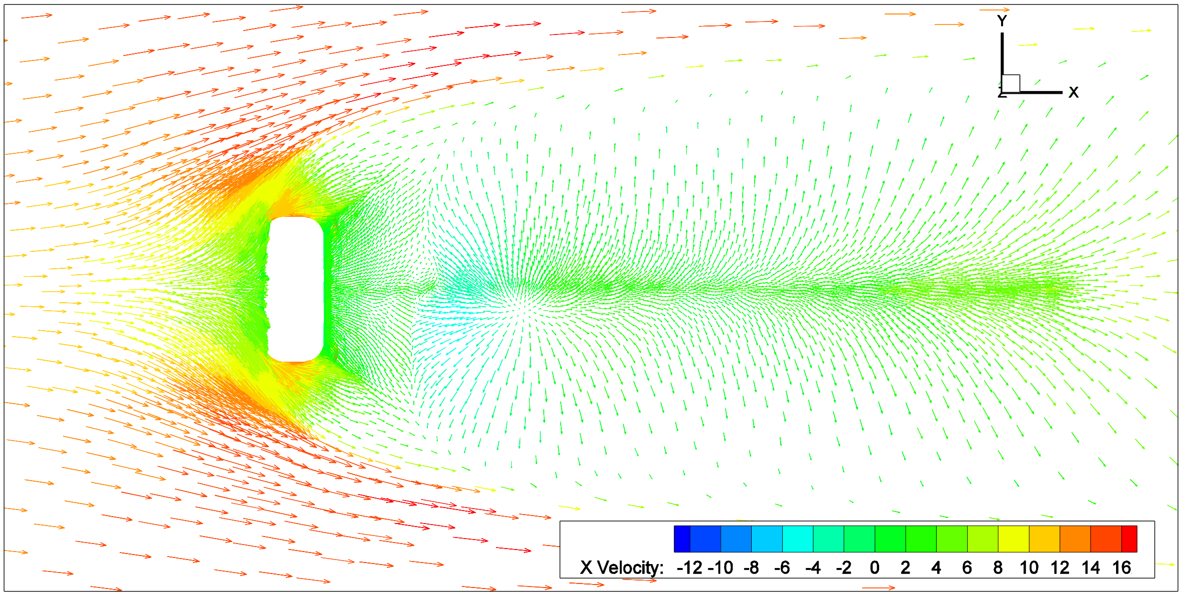

Figure33 (g) LES t=T_1

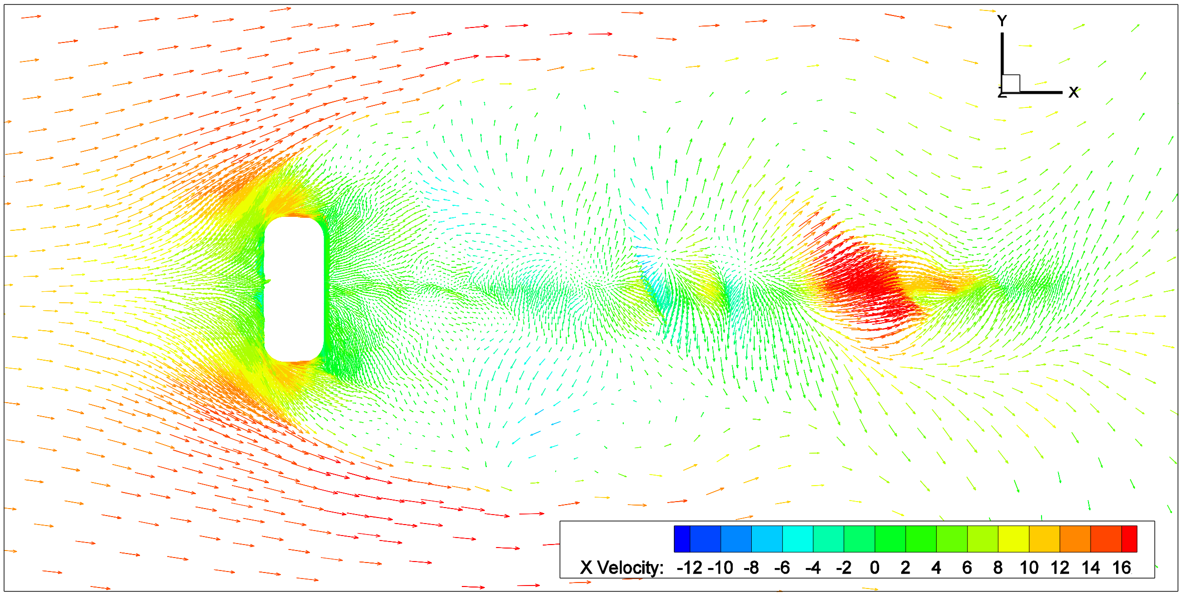

Figure33 (h) LES t=T_1-0.01sec

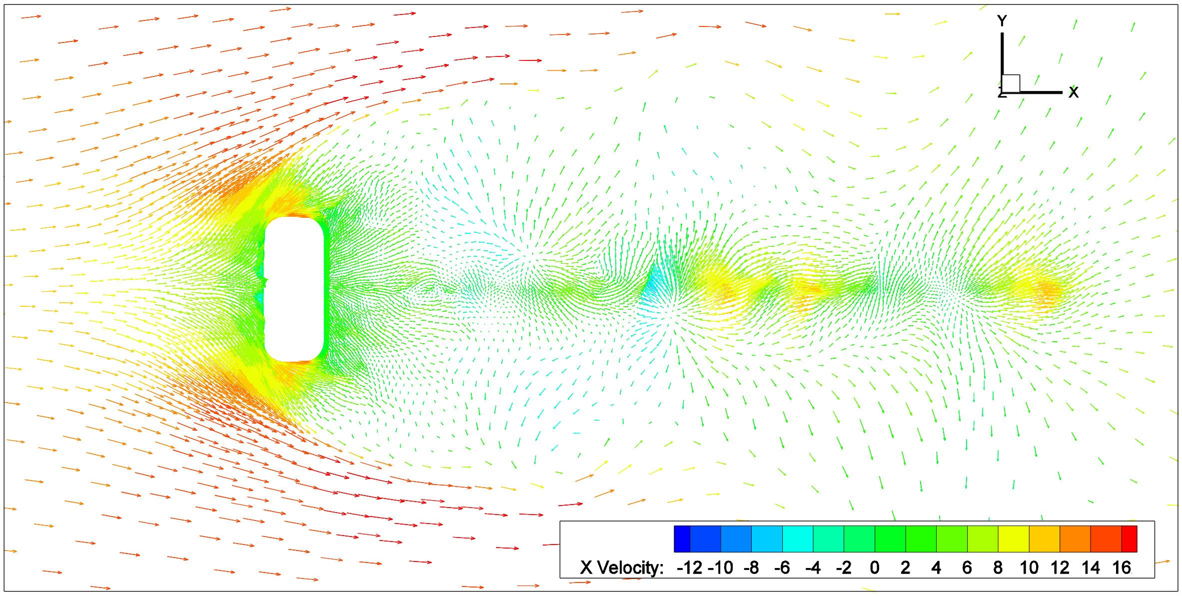

Figure33 (i) LES WALE t=T_1

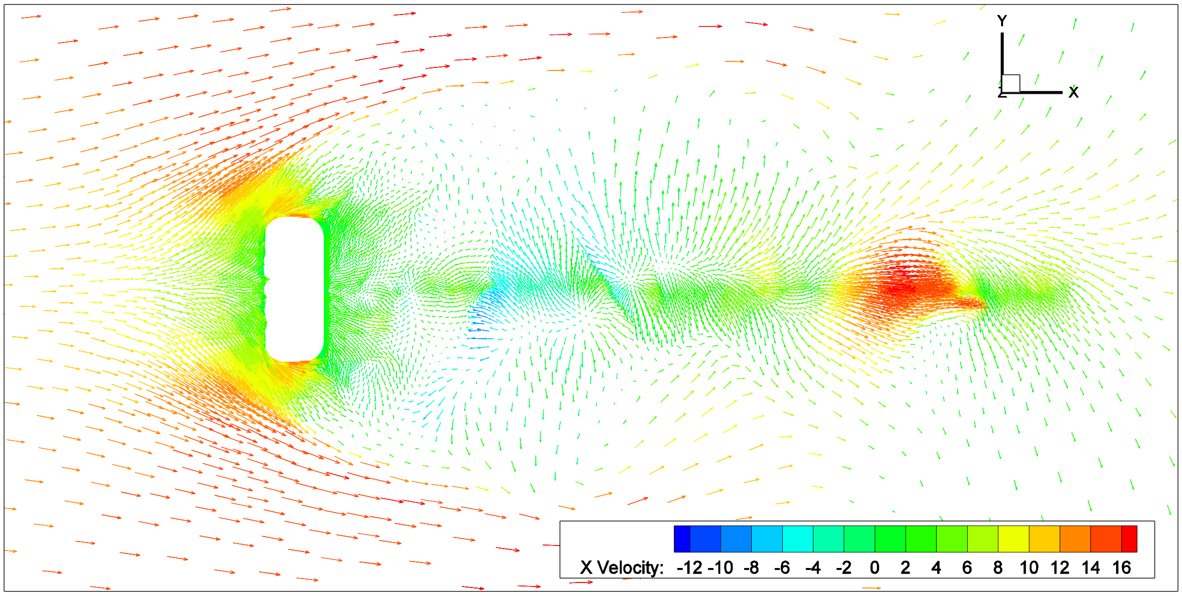

Figure33 (j) LES WALE t=T_1-0.01sec

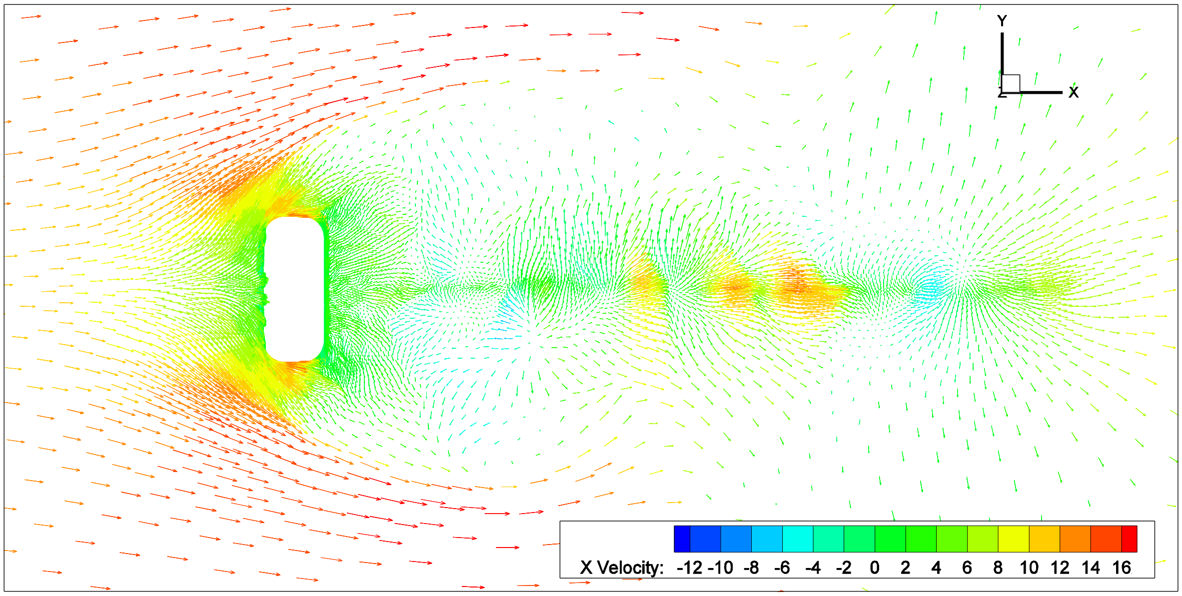

Figure 34 shows velocity component on the z-plane cutting through the height of one fourth of the tyre diameter from the ground plane. In RANS models, the two type of the flow pattern appeared. Realizable k-ε, S-A and trans-k-kl-ω models showed the free-stream velocity all the way on the side wall of the wheel and the flow separated in the wake whilst kω, kω-SST and trans-SST models show the separation over the wheel side wall.

As seen in kω families, LES models show very early separation over the sides. This resulted in Kelvin-Helmholtz instability leading to the roll-up of parts of the shear layer on the sides. The instability is initiated by the noise at the point of separation and develops into billows further down the shear layer. Again, WALE-SGS model didn't add any notable feature on the SL-SGS model.

As expected from its cavity feature, separation and recirculation are observed in the wheel centre hub. Especially in LES WALE, very asymmetric and violent appeared in the hub, which could be exaggerated by the roll-up of the shear layer discussed above.

Figure 34 velocity components on z=-0.06 plane

Figure34 (a) Realizable k-ε

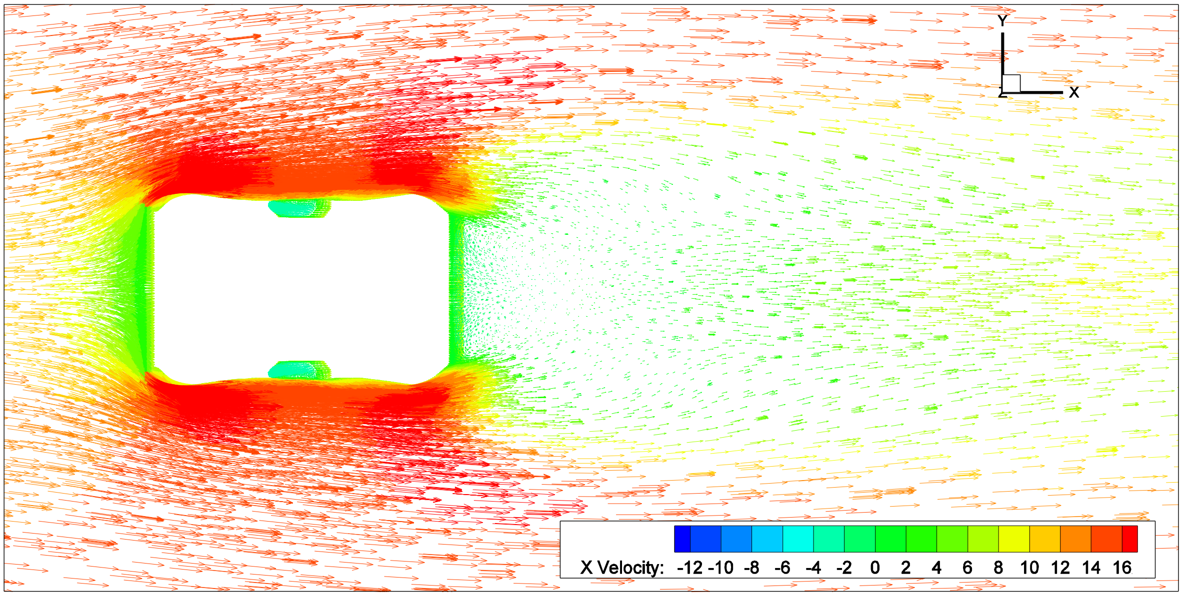

Figure34 (b) Spalart-Allmaras model

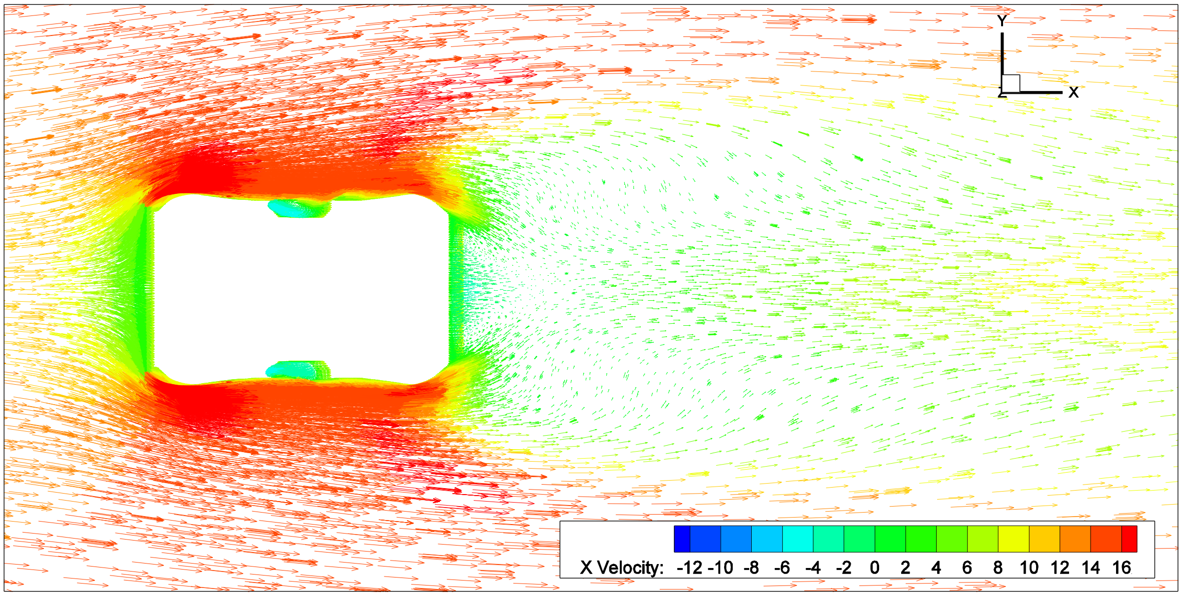

Figure34 (c) k-ω model

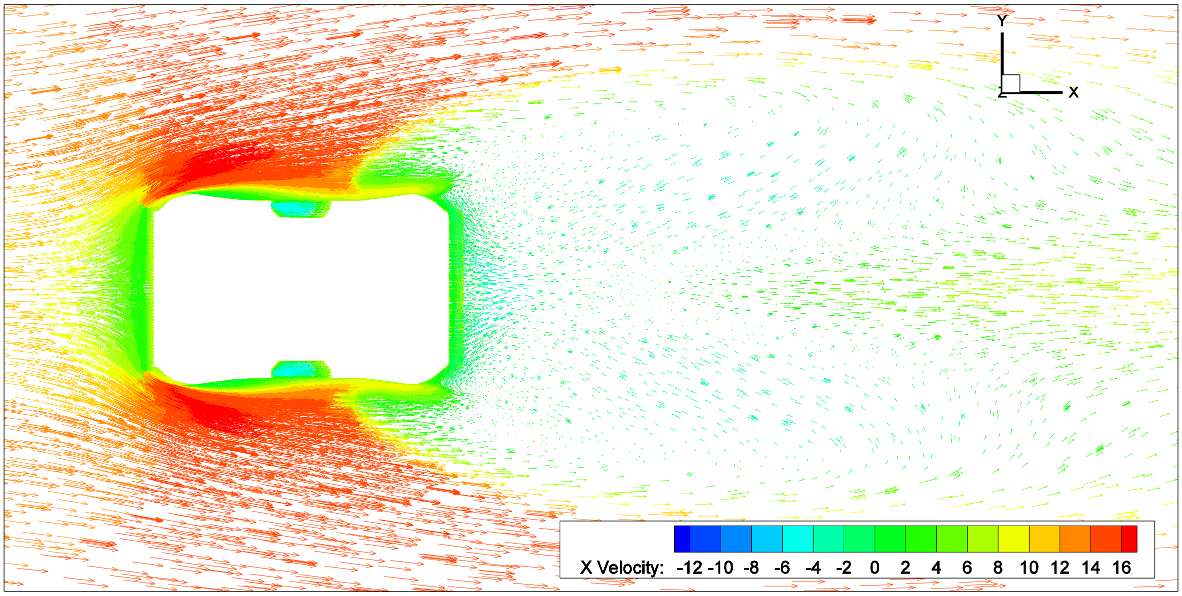

Figure34 (d) k-ω SST model

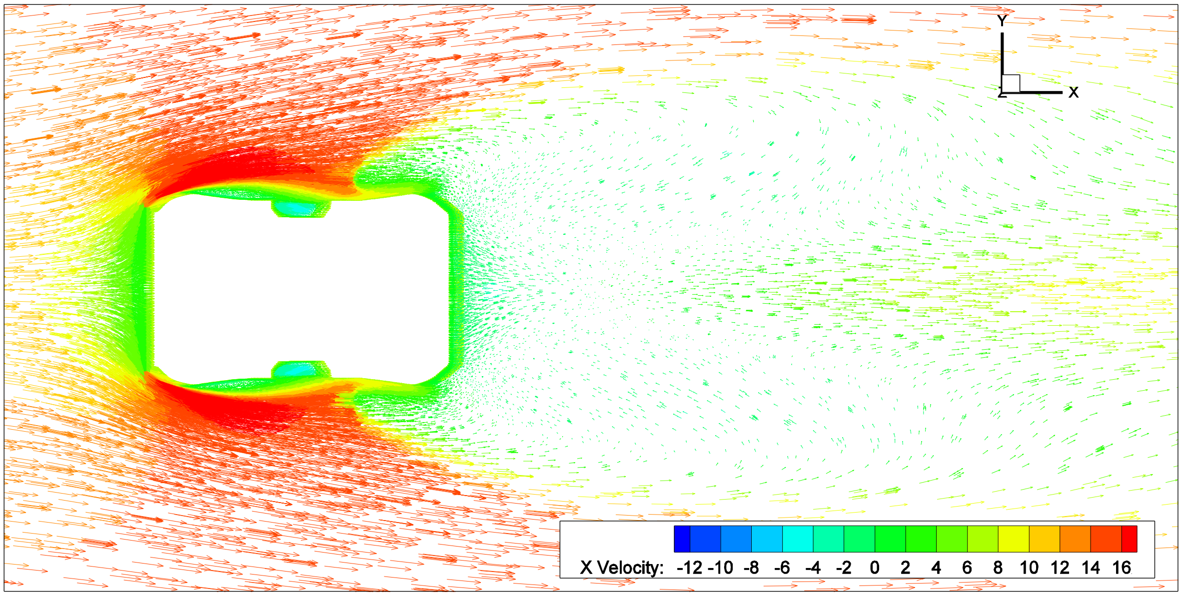

Figure34 (e) trans-k-kl-w model

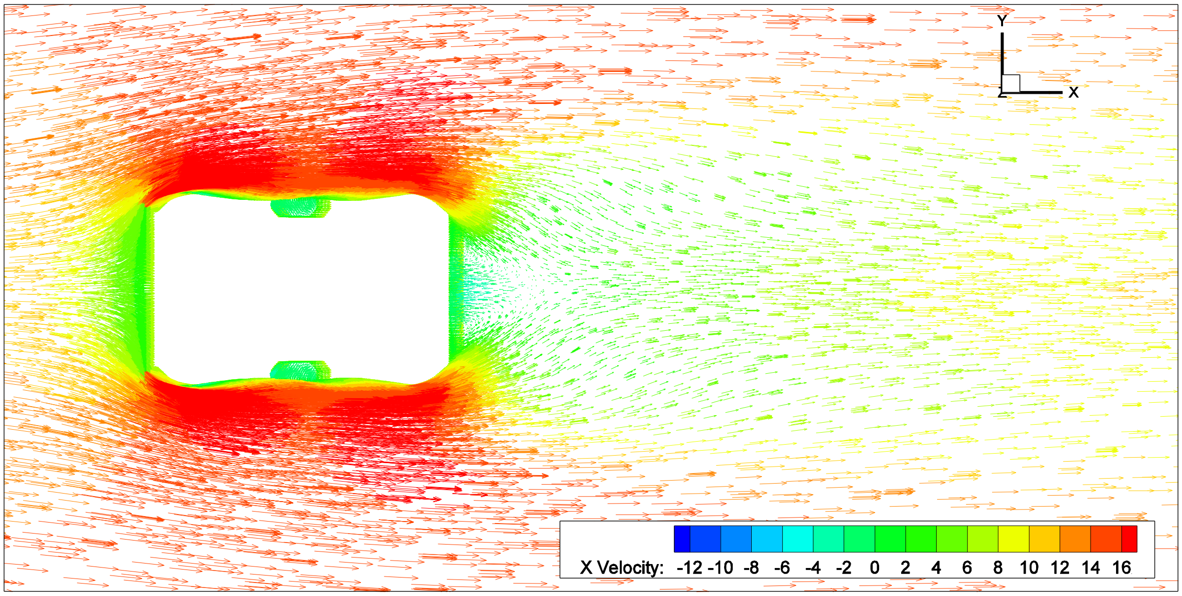

Figure34 (f) trans-SST model

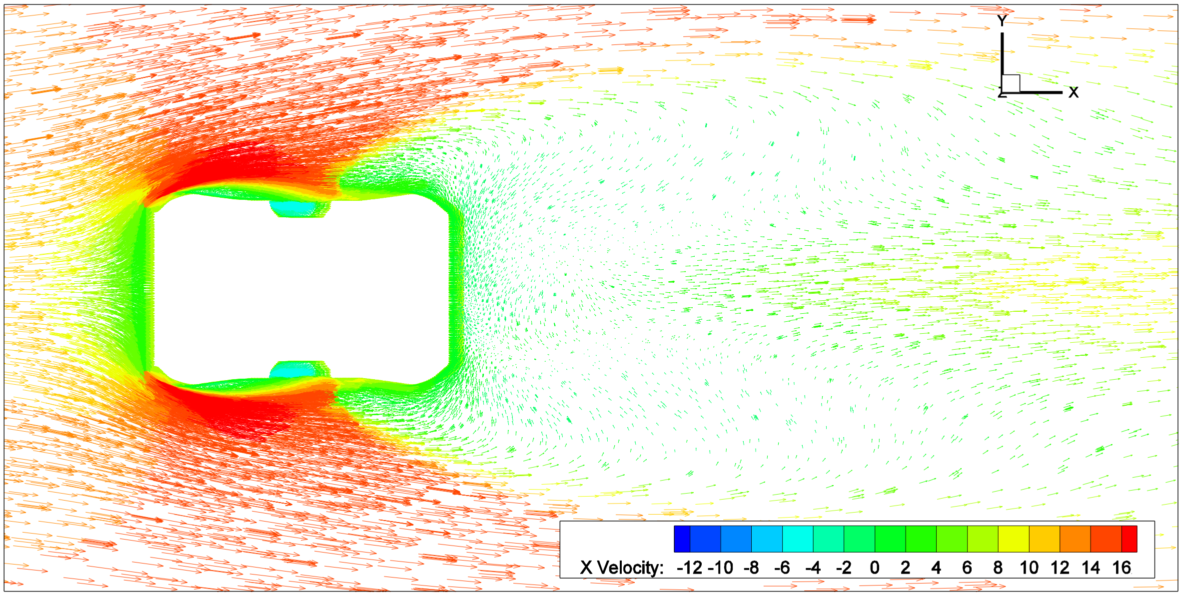

Figure34 (g) LES t=T_1

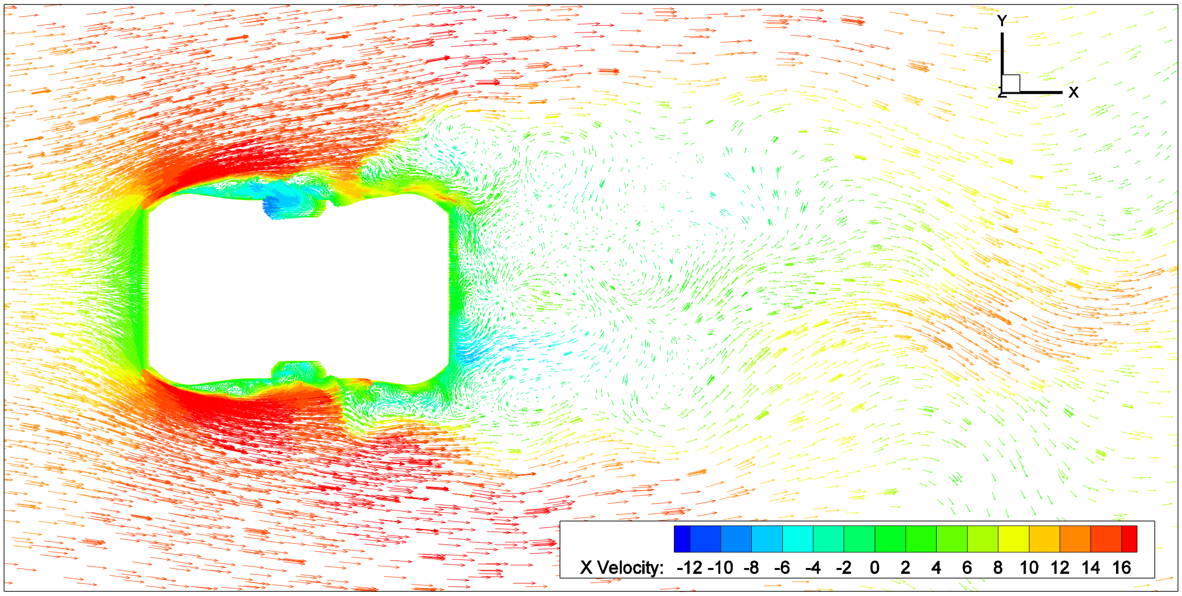

Figure34 (h) LES t=T_1-0.01sec

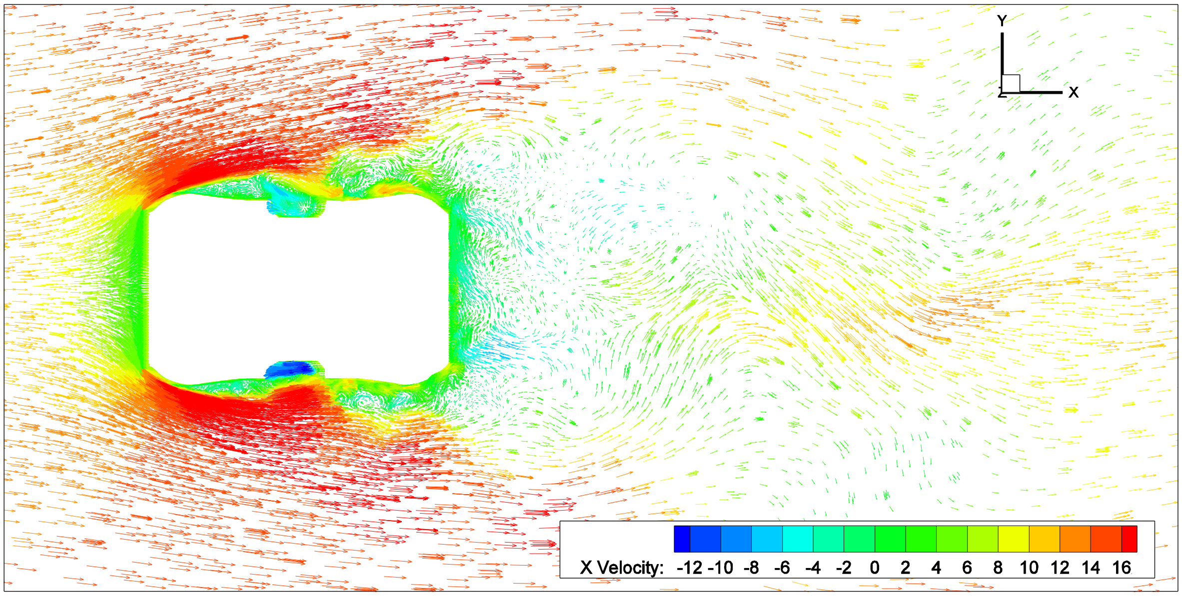

Figure34 (i) LES WALE t=T_1

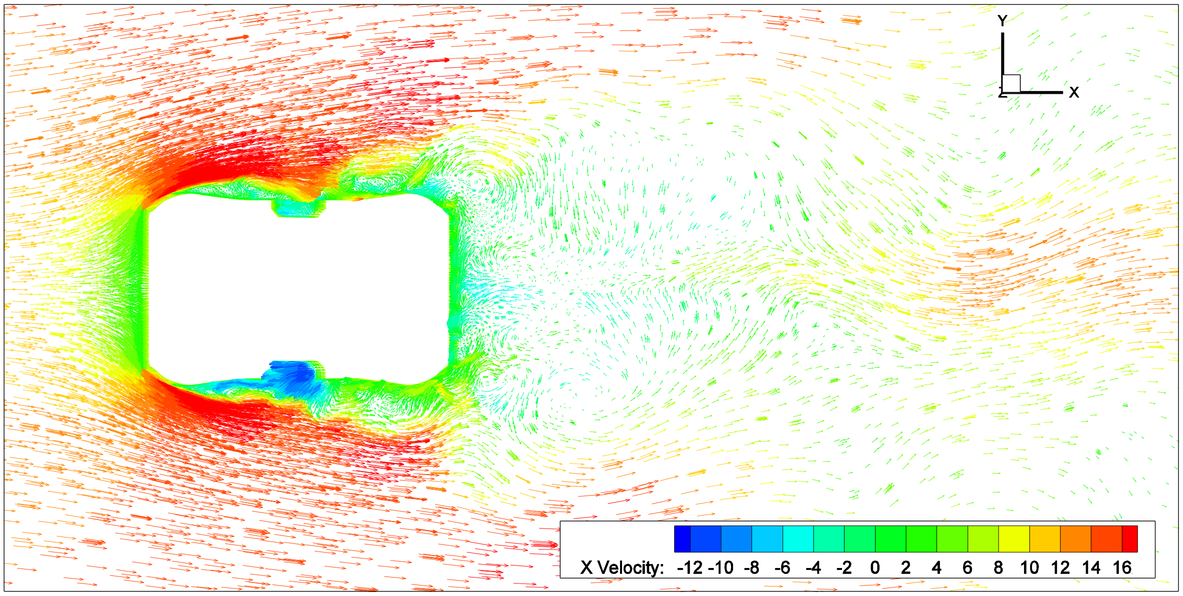

Figure34 (j) LES WALE t=T_1-0.01sec

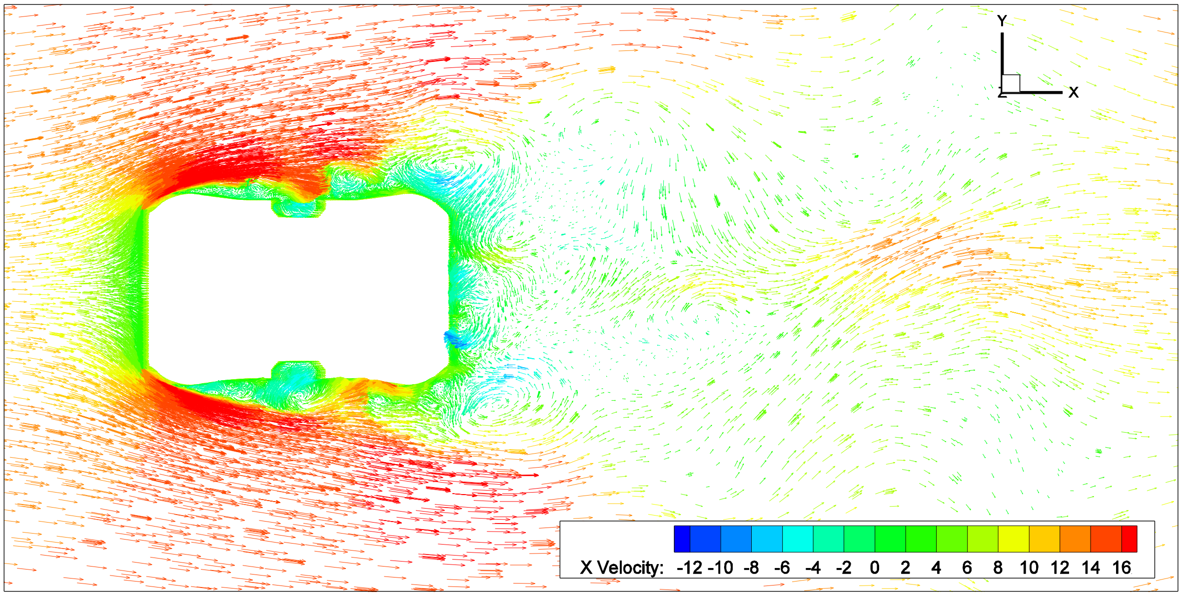

Figure 35 shows Turbulent Kinematic Energy (TKE) on the center plane for k-ε and k-ω models. Most notable difference appeared with k-ω models, which only showed the generation of the kinematic energy from the boundary layer and results in significantly lower magnitude of TKE as a whole. Furthermore, k-w model generated TKE from the stagnation region of the wheel, which is unclear from physical term. On the other hand, other all RANS models share similar generation process where boundary layer seeds initial generation and then it's amplified by the shear layer. Trans-k-kl showed more TKE magnitude in the wake. It corresponds to the fact it has the smallest shape, which would be cause by exaggerated dispassion of the turbulence.

Figure 36 shows TKE on the Y-plane just off the side wall of the wheel. Firstly, k-e realizable showed less generation of TKE than other RANS models. Kw, kw-SST and trans-SST showed very similar pattern where the generation from the leading edge and the front of the contact patch is observed generally. Again, trans-k-kl-w suggested very different picture with very intense generation all over the wheel. The generation of TKE from the contact patch, which probably corresponds to front tyre jet as discussed earlier, is very strong as well as other intense band appeared on the grand plane behind the contact patch.

Figure 35 Contour of turbulent kinetic energy on Y=0 plane (unit : m^2/s^2)

Realizable k-ε model

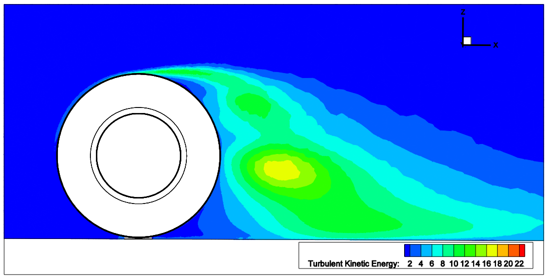

k-ω model

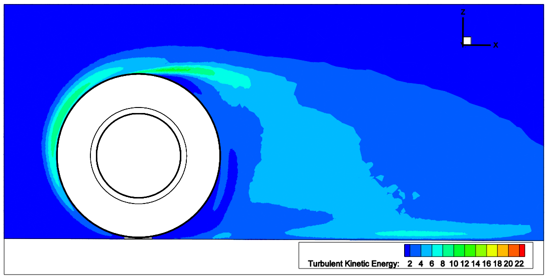

k-ω SST model

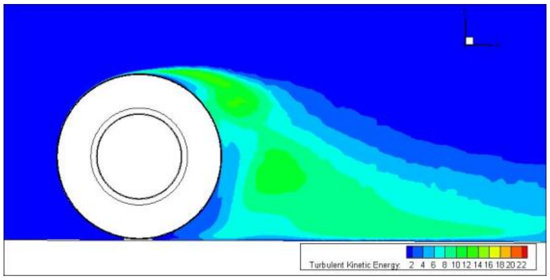

trans-k-kl-w model

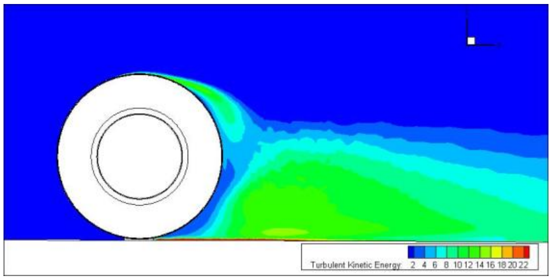

trans-SST model

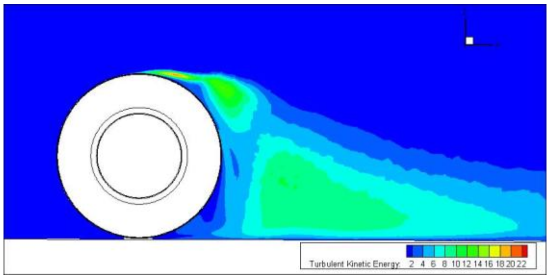

For the sake of completeness, an extended set of 2D slices with turbulence quantities is presented in Appendix B in order to further illustrate points discussed above.

Figure 36 contour of turbulent kinetic energy on Y=-0.07 plane (unit: m^2/s^2)

Realizable k-ε model

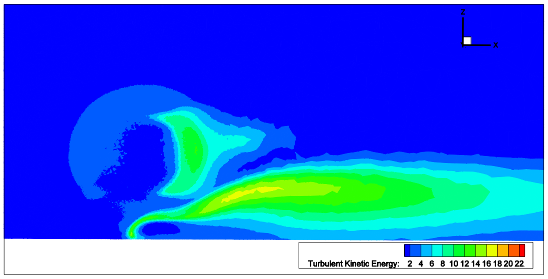

k-ω model

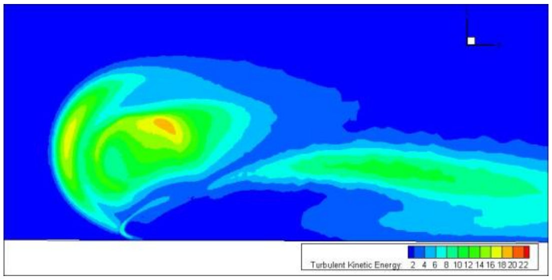

k-ω SST model

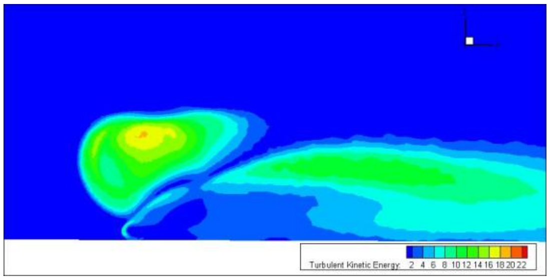

trans-k-kl-w model

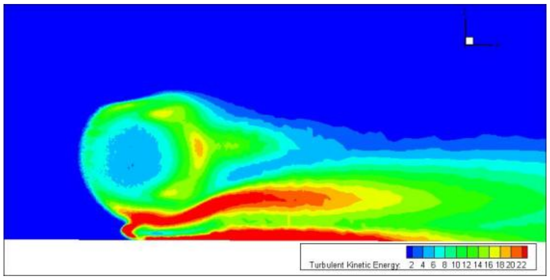

trans-SST model

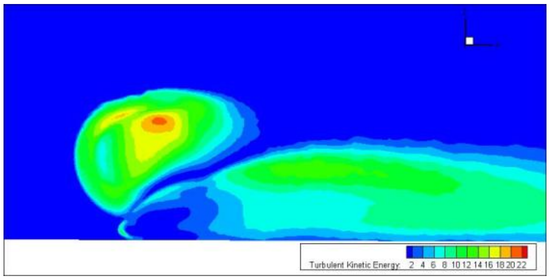

5.7 Comparison with Cp slice on the centre plane

Figure 37 and figure 38 show the coefficients of the static pressure on the wheel surface cut by the symmetrical plane for all turbulent model cases computed. The experimental data from the primary literacy [1] is also shown for comparison. Note that the repeatability of the surface pressure data was found to be within 1.5% in referred experimental data [1]. Please refer to figure 9 for the convention of the theta (the zero defined at the front most point of the section and the angle measured anticlockwise).

Firstly, Figure37 shows all no-transitional RANS results and its subfigures give magnified images for first bottom quadrant, recirculation zone and separation zone. Looking into the stagnation zone, 0 to 80 deg., all results follows a similar trend, decreasing from stagnation point and then increasing toward the front edge of the contact patch resulting in very sharp spike over unity in the end. This is supposed to be caused by viscous pumping effect from rotational wheel. In other words, the flow is forced to thrust into the contact patch by rotation. Experimental data suggest lower static pressure around 50deg than RANS results. RKE shows arguably lower pressure relatively but still significantly higher by 0.15 approximately.

In separation zone and recirculation zone, S-A showed the strongest suction peak and attached longer up to 280deg, 10deg forward from the top. This resulted in sharp pressure increase just after separation but bounces back quickly and keeps relatively low pressure up to 150deg where all results are arguably conversing. K-ω separates early hence weaker suction peak and then form slow recovery toward the back of the wheel. Kω-SST separates earlier than SA but recovery process is similar while RKE recovers very slowly despite very similar separation point to kω-SST. As an example, the flow structure around the separation point for kω-SST is shown in figure 39, showing very peculiar type of the separation, very thin feature formed by extremely acute flow direction change between freestream and rotational moving wall.

General trend toward higher pressure around stagnation point compared to experimental result could be explained to some extent by commonly known problem in RANS calculation [43].

Figure 38 is same picture as Figure 37 above but for transient RANS and LES. The lower front quadrant is very similar to non-transitional RANS, again, higher static pressure than experimental data at 50deg. Regarding separation point, Trans k-kl-ω showed very late separation at the top of the wheel as expected by all proceeding results. Trans SST and LES(S-L) showed very similar point around 280 deg. One notable feature compared to non-transitional RANS is a sharp pressure increase at

250deg (260deg in the case of trans k-kl-ω). The separation itself seems to be moderate but the flow separates completely around 10deg back from the top of the wheel. This feature is arguably observed with experimental data as well.

Note that LES data is averaged over the period of 0.1 sec and 0.05 sec for S-L and WALE respectively. Figure40 shows actual unsteady envelop, suggesting clear unsteadiness all over the back of the wheel after the separation point.

Figure 37 Cp slice on the centre plane for no-transitional RANS models

Figure 37 (a) Overview

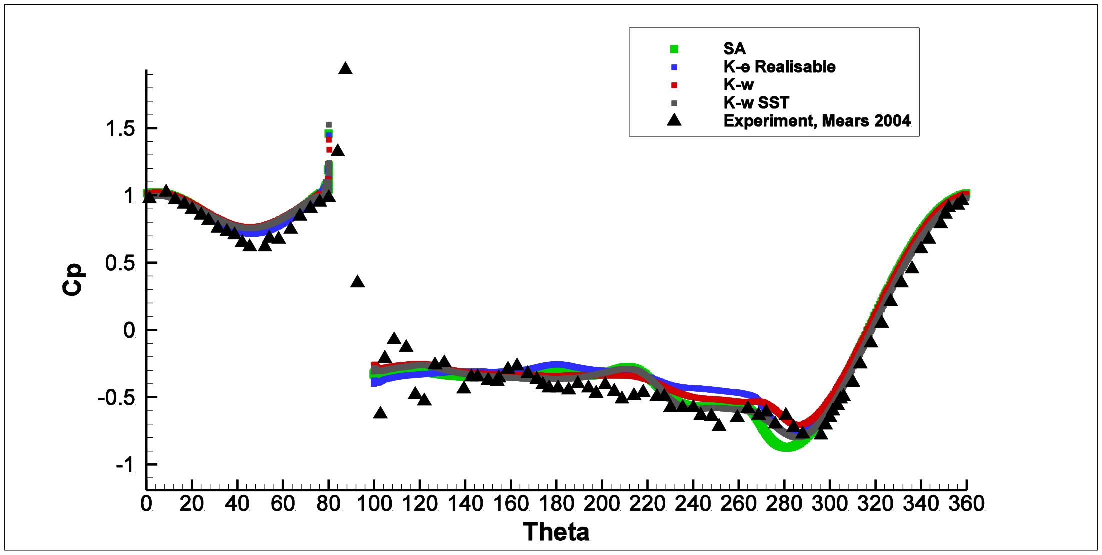

Figure 37 (b) Stagnation zone

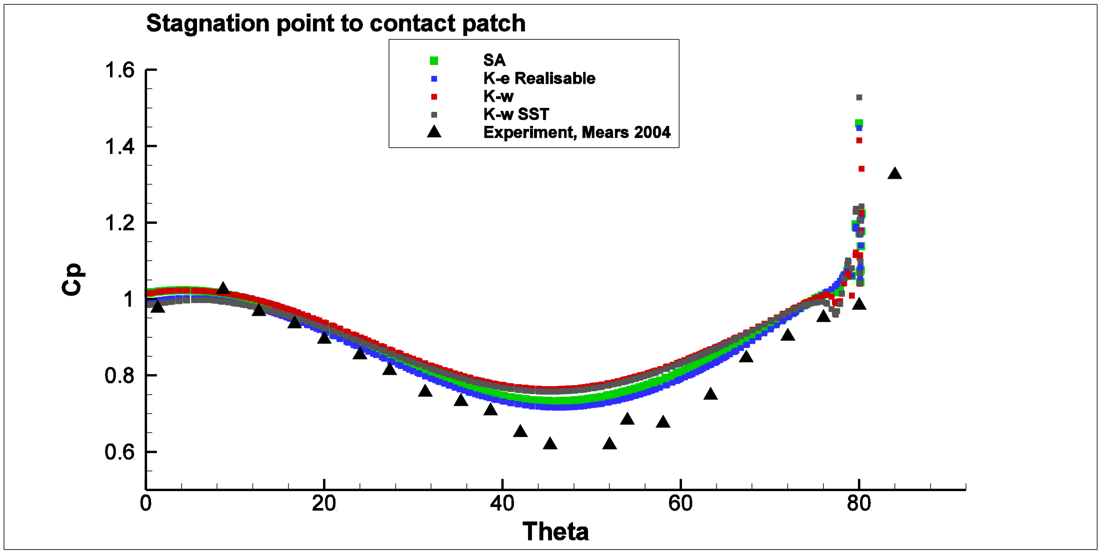

Figure 37 (c) Recirculation zone

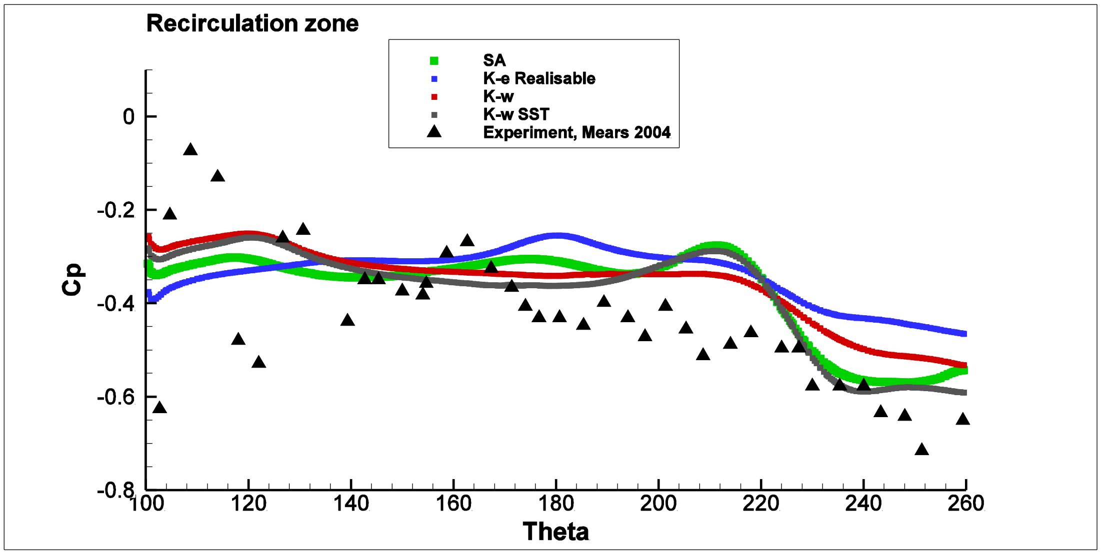

Figure 37 (d) Separation zone

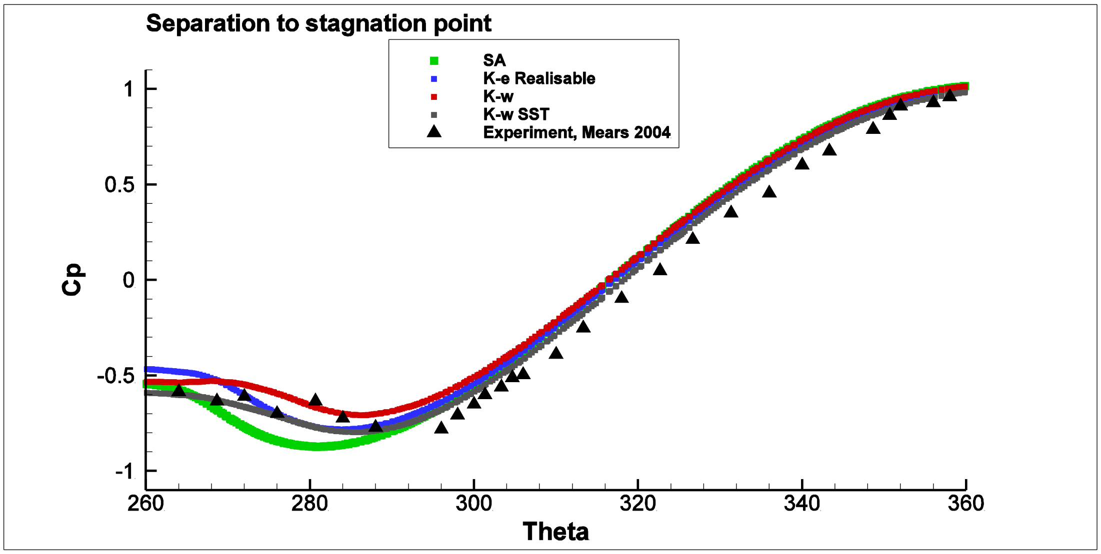

Figure 38 Cp slice on the centre plane for transitional RANS models and LES

Figure 38 (a) Overview

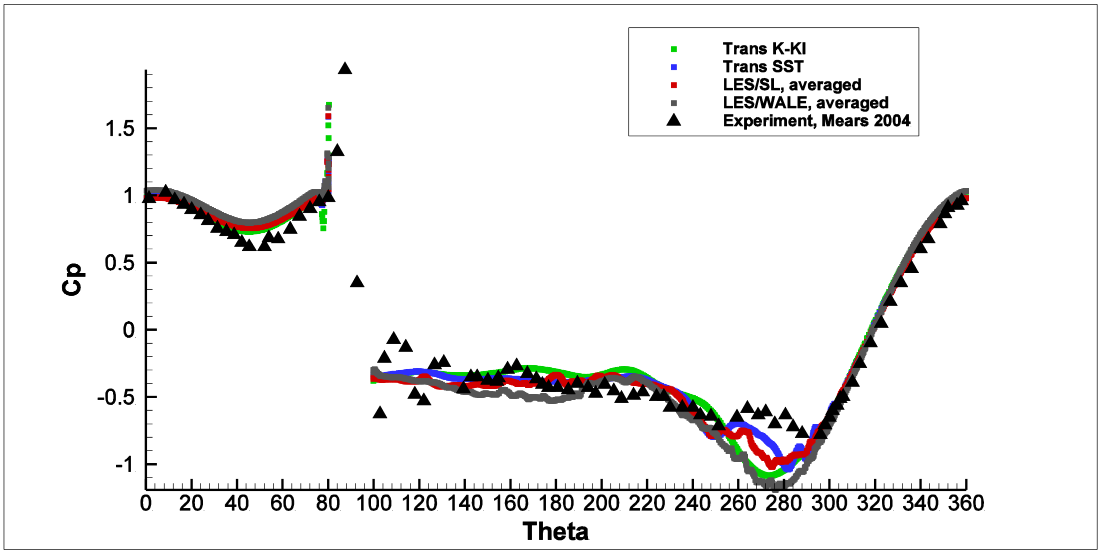

Figure 38 (b) Stagnation zone

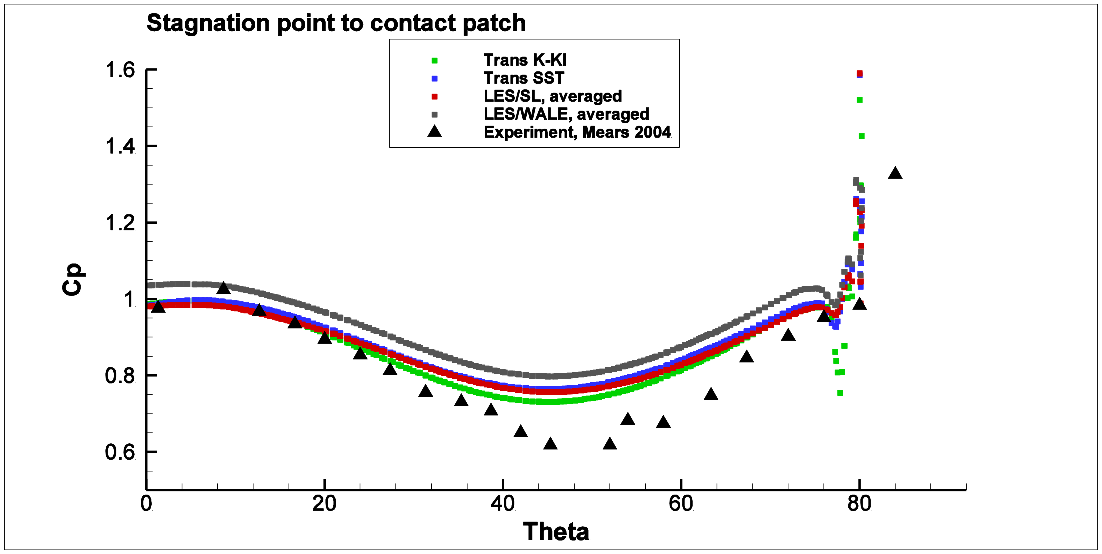

Figure 38 (c) Recirculation zone

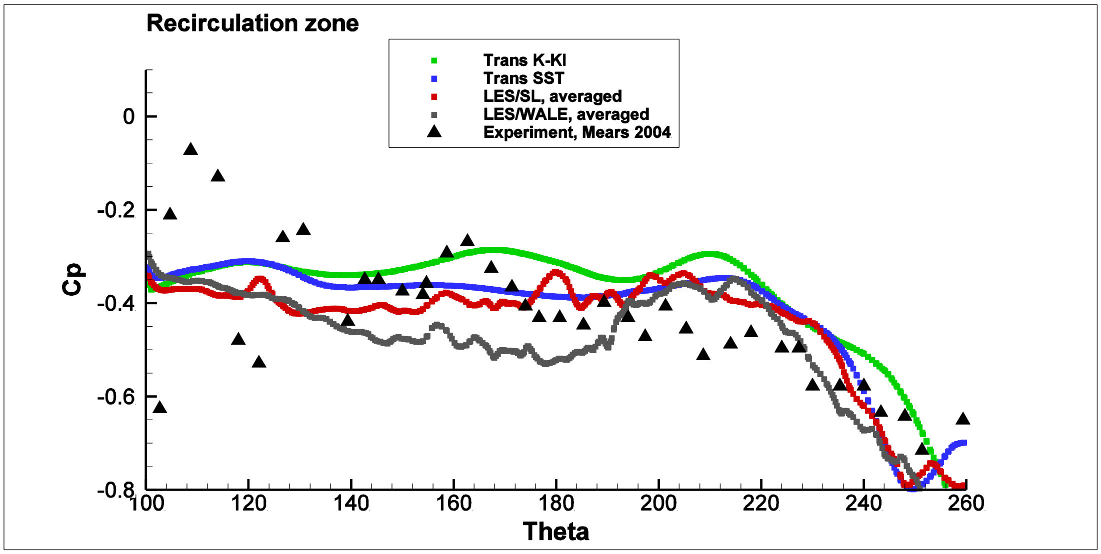

Figure 38 (d) Separation zone

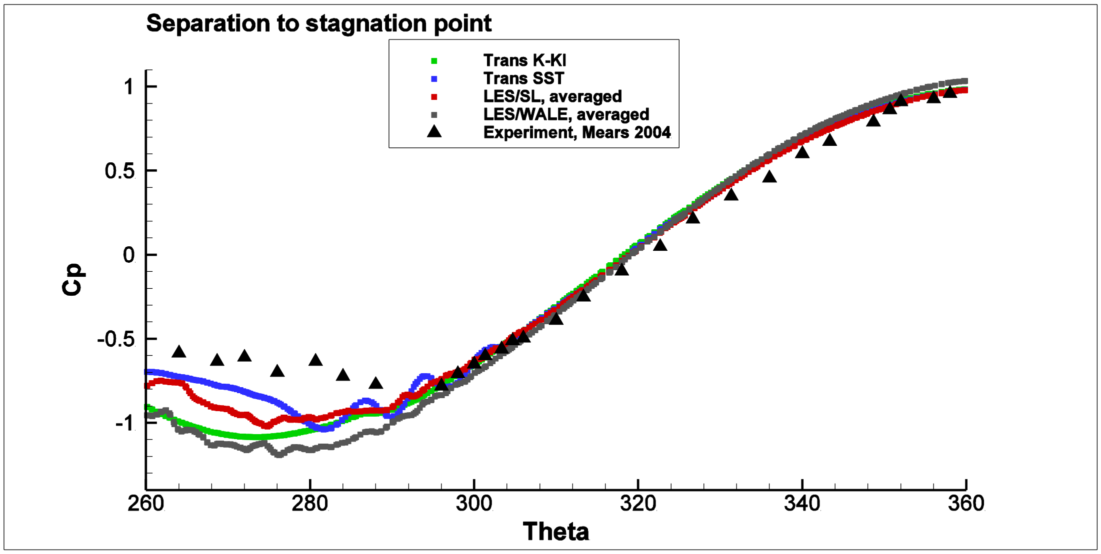

Figure 39 a schematic of the separation based on k-ω SST data

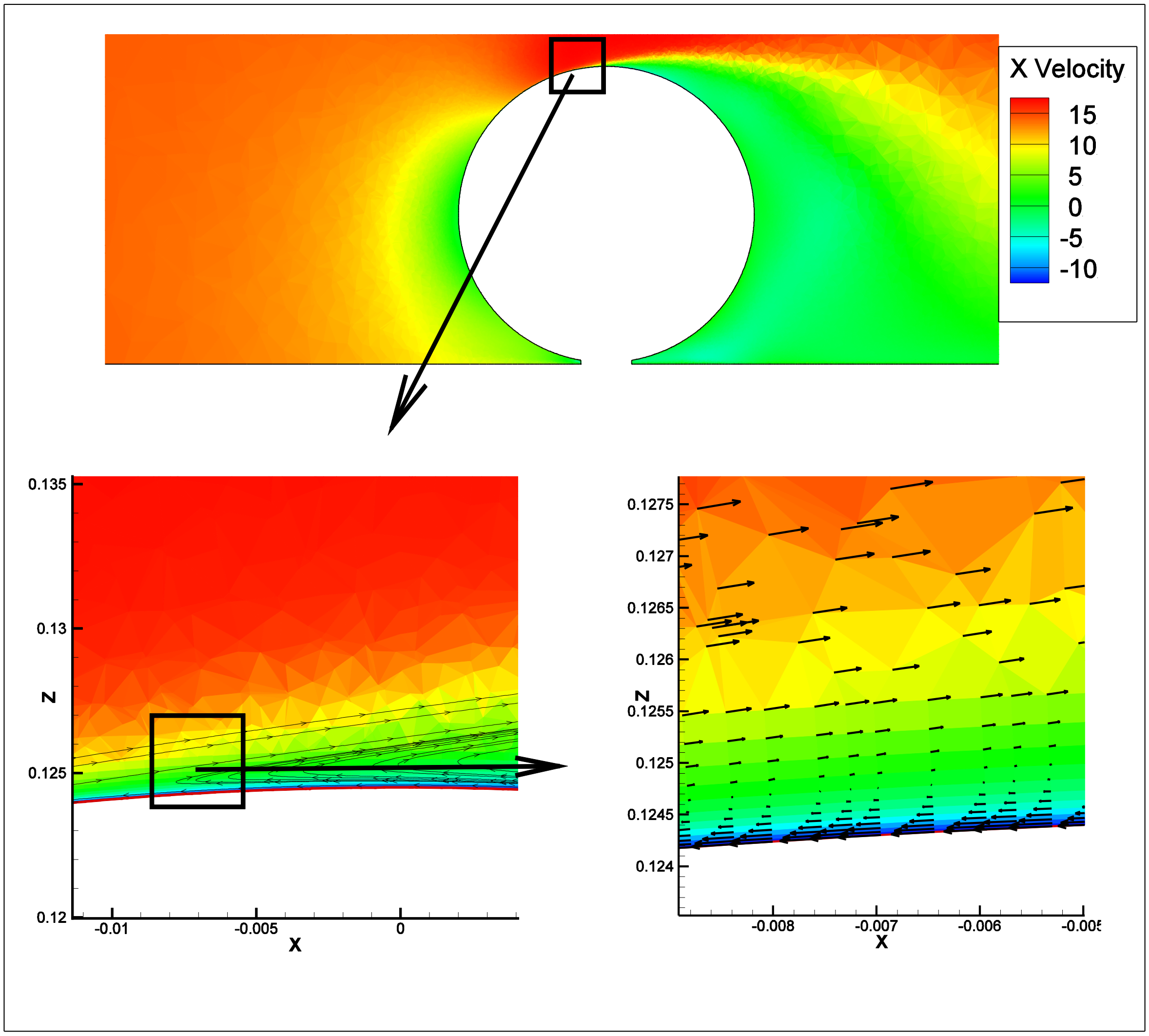

Figure 40 LES unsteady envelope in Cp (WALE SGS model)

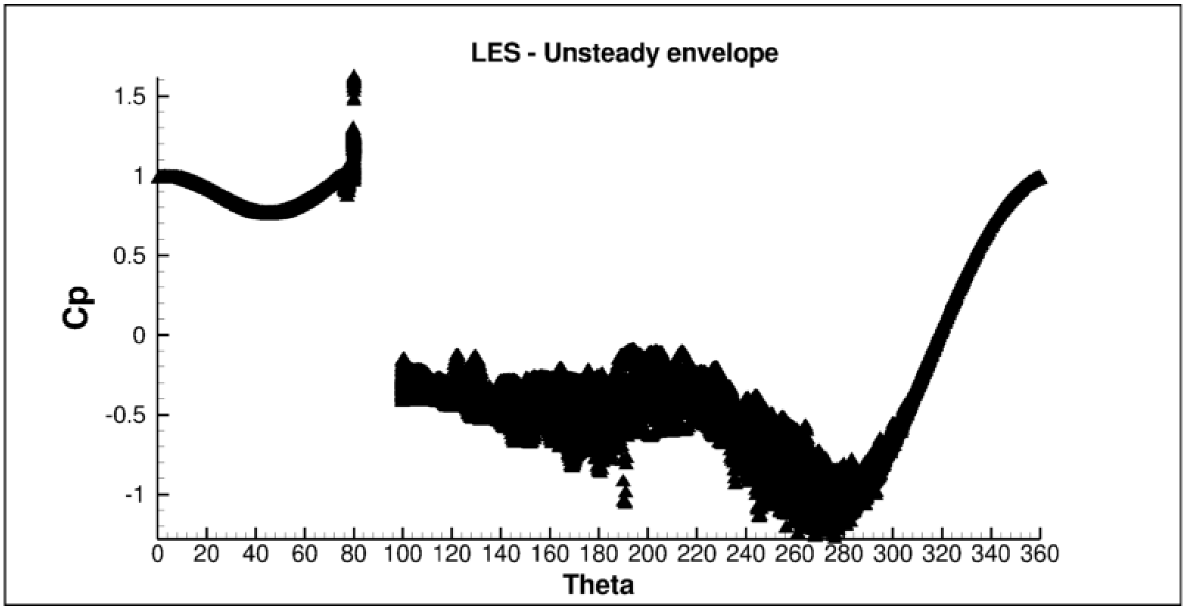

Table 9 Flow Separation point

Turbulence model	Separation angle (deg.)
RKE	286
S-A	280
k-ω	285
k- ω SST	286
Trans k-kl-ω	273
Trans-SST	282-296
LES S-L	275-289
LES WALE	276-289

5.8 Comparison with wall-shear stress on the centre plane

Figure 41 and figure 42 shows the shear stresses on the wheel surface on the centre line for all turbulence model computed. Please refer to previous chapter 5.7 for the convention.

Firstly, Realizable k-ε showed the peak point, which indicates the flow separation point, is around 300deg, or ahead the top of the wheel by 30deg. The shear stress decreases until 250deg and then recovering without distinctive peaks. S-A model follows the same trend for the first separation but a peak appeared at 200deg suggesting clear re-attachment of the flow.

In kω and kω-SST model, the flow separates around 300deg as seen in proceeding two models although the maximum shear stress is relatively low. The second peak is very clear with kw-SST model, which occurred around 200deg as in S-A model. Kw model doesn’t show this strong re-attachment.

It is remarkable that trans-k-kl model shows very different trend in the separation point. The peak of the shear stress appeared at 270 deg., at the top of the wheel. The peak profile is very acute spike. This is partly explainable by the transitional context this model adapts although trans-SST didn’t have this spike at all.

The second peak is observed at 190 deg., which follows the trend of SA or kw-SST.

Trans-SST shows very low shear stress all the way compared to other all RANS model. The separation point is not really clear but the first peak appears to be around 320deg. Another peak is observed at 270deg., the top of the wheel and then relatively higher peak appeared at 200deg.

LES WALE model showed similar profile to trans-SST. A moderate peak appeared at 320deg. And then multiple peaks appeared around the top of the wheel and the back of the wheel. Shear stress stays low over the separated zone in the comparison to all RANS models. Figure 43 shows unsteady envelope for LES WALE. Again, very unsteady behavior as seen in Cp but the peaks mentioned above are still observed this figure.

LES S-L shares same profile as WALE in first peak but and then it stays very low.

Figure 41 the coefficient of wall-shear stresses on the centre plane for no-transitional RANS models

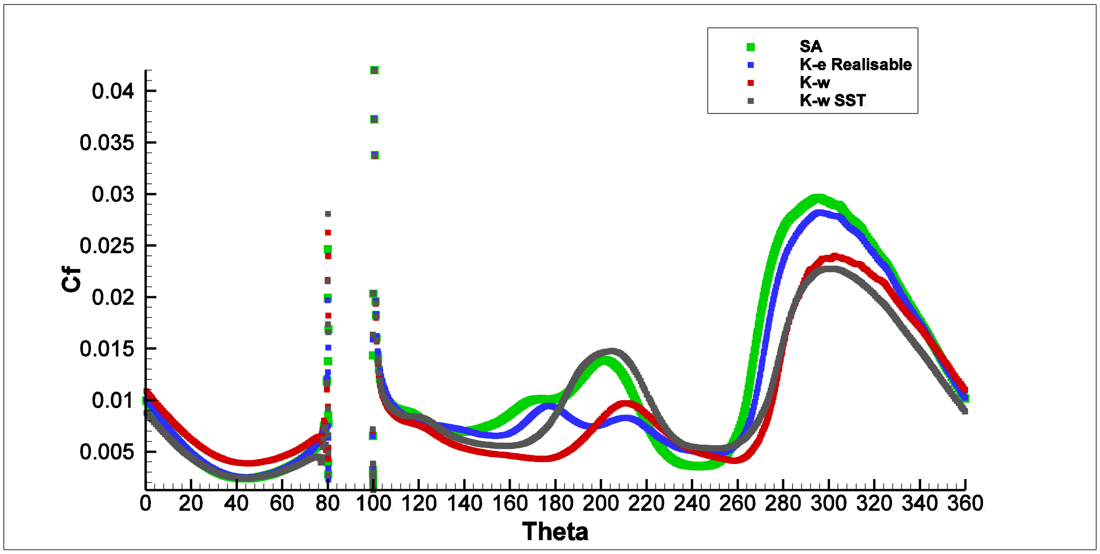

Figure 42 the coefficient of wall-shear stresses on the centre plane for transitional RANS and LES models

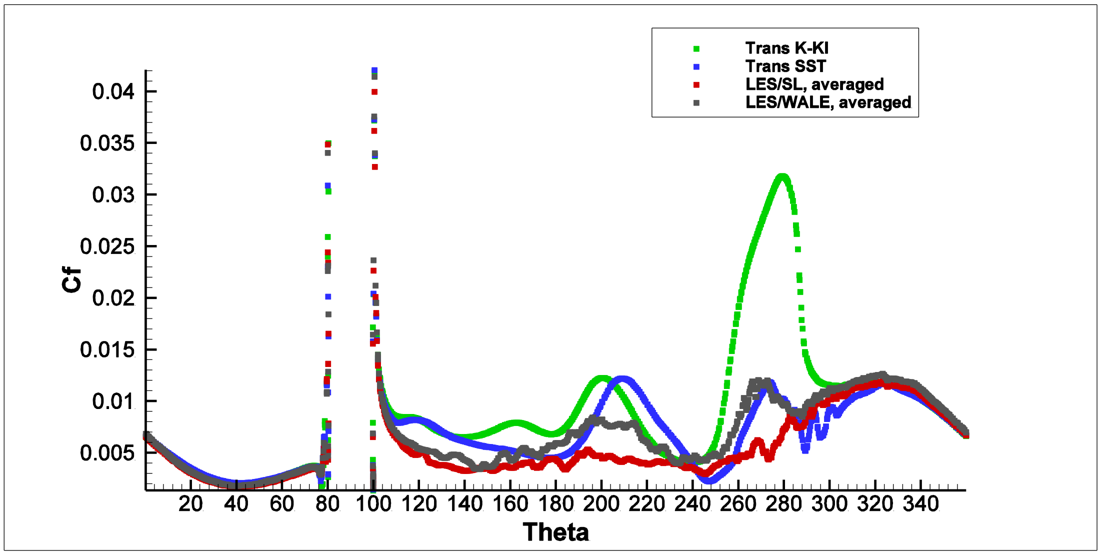

Figure 43 LES unsteady envelope in Cf (WALE SGS model)

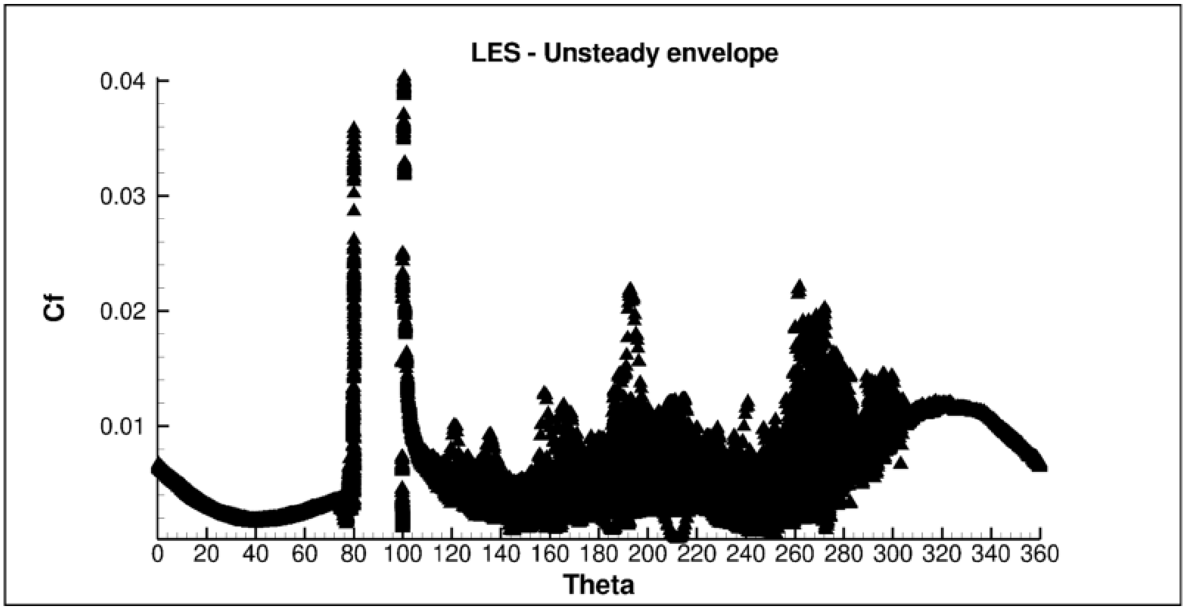

5.9 FFT results for LES data

FFT data process has been carried out over the period of 0.5sec approximately in time line in LES case with WALL SGS model.

The aerodynamics properties picked up were the friction coefficient (figure 44) and the velocity magnitude at the points arranged behind the top separation (figure 45) and just off the sidewall behind the wheel (figure 46) in the comparison with Kolomogorov's reference line. Please refer to the figure 47 for the locations of the markers.

Figure 44 FFT of Cd

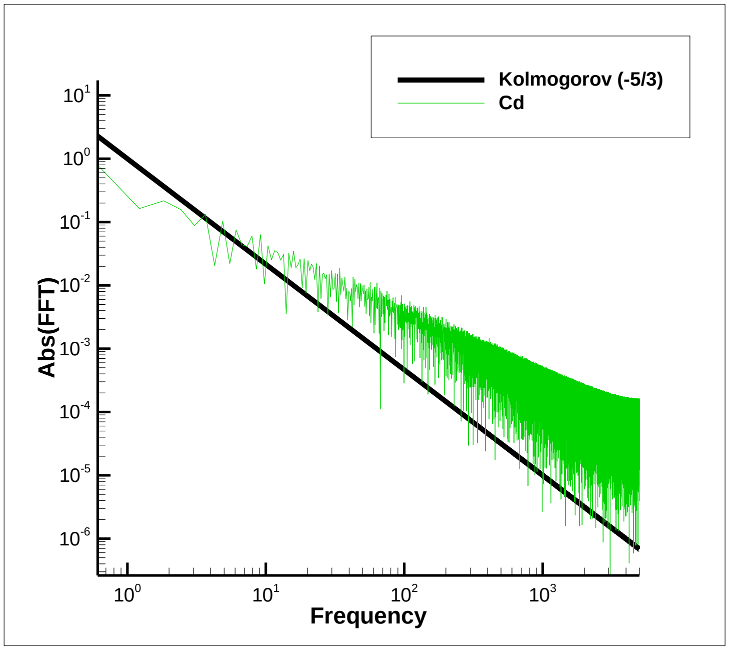

Figure 45 FFT of the velocity magnitude at top markers

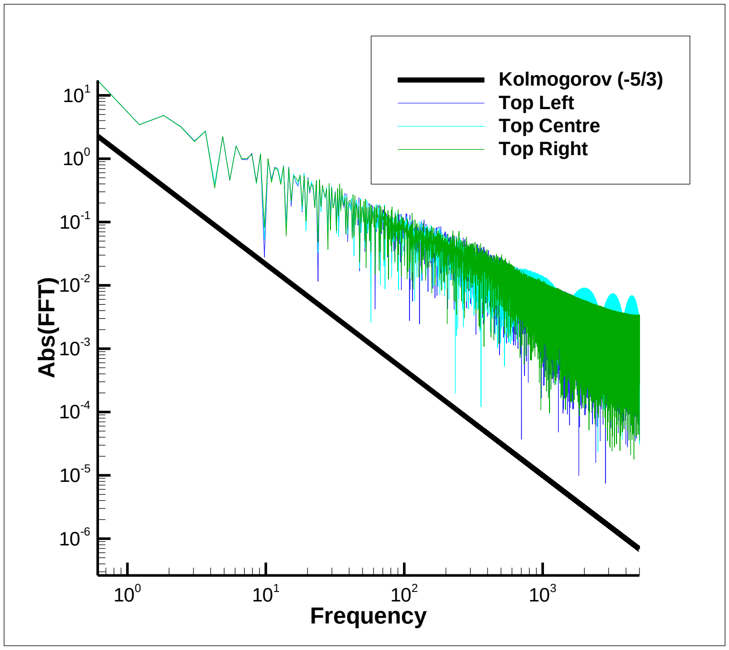

Figure 46 FFT of the velocity magnitude at the side markers

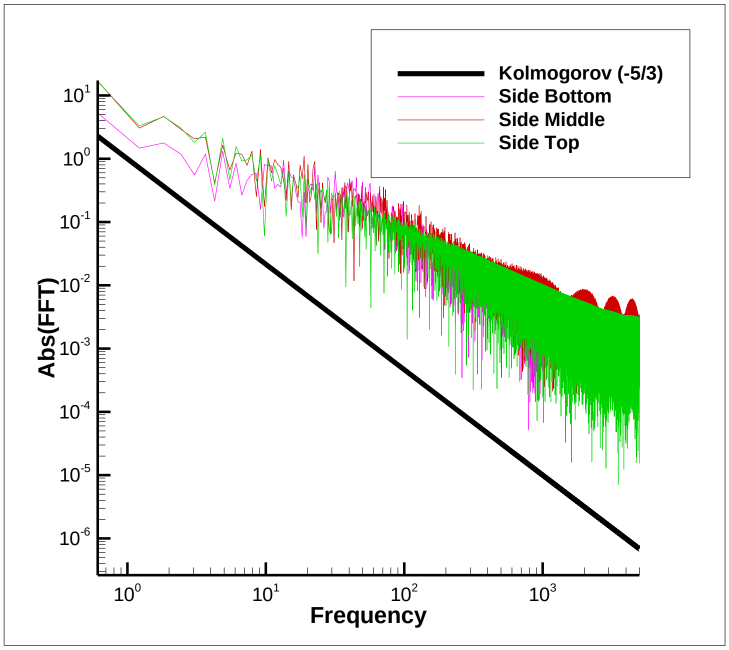

Figure 47 the locations of the markers

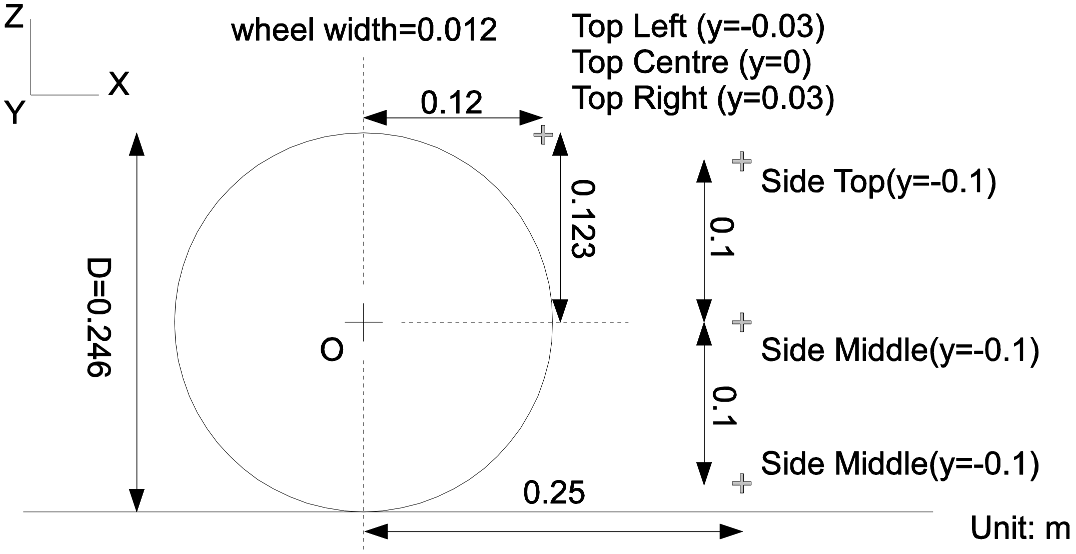

Although general agreement is observed in the gradient, less dispassion at high frequency appeared for all cases, which probably linked to higher Cd we ended up with in the comparison with the experimental data. It’s likely that the high oscillations on velocity at higher frequency are related to lower quality and resolution of the mesh. The lack of the consideration for backward cascading could be a factor to cause this high-frequency-biased distribution.

5.10 Maker points in the wake for LES

To give picture on unsteadiness in LES, X-velocity and SGS stress are extracted at selected X heights behind the wheel on the centre plane. Please refer to figure 48 for the locations.

Figure49 suggested that the amplitude at z=-0.06m where the probe situated in the middle of the wake structure got the peak ranged from -0.5m/s to 10m/s, which corresponds to the most fluctuated SGS profile shown in Figure 50.

Figure 48 the locations of the markers

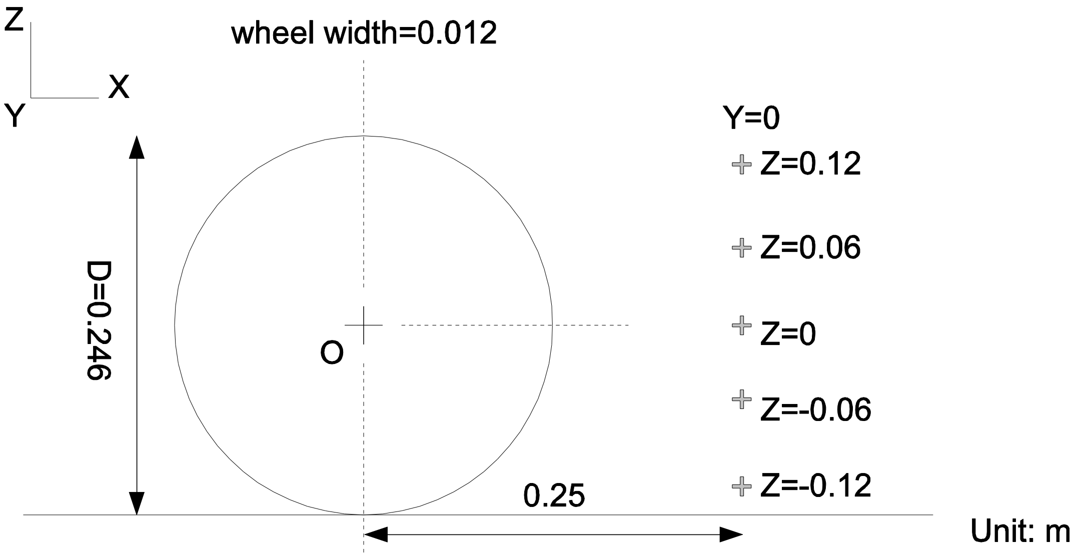

Figure 49 X velocity fluctuations

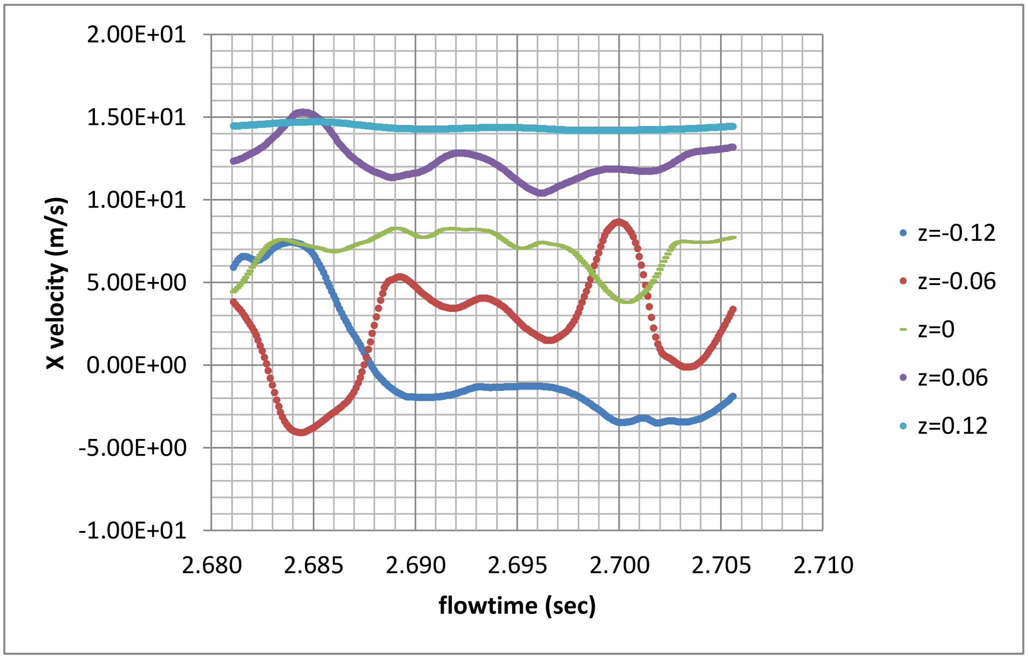

Figure 50 the fluctuations of SGS viscosity

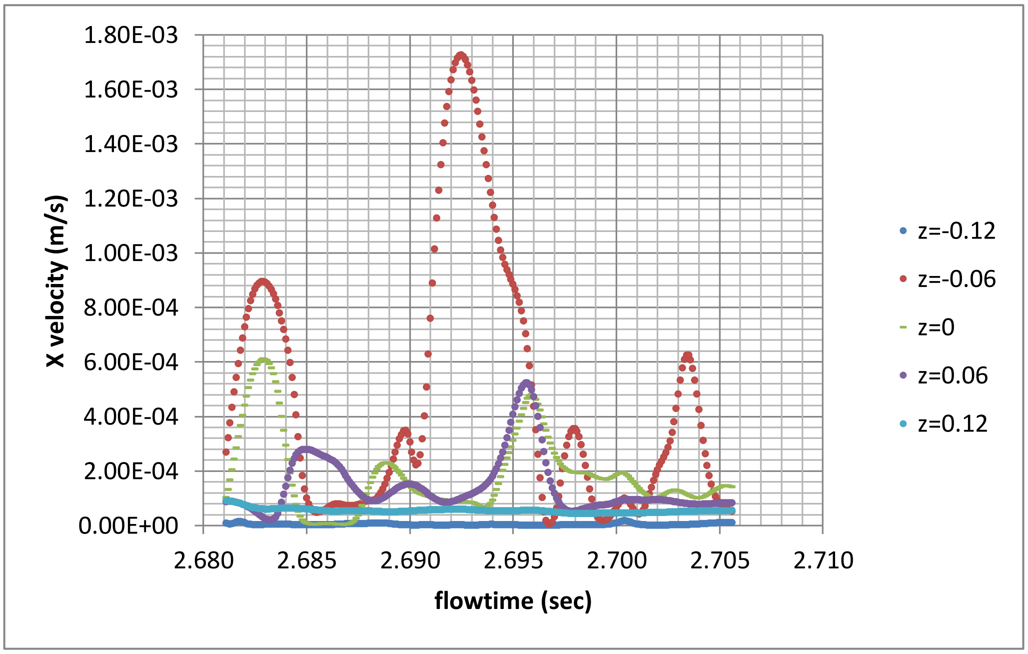

5.11 Boundary-layer transition

Figure 51 shows Y+ distribution on the surface for all turbulence models computed. Firstly, LES results suggest that Y+ value is distributed around 1 as aimed. Therefore, the grid resolution adapted is consider being adequate to meet the requirement of LES.

Secondly, Y+ distribution also gives an indication of the transition of the boundary layer because it’s essentially proportional to a square root of wall shear stress given a grid. Please remember that all computations share same grid arrangement in this thesis. In fact, trans k-kl-ω model shows very sharp increase of Y+ at the top of the wheel, suggesting laminar-to-turbulent transition occurred at that point. Other RANS models and LES didn’t show any shape increase.

Figure 52 also shows Y+ distribution but on front surface with TKE contour slice on centre plane. RKE and k-ω indicates moderate increase of Y+ earlier suggesting turbulent BL throughout as expected above. Notably, k-ω generates TKE more on front surface, which doesn’t seem to be explainable in physical term but contributes to keep wall shear stress low resulting in lower TKE level in the wake.

As observed above, trans k-kl-ω has very clear transition point at the top whilst trans-SST shows very low shear stress throughout indicating laminar boundary layer, which is quite dubious in physical term given the strong adverse pressure gradient appeared essentially in this type of flow.

Figure51 Y+ contour plot in rear isometric view

Figure51 (a) Realizable k-ε model

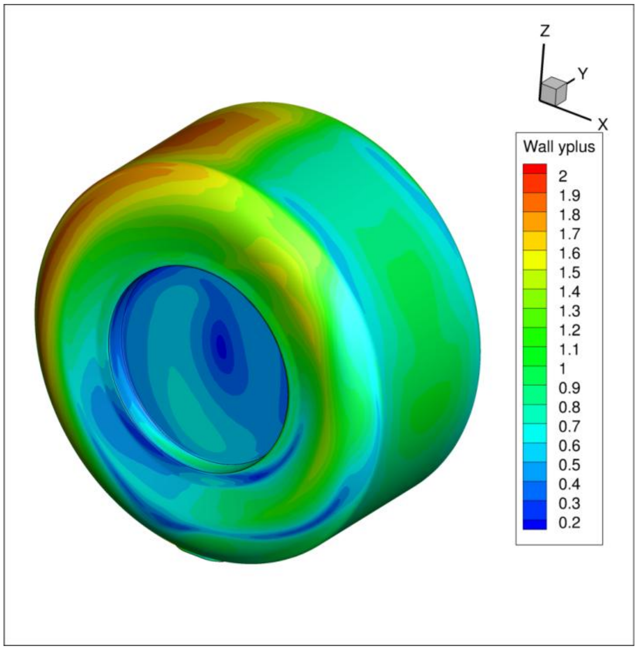

Figure51 (b) S-A model

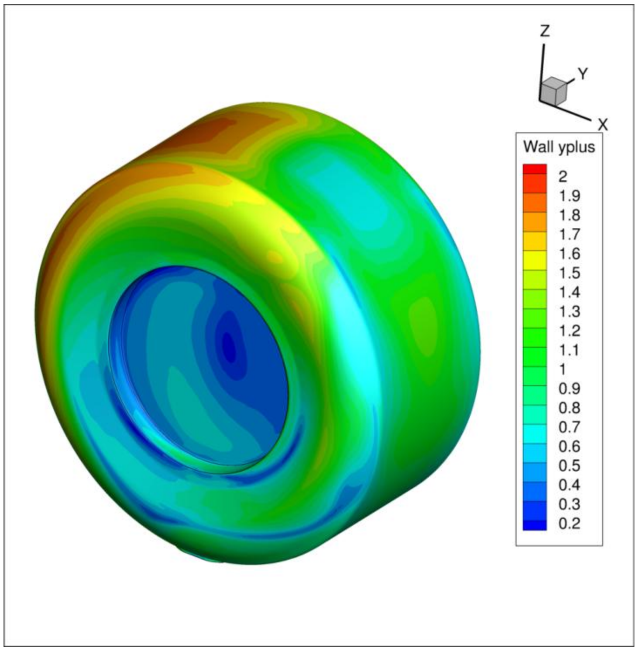

Figure51 (c) k-ω model

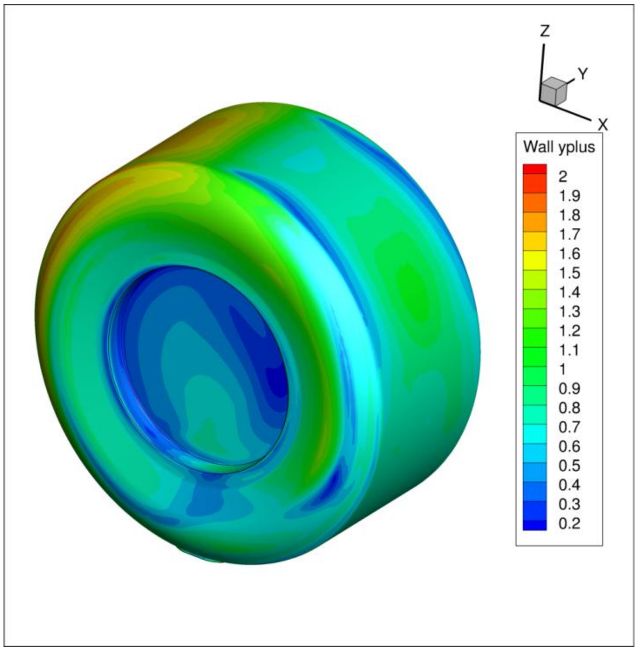

Figure51 (d) kω-SST model

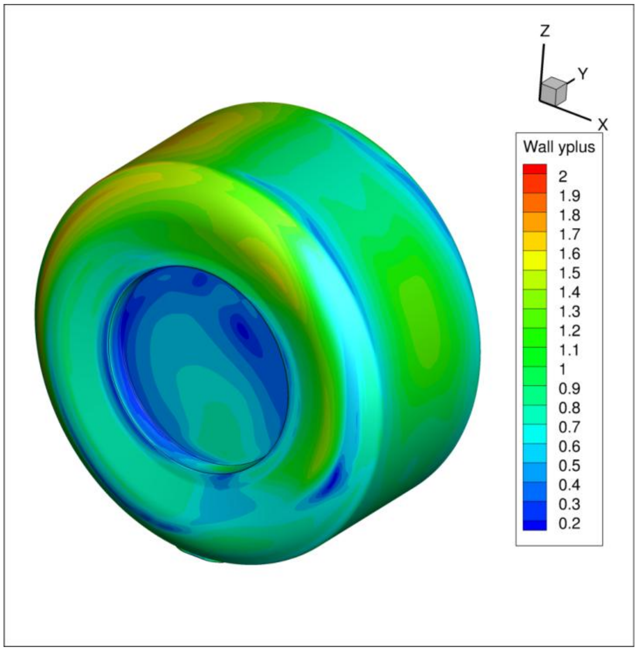

Figure51 (e) trans k-kl-ω

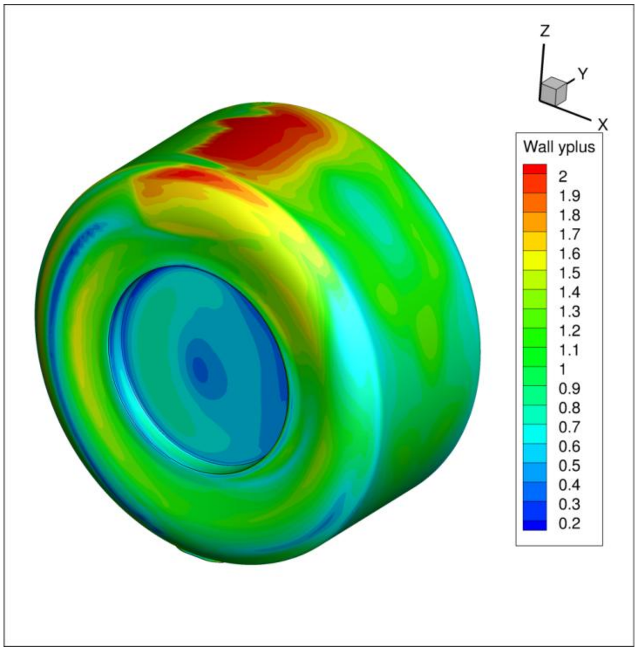

Figure51 (e) trans SST

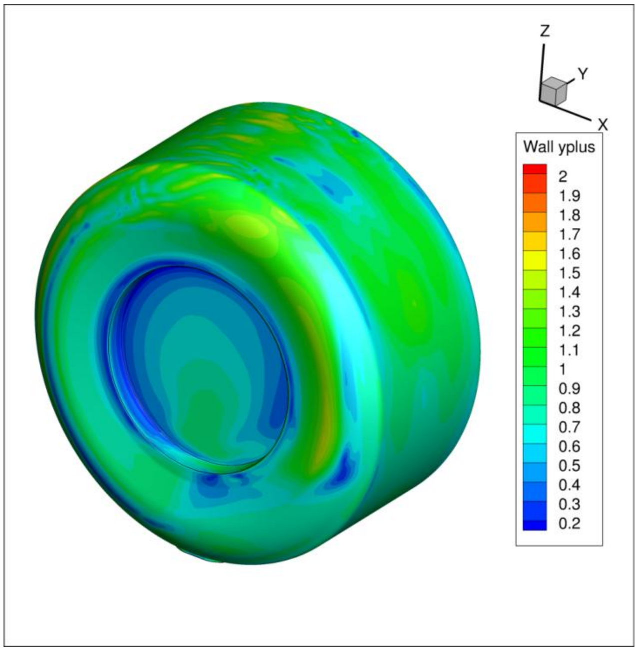

Figure51 (f) LES WALE (t=0)

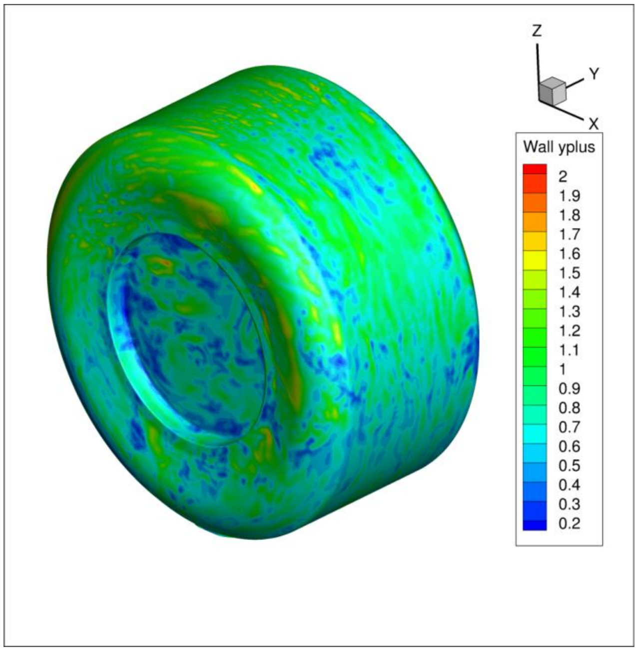

Figure51 (g) LES WALE (t=500)

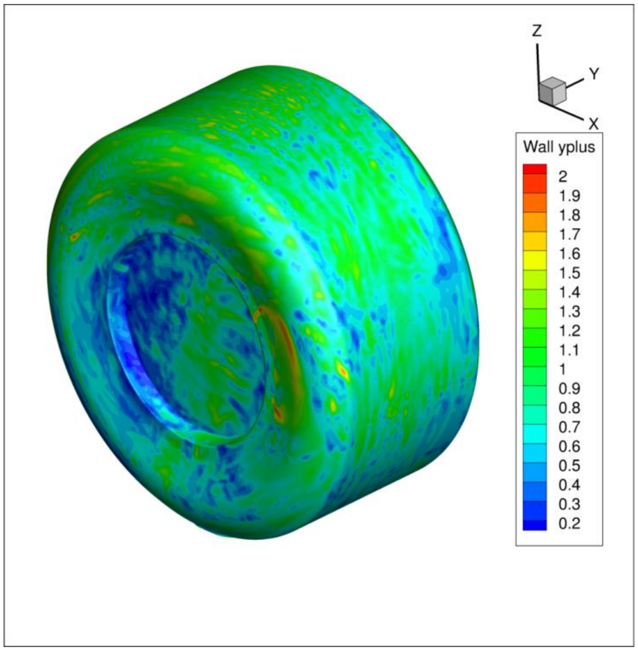

Figure 52 the contour plot of Y+ and TKE for RANS models in front isometric view

Figure52 (a) Realizable k-ε model

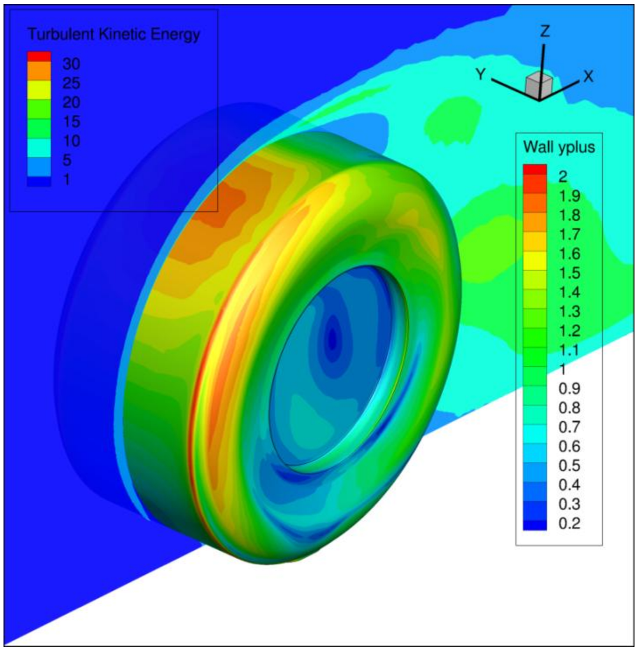

Figure52 (b) k-ω model

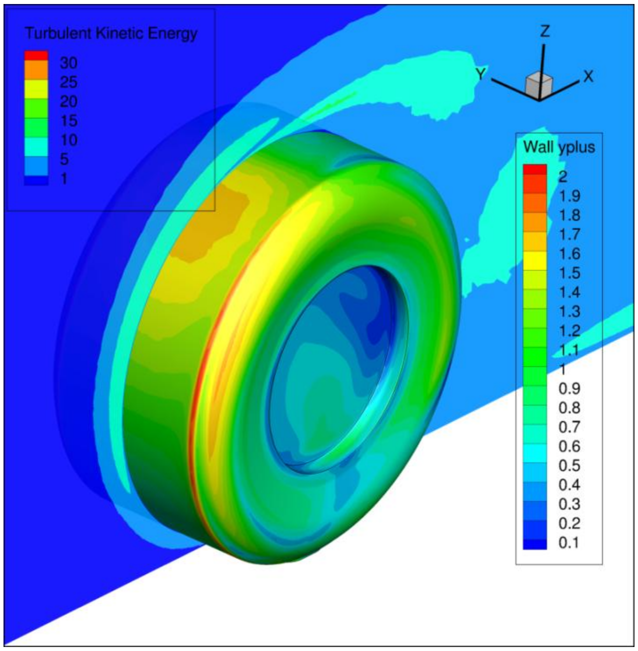

Figure52 (c) trans k-kl-ω model

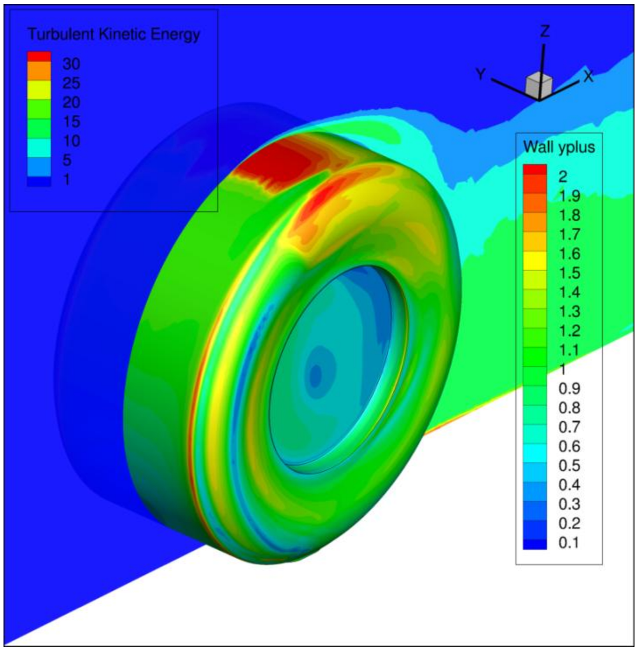

Figure52 (d) trans SST

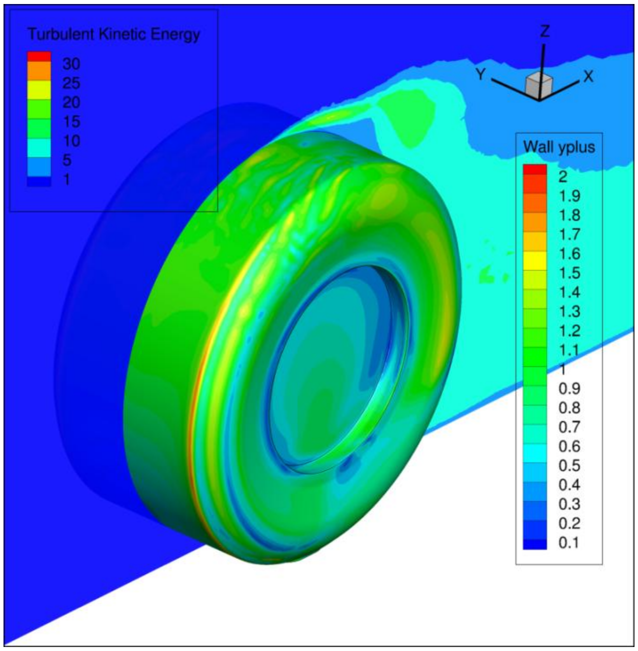

5.12 The drag coefficient

Table 10 shows Cd data for all turbulent models. As expected from all proceeding analysis, trans-k-kl-ω shows smallest value because of late separation and smaller wake structure. On the other hand, other transition model and LESs showed higher value, again, as expected from the separation point. Higher drag with S-A and RKE is explainable by the fact more late separation and higher wall-shear peak as seen above while less wall-shear peak and earlier separation for k-ω and k-ω SST happened to achieved a good agreement with the experimental data. We could conclude that the separation point and the wake height are correlated with the integrated drag value predominantly.

Table10 Cd comparison for turbulence models

Turbulence model	The drag coefficient	The error from the experimental result (%)
Experimental	0.63	N/A
Realizable k-ε	0.499	-20.8
S-A	0.570	-9.5
kω	0.626	-0.6
kω-SST	0.604	-4.1
trans-k-kl-ω	0.560	-11.1
trans-SST	0.651	3.33
LES (S-L)	0.699 (95% confident interval [0.636, 0.762])	11.0
LES (WALE)	0.719 (95% confident interval [0.664, 0.774])	14.1

6.0 Conclusions and Future Work

In this thesis we presented an investigation of RANS and LES models for the isolated rotating exposed wheel with moving ground with the aim of analysing the flow behavior and comparing the results in cost/quality context. To our knowledge this is the first application of LES for this case and the results provide a better insight into the physics of the flow and shed light on the overall envelope of the flow behavior obtained with different turbulence modeling approaches.

Overall the results indicate that adequate prediction of drag characteristics can be obtained with the reference experimental data providing a drag coefficient in the range of 0.56-0.63 and the overall computational envelope of RANS and LES models being 0.5-0.65 and 0.7-0.72 respectively. Remarkably, the standard k-w model yielded the best drag prediction among RANS models. The over-prediction of drag by LES models by ~10% correlates well with the observations made by Tsubokura et al. [6] for the simulation of the flow around a complete Formula 1 car model.

A closer examination of the flow features indicated that the drag results observed correlate quite well with the separation properties and the wake structure with LES simulation predicting, on average, earlier separation both over the top and the sides of the wheel and a more disturbed wake with a distinctive vortex shedding pattern and realisable k-e predicts overall a smaller separation, particularly over the sides of the wheel leading to a smaller drag coefficient.

The distribution of pressure near the contact patch was under-predicted by all models. However transitional models and LES led to a slightly higher peak pressure at the front of the contact patch. Furthermore, none of the models employed in this investigation could capture the fluctuations observed in the averaged Cp near the contact patch in the recirculation zone. The fact that these fluctuations are observed in the instantaneous LES data as well as asymmetry in the experimentally measured wake (e.g. [12]) may suggest that with further ensemble averaging these fluctuations may decrease in the experimental results as well.

LES simulations resulted in an almost steady flow over the front of the wheel with an unsteady separation point and unsteady wake. The spectral analysis of the LES results indicated that the inertial range is well resolved. However the unsteadiness is best captured near the wheel surface where the mesh resolution is good. The wake data by comparison only exhibits large-scale unsteadiness with a lack of observable high frequencies. One has to bear in mind that the grid convergence analysis indicated that although the near-wall region is fully resolved, better meshes might be required in order to improve the resolution of the wake region. The requirements in terms of computational hardware and licenses for the fine mesh of 6.8m cells employed in this study were close to the maximum capacity available for this thesis work, however further mesh refinement is worth exploring in future investigations focusing on a more narrow range of approaches.

Finally, it is remarkable that the LES simulations on a wall-resolved grid with a time step corresponding to ~26 multiples of the Kolmogorov time scale are much faster than what one would expect taking only ~2.7 times longer than the conventional k-w SST model for example with the same hardware resource. Although the time scale used for this particular simulation is not optimal, even with the time step of the order of Kolmogorov time scale, LES simulations are only ~10 times slower than current state-of-the-art RANS models. Bearing in mind that the hardware resource used in this thesis (16 cores) is relatively modest by comparison with the computational capabilities Formula 1 teams have access to, this indicates that the industrial applications of LES within the design cycle are becoming a reality.

There is a number of directions which can be suggested for future work. Firstly, one has to note that the flow regime investigated here corresponds to velocity which is lower than the typical average velocity on a lap encountered in Formula 1 competitions. The absence of experimental data for the more realistic velocities can be compensated by the CFD analysis based on validation for a lower velocity as presented in this thesis. The investigation then can be further extended to explore higher velocity regimes. Secondly, the scope of the present study can be further extended with respect to increased mesh resolution and the investigation of the effect of turbulent flow inlet conditions which may affect the results of transitional

RANS and LES models. Finally, enhancing the analysis through an experimental study confirming the averaged and unsteady wake behavior can benefit our understanding of the performance and fidelity of turbulence modeling approaches for this case.

7.0 References

[1] A. P. Mears, “The Aerodynamic Characteristics of an Exposed Racing Car Wheel”, PhD Thesis, University of Durham, 2004

[2] J. B. Barlow, W. H. Rae and Jr. A. Pope, “Low-speed wind tunnel testing”, 3rd ed., Chapter 14, John Wiley and Sons Inc., 1999

[3] FIA Formula one technical regulations, Chapter 12, 2007

[4] B. Agathangelou, and M. Gascoyne, “Aerodynamic Design Considerations of a Formula 1 Racing Car”, SAE 980399, 1998

[5] W. Mayer and J. Wiedemann, “The Influence of Rotating on Total Load”, SAE 2007-01-1047, 2007

[6] M. Tsubokura et al, “Large Eddy Simulation of Unsteady Flow Around a Formula Car on Earth Simulator”, SAE 2007-01-0106, 2007

[7] Silverstone Circuit Course layout, Alliantz circuit information http://sponsoring.allianz.com/en/formula1/illustrations/

[8] S. McBeath, “COMPETITION CAR DOWNFORCE”, ISBN 0 854429 977 7, 1998

[9] J.E. Fackrell and J.K. Harvey, “The Aerodynamics of an Isolated Wheel Rotating in Contact with the Ground”, PhD thesis, University of London, 1974

[10] A. Cogotti, “Aerodynamic Characteristics of Car Wheels”, International Journal of Vehicle Design, Special Publication SP3, 1983

[11] L. Axon, “The aerodynamic characteristics of automobile wheels-CFD prediction and wind tunnel experiment”, PhD Thesis, Cranfield University, 1999

[12] A.P. Mears, R.G.Dominy and D.B. Sims-Williams, “The Air Flow About an Exposed Racing Wheel”, SAE2002-01-3290, 2002

[13] A. P. Mears and R. G. Dominy, “Racing Car Wheel Aerodynamics – Comparisons between Experimental and CFD derived Flow-Field Data”, SAE2004-01-3555, 2004

[14] Fluent Incorporated, 2001, “FLUENT 6.0 *users guide*” Fluent Incorporated, Lebanon, New Hampshire, U.S.A.

[15] S. B. Pope, “Turbulent Flows”, Chapter 10.2, CUP, 2000

[16] B. E. Launder and B. I. Sharma, “Application of the energy-dissipation model of turbulence to the calculation of flow near a spinning disc”, Lett. Heat Mass Transf., 1, pp. 131-137, 1974

[17] T. J. Chung, “Computational Fluid Dynamics”, Chapter 21, CUP, 2010

[18] J. Smagorinsky, “General circulation experiments with the primitive equations”, I. The basis equations. Mon. Weather Rev., 91(3), p.99, 1963

[19] A. J. Scibor-Rylski, “Road Vehicle Aerodynamics”, 2nd ed., 1984

[20] P. R. Spalart, “Strategies for turbulence modeling and simulations”, Int. J. Heat and Fluid Flow, **21**, pp. 252-263, 2000

[21] K. B. Shah, “Large eddy simulation of the flow past a cubic obstacle”, PhD.

Thesis, Stanford University, 1998

[22] R. Martinuzzi, and C. Tropea, “The flow around surface mounted prismatic obstacles placed in a fully developed channel flow”, ASME Journal of Fluids Engineering, 115, pp. 85-93, 1993

[23] W. Rodi, “Comparison of LES and RANS calculations of the flow around bluff bodies”, Journal of Wind Engineering and Industrial Aerodynamics, 69-71, 1997

[24] W. P. Kellar, S. R. G. Pearse and A. M. Savill, “Formula 1 car wheel aerodynamics”, Sports Engineering **2**, pp. 203-212, 1999

[25] M. Breuer, N. Jovicic and K. Mazaev, “Comparison of DES, RANS and LES for the separated flow around a flat plate at high incidence”, Int. J. Num. Meth. Fluids 41, pp. 357-388, 2003

[26] L. Axon, K. Garry and J. Howell, “An Evaluation of CFD for Modeling the Flow Around Stationary and Rotating Isolated Wheels”, SAE 980032, 65- 75, 1998

[27] J. McManus and X. Zhang, “A Computational Study of the Flow Around an Isolated Wheel in Contact With the Ground”, J. Fluids Eng. 128(3), p. 520, 2006

[28] A. J. Saddington, R. D. Knowles and K. Knowles, “Laser Doppler anemometry measurement in the near-wake of an isolated Formula One wheel”, Exp. Fluids 42(5), pp. 671-681, 2007

[29] S. B. Pope, “Turbulent Flows”, Chapter 9, CUP, 2000

[30] S. B. Pope, “Turbulent Flows”, Chapter 11, CUP, 2000

[31] T. J. Chung, “Computational Fluid Dynamics”, Chapter 21, CUP, 2010

[32] M. Meldi, “Simulations of the flow around a circular cylinder by a continuous universal hybrid model”, PhD Thesis, University of Pisa, 2007

[33] ANSYS FLUENT 12.0 Theory Guide, April 2009

[34] D. Drikakis, B.J. Geurts (ed) "Turbulent Flow Computations", Kluwer Academic Publishers, 2004

[35] P. G. Drazin and W.H. Reid, “Hydrodynamic stability “, CUP, 2004

[36] L. Axon and K. Garry, “The Influence of Ground Condition on the Flow Around a Wheel Located Within a Wheelhouse Cavity”, SAE 1999-01-0806, 1999

[37] A. F. Skea and P. R. Bullen, “CFD Simulations and Experimental Measurements of the Flow Over a Rotating Wheel in a Wheel Arch”, SAE 2000-01-0487, 2000

[38] A. F. Skea, P. R. Bullen and J. Qiao, “The Use of CFD to Predict the Air Flow Around a Rotating Wheel,” Proceedings of the 2nd MIRA International Conference On Vehicle Aerodynamics, Coventry, UK, pp. 267–274, 1998

[39] A. Morelli, “A New Aerodynamic Approach to Advanced Automobile Basic Shapes”, SAE 2000-01-0491, 2000

[40] C. Landström, L. Löfdahl and T. Walker, “Detailed Flow Studies in Close Proximity of Rotating Wheels on a Passenger Car”, SAE 2009-01-0778, 2009

[41] B. Duncan, S. Kandasamy and K. Sbeih, “ Further CFD Studies for Detailed Tires using Aerodynamics Simulation with Rolling Road Conditions”, SAE 2010-01-0756, 2010

[42] A. Gaylard, D Lynch, J. Amodeo and R. Amunugama, The Simulation of Brake Dust Deposition”, 8th MIRA International Conference on Vehicle Aerodynamics, pp. 271-287, 2010

[43] N. Axelsson, M. Ramnefors and R. Gustafson, "Accuracy in Computational Aerodynamics, Part 1: Stagnation Pressure", SAE 980037, 1998

Appendix A Solver Configuration

A1 Case 1: Realizable k-ε model

```
FLUENT

Version: 3d, dp, pbns, ke-realizable (3d, double precision, pressure-based,
ke-realizable)

Release: 12.1.4

   Numerics


      Numeric                             Enabled

      --------------------------------------

      Absolute Velocity Formulation    yes


   Relaxation

      Variable                            Relaxation Factor

      ----------------------------------------------

      Pressure                             0.3

      Density                              1

      Body Forces                          1

      Momentum                               0.7

      Modified Turbulent Viscosity     0.8
```

```
      Turbulent Viscosity                  1


   Linear Solver

                                         Solver        Termination     Residual
Reduction
      Variable                          Type          Criterion       Tolerance
      ----------------------------------------------------------------------
      Pressure                           V-Cycle       0.1
      X-Momentum                           Flexible     0.1              0.7
      Y-Momentum                           Flexible     0.1              0.7
      Z-Momentum                           Flexible     0.1              0.7
      Modified Turbulent Viscosity     Flexible     0.1              0.7


   Pressure-Velocity Coupling

      Parameter                   Value
      ----------------------------
      Type                        SIMPLEC
      Skewness Correction      0


   Discretization Scheme
```

```
Variable                              Scheme
-----------------------------------------------
Pressure                              Second Order
Momentum                                 Second Order Upwind
Modified Turbulent Viscosity    Second Order Upwind
```

Solution Limits

```
Quantity                              Limit
-------------------------------------
Minimum Absolute Pressure          1
Maximum Absolute Pressure          5e+10
Minimum Temperature                  1
Maximum Temperature                  5000
Maximum Turb. Viscosity Ratio    100000
```

A2 Case2: Spalart-Allmaras model

FLUENT

Version: 3d, dp, pbns, S-A (3d, double precision, pressure-based, Spalart-Allmaras)

```
Release: 12.1.4

    Numerics


        Numeric                                   Enabled

        --------------------------------------

        Absolute Velocity Formulation      yes


    Relaxation

        Variable                                  Relaxation Factor

        -----------------------------------------------

        Pressure                                  0.3

        Density                                   1

        Body Forces                               1

        Momentum                                     0.7

        Modified Turbulent Viscosity     0.8

        Turbulent Viscosity                 1


    Linear Solver

                                                  Solver        Termination     Residual

Reduction
```

```
   Variable                              Type          Criterion       Tolerance
   ----------------------------------------------------------------------
   Pressure                               V-Cycle      0.1
   X-Momentum                               Flexible     0.1                 0.7
   Y-Momentum                               Flexible     0.1                 0.7
   Z-Momentum                               Flexible     0.1                 0.7
   Modified Turbulent Viscosity     Flexible     0.1                 0.7

Pressure-Velocity Coupling
   Parameter                  Value
   -----------------------------
   Type                       SIMPLEC
   Skewness Correction     0

Discretization Scheme
   Variable                              Scheme
   -------------------------------------------------
   Pressure                               Second Order
   Momentum                                 Second Order Upwind
   Modified Turbulent Viscosity     Second Order Upwind
```

```
    Solution Limits

       Quantity                           Limit
       -------------------------------------
       Minimum Absolute Pressure           1
       Maximum Absolute Pressure           5e+10
       Minimum Temperature                 1
       Maximum Temperature                 5000
       Maximum Turb. Viscosity Ratio     100000
```

A3 Case3: k-ω model

FLUENT

Version: 3d, dp, pbns, skw (3d, double precision, pressure-based, standard k-omega)

Release: 12.1.4

Title:

Numerics

```
    Numeric                                   Enabled

    -------------------------------------

    Absolute Velocity Formulation     yes


  Relaxation

    Variable                             Relaxation Factor

    -------------------------------------------

    Pressure                              0.3

    Density                               1

    Body Forces                           1

    Momentum                                0.7

    Turbulent Kinetic Energy      0.8

    Specific Dissipation Rate     0.8

    Turbulent Viscosity              1


  Linear Solver

                                          Solver       Termination     Residual

Reduction

    Variable                             Type          Criterion       Tolerance

    --------------------------------------------------------------------
```

```
   Pressure                        V-Cycle     0.1
   X-Momentum                        Flexible    0.1              0.7
   Y-Momentum                        Flexible    0.1              0.7
   Z-Momentum                        Flexible    0.1              0.7
   Turbulent Kinetic Energy     Flexible    0.1              0.7
   Specific Dissipation Rate    Flexible    0.1              0.7

Pressure-Velocity Coupling
   Parameter                  Value
   -----------------------------
   Type                       SIMPLEC
   Skewness Correction    0

Discretization Scheme
   Variable                        Scheme
   -----------------------------------------------
   Pressure                        Second Order
   Momentum                          Second Order Upwind
   Turbulent Kinetic Energy     Second Order Upwind
   Specific Dissipation Rate    First Order Upwind
```

Solution Limits

Quantity	Limit
Minimum Absolute Pressure	1
Maximum Absolute Pressure	5e+10
Minimum Temperature	1
Maximum Temperature	5000
Minimum Turb. Kinetic Energy	1e-14
Minimum Spec. Dissipation Rate	1e-20
Maximum Turb. Viscosity Ratio	100000

A4 Case4: k-ω-sst model

FLUENT

Version: 3d, dp, pbns, sstkw (3d, double precision, pressure-based, SST k-omega)

Release: 12.1.4

Numerics

Numeric Enabled

```
    Absolute Velocity Formulation     yes


Relaxation

    Variable                          Relaxation Factor

    -------------------------------------------

    Pressure                           0.3

    Density                           1

    Body Forces                        1

    Momentum                              0.7

    Turbulent Kinetic Energy      0.8

    Specific Dissipation Rate    0.8

    Turbulent Viscosity              1


Linear Solver

                                       Solver       Termination     Residual

Reduction

    Variable                          Type          Criterion       Tolerance

    --------------------------------------------------------------------

    Pressure                           V-Cycle      0.1

    X-Momentum                            Flexible    0.1                0.7
```

```
   Y-Momentum                     Flexible   0.1           0.7
   Z-Momentum                     Flexible   0.1           0.7
   Turbulent Kinetic Energy       Flexible   0.1           0.7
   Specific Dissipation Rate      Flexible   0.1           0.7

Pressure-Velocity Coupling
   Parameter              Value
   ----------------------------
   Type                   SIMPLEC
   Skewness Correction    0

Discretization Scheme
   Variable                     Scheme
   ---------------------------------------------
   Pressure                     Second Order
   Momentum                     Second Order Upwind
   Turbulent Kinetic Energy     Second Order Upwind
   Specific Dissipation Rate    First Order Upwind

Solution Limits
```

```
      Quantity                           Limit
      ---------------------------------------
      Minimum Absolute Pressure            1
      Maximum Absolute Pressure            5e+10
      Minimum Temperature                   1
      Maximum Temperature                   5000
      Minimum Turb. Kinetic Energy       1e-14
      Minimum Spec. Dissipation Rate     1e-20
      Maximum Turb. Viscosity Ratio      100000
```

A5 Case5: transition k-kl-ω model

```
FLUENT
Version: 3d, dp, pbns, k-kl-w (3d, double precision, pressure-based, k-kl-omega
model)
Release: 12.1.4
   Numerics
      Numeric                            Enabled
      ---------------------------------------
      Absolute Velocity Formulation   yes
```

```
   Relaxation

      Variable                          Relaxation Factor
      ---------------------------------------------
      Pressure                           0.3
      Density                            1
      Body Forces                        1
      Momentum                             0.7
      Turbulent Kinetic Energy      0.8
      Laminar Kinetic Energy         0.8
      Specific Dissipation Rate    0.8
      Turbulent Viscosity             1

   Linear Solver
                                         Solver        Termination     Residual
Reduction
      Variable                          Type           Criterion        Tolerance
      -----------------------------------------------------------------------
      Pressure                           V-Cycle       0.1
      X-Momentum                           Flexible     0.1                 0.7
```

```
Y-Momentum                     Flexible   0.1          0.7

Z-Momentum                     Flexible   0.1          0.7

Turbulent Kinetic Energy    Flexible   0.1          0.7

Laminar Kinetic Energy      Flexible   0.1          0.7

Specific Dissipation Rate   Flexible   0.1          0.7


Pressure-Velocity Coupling

Parameter              Value

-----------------------------

Type                   SIMPLEC

Skewness Correction    0


Discretization Scheme

Variable                      Scheme

---------------------------------------------

Pressure                      Second Order

Momentum                        Second Order Upwind

Turbulent Kinetic Energy    Second Order Upwind

Laminar Kinetic Energy      First Order Upwind

Specific Dissipation Rate   First Order Upwind
```

Solution Limits

Quantity	Limit
Minimum Absolute Pressure	1
Maximum Absolute Pressure	5e+10
Minimum Temperature	1
Maximum Temperature	5000
Minimum Turb. Kinetic Energy	1e-14
Minimum Spec. Dissipation Rate	1e-20
Maximum Turb. Viscosity Ratio	100000

A6 Case6: transition-SST model

FLUENT

Version: 3d, dp, pbns, trans-sst (3d, double precision, pressure-based, trans-sst model)

Release: 12.1.4

Numerics

Numeric Enabled

```
   ---------------------------------------

   Absolute Velocity Formulation     yes


Relaxation


   Variable                              Relaxation Factor

   ---------------------------------------------

   Pressure                               0.3

   Density                               1

   Body Forces                            1

   Momentum                                  0.7

   Turbulent Kinetic Energy      0.8

   Specific Dissipation Rate    0.8

   Intermittency                        0.8

   Momentum Thickness Re             0.8

   Turbulent Viscosity              1


Linear Solver

                                          Solver        Termination     Residual

Reduction
```

```
   Variable                          Type          Criterion       Tolerance
   ------------------------------------------------------------------
   Pressure                           V-Cycle       0.1
   X-Momentum                           Flexible     0.1                  0.7
   Y-Momentum                           Flexible     0.1                  0.7
   Z-Momentum                           Flexible     0.1                  0.7
   Turbulent Kinetic Energy       Flexible     0.1                  0.7
   Specific Dissipation Rate     Flexible     0.1                  0.7
   Intermittency                     Flexible     0.1                  0.7
   Momentum Thickness Re           Flexible     0.1                  0.7

Pressure-Velocity Coupling
   Parameter                   Value
   -----------------------------
   Type                        SIMPLEC
   Skewness Correction     0

Discretization Scheme
   Variable                          Scheme
   ---------------------------------------------
```

```
   Pressure                          Second Order

   Momentum                            Second Order Upwind

   Turbulent Kinetic Energy      Second Order Upwind

   Specific Dissipation Rate     First Order Upwind

   Intermittency                      First Order Upwind

   Momentum Thickness Re           First Order Upwind


Solution Limits

   Quantity                                Limit

   ---------------------------------------

   Minimum Absolute Pressure            1

   Maximum Absolute Pressure             5e+10

   Minimum Temperature                     1

   Maximum Temperature                      5000

   Minimum Turb. Kinetic Energy        1e-14

   Minimum Spec. Dissipation Rate     1e-20

   Maximum Turb. Viscosity Ratio      100000
```

A7 Case7: Large eddy simulation

```
FLUENT
Version: 3d, dp, pbns, LES, transient (3d, double precision, pressure-based, large eddy simulation, transient)
Release: 12.1.4
    Numerics

        Numeric                                 Enabled
        ---------------------------------------
        Absolute Velocity Formulation    yes


    Unsteady Calculation Parameters
        --------------------------------------
        Time Step (s)                           0.0001
        Max. Iterations Per Time Step    100


    Relaxation
        Variable        Relaxation Factor
        -------------------------------
        Pressure         0.3
        Density          1
```

```
   Body Forces    1
   Momentum        0.7

Linear Solver
                     Solver       Termination    Residual Reduction
   Variable        Type           Criterion        Tolerance
   --------------------------------------------------------
   Pressure        V-Cycle      0.1
   X-Momentum    Flexible    0.1                  0.7
   Y-Momentum    Flexible    0.1                  0.7
   Z-Momentum    Flexible    0.1                  0.7

Pressure-Velocity Coupling
   Parameter                    Value
   -----------------------------
   Type                            SIMPLEC
   Skewness Correction     0

Discretization Scheme          Variable     Scheme
   ---------------------------------------
```

```
   Pressure    Second Order
   Momentum    Bounded Central Differencing

Solution Limits

   Quantity                         Limit
   ---------------------------------------
   Minimum Absolute Pressure          1
   Maximum Absolute Pressure          5e+10
   Minimum Temperature                1
   Maximum Temperature                5000
   Maximum Turb. Viscosity Ratio    100000
```

Appendix B Supplemental Post-processing Results

B1 Velocity components on y=-0.03 plane

[k-e realizable]

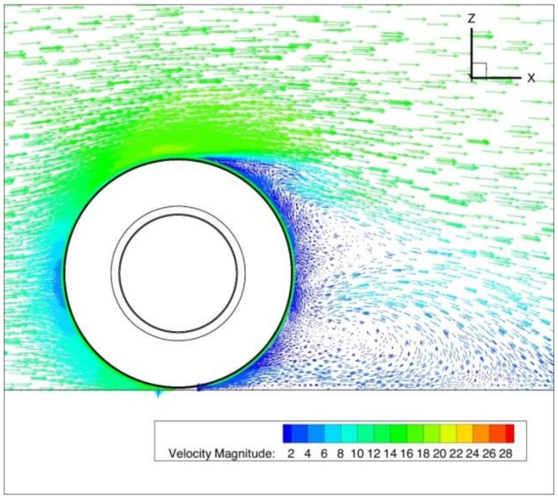

[kw]

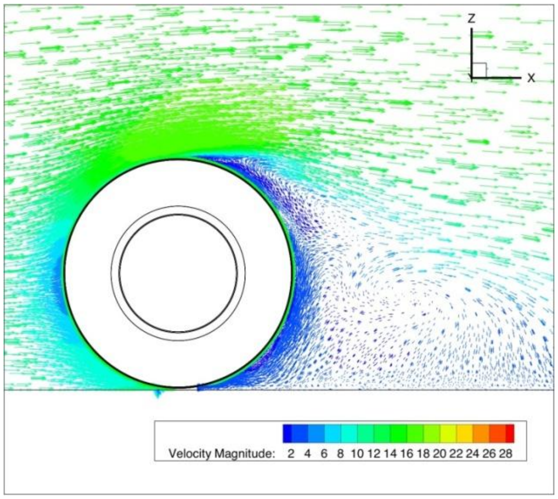

[Spalart-Allmaras]

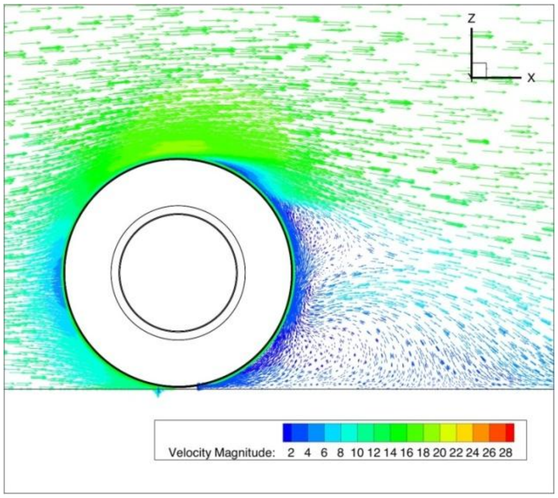

[kw-sst]

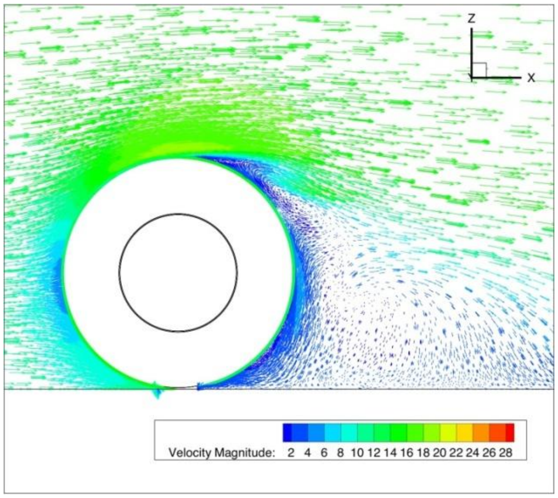

[trans-k-kl-w]

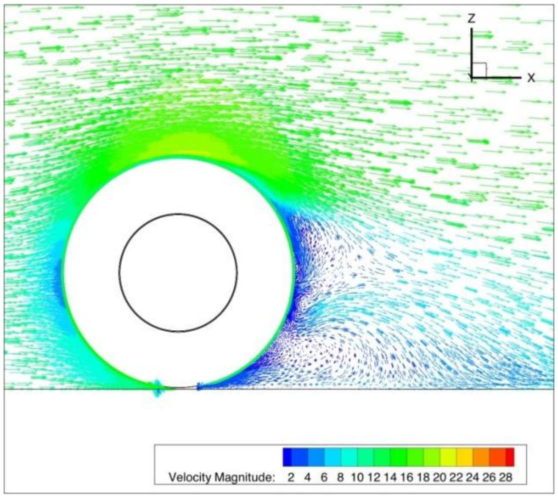

[LES]

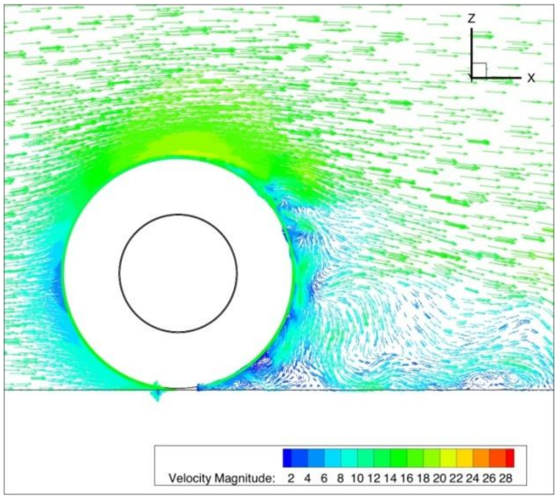

[trans-sst]

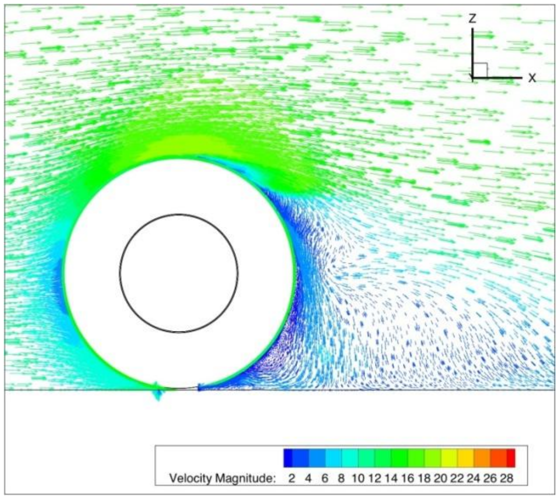

B2 Velocity components on y=+0.03 plane

[k-e realizable]

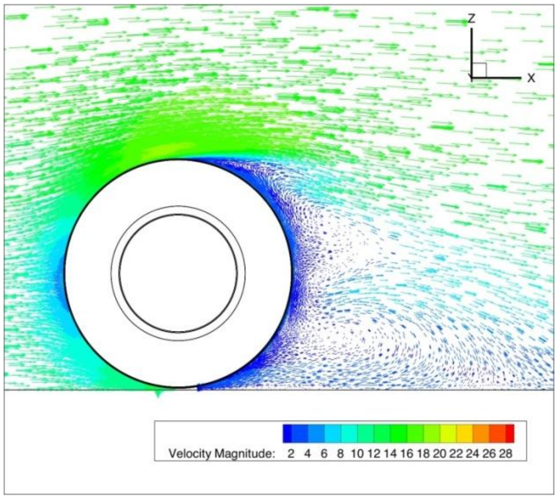

[kw]

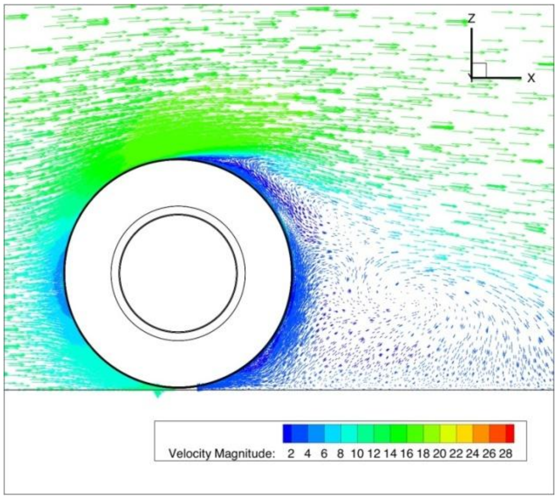

[Spalart-Allmaras]

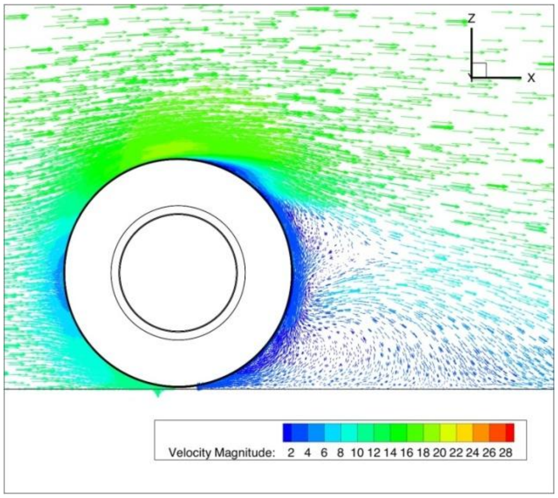

[kw-sst]

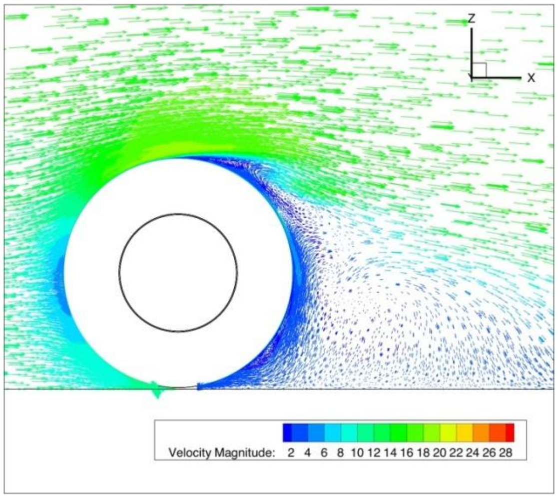

[trans-k-kl-w]

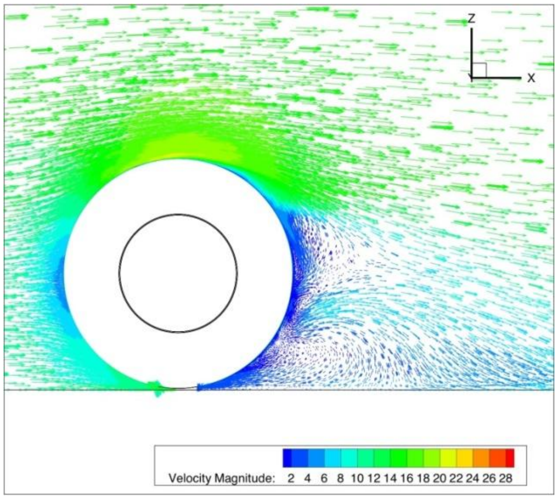

[trans-sst]

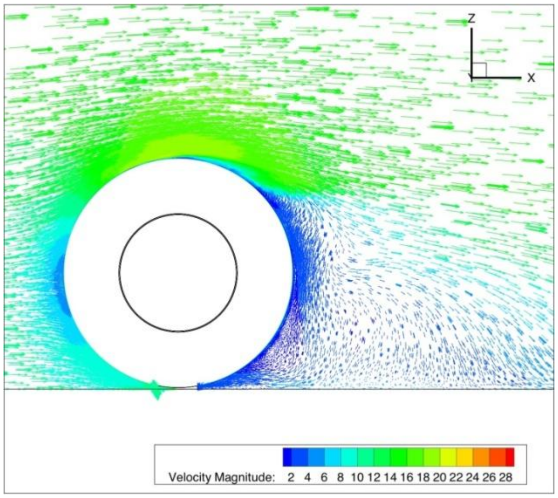

[LES]

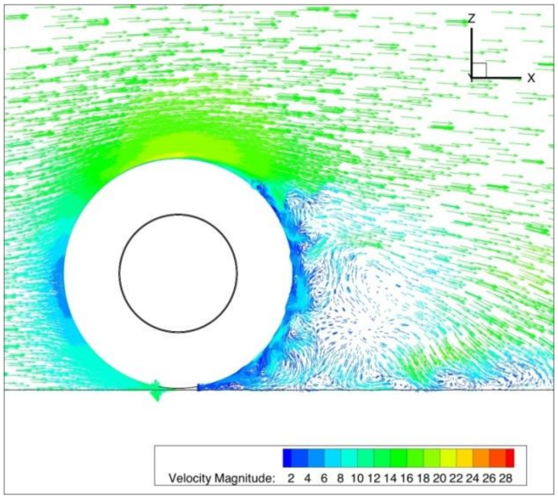

B3 Velocity components on y=-0.07 plane

[k-e realizable]

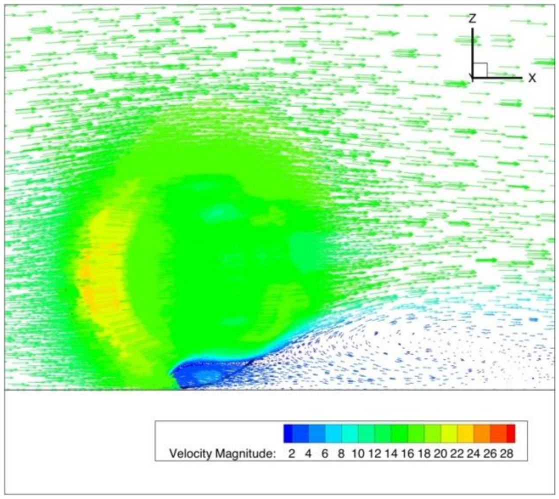

[kw]

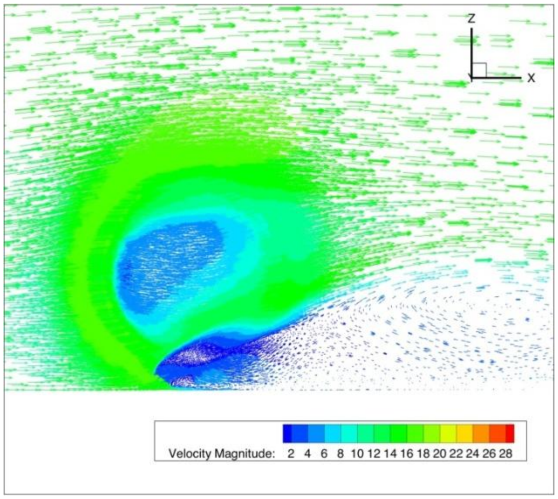

[Spalart-Allmaras]

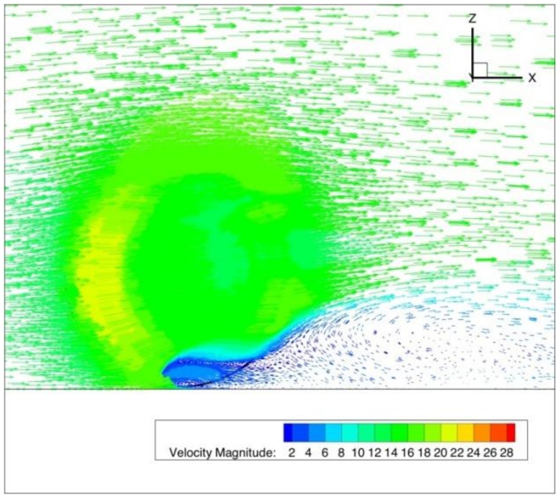

[kw-sst]

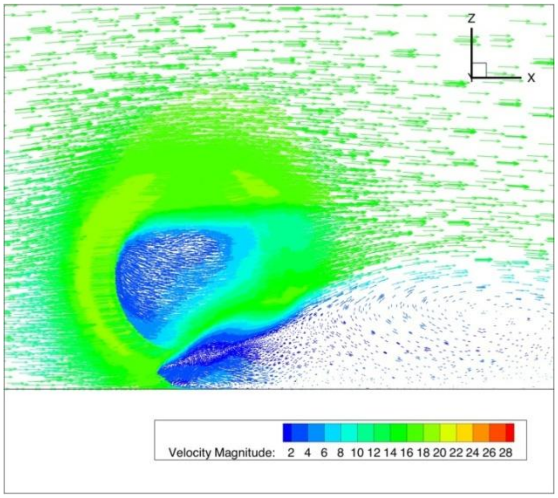

[trans-k-kl-w]

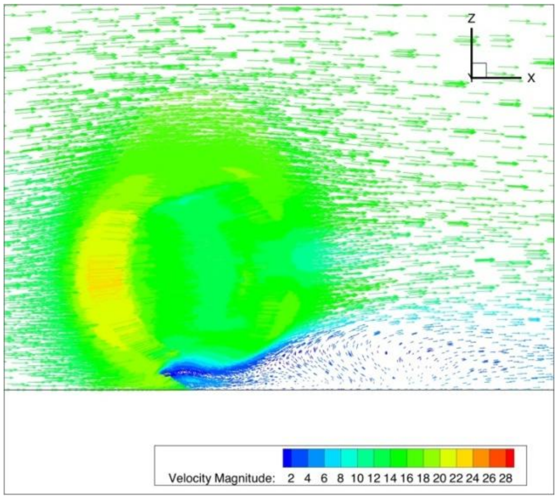

[trans-sst]

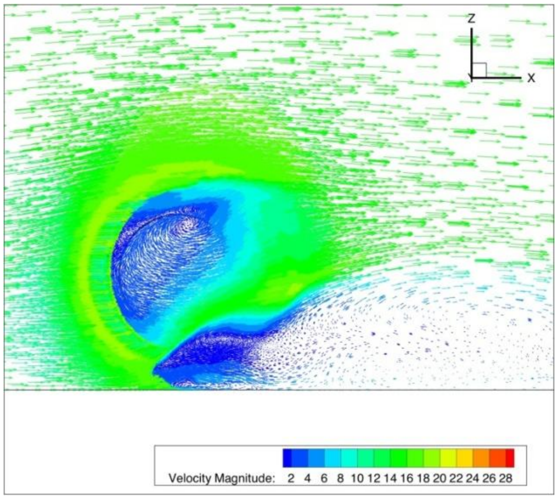

[LES]

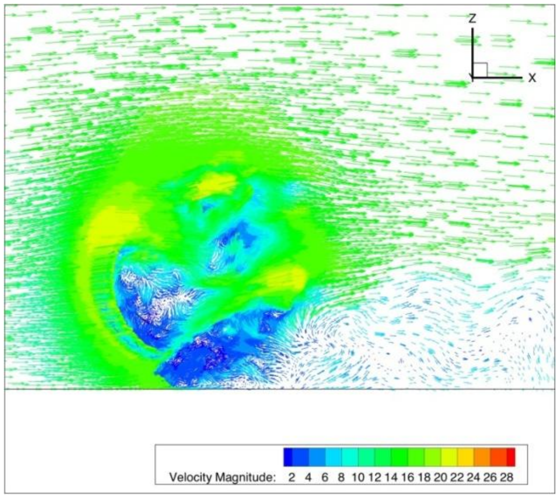

B4 Velocity components on y=+0.07 plane

[k-e realizable]

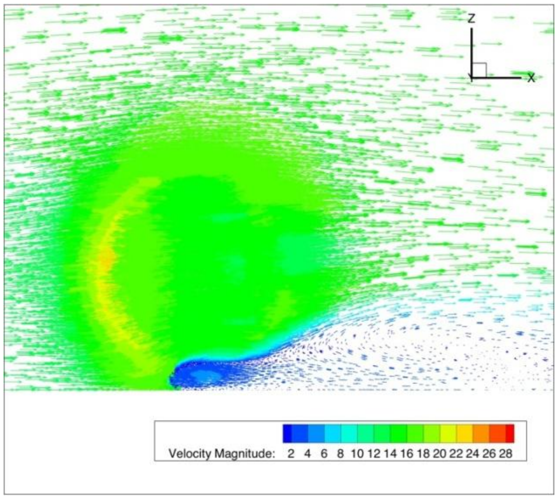

[kw]

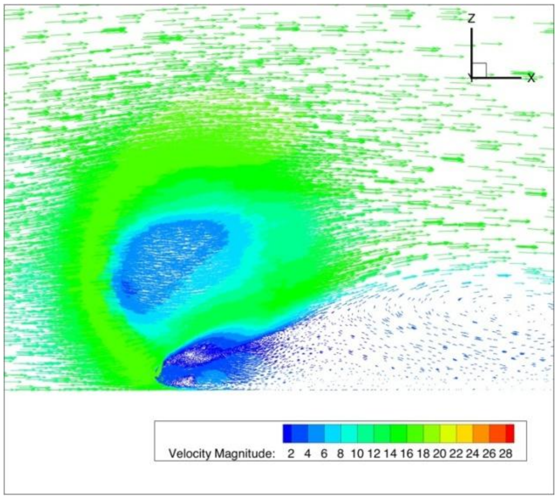

[Spalart-Allmaras]

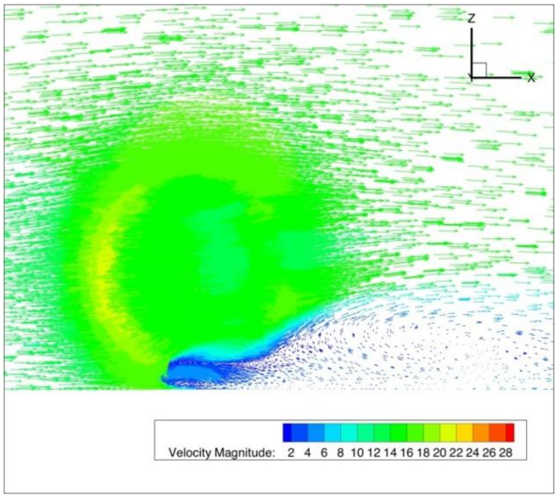

[kw-sst]

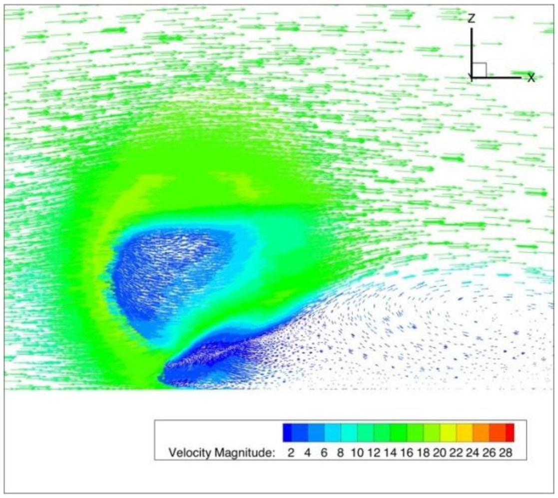

[trans-k-kl-w]

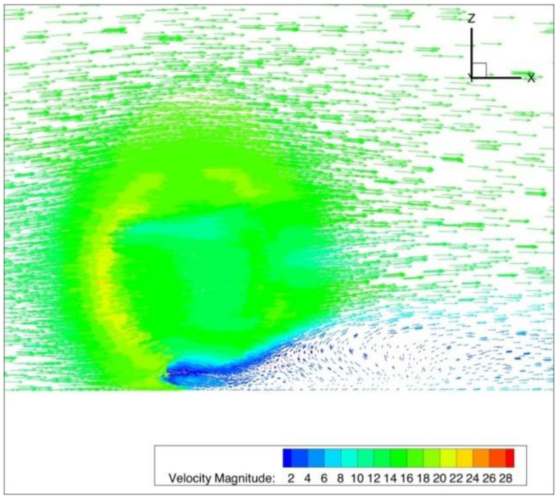

[trans-sst]

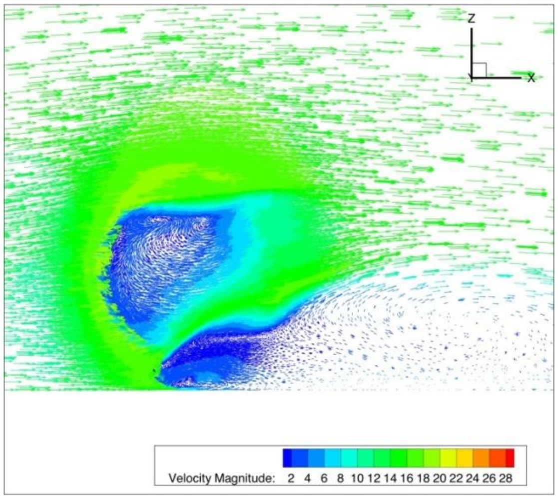

[LES]

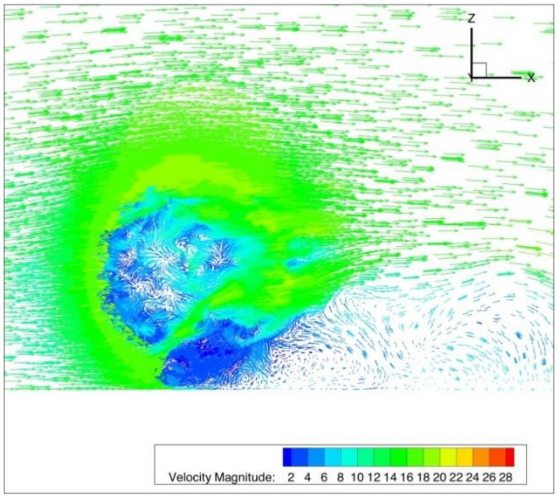

B5 Velocity components in the hub on z=0 plane

[k-e realizable]

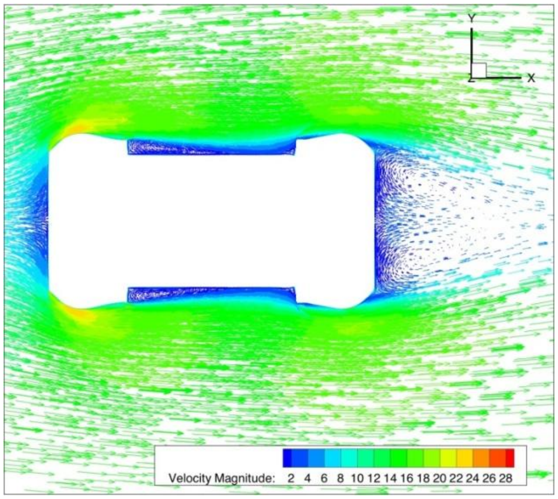

[kw]

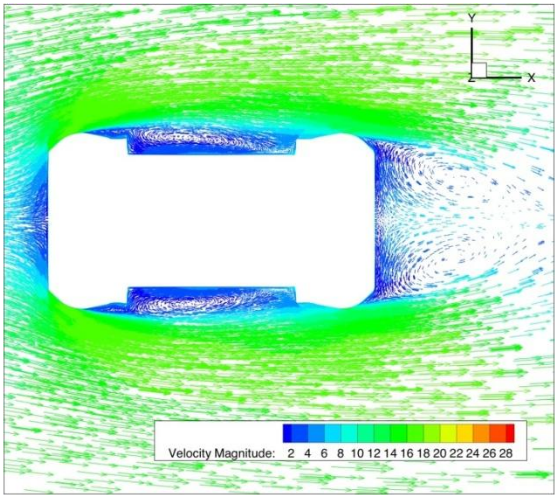

[Spalart-Allmaras]

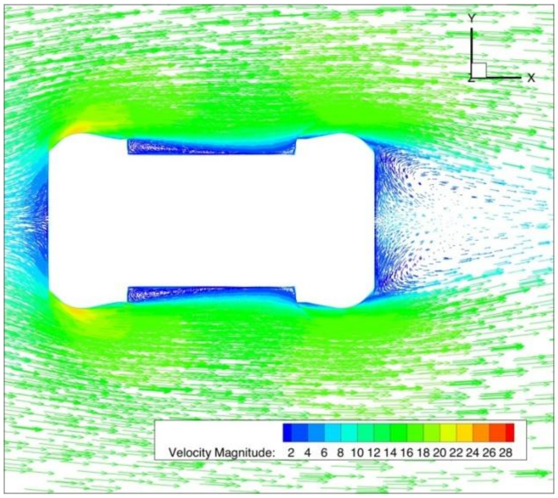

[kw-sst]

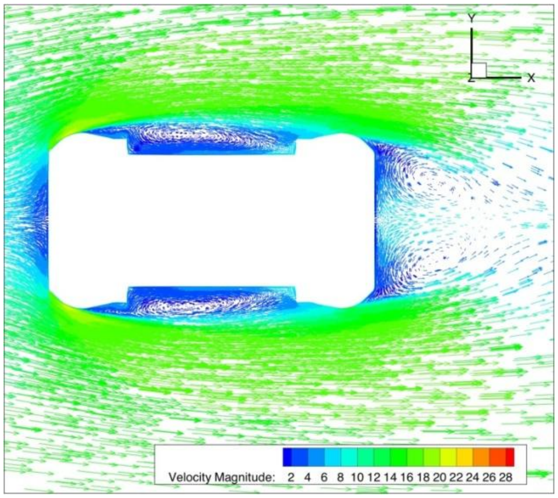

[trans-k-kl-w]

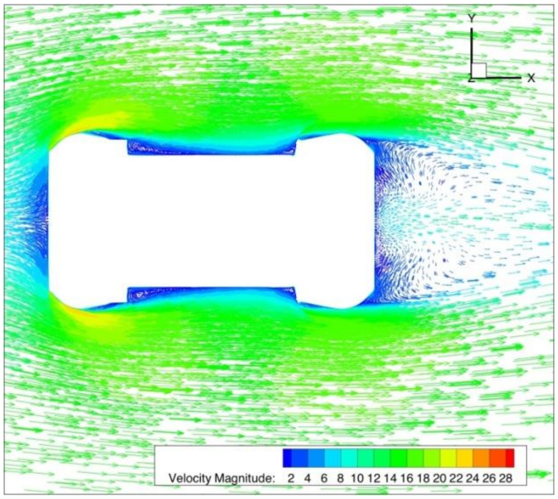

[LES]

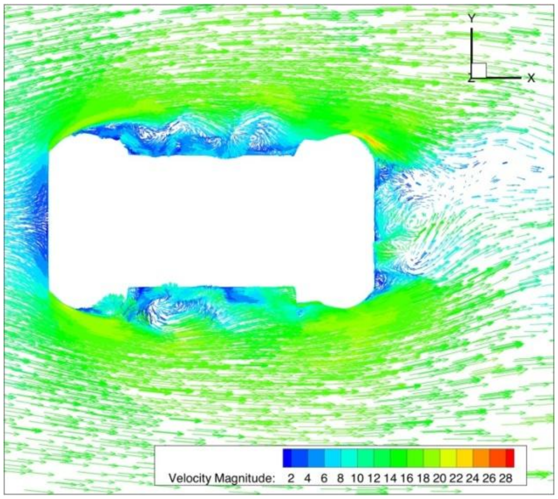

[trans-sst]

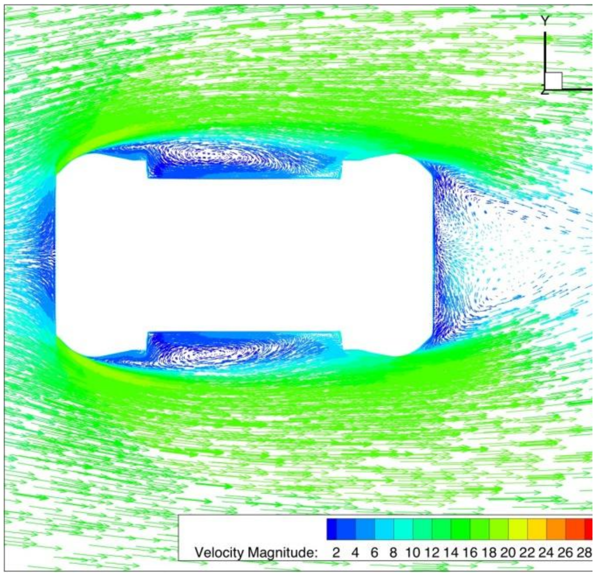

B6 Velocity components on z=0.06 plane

[k-e realizable]

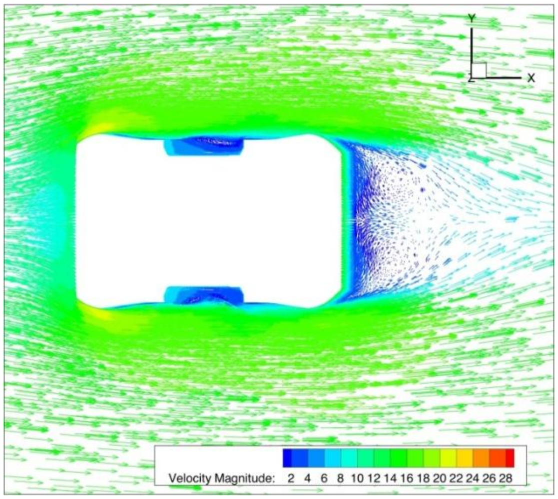

[kw]

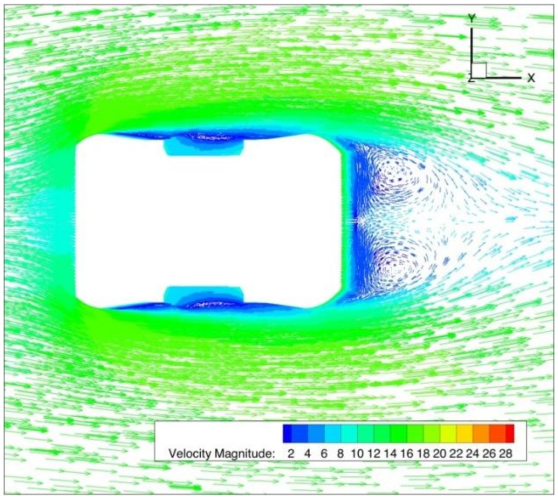

[Spalart-Allmaras]

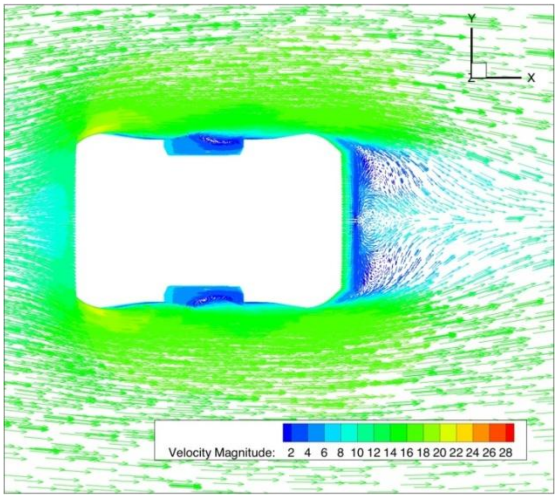

[kw-sst]

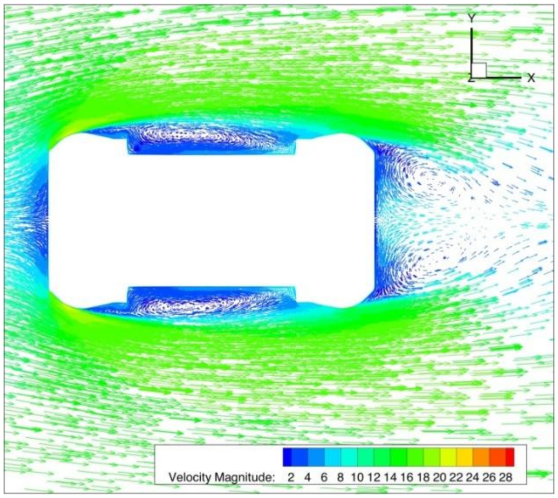

[trans-k-kl-w]

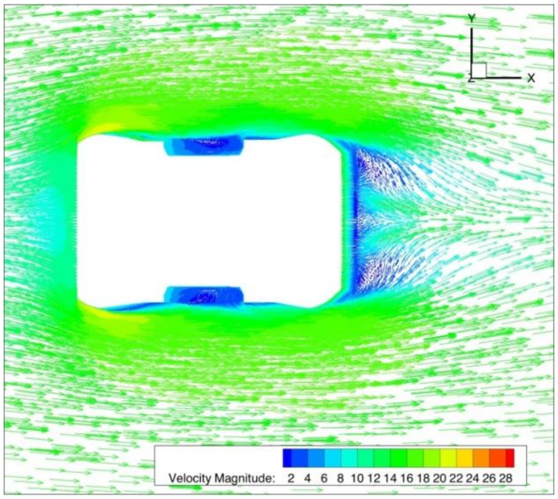

[LES]

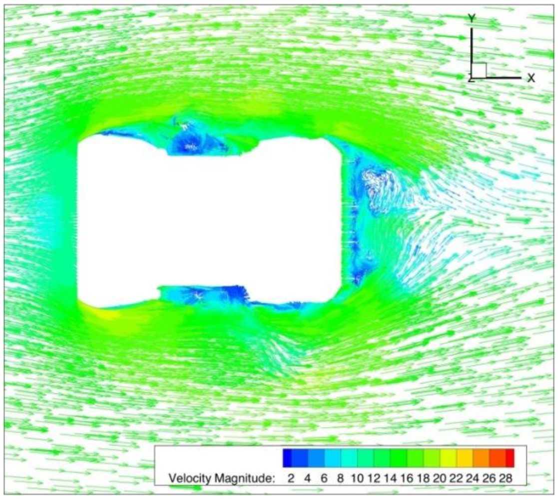

[trans-sst]

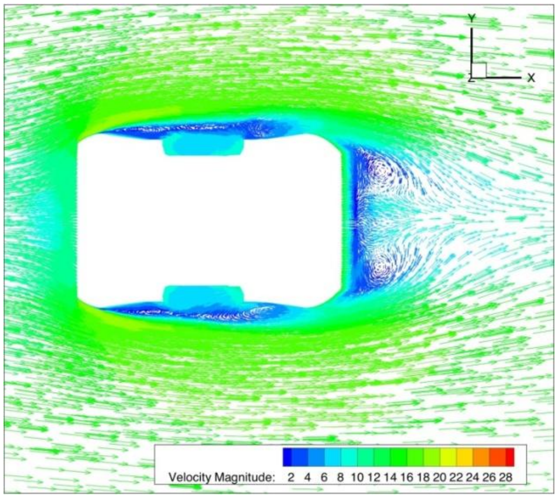

B7 Contour of streamwise velocity on Y=0 plane

[k-e realizable]

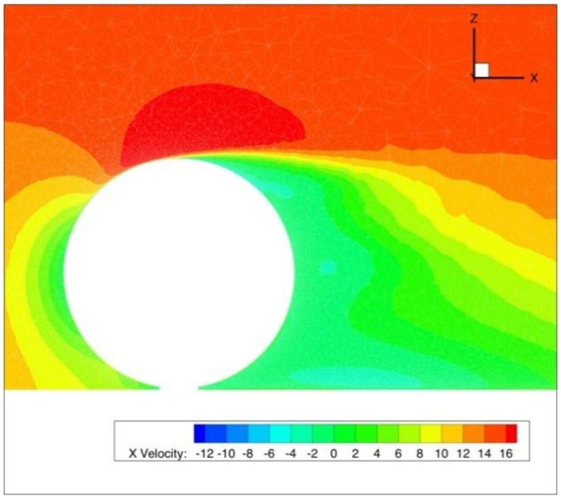

[kw]

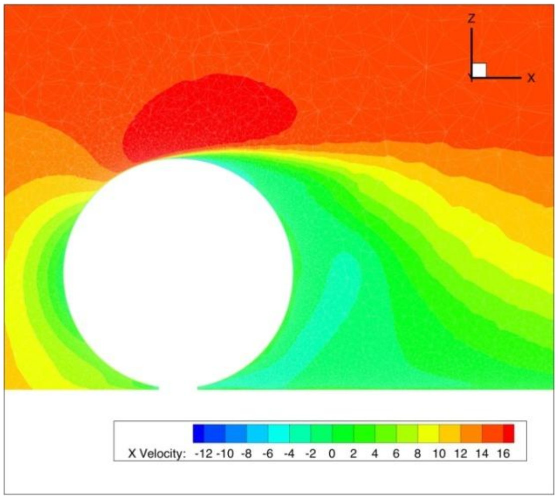

[Spalart-Allmaras]

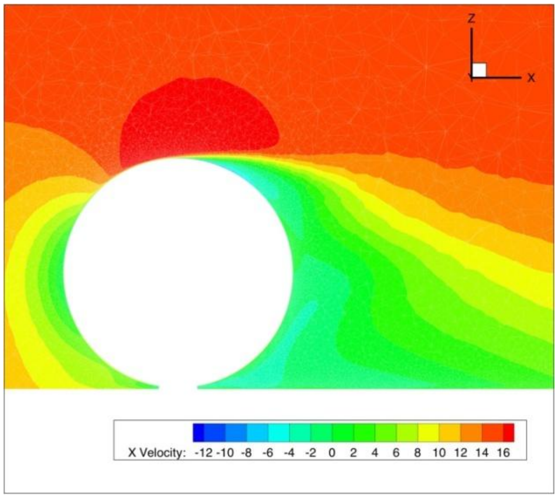

[kw-sst]

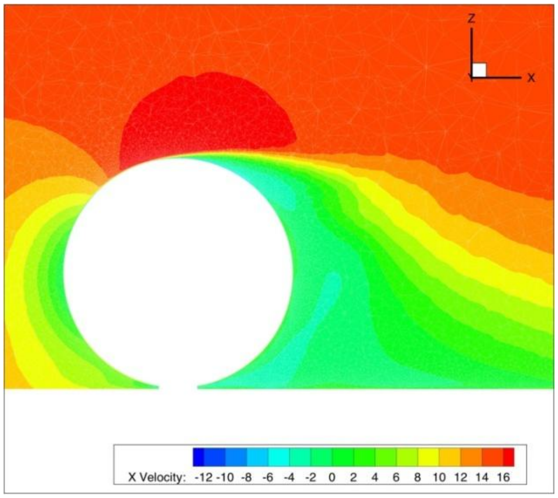

[trans-k-kl-w]

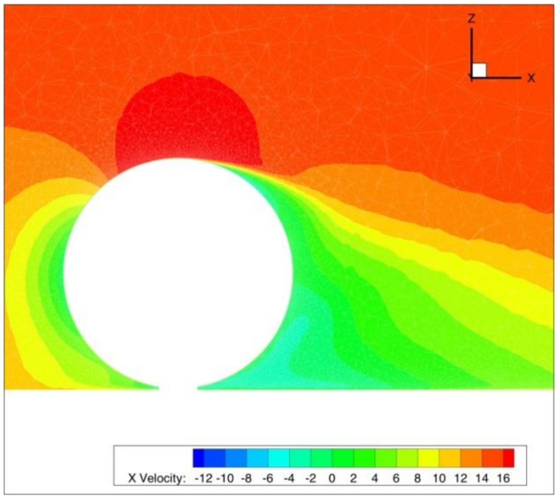

[LES]

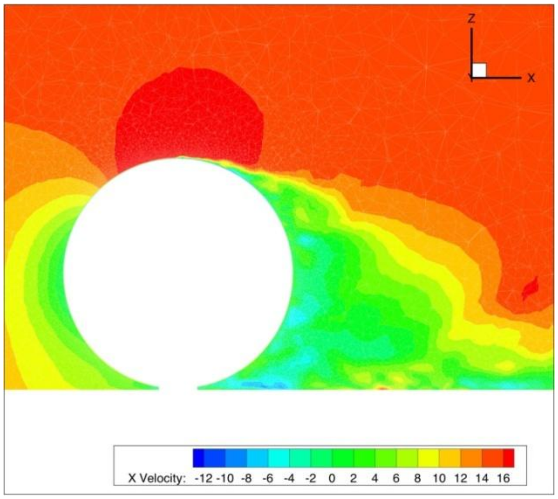

[trans-sst]

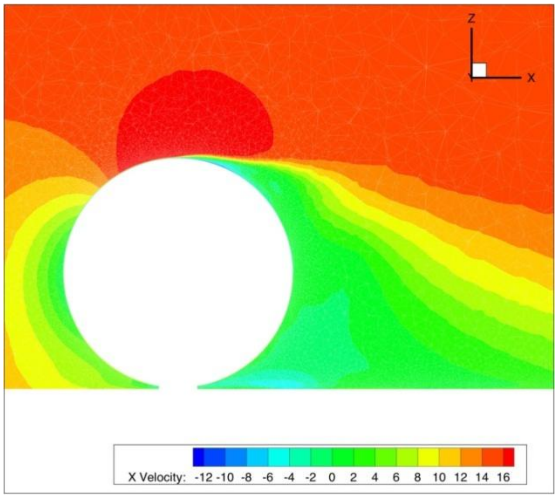

B8 Contour of streamwise velocity on Y=-0.03 plane

[k-e realizable]

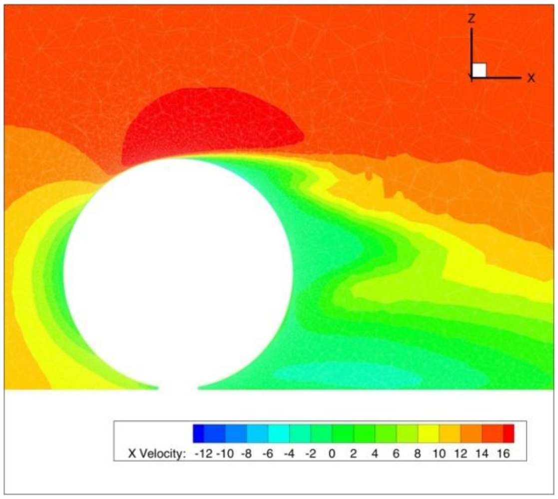

[kw]

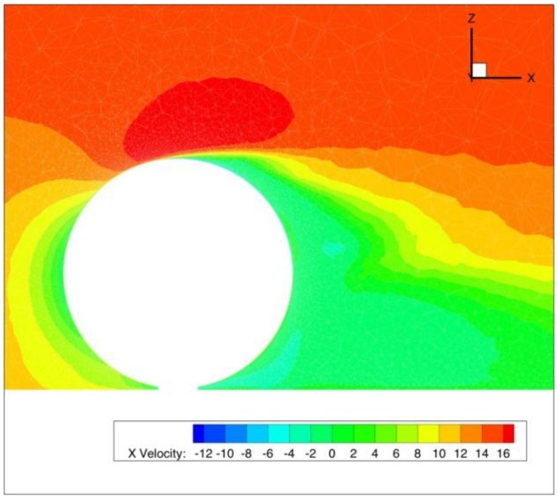

[Spalart-Allmaras]

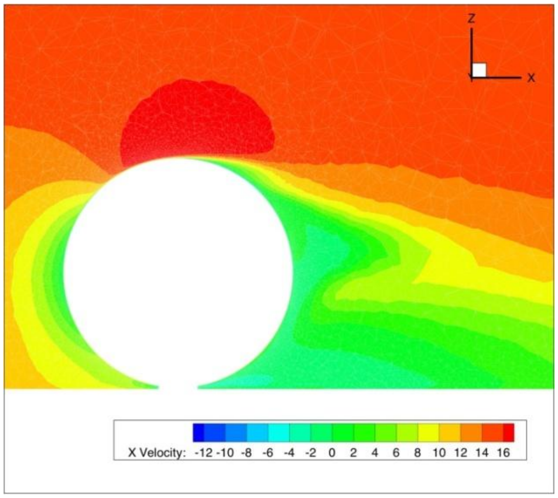

[kw-sst]

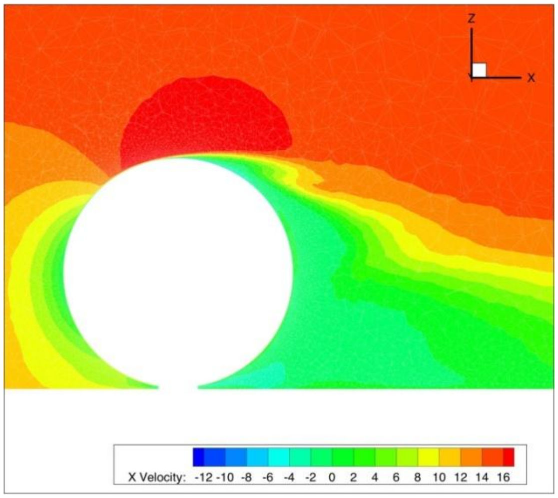

[trans-k-kl-w]

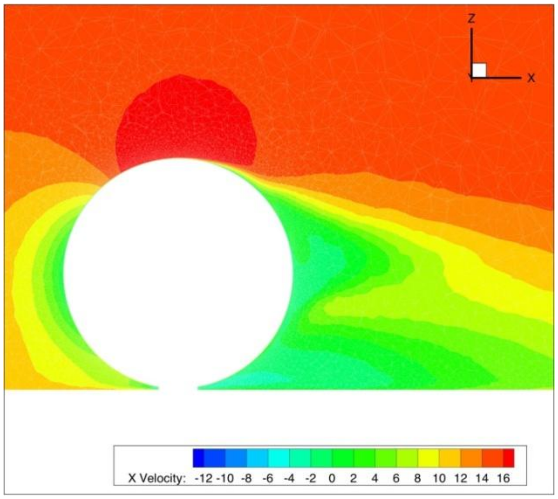

[LES]

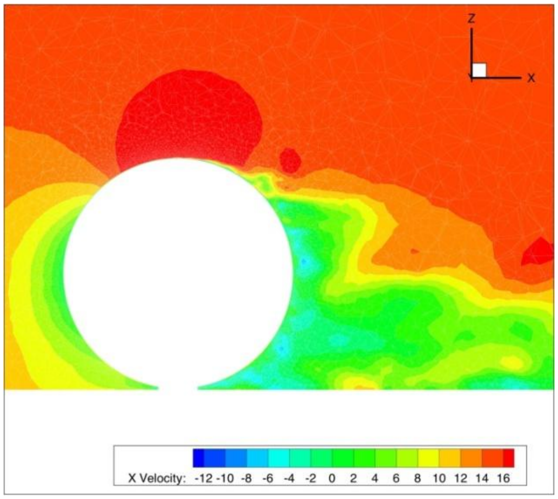

[trans-sst]

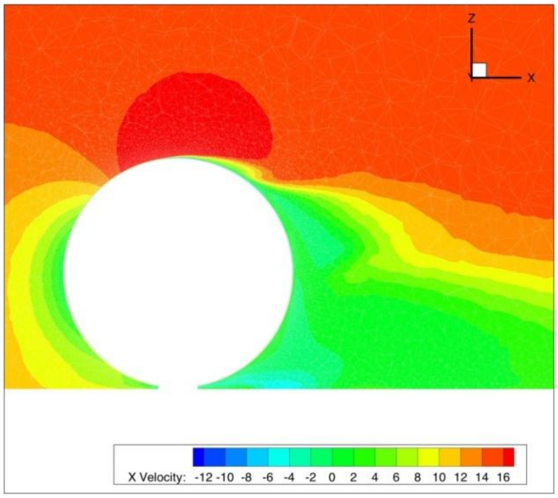

B9 Contour of streamwise velocity on Y=+0.03 plane

[k-e realizable]

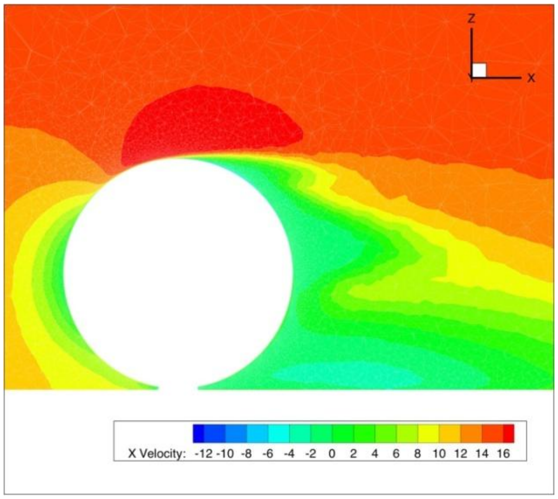

[kw]

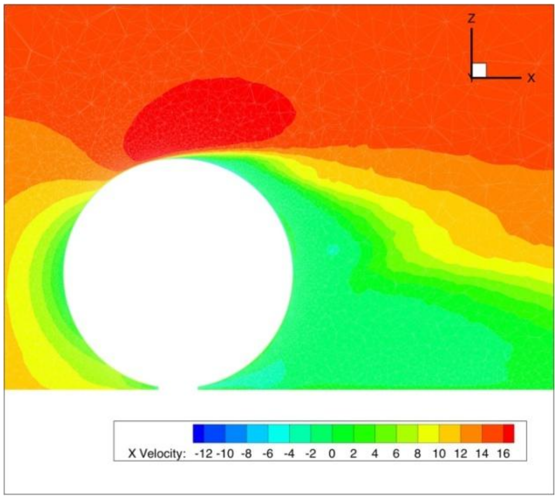

[Spalart-Allmaras]

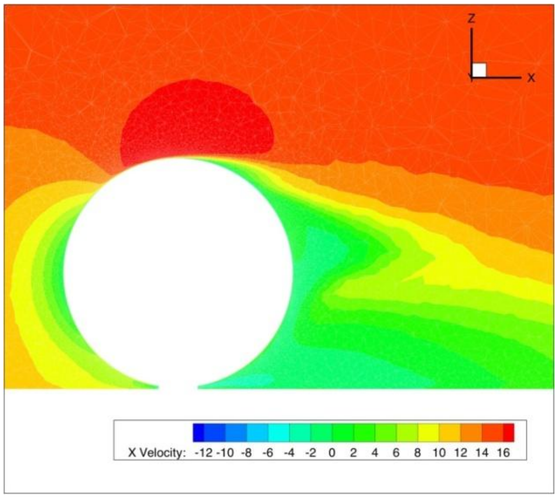

[kw-sst]

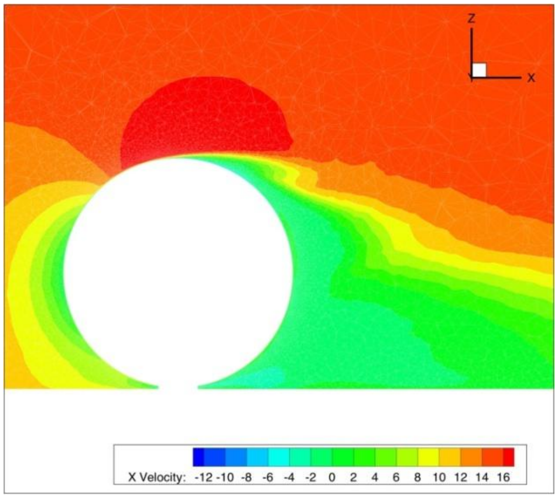

[trans-k-kl-w]

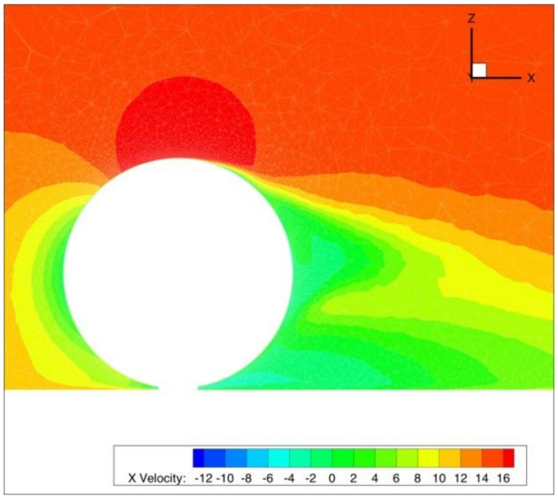

[LES]

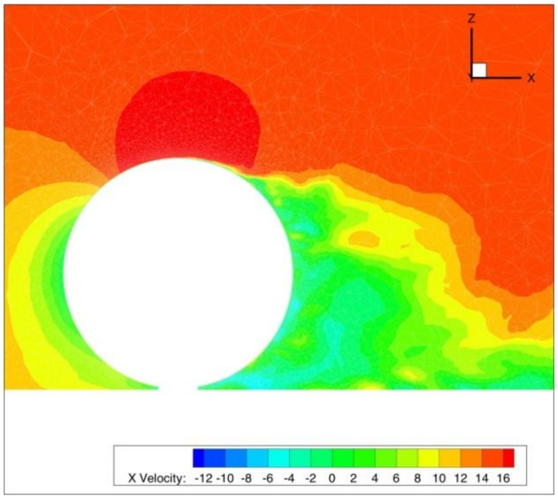

[trans-sst]

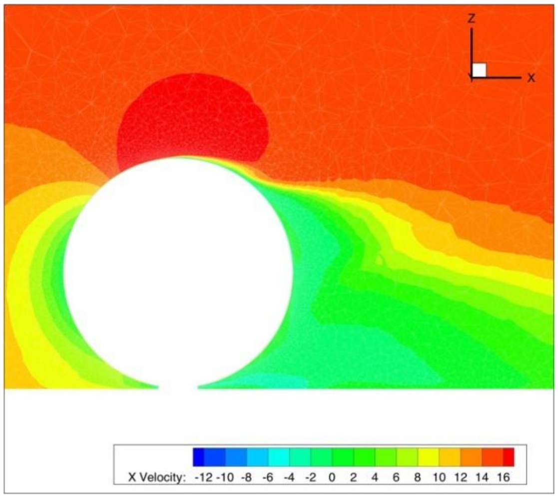

B10 Contour of streamwise velocity on Y=-0.07 plane

[k-e realizable]

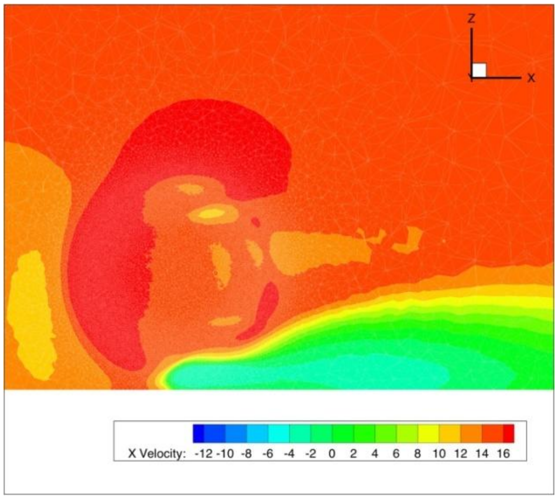

[kw]

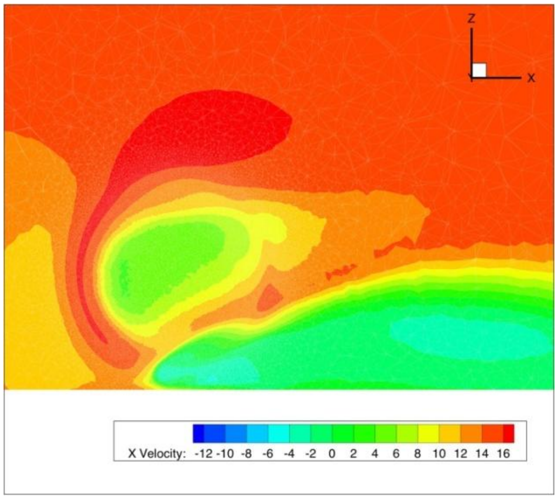

[Spalart-Allmaras]

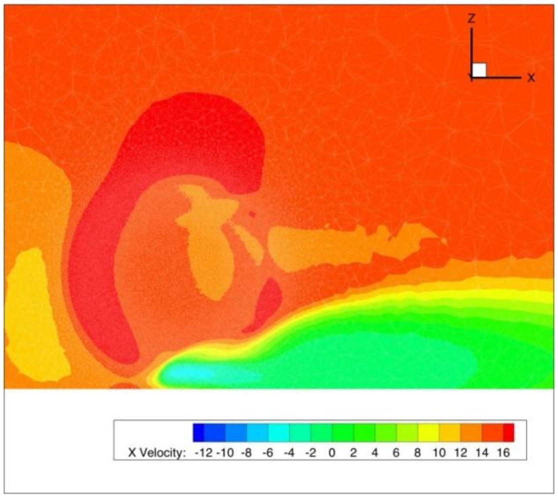

[kw-sst]

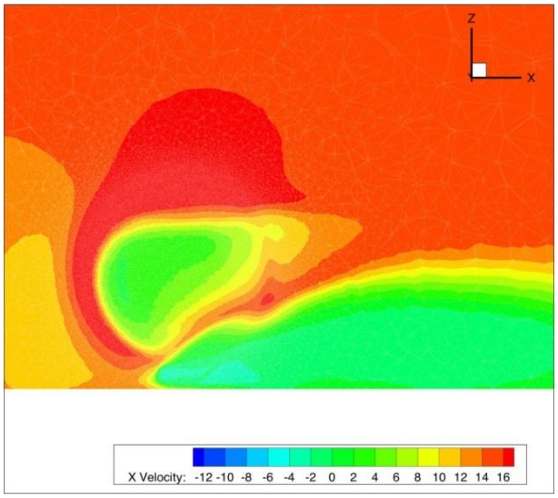

[trans-k-kl-w]

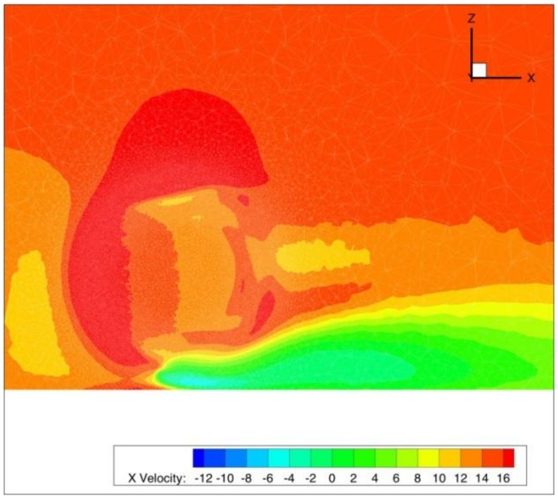

[LES]

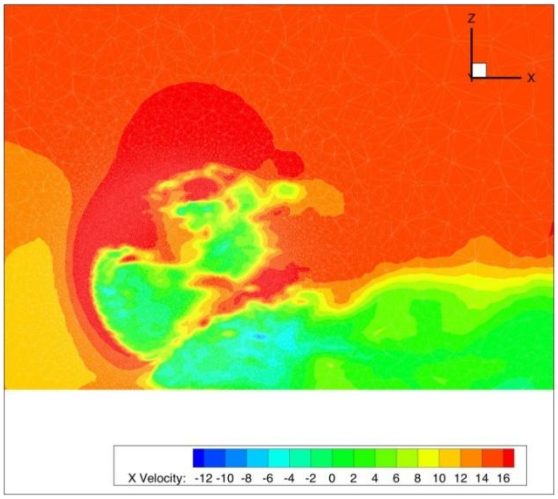

[trans-sst]

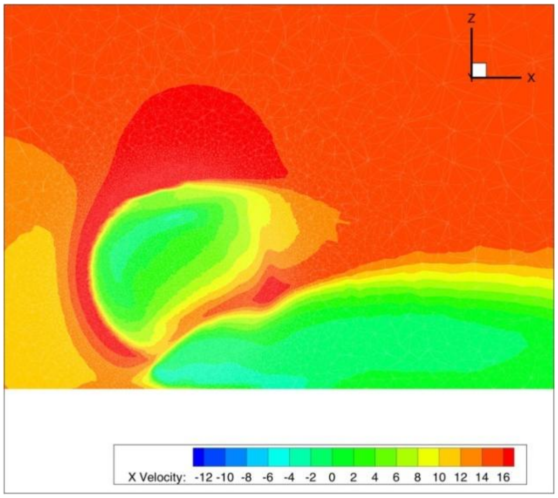

B11 Contour of streamwise velocity on Y=+0.07 plane

[k-e realizable]

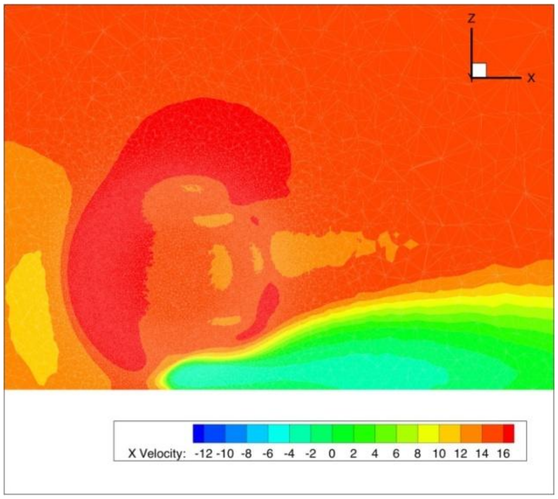

[kw]

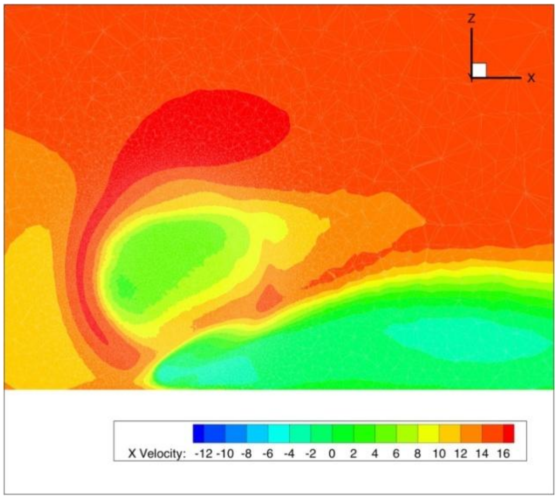

[Spalart-Allmaras]

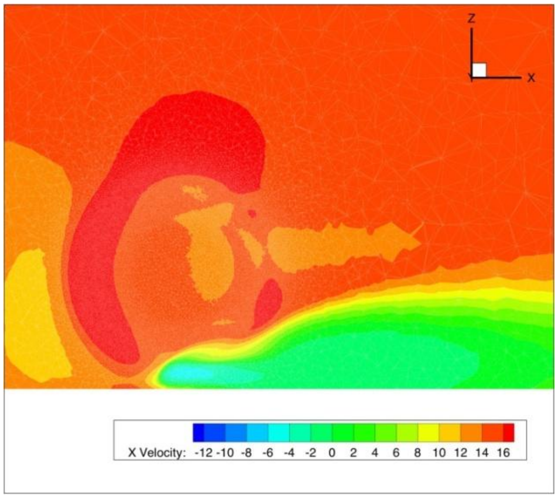

[kw-sst]

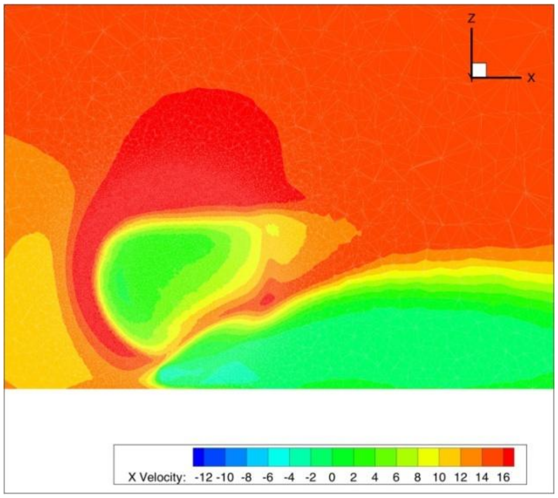

[trans-k-kl-w]

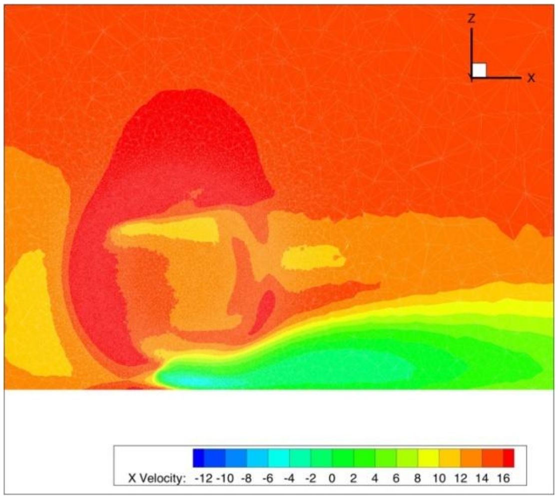

[LES]

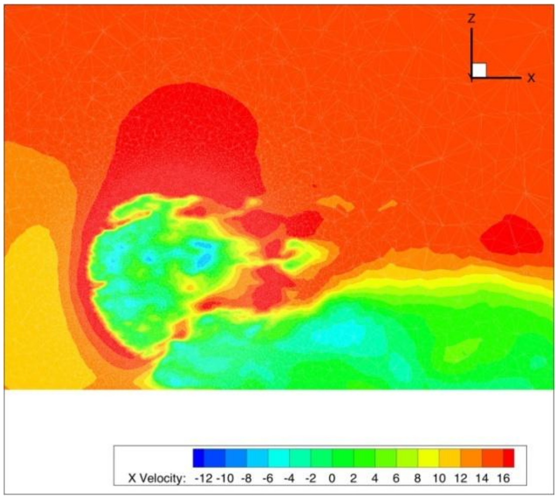

[trans-sst]

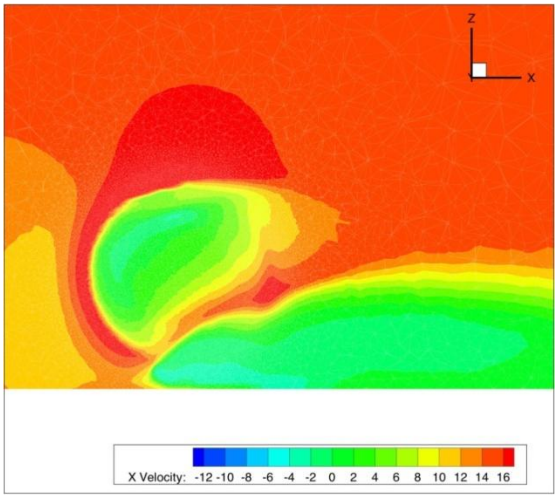

B12 Contour of streamwise velocity on Z=-0.123 plane

[k-e realizable]

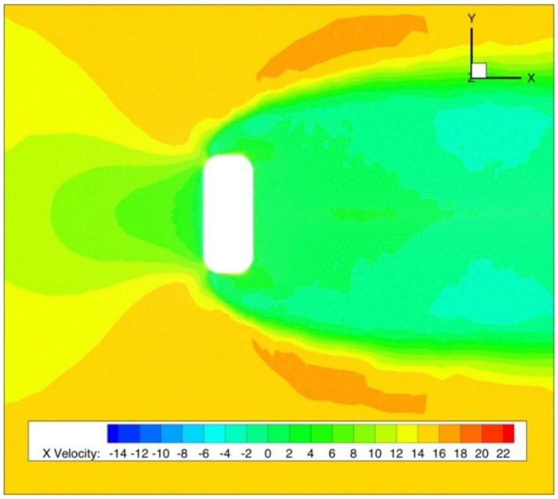

[kw]

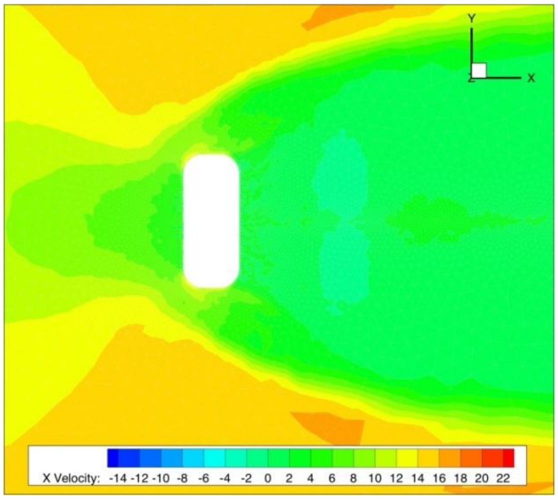

[Spalart-Allmaras]

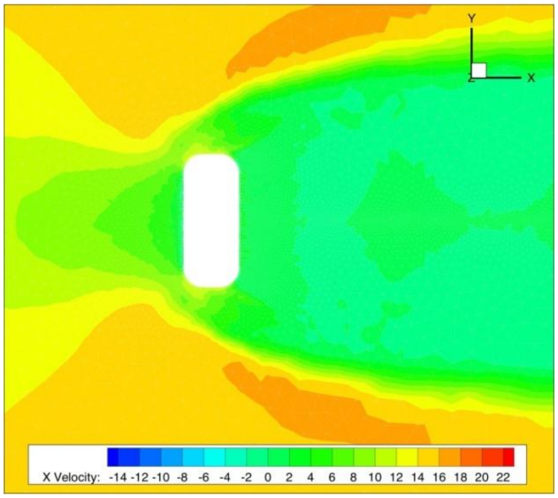

[kw-sst]

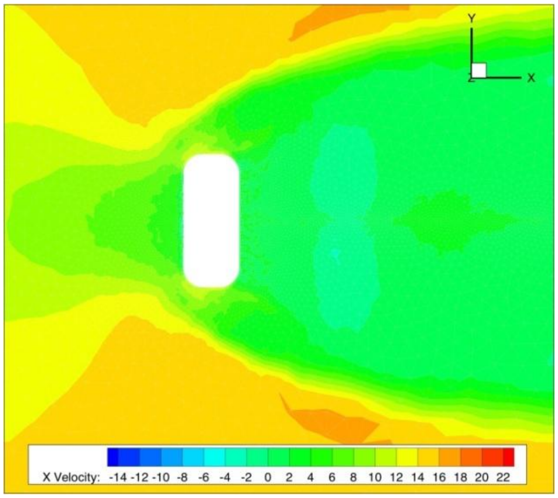

[trans-sst]

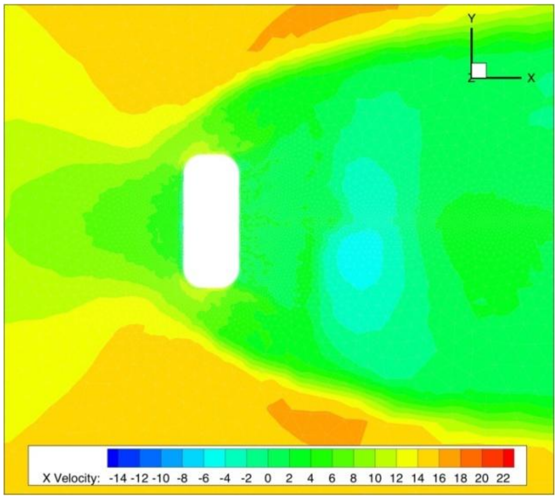

[trans-k-kl-w]

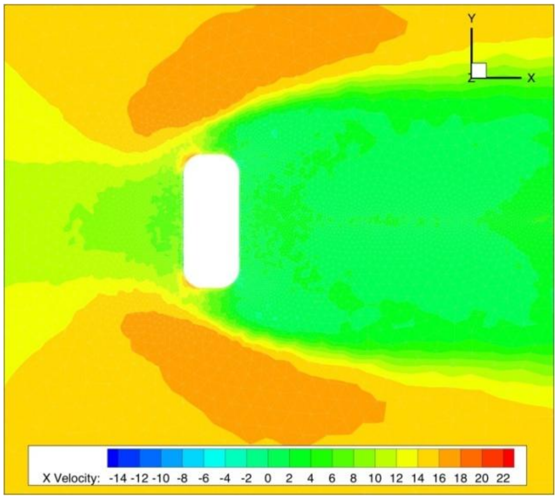

[LES]

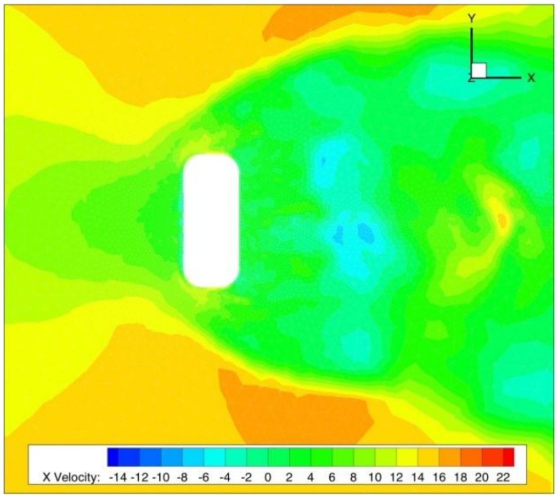

B13 Contour of streamwise velocity on Z=-0.06 plane

[k-e realizable]

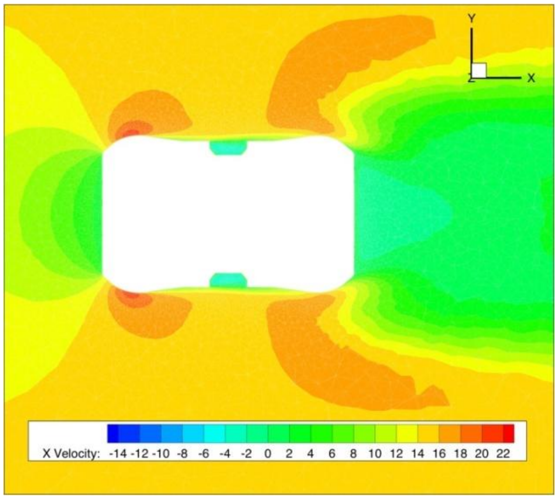

[kw]

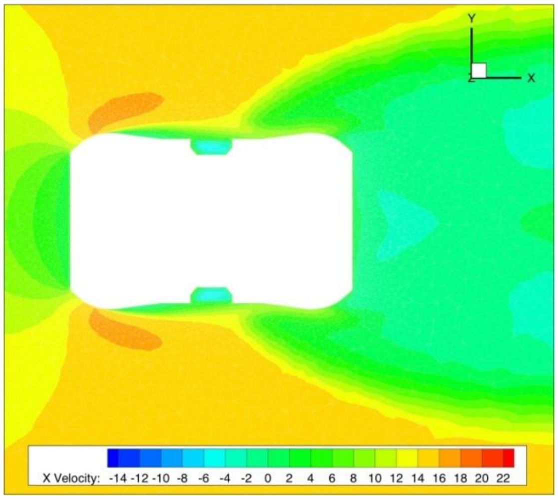

[Spalart-Allmaras]

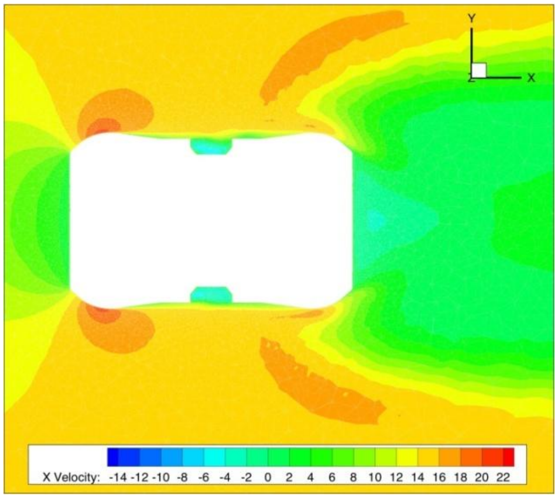

[kw-sst]

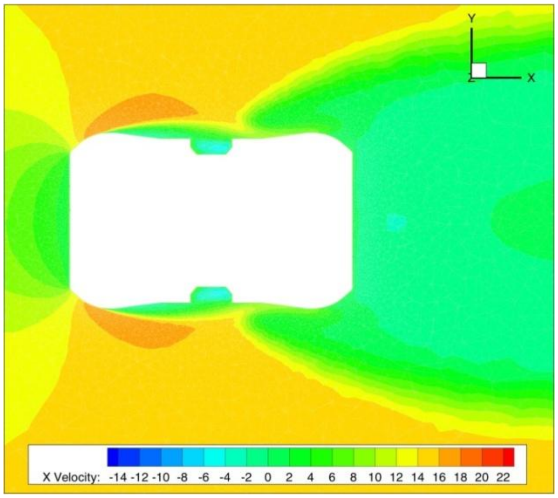

[trans-k-kl-w]

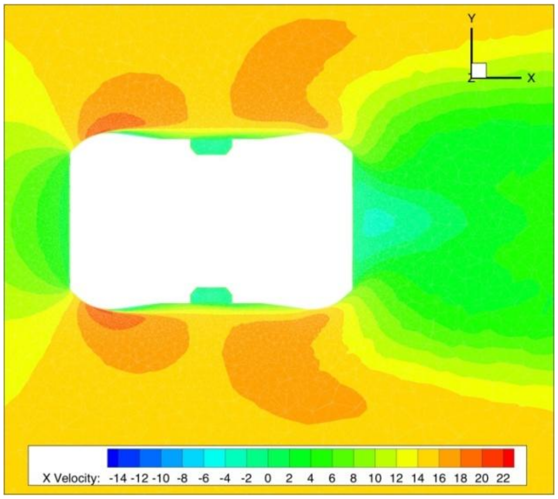

[LES]

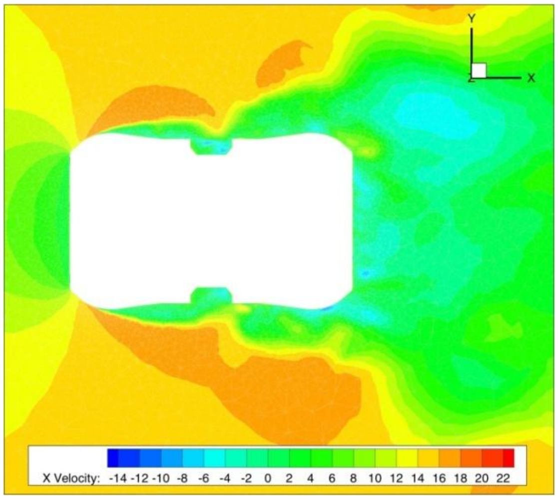

[trans-sst]

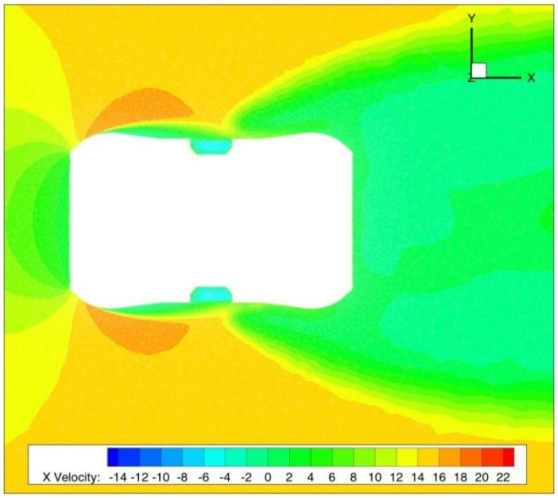

B14 Contour of streamwise velocity on Z=0 plane

[k-e realizable]

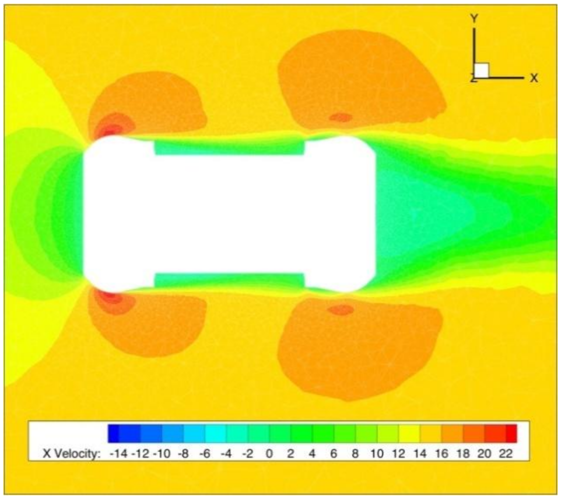

[kw]

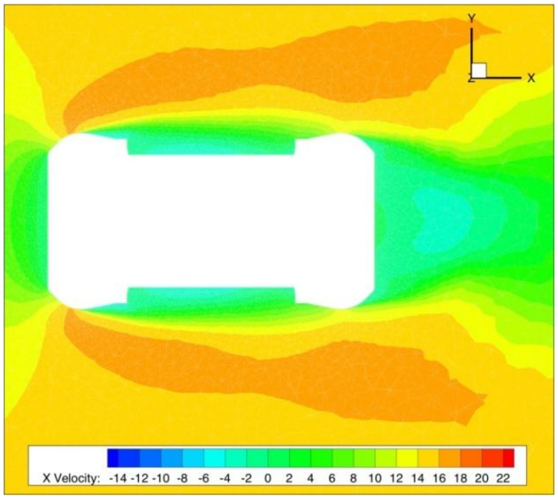

[Spalart-Allmaras]

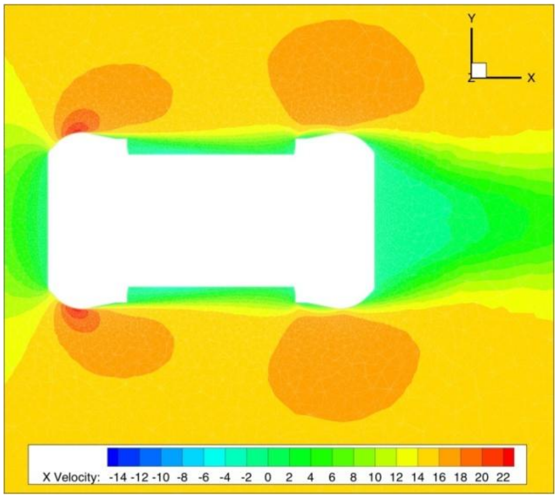

[kw-sst]

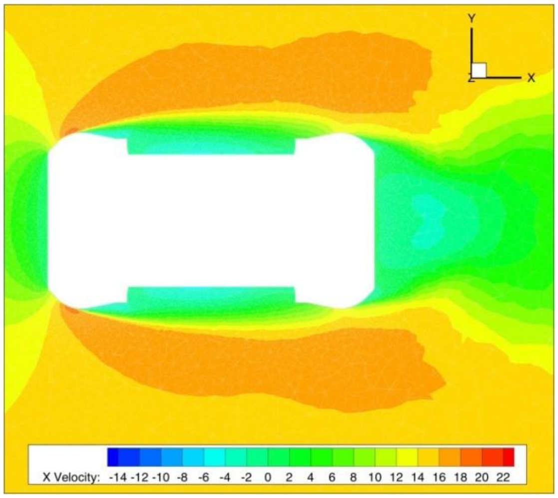

[trans-k-kl-w]

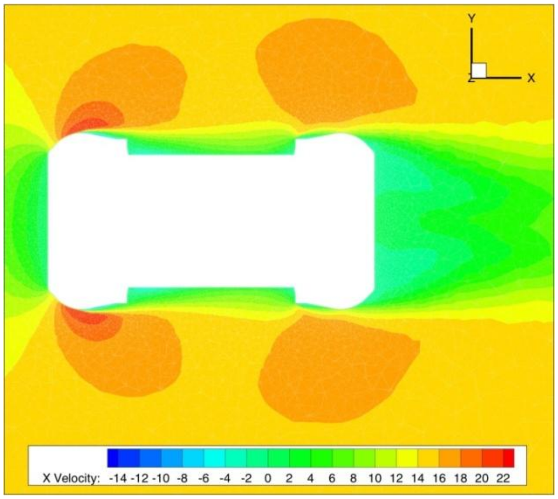

[LES]

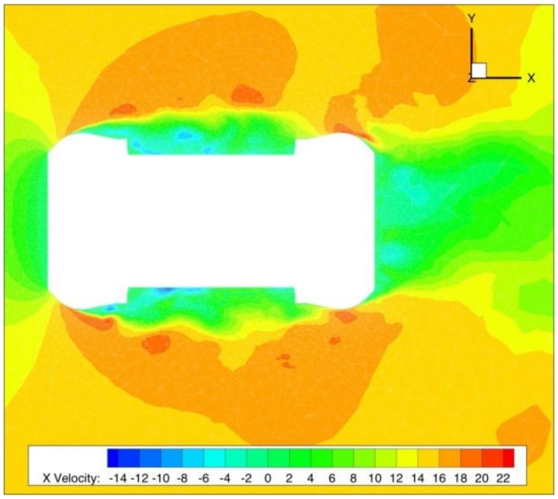

[trans-sst]

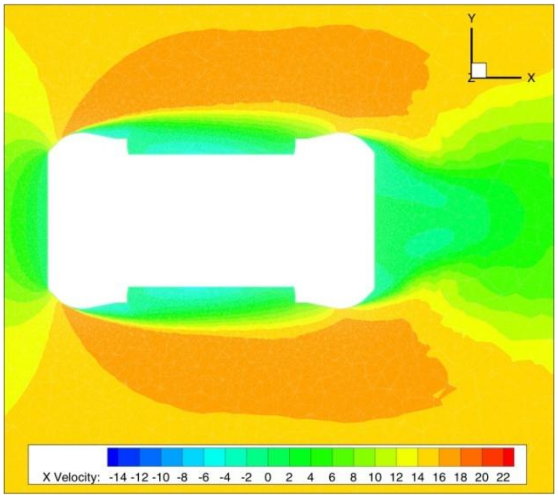

B15 Contour of streamwise velocity on Z=+0.06 plane

[k-e realizable]

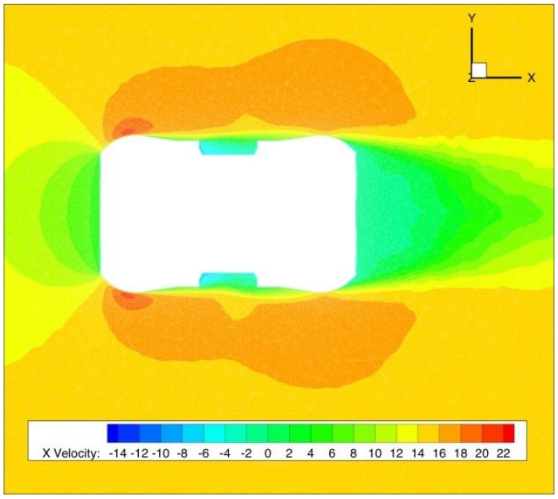

[kw]

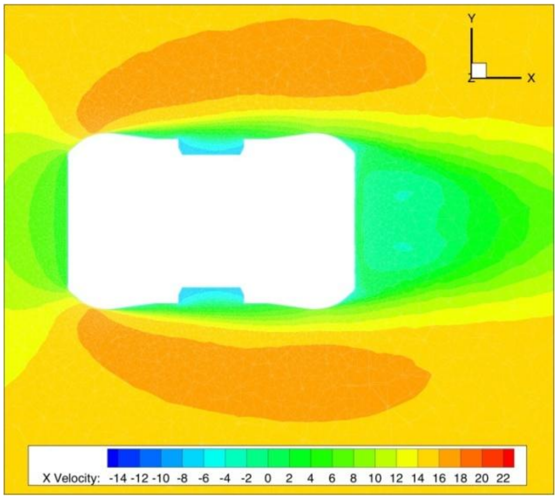

[Spalart-Allmaras]

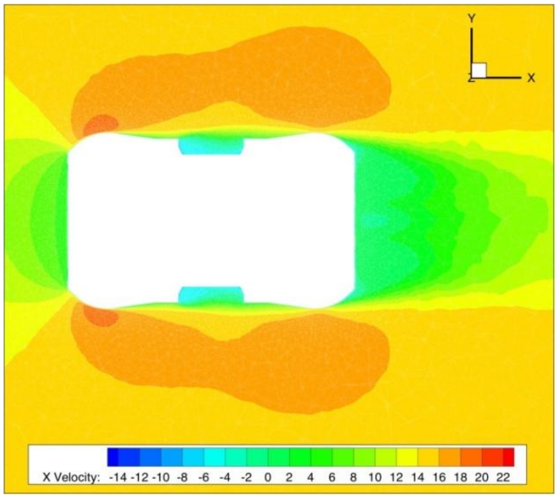

[kw-sst]

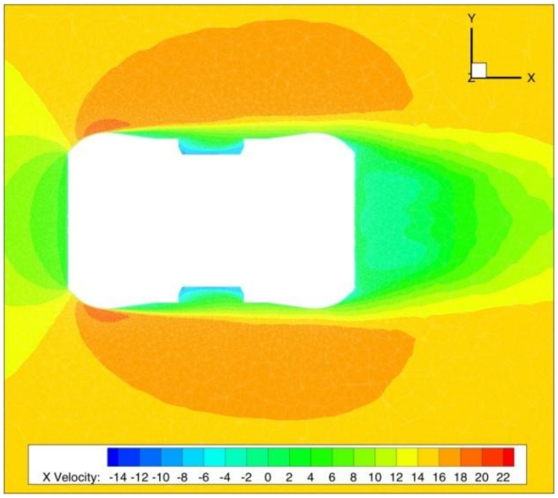

[trans-k-kl-w]

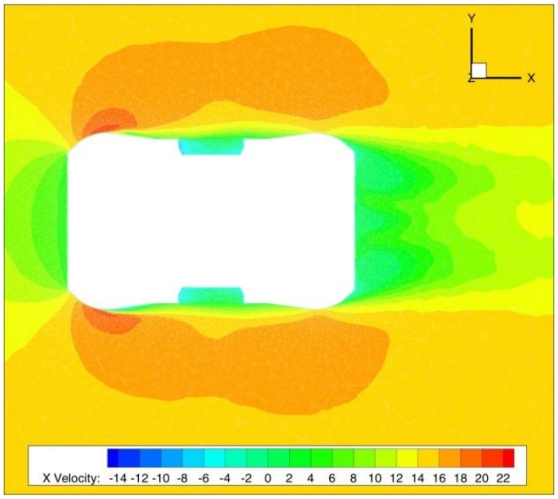

[LES]

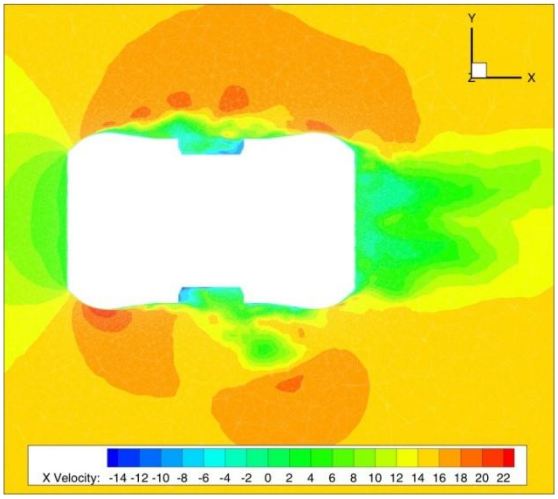

[trans-sst]

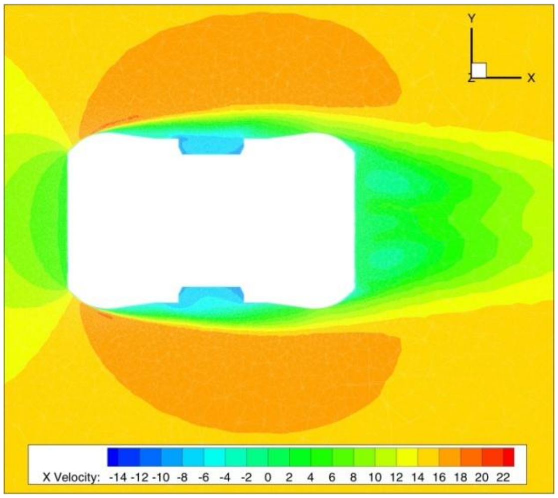

B16 Contour of static pressure on Y=0 plane

[k-e realizable]

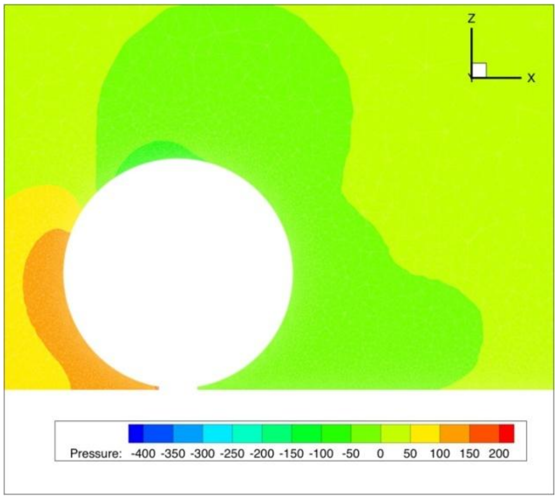

[kw]

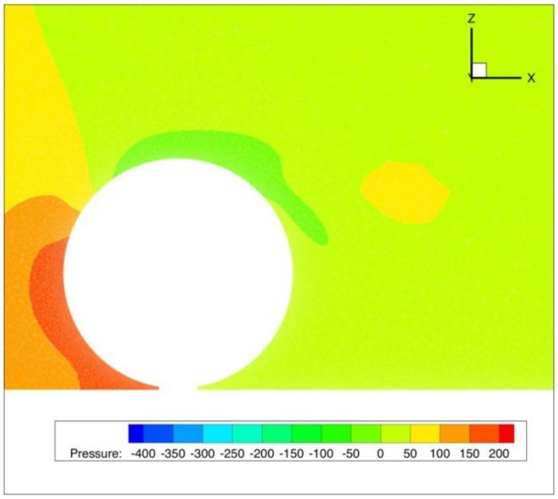

[Spalart-Allmaras]

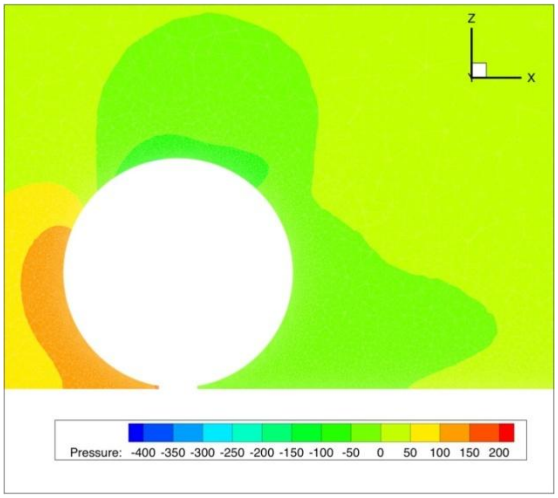

[kw-sst]

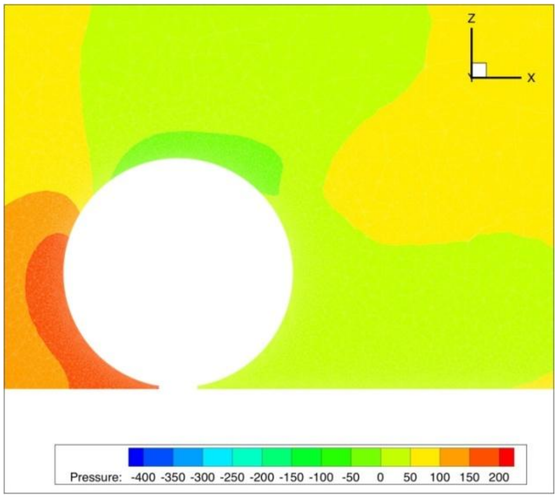

[trans-k-kl-w]

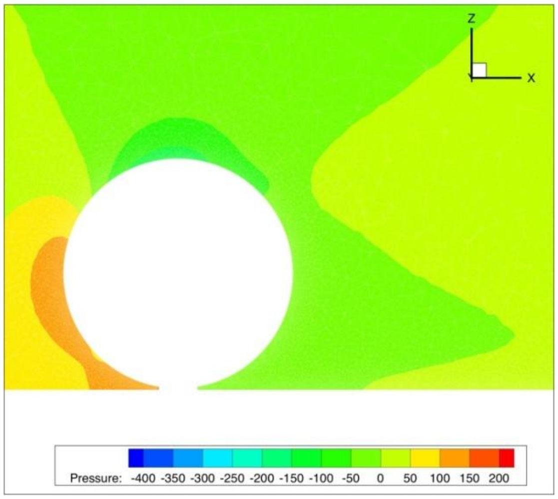

[LES]

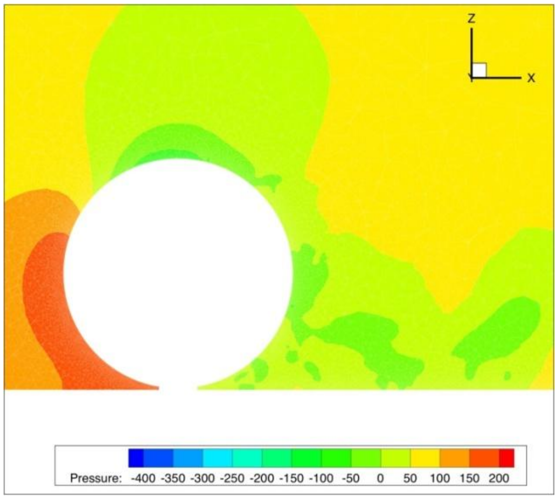

[trans-sst]

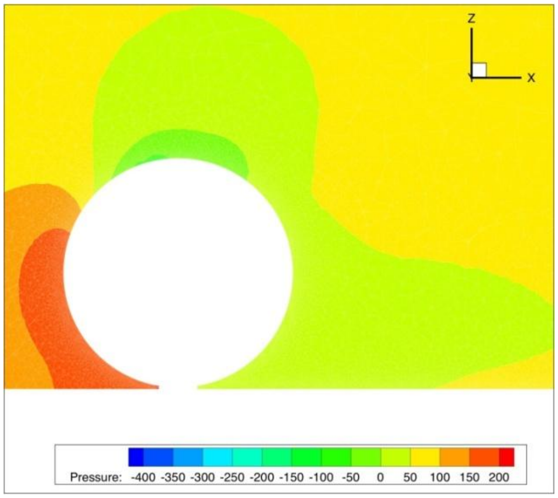

B17 Contour of static pressure on Y=-0.03 plane

[k-e realizable]

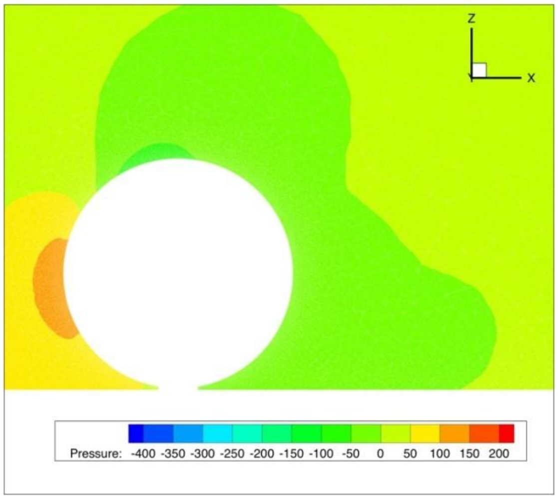

[kw]

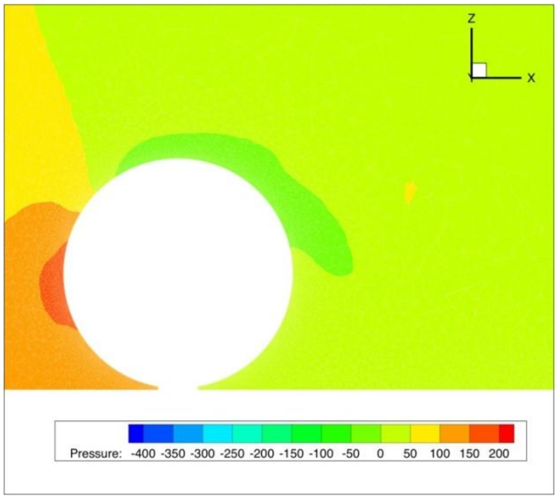

[Spalart-Allmaras]

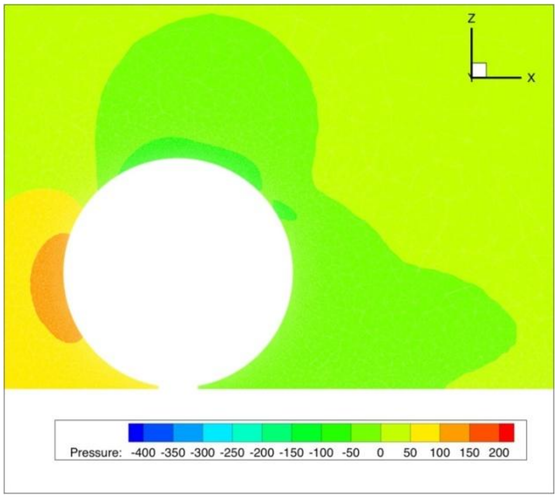

[kw-sst]

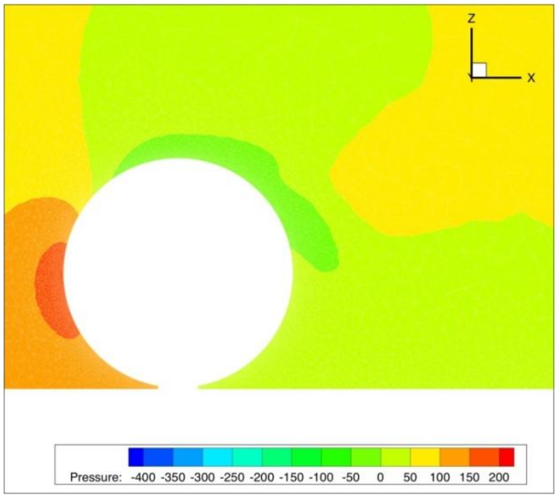

[trans-k-kl-w]

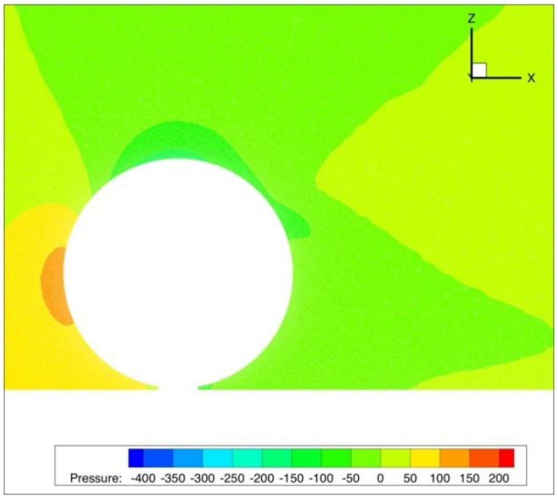

[LES]

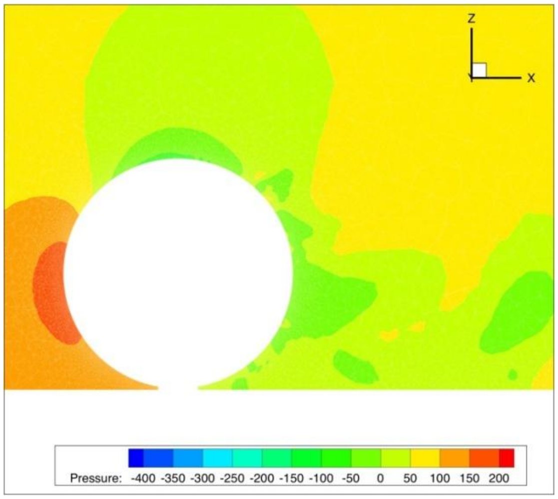

[trans-sst]

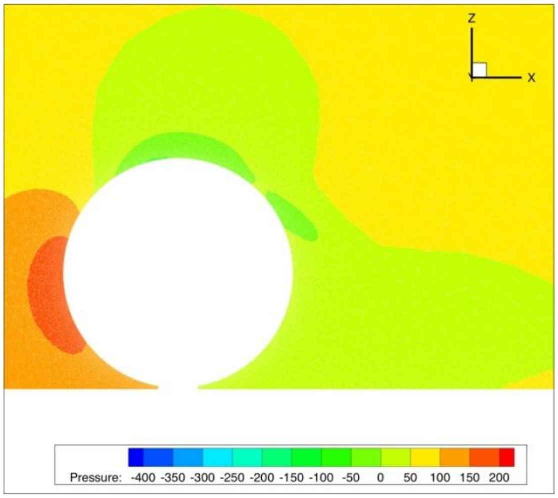

B18 Contour of static pressure on Y=+0.03 plane

[k-e realizable] **[kw]**

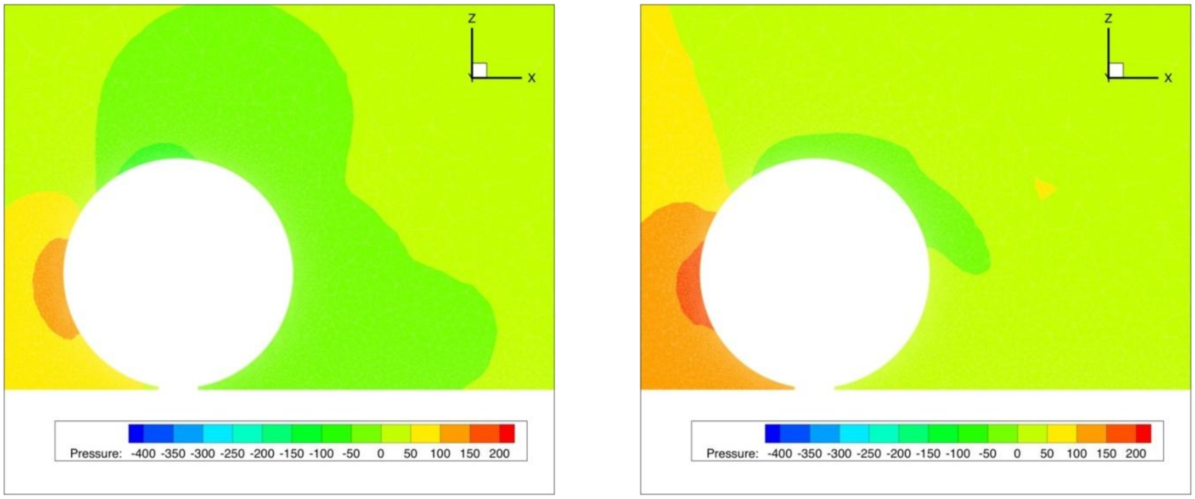

[Spalart-Allmaras] **[kw-sst]**

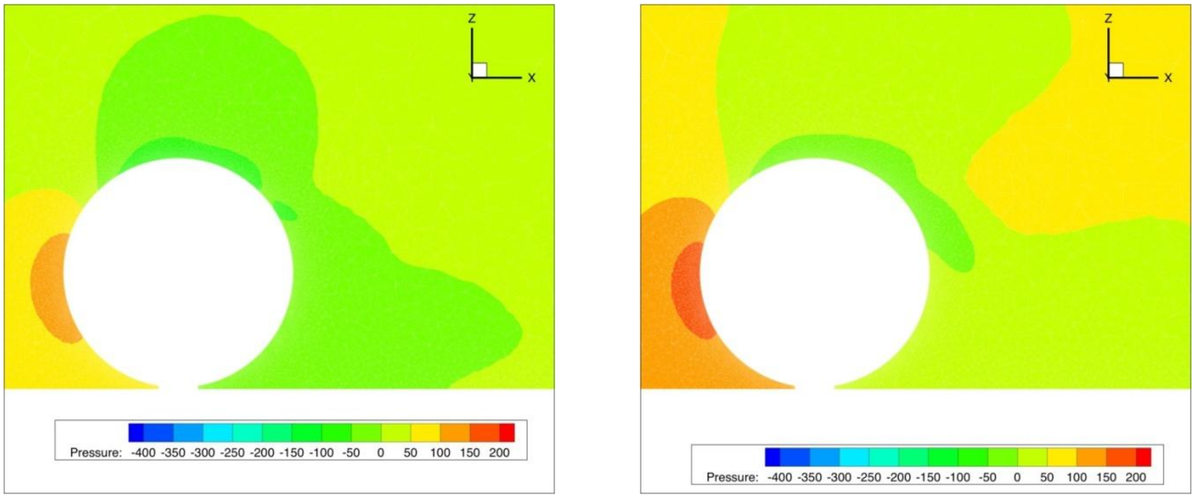

[trans-k-kl-w]

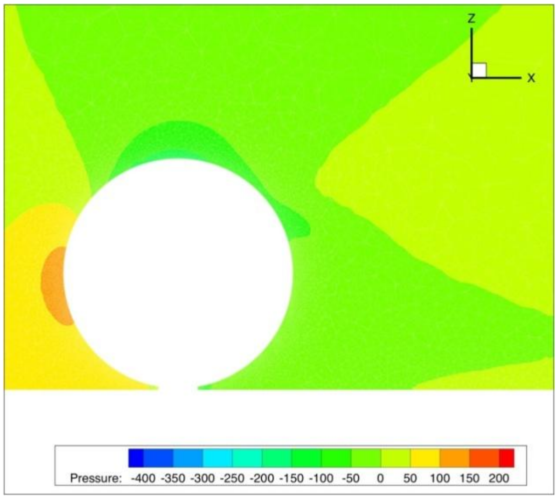

[LES]

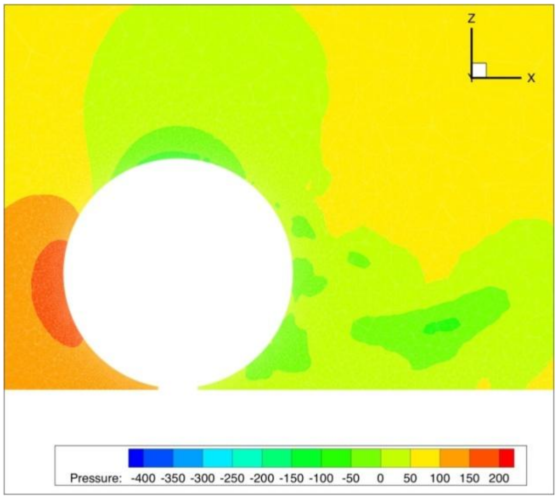

[trans-sst]

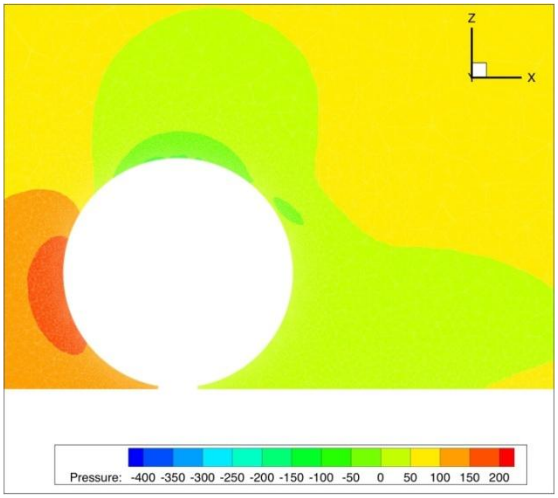

B19 Contour of static pressure on Y=-0.07 plane

[k-e realizable]

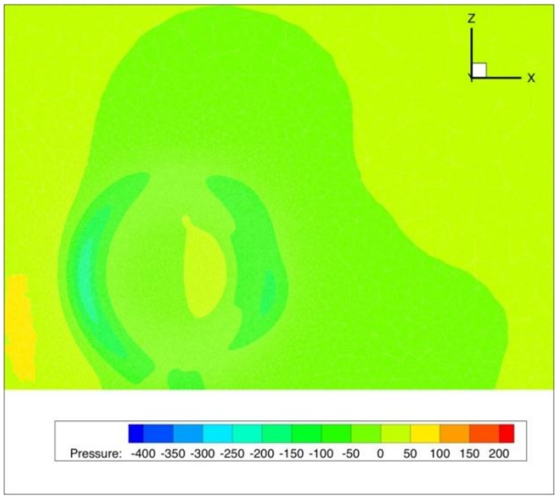

[kw]

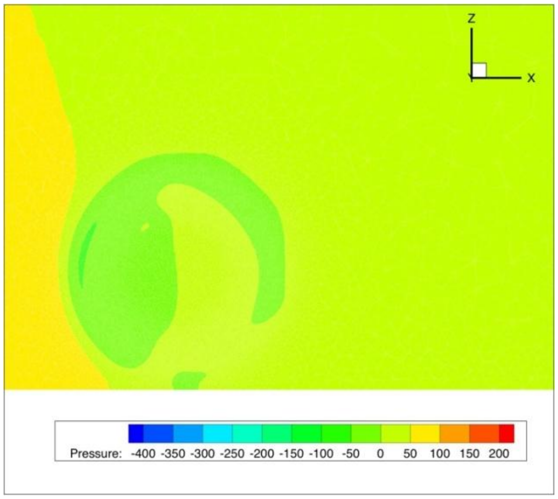

[Spalart-Allmaras]

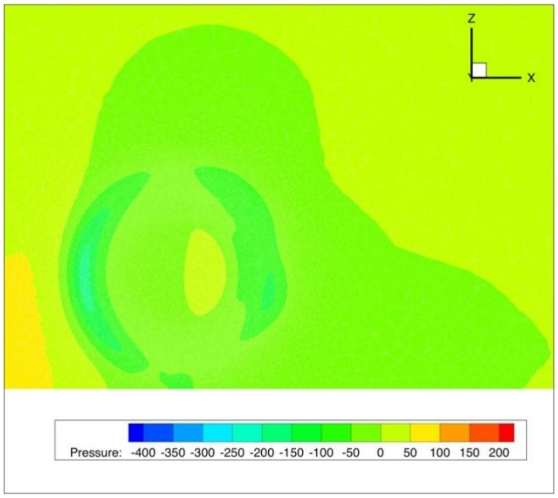

[kw-sst]

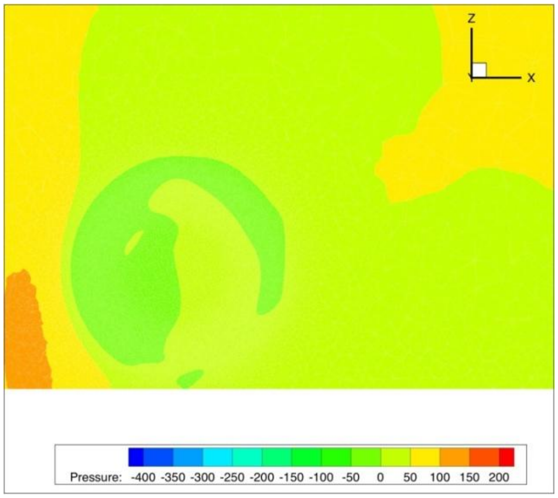

[trans-k-kl-w]

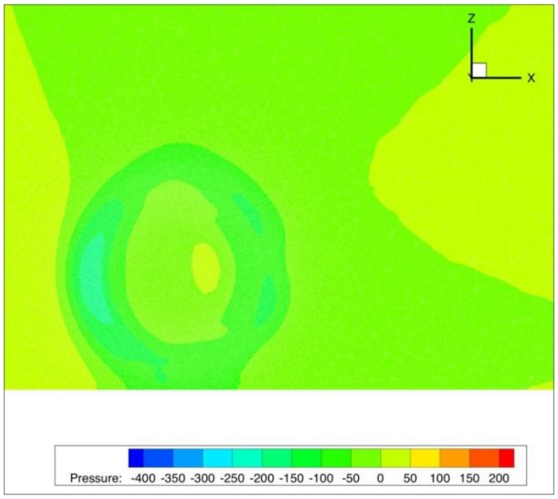

[LES]

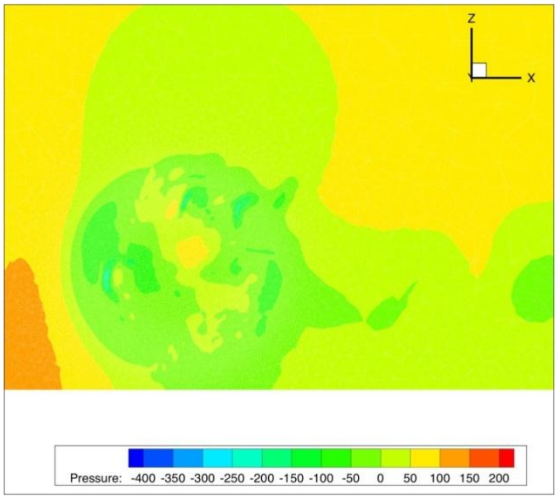

[trans-sst]

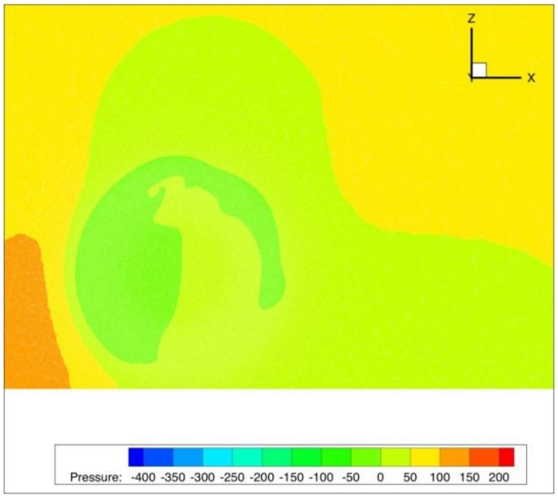

B20 Contour of static pressure on Y=+0.07 plane

[k-e realizable]

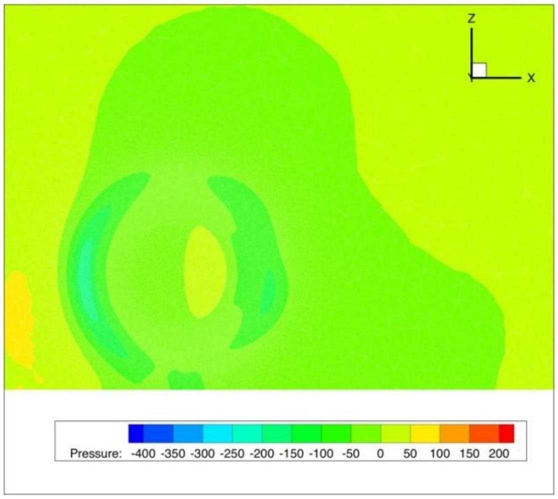

[kw]

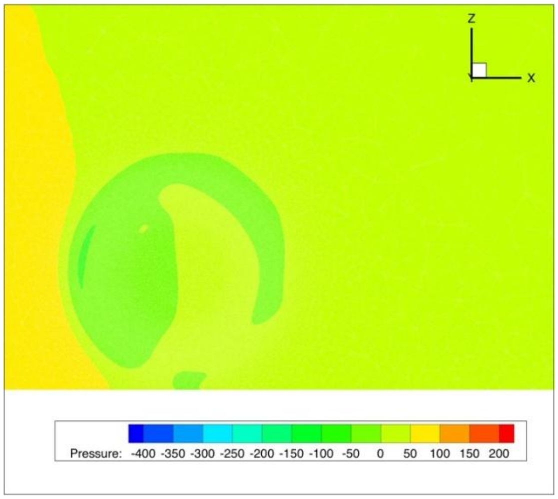

[Spalart-Allmaras]

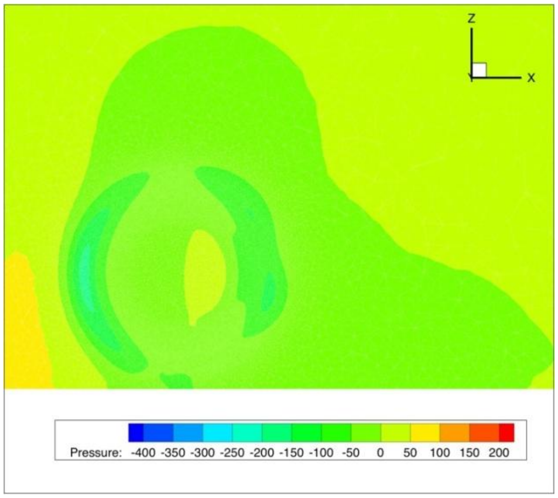

[kw-sst]

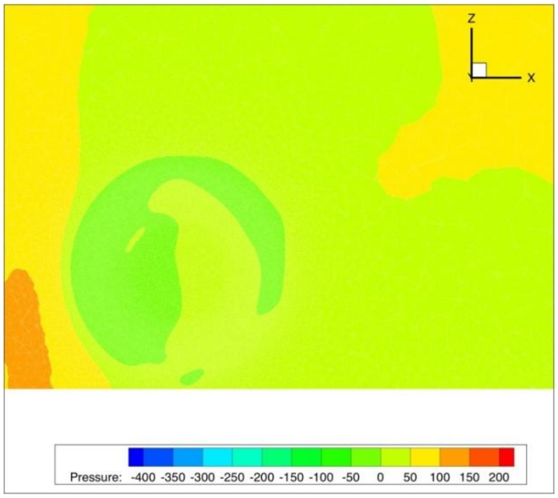

[trans-k-kl-w]

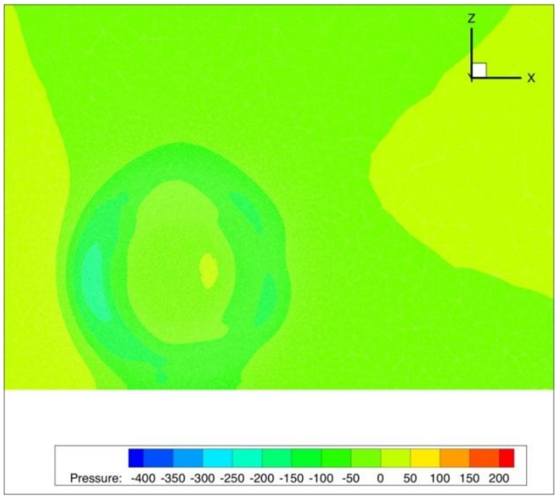

[LES]

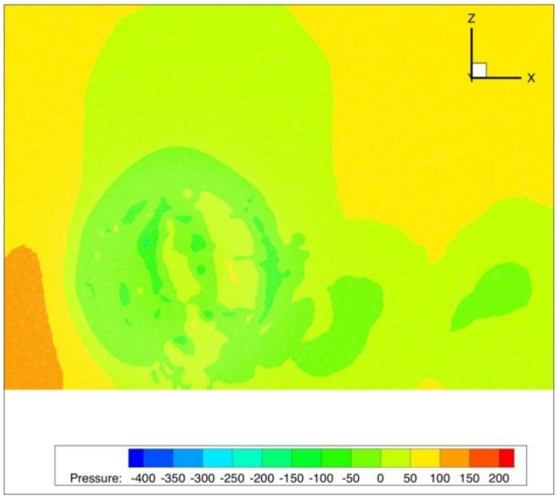

[trans-sst]

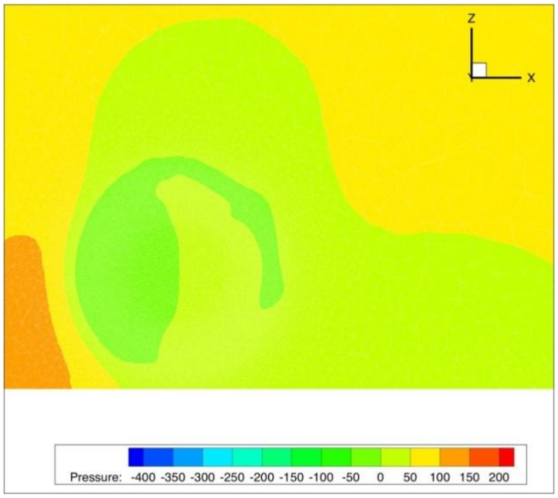

B21 Contour of static pressure on Z=-0.123 plane

[k-e realizable]

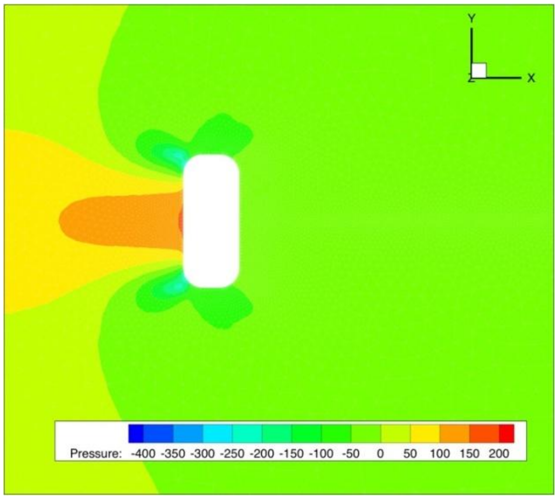

[kw]

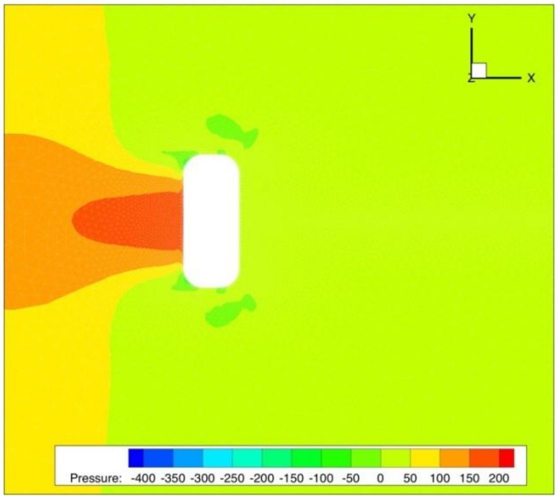

[Spalart-Allmaras]

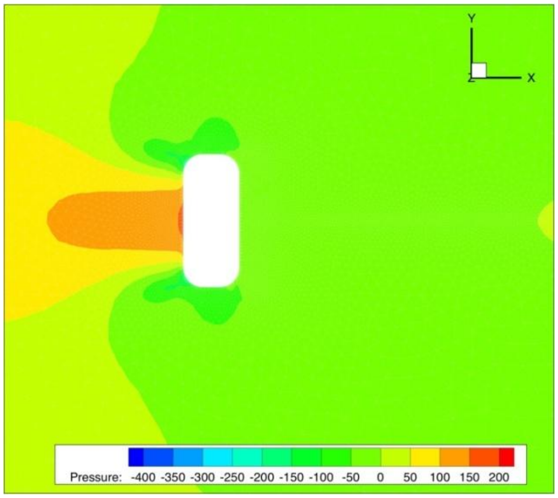

[kw-sst]

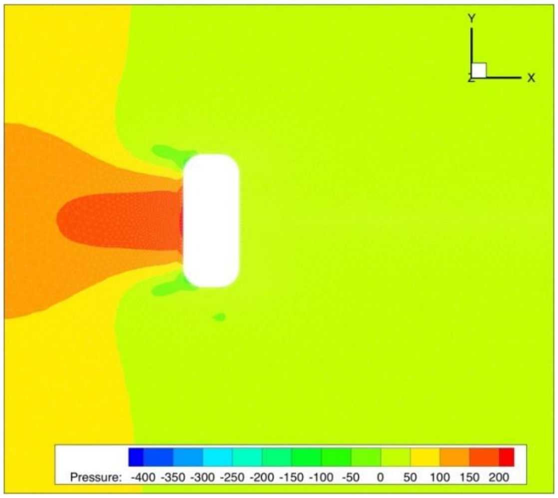

[trans-k-kl-w]

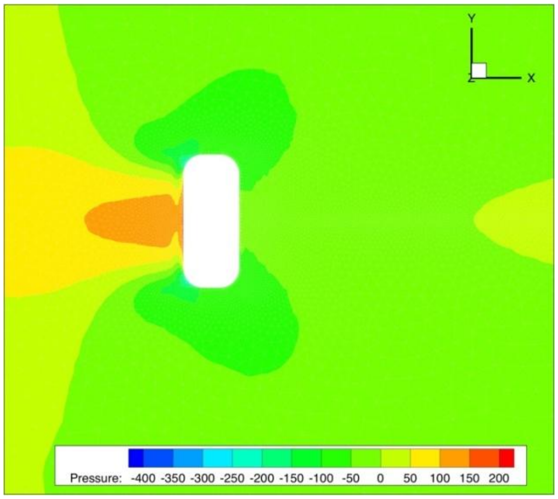

[LES]

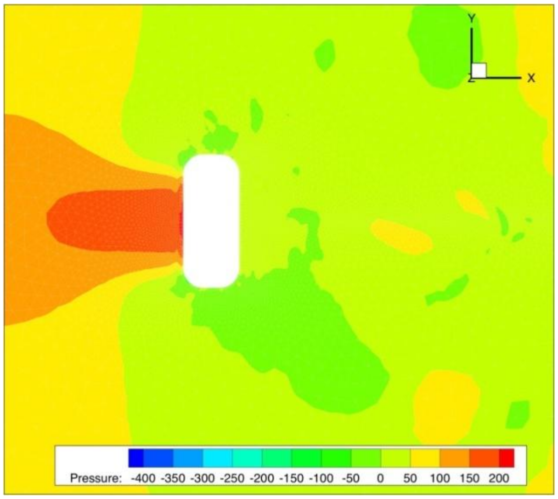

[trans-sst]

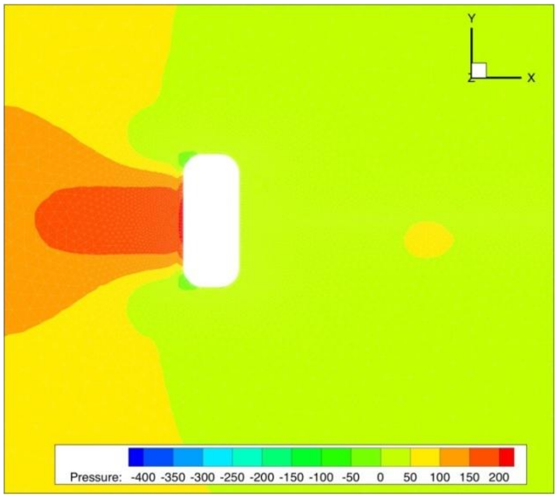

B22 Contour of static pressure on Z=-0.06 plane

[k-e realizable]

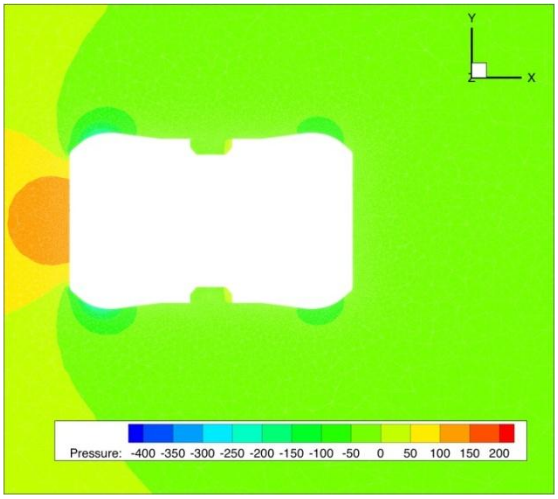

[kw]

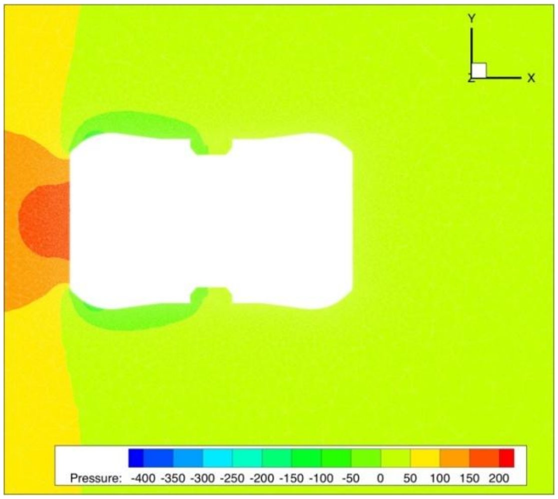

[Spalart-Allmaras]

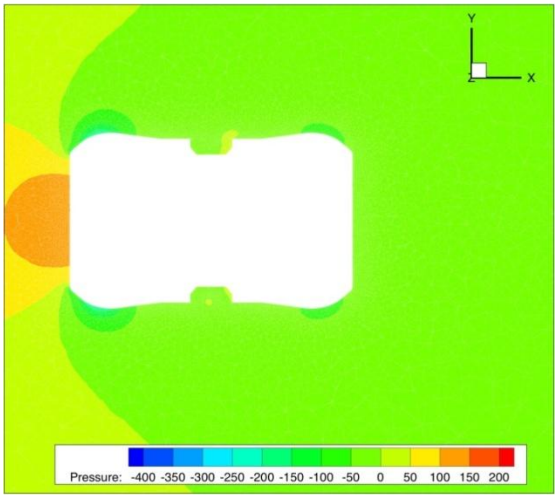

[kw-sst]

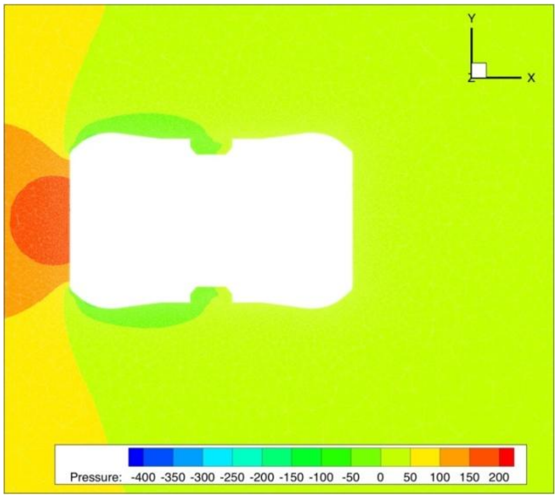

[trans-k-kl-w]

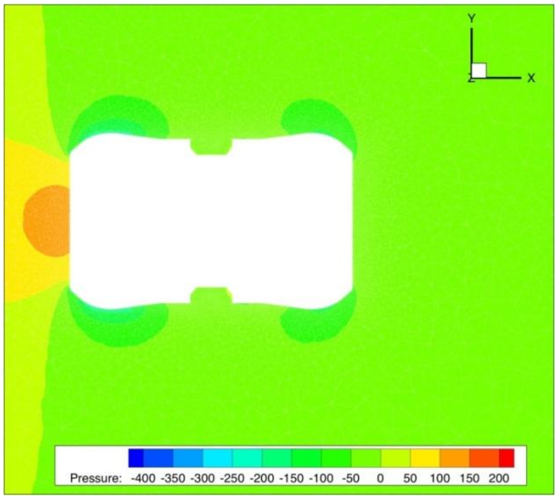

[LES]

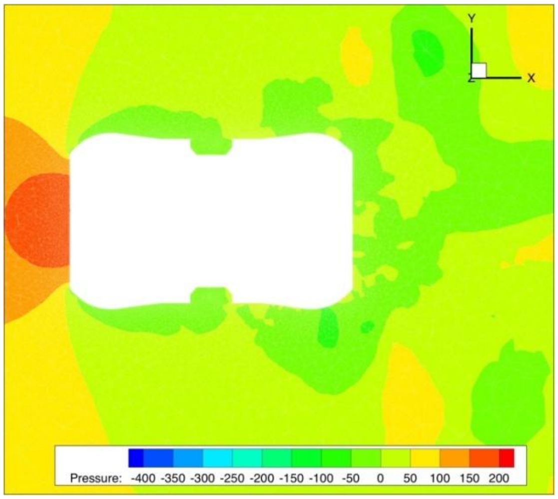

[trans-sst]

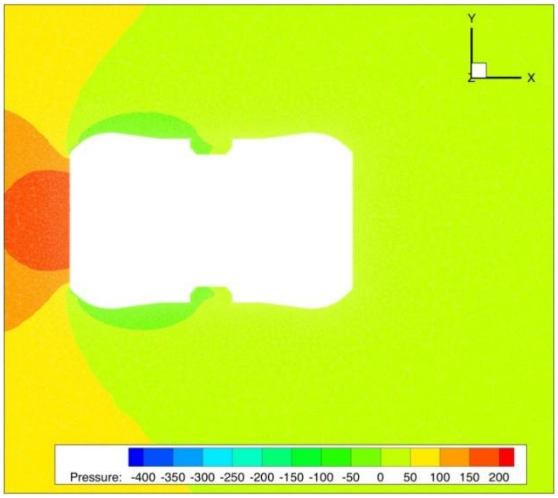

B23 Contour of static pressure on Z=0 plane

[k-e realizable]

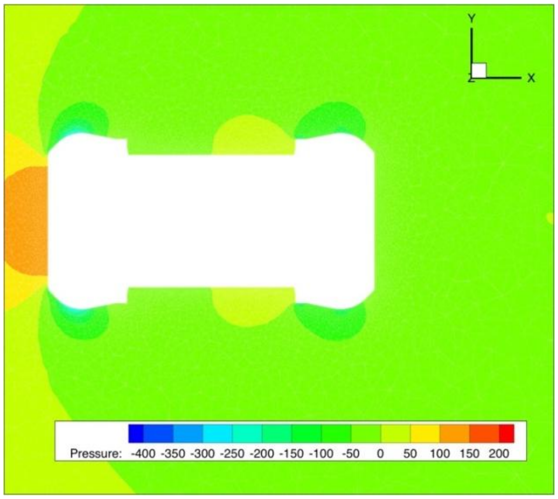

[kw]

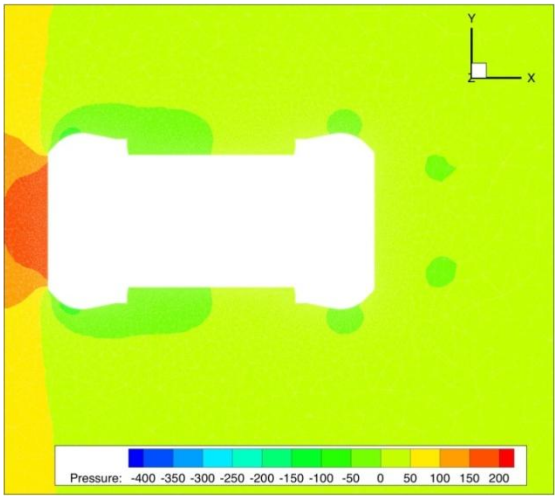

[Spalart-Allmaras]

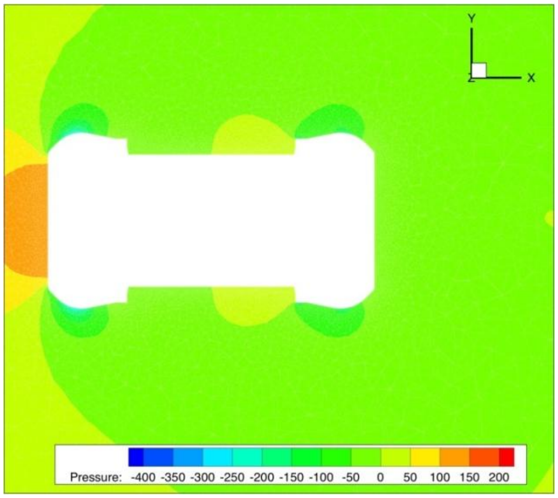

[kw-sst]

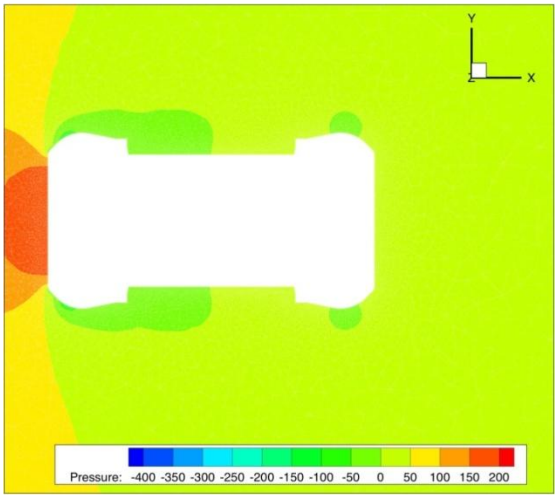

[trans-k-kl-w]

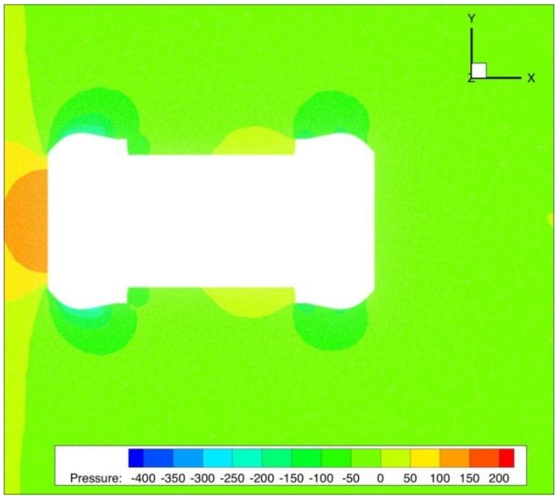

[LES]

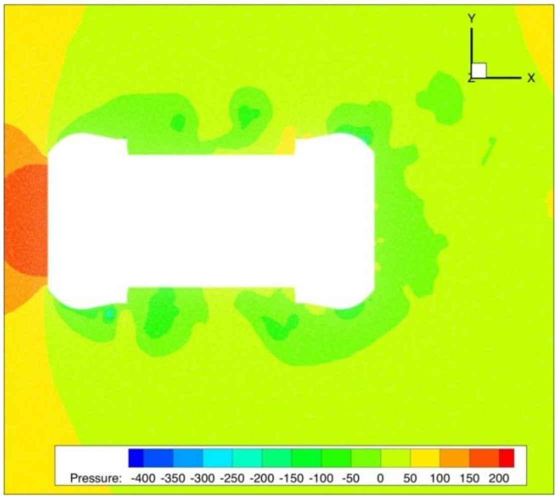

[trans-sst]

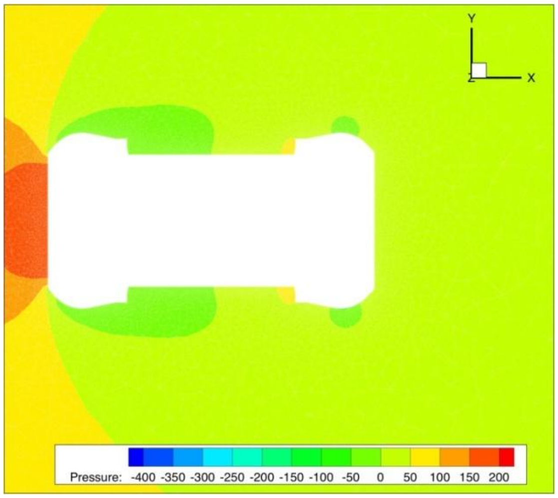

B24 Contour of static pressure on Z=+0.06 plane

[k-e realizable] **[kw]**

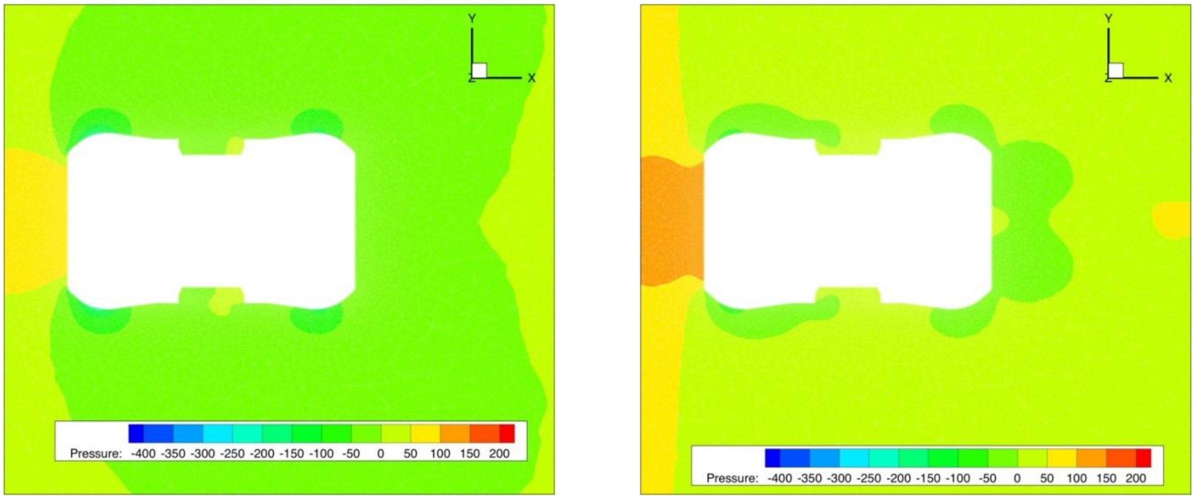

[Spalart-Allmaras] **[kw-sst]**

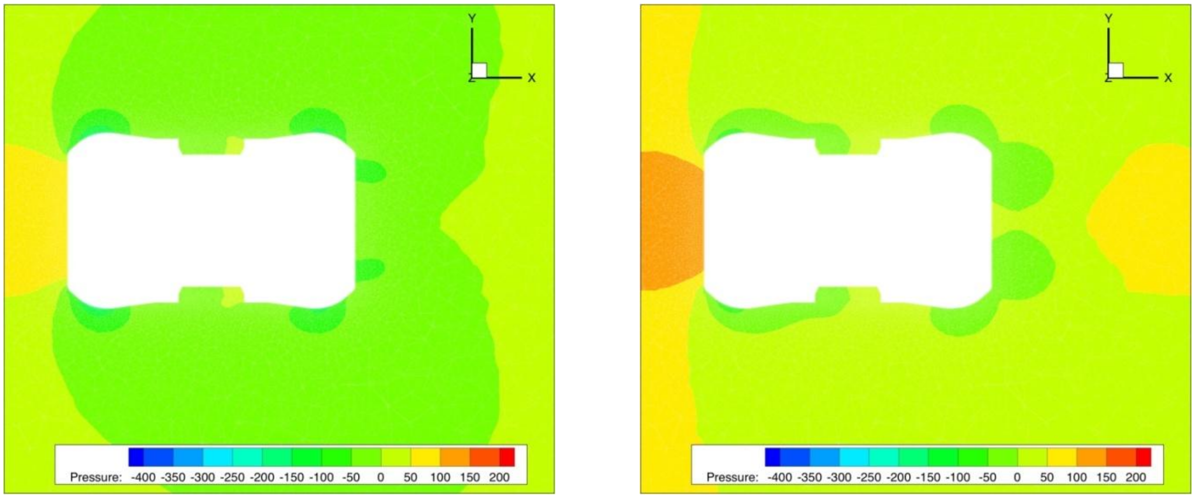

[trans-k-kl-w]

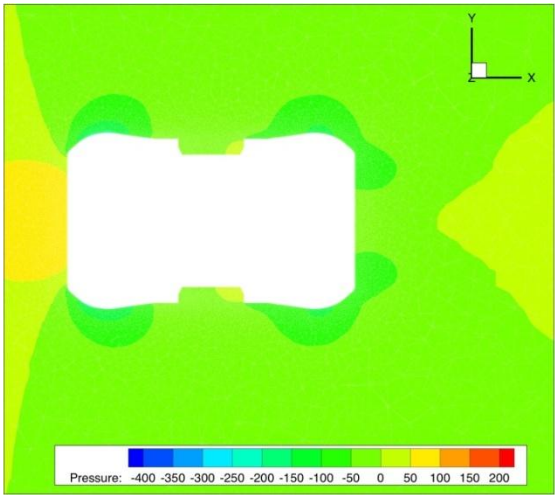

[LES]

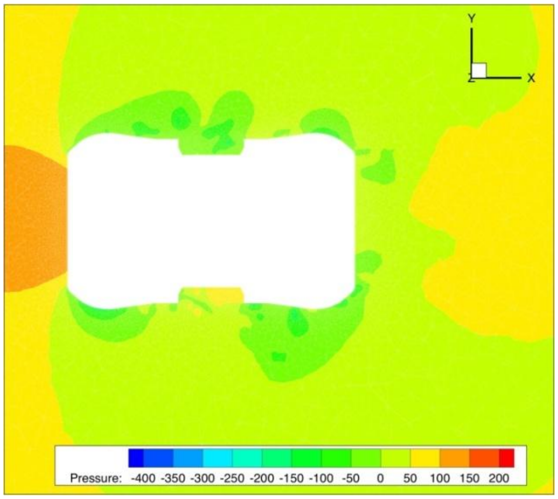

[trans-sst]

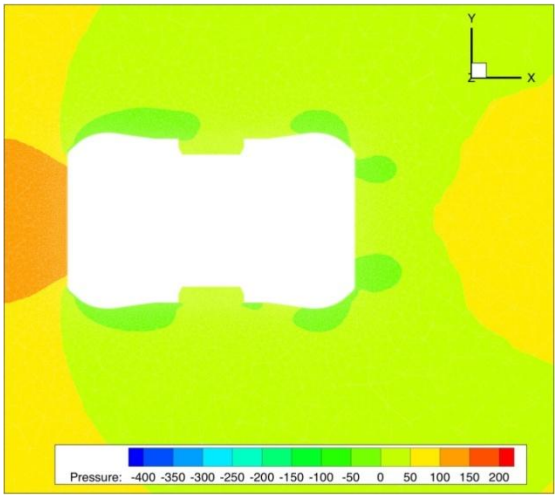

B25 Contour of turbulent kinetic energy on Y=-0.03 plane

[k-e realizable]

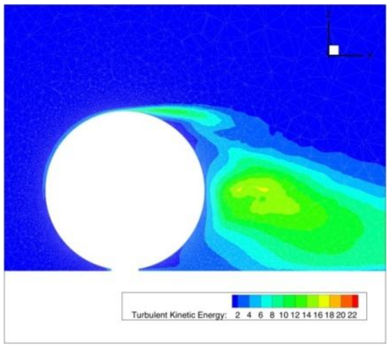

[trans-k-kl-w]

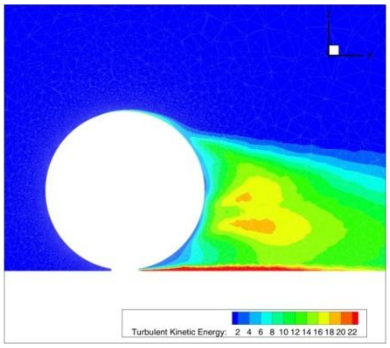

[kw]

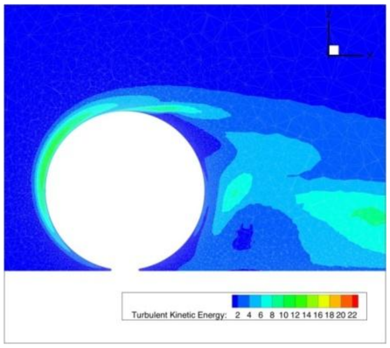

[trans-sst]

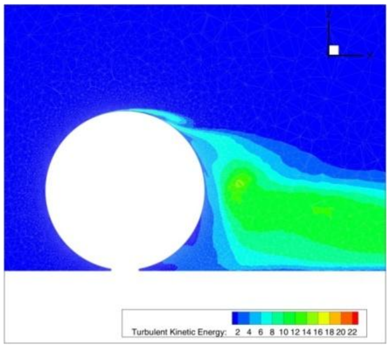

[kw-sst]

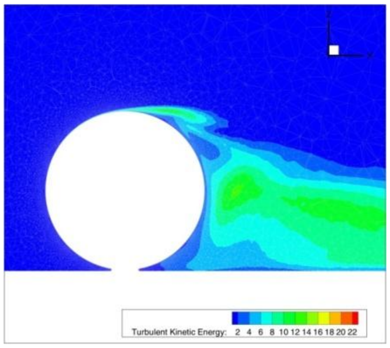

B26 Contour of turbulent kinetic energy on Y=+0.03 plane

[k-e realizable]

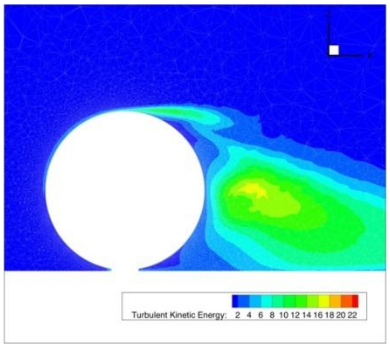

[trans-k-kl-w]

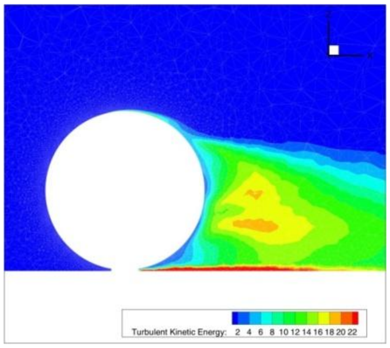

[kw]

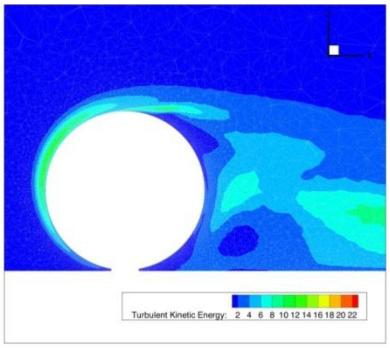

[trans-sst]

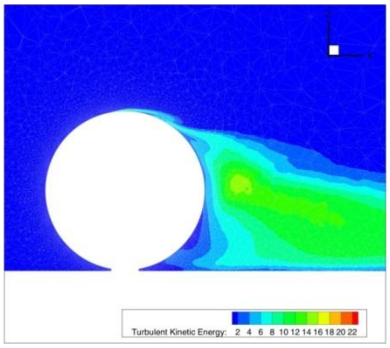

[kw-sst]

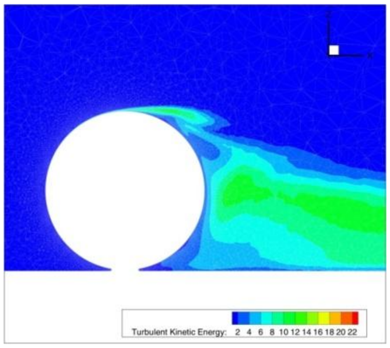

B27 Contour of turbulent kinetic energy on Y=+0.07 plane

[k-e realizable]

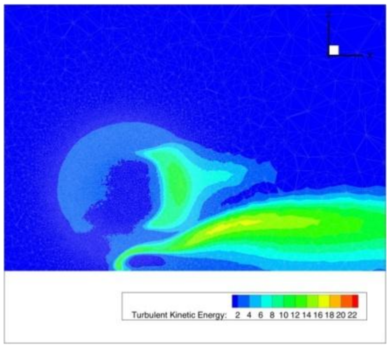

[trans-k-kl-w]

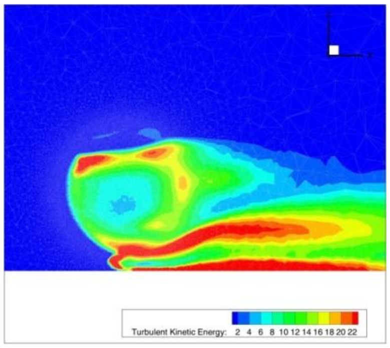

[kw]

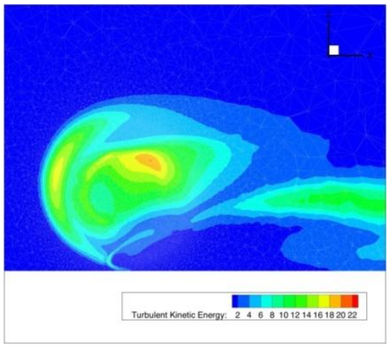

[trans-sst]

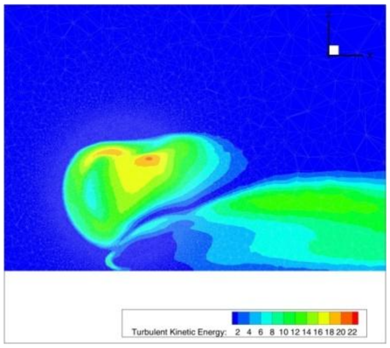

[kw-sst]

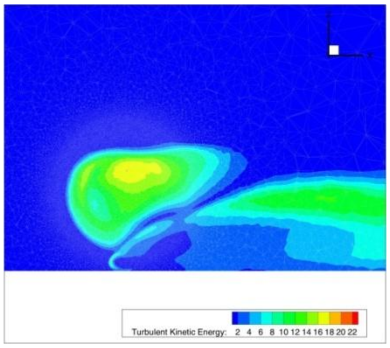

B28 Contour of turbulent kinetic energy on Z=-0.123 plane

[k-e realizable]

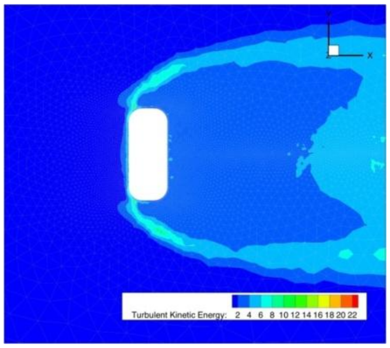

[trans-k-kl-w]

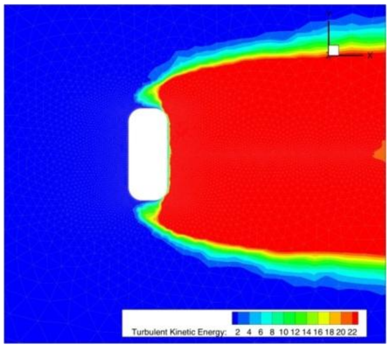

[kw]

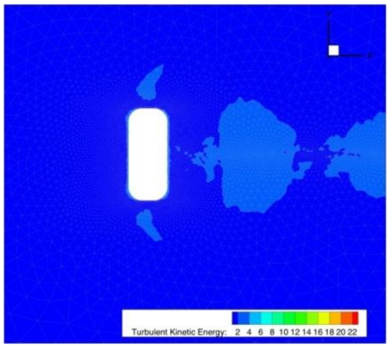

[trans-sst]

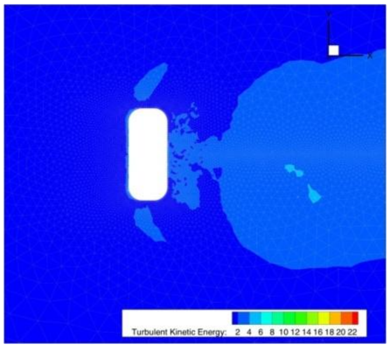

[kw-sst]

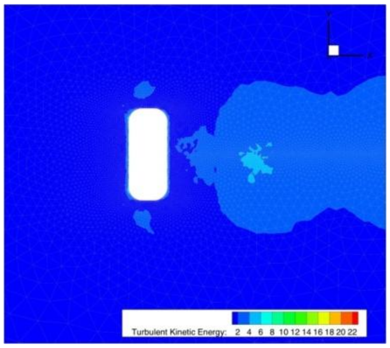

B29 Contour of turbulent kinetic energy on Z=-0.06 plane

[k-e realizable]

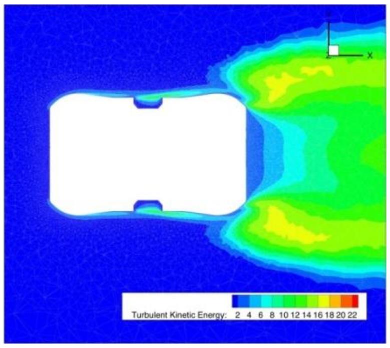

[trans-k-kl-w]

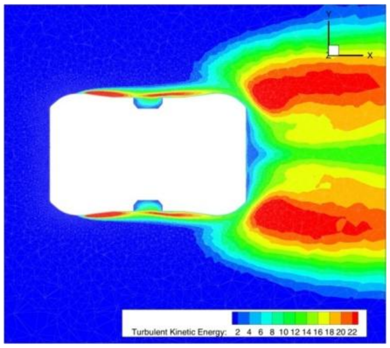

[kw]

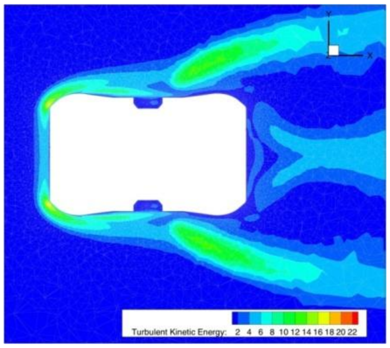

[trans-sst]

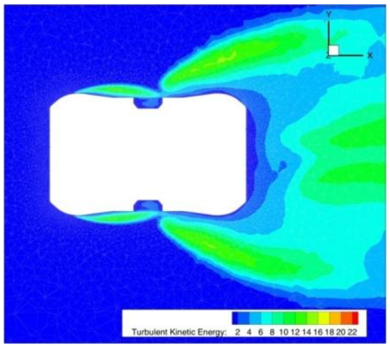

[kw-sst]

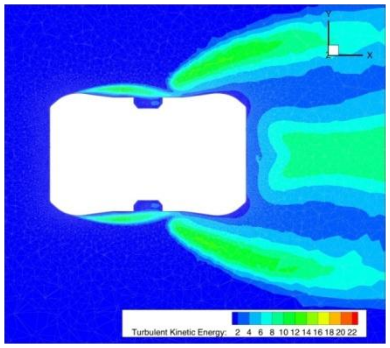

B30 Contour of turbulent kinetic energy on Z=0 plane

[k-e realizable]

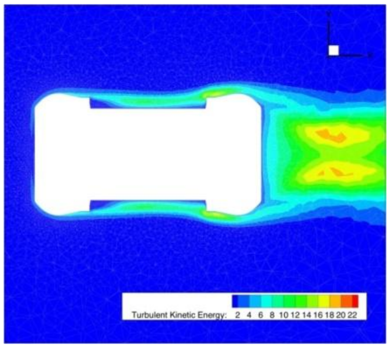

[trans-k-kl-w]

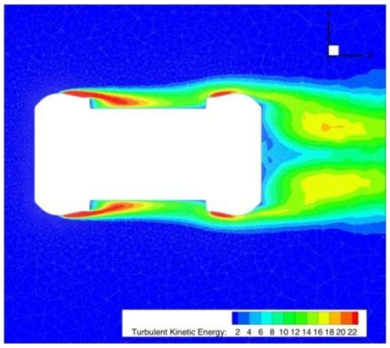

[kw]

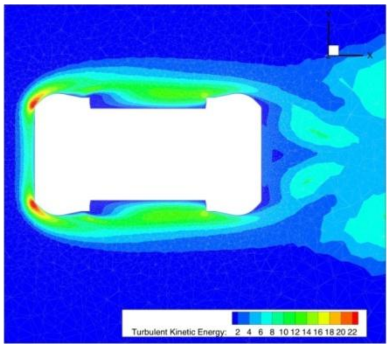

[trans-sst]

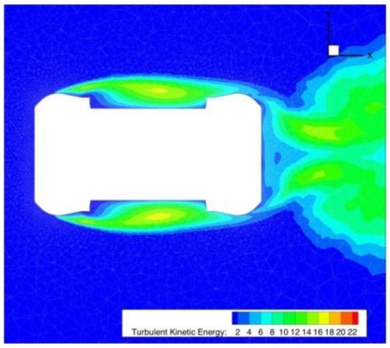

[kw-sst]

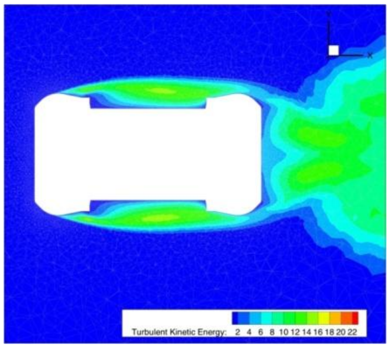

B31 Contour of turbulent kinetic energy on Z=+0.06 plane

[k-e realizable]

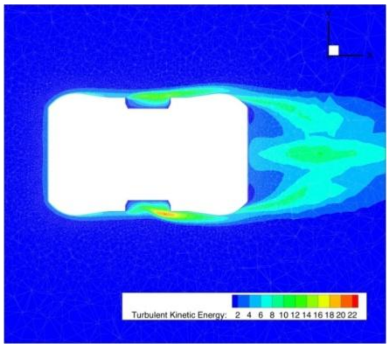

[trans-k-kl-w]

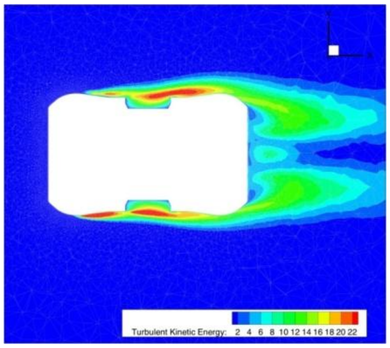

[kw]

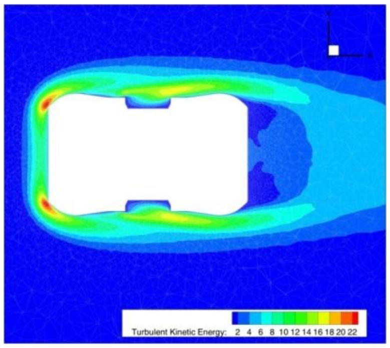

[trans-sst]

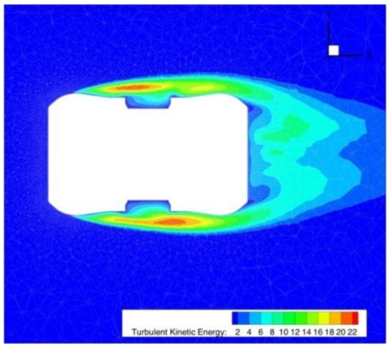

[kw-sst]

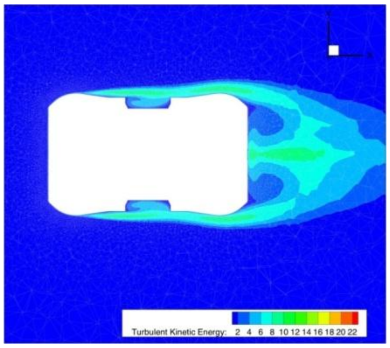

B32 Contour of turbulent dissipation rate on Y=0 plane

[k-e realizable]

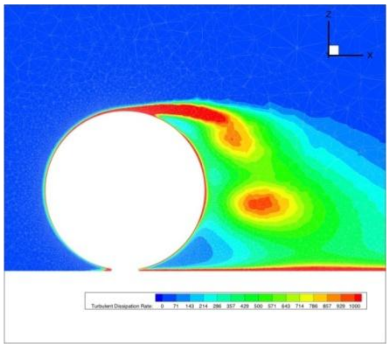

[trans-k-kl-w]

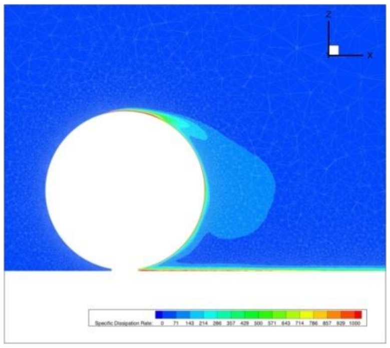

[kw]

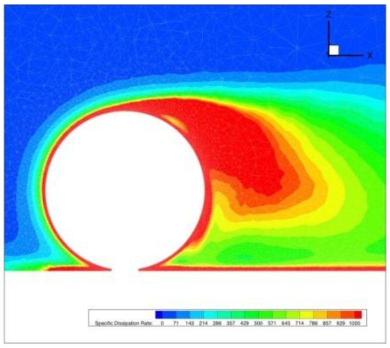

[trans-sst]

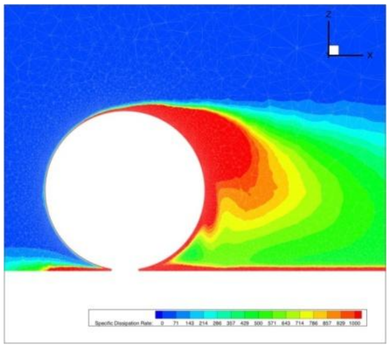

[kw-sst]

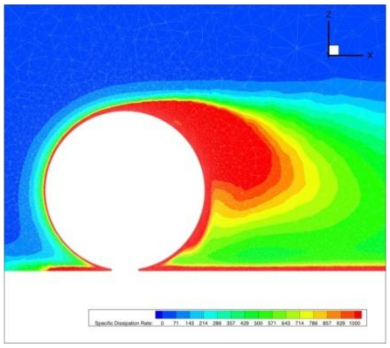

B33 Contour of turbulent dissipation rate on Y=-0.03 plane

[k-e realizable]

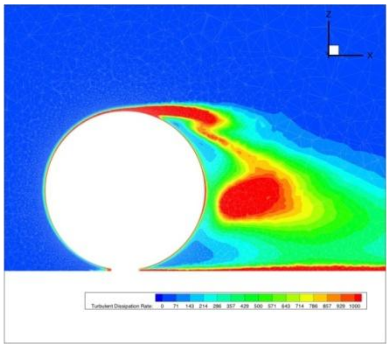

[trans-k-kl-w]

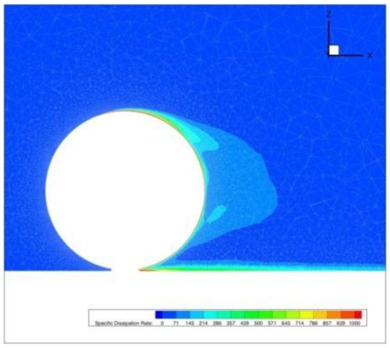

[kw]

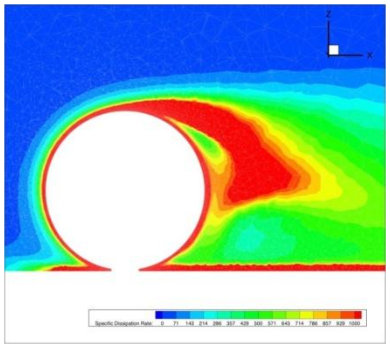

[trans-sst]

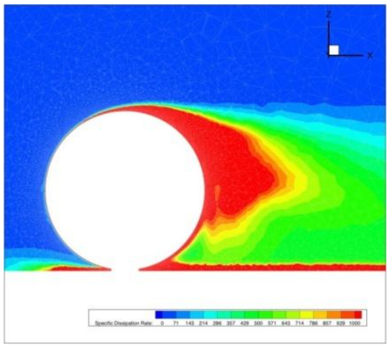

[kw-sst]

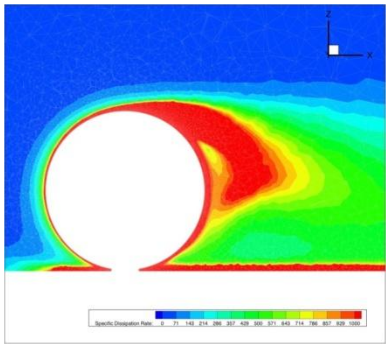

B34 Contour of turbulent dissipation rate on Y=+0.03 plane

[k-e realizable]

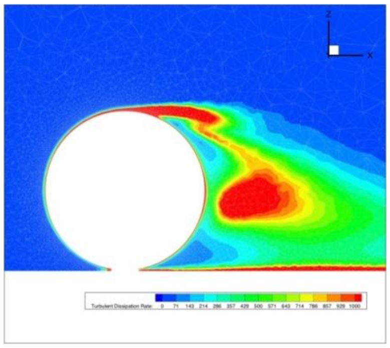

[trans-k-kl-w]

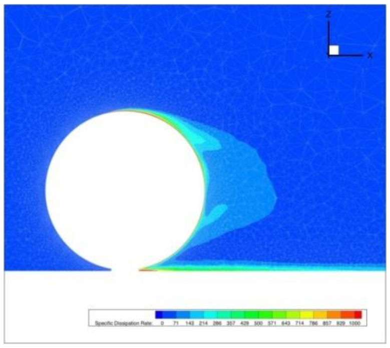

[kw]

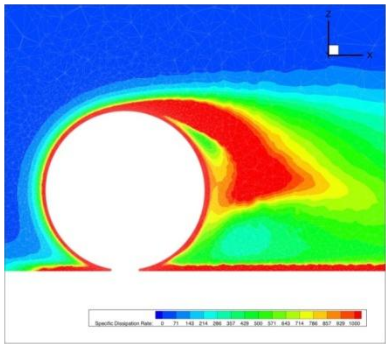

[trans-sst]

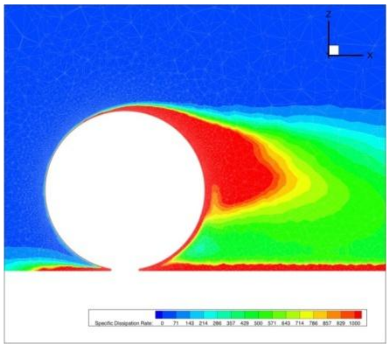

[kw-sst]

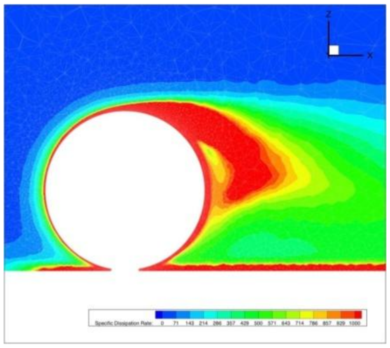

B35 Contour of turbulent dissipation rate on Y=-0.07 plane

[k-e realizable]

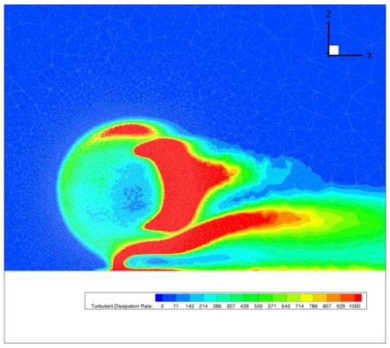

[kw]

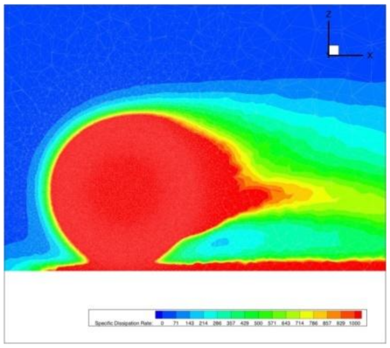

[kw-sst]

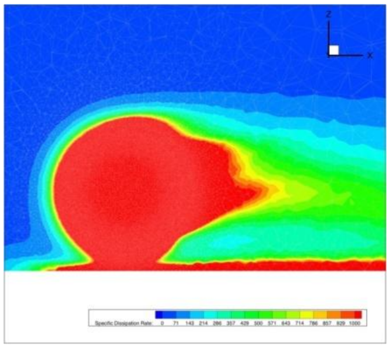

[trans-k-kl-w]

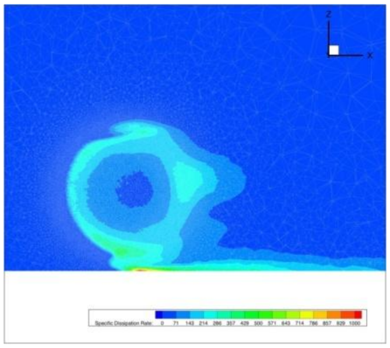

[trans-sst]

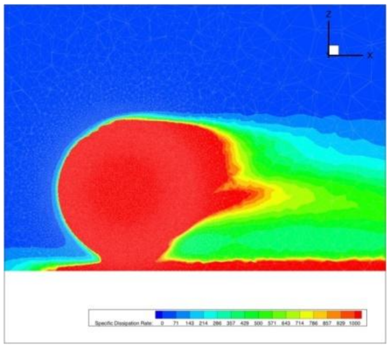

B36 Contour of turbulent dissipation rate on Y=+0.07 plane

[k-e realizable]

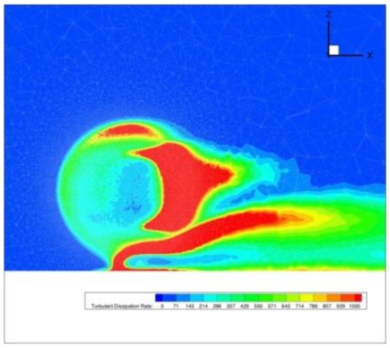

[trans-k-kl-w]

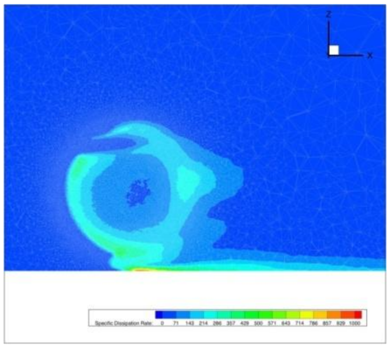

[kw]

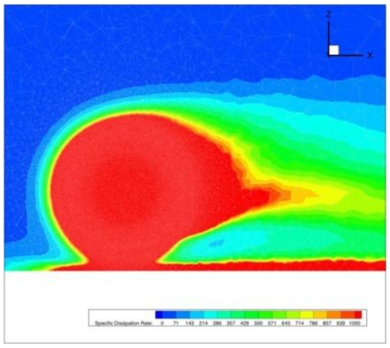

[trans-sst]

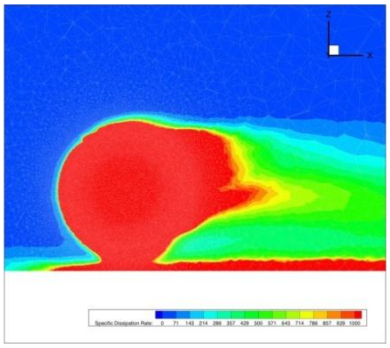

[kw-sst]

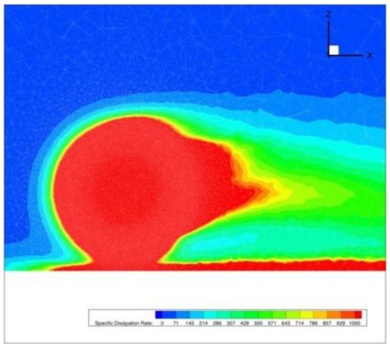

B37 Contour of turbulent dissipation rate on Z=-0.123 plane

Special dispassion rate is shown for kw-based models.

[k-e realizable]

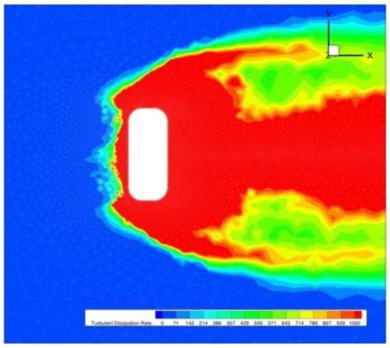

[trans-k-kl-w]

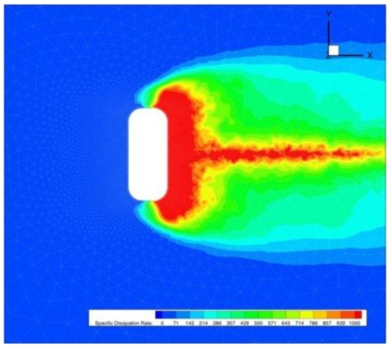

[kw]

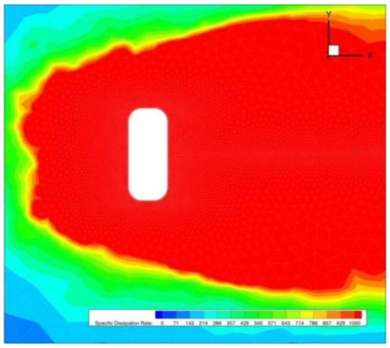

[trans-sst]

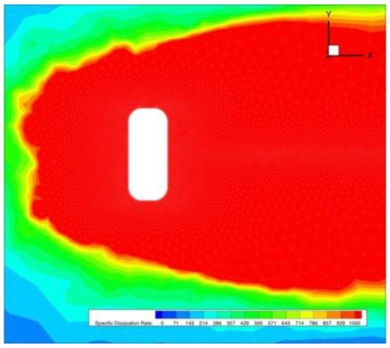

[kw-sst]

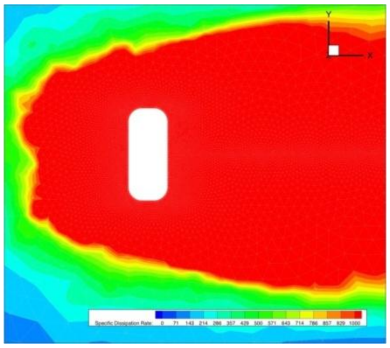

B38 Contour of turbulent dissipation rate on Z=-0.06 plane

Special dispassion rate is shown for kw-based models.

[k-e realizable]

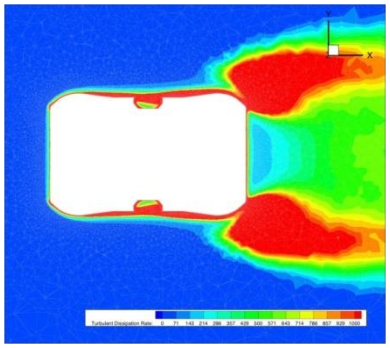

[trans-k-kl-w]

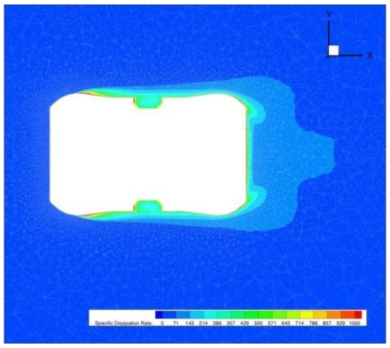

[kw]

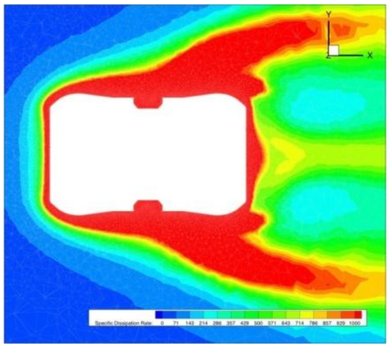

[trans-sst]

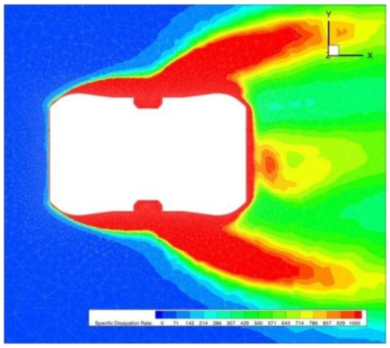

[kw-sst]

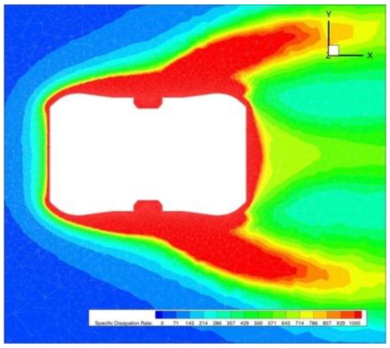

B39 Contour of turbulent dissipation rate on Z=0 plane

Special dispassion rate is shown for kw-based models.

[k-e realizable]

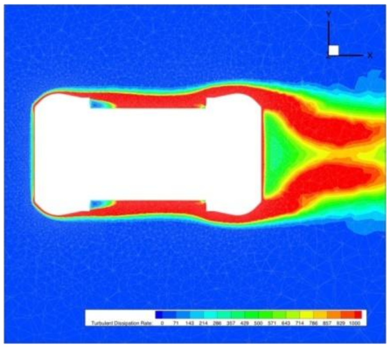

[trans-k-kl-w]

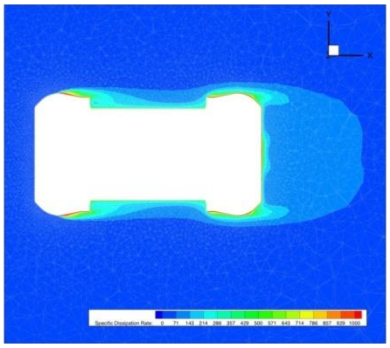

[kw]

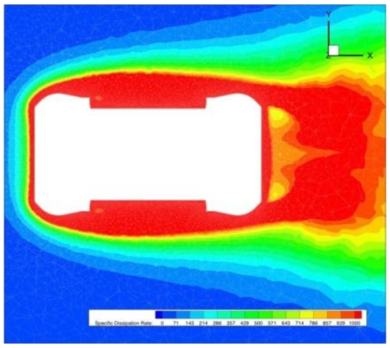

[trans-sst]

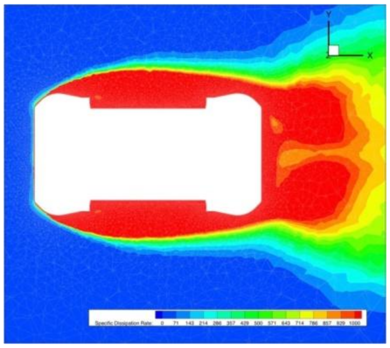

[kw-sst]

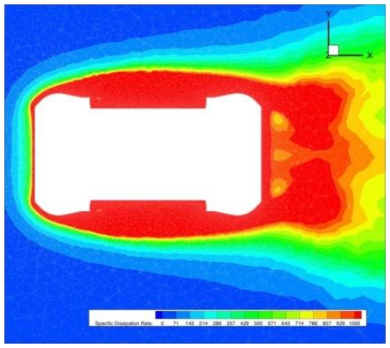

B40 Contour of turbulent dissipation rate on Z=+0.06 plane

Special dispassion rate is shown for kw-based models.

[k-e realizable]

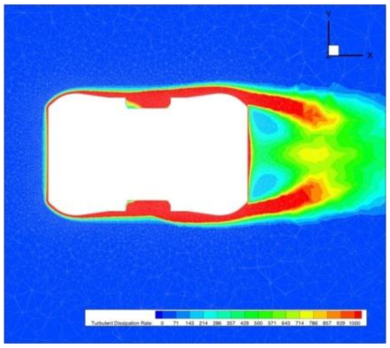

[trans-k-kl-w]

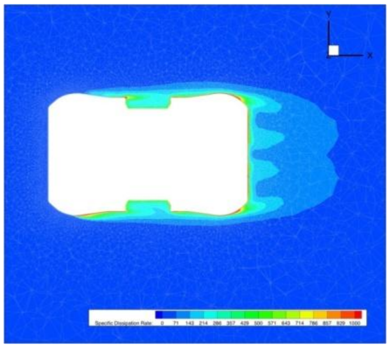

[kw]

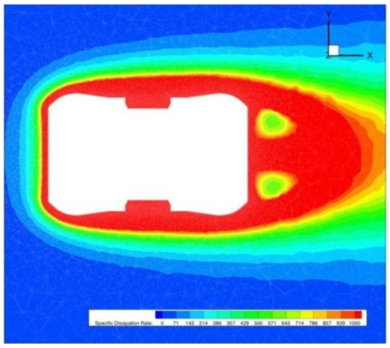

[trans-sst]

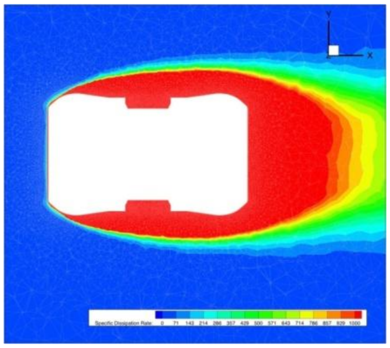

[kw-sst]